Beyond symmetry: normality-based analysis of velocity gradients in turbulent flows

Thesis by
Rahul Arun

In Partial Fulfillment of the Requirements for the
Degree of
Doctor of Philosophy in Aeronautics

CALIFORNIA INSTITUTE OF TECHNOLOGY
Pasadena, California

2025
Defended May 27, 2025

Rahul Arun
ORCID: 0000-0002-5942-169X
https://www.rahularun.com

DEDICATION

In loving memory of Vatsala Nagarajan, October 1, 1932 – May 15, 2019.

ACKNOWLEDGEMENTS

My advisor, Tim Colonius, has profoundly impacted my life. Tim generously welcomed me into his group in a time of uncertainty, gave me freedom to explore beyond the traditional route, showed genuine interest in my ideas, and patiently provided guidance well beyond what was required or expected. His approach afforded me ample opportunity to steer the wheel, navigate obstacles, sometimes make wrong turns, and, most importantly, learn from my mistakes. Tim's mentorship has instilled in me the confidence—and the desire—to be a creative, thoughtful, and honest researcher.

Throughout my academic career, I have been fortunate to receive guidance from a legion of supportive mentors. In high school, the exceptionally generous support Sandip Ghosal and Sheila Edstrom first pointed me in the direction of graduate school. When I was an undergraduate, Beverley McKeon introduced me to turbulence research and endowed me with ample hands-on experience that set the foundations for my graduate work. She was also instrumental in advising me as an undergraduate and a first-year graduate student. I would also like to thank Jane Bae, Scott Dawson, Angeliki Laskari, Peter Schmid, and Melany Hunt for their mentorship during those formative years of my career. I am particularly grateful to Michael Mello, whose teaching and mentorship efforts have inspired me to appreciate the value of a dedicated teacher. I owe additional thanks to Jane Bae and Dale Pullin for allowing me to serve as the teaching assistant for Ae 239: Turbulence and Ae 201: Advanced Fluid Mechanics; my experience in that capacity has solidified my love for teaching. I am grateful to Adrián Lozano-Durán, Dale Pullin, and Tony Leonard for serving on my thesis defense committee, as well as Jane Bae for serving on my candidacy committee. I also acknowledge my collaborators, including Perry Johnson, Mostafa Kamal, and Di Zhou, for their significant contributions to the work leading to this thesis. Finally, I am grateful to Jörn Callies for captivating me with the puzzles of the ocean and believing in me enough to support my upcoming postdoctoral studies in that direction.

In my eight years (so far) at Caltech, I have been lucky to find a handful of close friends. Michael Wadas and Akhil Nekkanti, who are both extraordinary researchers, have offered me countless hours of their time for fun discussions about vortex rings, instabilities, and turbulence. Victor Lopez has also been a great friend and served the essential role of making sure my apartment does

not flood when I traveled to conferences. From my undergraduate days, I deeply appreciate Nicholas Redd, Eshan Govil, and Christie Huang for their continued support and friendship throughout my graduate studies. I also appreciate Tanner Harms, Greg Stroot, and Salvador Gomez for their kindness and friendship over the years. Additionally, I would like to thank Jon Bonafede and the Caltech water polo team for allowing me to relive the glory days as a volunteer assistant coach as well as the Takataka club for providing a fun, supportive, and impactful way to spend Tuesday and Saturday mornings.

Caltech is fortunate to have many administrators who are passionate about improving the student experience. I am most grateful to Marie Lara, Beth Larranaga, and (the now retired) Barbara Green for their unwavering support, accommodations, and lasting positive impacts on my life. I am also grateful to Mikaela Laite, Liza Bradulina, Lynn Seymour, Jamie Meighen-Sei, and Christine Ramirez for their administrative support over the years, as well as Joanna Austin for her service as option representative.

I must also extend twenty-six years of thanks to my parents, K.N. Arun and Urvashi Kaul. I admire their ability to selflessly support my pursuits, despite not fully understanding them, and I am particularly grateful for their patience with a son who is often stubborn and impatient. I am also grateful to my older brother, Nikhil Arun, for setting an example of diligence and dedication.

Although she cannot read this, I feel it necessary to recognize the life-changing companionship of my dog, Frankie, over the past seven years. As the center of my life, she is responsible for the most significant contributions to my health, happiness, and sense of purpose during my undergraduate and graduate years. It is fair to say that, having spent more time at Caltech than most students, Frankie has earned her Honorary Dogtorate.

Lastly, but most importantly, I offer my most heartfelt gratitude to my late grandma, Vatsala Nagarajan, to whom this thesis is dedicated. Though short in stature, she epitomized uprightness, resilience, and generosity. Whenever I visited her in India or talked to her on the phone, she would not let me leave without reminding me: *"whenever something good happens, think of Paati!"* Given the warm memories embodied by this thesis, it seems fitting to end by acknowledging her uniquely significant contributions to my identity as a researcher, teacher, and person.

The work leading to this thesis was supported by the National Defense Science and Engineering Graduate (NDSEG) Fellowship and the Philip G. Saffman Endowed Graduate Fellowship at Caltech.

ABSTRACT

Small-scale turbulence is a hallmark of countless natural and engineered flows. Its features are often described and modeled using the velocity gradient tensor (VGT), which is conventionally decomposed into the (symmetric) strain-rate tensor and the (antisymmetric) vorticity tensor. Although this symmetry-based decomposition has found use in areas such as vortex identification and closure modeling, it provides limited insight into local flow structure. A more refined description can be obtained by further distinguishing the normal and non-normal parts of the VGT. The resulting normality-based decomposition identifies contributions associated with normal straining (symmetric/normal), rigid rotation (antisymmetric/normal), and pure shearing (non-normal). We use this decomposition to identify flow features that are obscured by symmetry-based analyses yet have significant implications for efforts to understand and model turbulent flows.

We first demonstrate that partitioning the strength of velocity gradients using our normality-based approach can distinguish between different regimes in various turbulent flows. In wall-bounded flows, the near-wall partitioning is dominated by shearing whereas the partitioning far from the wall collapses onto the partitioning associated with isotropic turbulence. In an unbounded vortex ring collision, our analysis distinguishes the initial vortex rings, which have a strong imprint from rigid rotation, from the decaying turbulent cloud produced by their collision, for which the partitioning is similar to that of isotropic turbulence. It also identifies enhanced shear–rotation correlations as a distinctive fingerprint of the elliptic instability during transition, which can be interpreted using relevant geometric features of local streamlines. By deriving algebraic expressions for the partitioning constituents in terms of the invariants of the VGT and an additional parameter, which represents the alignment of shear vorticity with the local rotation axis, we identify a key facet of our analysis that goes beyond previous analyses of the VGT.

We then apply our normality-based framework to filtered velocity gradients in direct and large-eddy simulations of isotropic turbulence. Our analysis enables shear layers, which are associated with shear vorticity, to be distinguished from vortex cores, which are associated with rigid rotation, in a multiscale setting. It reveals that filtering mitigates the relative contribution of shear layers in

the subinertial range of the energy cascade. Moreover, it identifies crucial (yet perhaps overlooked) contributions from shear layers to fundamental energy transfer mechanisms, including strain self-amplification, vortex stretching, and backscatter associated with strain–vorticity covariance. The dominant role of shear layers in the backscatter mechanism suggests that they contribute significantly to the bottleneck effect in the subinertial range of the cascade. Our analysis of large-eddy simulation data shows that they also amplify the artificial bottleneck effect produced by an eddy viscosity model in the inertial range. This reflects that the eddy viscosity model mimics an unfiltered direct numerical simulation at a lower Reynolds number. A mixed model can be used to mitigate the artificial bottleneck effect since it more accurately mimics a filtered direct numerical simulation.

PUBLISHED CONTENT AND CONTRIBUTIONS

[1]**Arun, R.**, Kamal, M., Colonius, T., and Johnson, P.L. Normality-based analysis of multiscale velocity gradients and energy transfer in direct and large-eddy simulations of isotropic turbulence. *J. Fluid Mech.* **1021**, A47 (2025).

R.A. designed and performed the analyses, wrote the manuscript, and is the corresponding author. This paper constitutes Chapter 4 of the thesis.

[2]**Arun, R.** and Colonius, T. Velocity gradient partitioning in turbulent flows. *J. Fluid Mech.* **1000**, R5 (2024).

R.A. designed and performed the analyses, wrote the manuscript, and is the corresponding author. This paper constitutes Chapter 3 of the thesis.

[3]**Arun, R.** and Colonius, T. Velocity gradient analysis of a head-on vortex ring collision. *J. Fluid Mech.* **982**, A16 (2024).

R.A. designed and performed the analyses, wrote the manuscript, and is the corresponding author. This paper constitutes Chapter 2 of the thesis.

[4]**Arun, R.**, Bae, H.J., and McKeon, B.J. Towards real-time reconstruction of velocity fluctuations in turbulent channel flow. *Phys. Rev. Fluids* **8**, 064612 (2023).

R.A. designed and performed the analyses, wrote the manuscript, and is the corresponding author. This paper is not included in the thesis.

[5]Zhou, D., **Arun, R.**, Colonius, T., and Bae, H.J. Grid resolution assessment in wall-modeled large-eddy simulation via velocity gradient partitioning. *AIAA SciTech 2025 Forum*, 2025-1376 (2025).

R.A. contributed to the analyses and helped write and revise the manuscript. This paper is not included in the thesis.

TABLE OF CONTENTS

Dedication . . . iii
Acknowledgements . . . iv
Abstract . . . vi
Published Content and Contributions . . . viii
Table of Contents . . . ix
List of Illustrations . . . xi
List of Tables . . . xvii
Chapter I: Introduction . . . 1
1.1 A foreword on the many faces of turbulence . . . 1
1.2 The role of velocity gradients in turbulent flows . . . 1
1.3 Normality-based analysis of velocity gradients . . . 4
1.4 Overview of thesis . . . 9
References . . . 11
Chapter II: Velocity gradient analysis of a head-on vortex ring collision 15
2.1 Introduction . . . 16
2.1.1 Vortex rings . . . 16
2.1.2 Velocity gradients and vortices . . . 19
2.1.3 Contributions . . . 23
2.2 Methods . . . 23
2.2.1 Computational method . . . 23
2.2.2 Vortex ring collision simulation . . . 25
2.2.3 Simulation integral metrics . . . 26
2.3 Evolution of integral metrics and vortical structures . . . 27
2.3.1 Evolution of integral metrics . . . 27
2.3.2 Evolution of vortical flow structures . . . 31
2.4 Partitioning of velocity gradients . . . 34
2.5 Statistical geometry of local streamlines . . . 38
2.5.1 Phase space transformations . . . 38
2.5.2 Phase space distributions . . . 41
2.6 Concluding remarks . . . 46
2.A1 Computational formulation . . . 49
2.A2 Instability development during transition . . . 52
2.A3 Shear–rotation correlations and vortical flow structures . . . 55
2.A4 Effect of shear–rotation alignment . . . 56
References . . . 58
Chapter III: Velocity gradient partitioning in turbulent flows . . . 66
3.1 Introduction . . . 67
3.2 Partitioning framework . . . 68
3.3 Turbulence datasets . . . 69

3.4 Partitioning in nearly isotropic turbulence . . . 71
3.5 Partitioning in wall-bounded turbulence . . . 72
3.5.1 Effect of mean shearing . . . 72
3.5.2 Effect of friction Reynolds number . . . 75
3.6 Concluding remarks . . . 76
3.A1 Symmetry-based partitioning profiles . . . 77
References . . . 78
Chapter IV: Normality-based analysis of multiscale velocity gradients and energy transfer in direct and large-eddy simulations of isotropic turbulence . . . 81
4.1 Introduction . . . 82
4.1.1 Normality-based analysis of velocity gradients in turbulent flows . . . 82
4.1.2 Multiscale velocity gradients and interscale energy transfer 85
4.1.3 Contributions . . . 90
4.2 Theoretical framework . . . 90
4.3 Simulation details . . . 95
4.4 Results . . . 97
4.4.1 Multiscale velocity gradient partitioning . . . 97
4.4.1.1 The DNS cases: the effect of filtering . . . 97
4.4.1.2 The LES cases: the effect of closure modeling . 99
4.4.2 Tube-like and sheet-like vortical structures . . . 101
4.4.3 Interscale energy transfer analysis . . . 103
4.4.3.1 The DNS cases: multiscale mechanisms in the energy cascade . . . 104
4.4.3.2 The LES cases: closure models and the artificial bottleneck effect . . . 110
4.5 Concluding remarks . . . 114
4.A1 Normality-based analysis of Burgers vortex layers and tubes . 116
4.A2 Collapse of the multiscale velocity gradient partitioning . . . 119
References . . . 122
Chapter V: Concluding remarks . . . 128
5.1 Summary of contributions . . . 128
5.2 Outlook for future work . . . 130
5.3 An afterword on the anatomy of turbulence . . . 132
References . . . 133

LIST OF ILLUSTRATIONS

Number *Page*

1.1 Misalignment of the coordinate axes of the principal frame (blue), the coordinate axes of the strain-rate eigenframe (black), and the unit vorticity vector (red) for the VGT in (1.16). 8

1.2 Depictions of fluid particle trajectories (left) and normality-based constituents (right) for a spatially linear velocity field undergoing vortex stretching. The trajectories progress from darker to lighter colors. The black arrows, red vortex tube, and blue shear layer correspond to normal straining, rigid rotation, and pure shearing, respectively. 10

2.1 Initial geometry of the flow configuration used to simulate the head-on collision between vortex rings. The shading of the vortex cores reflects their Gaussian vorticity profiles. 25

2.2 Temporal evolution of the integral metrics defined in §2.2.3 over the course of the simulation. The vertical lines correspond to the reference times in Table 2.1 and they are colored accordingly. The horizontal lines in the Re^{eff} panel represent Re_{Γ_0} (solid) with 10% margins (dashed). The impulse magnitude is normalized by that of each vortex ring in isolation, $|\boldsymbol{I}_{V1}| \approx 1.02\pi \approx 3.204$. The enstrophies $E_{\mathcal{E}}$ and $E_{\mathcal{C}}$ are computed using vorticities located at the edges and centers, respectively, of the computational cells. . 28

2.3 Visualizations of the vortex boundaries ($\Omega_r = 0.52$, left side) and vortex cores ($\Omega_r = 0.93$, right side), colored by $\cos\theta^*$, for each reference time from Table 2.1. A movie depicting the evolution of the vortex boundaries from the auxiliary viewpoint (leftmost column) is provided as supplementary material available at https://doi.org/10.1017/jfm.2024.90. 32

2.4 Relative contributions of the constituents of the Cauchy–Stokes decomposition and the triple decomposition to A^2. The vertical lines correspond to the reference times in Table 2.1 and they are colored accordingly. 35

2.5 Shear–rotation phase space trajectory of the flow, highlighting the evolution during equilibration (left inset) and transition and turbulent decay (right inset). The contours represent increments of 0.05 in the color scale. The white circle marks the initial condition and the fill colors of the black circles correspond to the reference times they represent from Table 2.1. 37

2.6 The $q_A - r_A$ phase space (top left) and the variations in $\dot{\epsilon}^2$, $\dot{\gamma}^2$, $\dot{\varphi}^2$, $2\dot{\boldsymbol{\varphi}} : \dot{\boldsymbol{\gamma}}$, and ζ in this space when $\theta_\omega = 43.57°$ is held constant. The top left panel shows the boundaries corresponding to the symmetry-based (dotted green) and the geometry-based (solid blue) vortex criteria (see §2.1.2). It also labels the four classes of non-degenerate local streamline topologies: stable-focus–stretching (SFS), unstable-focus–compression (UFC), stable-node–saddle-saddle (SNSS), and unstable-node–saddle-saddle (UNSS). 40

2.7 Joint p.d.f.s of the velocity gradients satisfying $A^2/\max(A^2) \geq 0.1\%$ in the $q_A - r_A$ phase space (left) and $W^2/\max(W^2) \geq 0.1\%$ in the shear–rotation phase space (right) at times $t = 0.75t^*$, $0.90t^*$, $1.00t^*$, and $1.25t^*$ (from top to bottom). The blue triangles represent the centroids of the distributions and the magenta contours represent the p.d.f. levels for which 90% of the flow (by volume) resides at higher p.d.f. levels. These contours are smoothed by using coarser p.d.f. bins to ensure that they roughly enclose the regions with higher p.d.f. levels. 42

2.8 Joint p.d.f.s (top and middle) of the velocity gradients in the $\zeta - \theta_\omega$ phase space at the same times, at the same points, and in the same style as those in Figure 2.7. The bottom plots superimpose the 90% contours and centroids for $t = 0.75t^*$ (red) and $t = 1.25t^*$ (black) on $2\dot{\boldsymbol{\varphi}}:\dot{\boldsymbol{\gamma}}/\tilde{W}^2$ (left) and on Ω_r (right), as given by (2.15). 45

2.9 Unit cells of the staggered Cartesian grid at the base and refinement levels of the mesh, showing the locations of relevant flow variables. 50

2.10 Magnified versions of the auxiliary viewpoints in Figure 2.3 at the reference times associated with instability growth and transition. 53

2.11 Fourier coefficient amplitudes: $|\hat{\omega}_z|$ (colored by radial displacement from $\bar{R}_p$) and $|\hat{R}_p|$ (black). At each of the reference times shown, δ represents the average slenderness ratio of the vortex rings. The values of $|\hat{\omega}_z|$ at wavenumbers pertinent to instability development are marked by symbols and the shaded regions represent wavenumbers for which $C > 10$. 54

2.12 Visualizations of the vortex boundaries ($\Omega_r = 0.52$, left side) and vortex cores ($\Omega_r = 0.93$, right side), colored by $2\dot{\boldsymbol{\varphi}}{:}\dot{\boldsymbol{\gamma}}/\tilde{W}^2$, for each reference time from Table 2.1. A movie depicting the evolution of the vortex boundaries from the auxiliary viewpoint (leftmost column) is provided as supplementary material. . . . 57

2.13 Transformations to $\dot{\varphi}^2$, $2\dot{\boldsymbol{\varphi}}{:}\dot{\boldsymbol{\gamma}}$, and ζ from the $q_A - r_A$ phase space for various alignment angles, θ_ω. The plots are in the same style as those in Figure 2.6. 58

3.1 Total (a,c,e) and fluctuation (b,d,f) partitioning profiles for the channels and boundary layers in terms of wall-normal location in inner units (a,b) and mean shearing strength (c–f). The vertical lines represent the isotropic values. The BL0729 and BL1024 profiles are shown for $Re_\tau \approx 729$ and 1000, respectively, and the top boundary of the log-law region represents Ch1000. The dashed white lines in (a,b) represent the locations of the partitioning values reported in Table 3.2 for BL0729 and BL1024. In (a,b), the markers are used to distinguish between the profiles and, in (c–f), they represent actual data points. In (c–f), the mean shearing axis is reversed and the dashed lines represent comparable linear–log trends for each dataset, with the partitioning as the dependent variable. 73

3.2 Streamwise development of BL0729 (a,b) and BL1024 (c,d) in terms of Re_τ, where the color axis represents $\bar{A}^2_\gamma/\bar{A}^2_{\gamma,w}$. The white, gray, and black contours represent $\Delta_{iso} = 1\%$, $\Delta_{iso} = 2\%$, and $\Delta_{iso} = 5\%$, respectively, for the total partitioning (a,c) and $\Delta'_{iso} = 1\%$, $\Delta'_{iso} = 2\%$, and $\Delta'_{iso} = 5\%$, respectively, for the fluctuation partitioning (b,d). The dashed and dash-dotted black lines represent the top of the viscous sublayer ($y^+ = 5$) and the top of the buffer layer ($y^+ = 30$), respectively, and the dotted black lines represent $y^+ = 100$ and $y^+ = 150$. The black circles represent the locations of the partitioning values reported in Table 3.2 and δ represents the boundary-layer thickness. . . 75

3.3 Symmetry-based total (a) and fluctuation (b) partitioning profiles for the channels and boundary layers in terms of wall-normal location in inner units. The plots are in the same style as those in Figure 3.1. 78

4.1 (a) Symmetry-based scale-local and scale-nonlocal contributions to interscale energy transfer in forced isotropic turbulence. The symbols represent DNS datasets at Taylor-scale Reynolds numbers of $Re_\lambda \approx 315$ (DNS315) and $Re_\lambda \approx 400$ (DNS400) and the curves represent the $Re_\lambda \approx 400$ results of Johnson [1, 2]. The shaded region captures the bottom of the inertial range for DNS400. (b) Energy spectra for the unfiltered and filtered velocity fields in DNS400 as well as LES cases that employ eddy viscosity (Vis400) and mixed (Mix400) models at $Re_\lambda \approx 400$. The filtered DNS and LES cases employ a filter width of $2\ell/\eta = 48$. The dotted line represents the inertial range scaling, $E(k) = 1.6\,\langle\Phi\rangle^{2/3}\,k^{-5/3}$, and the inset depicts a linear–log plot of the compensated energy spectra. Technical details of the simulations are described in §4.3. 89

4.2 Partitioning of filtered velocity gradients for the DNS cases, where shearing is represented using $S^2_{\ell,\gamma} = \Omega^2_{\ell,\gamma} = \frac{1}{2}A^2_{\ell,\gamma}$. The horizontal dashed lines represent the unfiltered partitioning in the high-Re_λ limit, the vertical dotted line represents the typical thickness of small-scale shear layers, $\delta_\gamma = 9\eta$, and the shaded region approximates the inertial range for DNS400 as $50 \le 2\ell/\eta \le 150$. 98

4.3 (a) Partitioning of filtered velocity gradients for the LES cases. The solid curves represent the filtered DNS400 partitioning and the horizontal dashed lines represent the unfiltered partitioning in the high-Re_λ limit. The lower limit of the filter width axis represents the LES filter width, $2\ell_{LES}/\eta = 48$, and the shaded region approximates the inertial range. (b) Partitioning for Vis400 replotted as a function of $2\ell_*/\eta_*$, where $\ell_* = \sqrt{\ell^2 - \ell_{LES}^2}$ is the complementary filter width and $\eta_* \approx 15\eta$ is an effective Kolmogorov scale. The solid curves represent the partitioning produced by a DNS at $Re_\lambda \approx 61$, which has a Kolmogorov scale of approximately η_*. The vertical dotted line represents the typical thickness of small-scale shear layers, $\delta_\gamma = 9\eta$. 100

4.4 Vortical flow structures associated with rigid rotation and shear vorticity for an unfiltered ($\ell = 0$) DNS at $Re_\lambda \approx 61$ (a,b), DNS400 filtered at $2\ell/\eta = 48$ (c,d), and Vis400 (e,f) and Mix400 (g,h) at the LES filter width, $2\ell_{LES}/\eta = 48$. The grayscale visualizations depict the strengths of rigid rotation, $\omega_{\ell,\varphi}^2$, and shear vorticity, $\omega_{\ell,\gamma}^2$, normalized by the spatially averaged vorticity strength, $\left\langle \omega_\ell^2 \right\rangle$, and the isosurfaces represent $\omega_{\ell,\varphi}^2 \big/ \left\langle \omega_\ell^2 \right\rangle = 2$ (red) and $\omega_{\ell,\gamma}^2 \big/ \left\langle \omega_\ell^2 \right\rangle = 2$ (blue). 102

4.5 Normality-based contributions to interscale energy transfer for the DNS cases. The contributions represent multiscale strain self-amplification (a), vortex stretching (b), strain–vorticity covariance (c), and aggregates across these three mechanisms (d). The vertical dotted lines represent the typical thickness of small-scale shear layers, $\delta_\gamma = 9\eta$, and the shaded regions capture the bottom of the inertial range for DNS400. 105

4.6 Normality-based contributions (as defined in §4.2) to the cascade rates associated with scale-local strain self-amplification (a) and vortex stretching (b) and scale-nonlocal strain self-amplification (c) and vortex stretching (d). The vertical dotted lines represent the typical thickness of small-scale shear layers, $\delta_\gamma = 9\eta$, and the shaded regions capture the bottom of the inertial range for DNS400. 108

4.7 (a,c) Resolved symmetry-based scale-local and scale-nonlocal cascade rates for Mix400 (a) and Vis400 (c) overlaid on curves that represent the DNS results of Johnson [1, 2] in the same style as Figure 4.1(a). (b,d) Normality-based contributions to $\tilde{\Pi}^{\ell,c}$ for Mix400 (b) and Vis400 (d). Panels (e) and (f) replot the Vis400 results from panels (c) and (d), respectively, normalized by $\left\langle \tilde{\Pi}^{\ell} \right\rangle$ and as a function of $2\ell_*/\eta_*$, where $\eta_* \approx 15\eta$. The curves (e,f) represent a DNS at $Re_\lambda \approx 61$, which has a Kolmogorov scale of approximately η_*. The shaded regions approximate the inertial range and the vertical dotted lines represent $\delta_\gamma = 9\eta$. 112

4.8 Resolved normality-based cascade rates for Vis400, plotted in the same style as Figure 4.7(e,f). 113

4.9 (a) Velocity gradient partitioning for Burgers vortex layers at $Re_U = 10^2$ (solid), $Re_U = 10^4$ (dashed), and $Re_U = 10^6$ (dotted). (b) Velocity gradient partitioning for the Burgers vortex tube in the limit of $Re_\Gamma \to \infty$. (c) Normality-based contributions to strain self-amplification (SS) and vortex stretching (VS) for the Burgers vortex tube from (b). The vertical dotted lines (b,c) represent the vortex boundary as identified by $Q = 0$ and $\Delta = 0$, where Q is the second invariant of the VGT and Δ is the discriminant of the VGT. 118

4.10 (a) Partitioning of filtered velocity gradients for DNS cases at various Reynolds numbers. The symbols represent averages over all snapshots and the shading represents ranges for single-snapshot averages. In all panels, the solid curves represent the averaged partitioning at $Re_\lambda \approx 400$, the horizontal dashed lines represent the unfiltered partitioning in the high-Re_λ limit, and the vertical dotted lines represent the typical thickness of small-scale shear layers, $\delta_\gamma = 9\eta$. 120

5.1 Visualization of the vorticity strength, ω^2, in a slice of isotropic turbulence at a Taylor-scale Reynolds number of $Re_\lambda \approx 400$ overlaid with contours of the contributions from rigid rotation (red) and shear vorticity (blue) at a threshold of $0.15\,\langle\omega^2\rangle$, where $\langle\cdot\rangle$ denotes averaging over the slice. 133

LIST OF TABLES

Number *Page*

2.1 Reference times used to analyze the initial (red), transitional (green), and turbulent (blue) regimes of the present vortex ring collision, where $t^* = 14.77$ is the time of maximum dissipation. Here, $\bar{R}_p$ represents the mean vortex ring radius (see Appendix 2.A2), V is the volume of the computational domain, and ϕ_k is the fraction of V occupied by level k of the AMR grid, which has grid spacing $\Delta x_k = \Delta x_{\text{base}}/2^k$ with $\Delta x_{\text{base}} = 0.04$. 29

2.2 Comparison of the equilibrium partitioning of the velocity gradients for the present vortex ring collision with the partitioning computed for forced isotropic turbulence [3]. Here, the equilibrium partitioning is computed as the mean over the turbulent decay regime ($t \gtrsim t^*$) and it is insensitive to the length of the averaging interval. 36

3.1 Turbulence datasets considered in the present analyses. Taylor-scale and friction Reynolds numbers are denoted by Re_λ and Re_τ, respectively, and N_t denotes the number of snapshots. The grid sizes correspond to the streamwise (x), wall-normal (y), and spanwise (z) directions, respectively. 70

3.2 Velocity gradient partitioning for each flow and the corresponding deviation metrics. The partitioning is reported at the channel centerline for Ch0186 and Ch1000 and at $(Re_\tau, y^+) \approx (729, 159)$ and $(1000, 155)$ for BL0729 and BL1024, respectively. The column shadings reflect our partitioning color scheme. 71

4.1 Primary simulations considered in the present study. The DNS cases employ $N_x^3 = 1024^3$ collocation points and are dealiased using the $2\sqrt{2}/3$ truncation rule with phase-shifting [4] such that $k_{max} = N_x\sqrt{2}/3$. The LES cases employ $N_x^3 = 128^3$ collocation points and filter widths of $2\ell_{LES}/\eta = 48$. They are dealiased using the 2/3 truncation rule such that $k_{max} = N_x/3$. Additional cases, including random velocity gradients, DNS cases at lower Reynolds numbers, and LES cases with different filter widths are described and analyzed in Appendix 4.A2. 95

4.2 Comparison of the normality-based contributions to strain self-amplification (SS) and vortex stretching (VS) for the unfiltered DNS cases. The contributions to SS and VS are normalized by $\left\langle -S_{ij}S_{ik}S_{jk} \right\rangle$ and $\left\langle -S_{ij}\Omega_{ik}\Omega_{jk} \right\rangle$. respectively, such that they sum to unity for each mechanism. 109

4.3 Partitioning statistics produced by random velocity gradients and various DNS and LES cases. Each LES case represents a separate simulation where $\ell = \ell_{LES}$ represents the LES filter width. 121

Chapter 1

INTRODUCTION

"Finally, there is a physical problem that is common to many fields, that is very old, and that has not been solved. It is not the problem of finding new fundamental particles, but something left over from a long time ago—over a hundred years. Nobody in physics has really been able to analyze it mathematically satisfactorily in spite of its importance to the sister sciences. It is the analysis of circulating or turbulent fluids."

—Richard P. Feynman [1]

1.1 A foreword on the many faces of turbulence

The significance of turbulence—which captures the multiscale structures and chaotic dynamics of fluid motions at high Reynolds numbers—is in the eye of the beholder. For mathematicians, it embodies challenges associated with nonlinear partial differential equations [2]. For solar physicists, it is crucial for generating and heating the solar wind [3]. For environmental scientists, it transports and mixes tracers and limits weather prediction capabilities [4]. For engineers, it can generate undesirable noise in jets [5] as well as costly drag along ships, airplanes, and pipelines [6]. For cardiologists, it may be a sign of cardiovascular disease [7]. For Vincent van Gogh, it inspired subtle yet strikingly accurate details in his famed painting, *The Starry Night* [8]. For me, turbulence makes tangible the inescapable yet beautiful complexity of reality.

1.2 The role of velocity gradients in turbulent flows

The broad spectrum of turbulent flows is unified by the presence and, to a large extent, the behavior of small-scale turbulence. As a result, the statistical and structural features of small-scale turbulence have guided efforts to simplify the complexity of turbulent flows for many decades [9–13]. The velocity gradient tensor (VGT), $A_{ij} = \partial u_i/\partial x_j$, is essential to the description of these features. We refer to the reviews of Wallace [14], Meneveau [15], and Johnson and Wilczek [16] for background on the rich history of research on velocity gradients in turbulent flows. In this section, we develop and discuss a selection of well-established results that are foundational to the contributions of this thesis.

The VGT contributes to the first-order Taylor expansion of the local velocity field about a point $\boldsymbol{x_0}$, which can be expressed as

$$u_i(\boldsymbol{x}, t) = u_i(\boldsymbol{x_0}, t) + (x_j - x_{0,j}) A_{ij}(\boldsymbol{x_0}, t) + \text{H.O.T.} \tag{1.1}$$

In a materially advecting reference frame, the zeroth-order term vanishes and the VGT completely describes the structure of local streamlines captured by this linear approximation. The invariants of the VGT (P, Q, and R) capture the topological characteristics of these streamlines [17–19] which, for incompressible flows ($P = -A_{ii} = 0$), are fully classified by the second and third invariants,

$$Q = -\frac{1}{2} A_{ij} A_{ji}, \quad R = -\frac{1}{3} A_{ij} A_{jk} A_{ki}. \tag{1.2}$$

These invariants underlie the commonly used Q [20] and Δ [19] criteria for vortex identification, where $\Delta = Q^3 + \frac{27}{4} R^2$ represents the discriminant of the VGT. They can also be expressed as

$$Q = \frac{1}{2} \left(\Omega_{ij} \Omega_{ij} - S_{ij} S_{ij} \right), \quad R = -\frac{1}{3} S_{ij} S_{ik} S_{jk} + S_{ij} \Omega_{ik} \Omega_{jk}. \tag{1.3}$$

Here, $S_{ij} = \frac{1}{2}(A_{ij} + A_{ji})$ is the (symmetric) strain-rate tensor and $\Omega_{ij} = \frac{1}{2}(A_{ij} - A_{ji})$ is the (antisymmetric) vorticity tensor, which is related to the vorticity vector through $\Omega_{ij} = -\frac{1}{2} \varepsilon_{ijk} \omega_k$, where ε_{ijk} represents the Levi-Civita tensor. These definitions reveal that Q provides a comparison of the strengths of rotational and straining motions and, as will be discussed subsequently, R provides a comparison of source terms that contribute to strain and enstrophy production. The omnipresence of the symmetry-based decomposition of the VGT,

$$A_{ij} = S_{ij} + \Omega_{ij}, \tag{1.4}$$

will be a recurring theme of this section.

The VGT is also a crucial element of the dynamics of turbulent flows. In this thesis, we primarily consider the dynamics associated with the incompressible Navier–Stokes equations, which are given by

$$\frac{\partial u_i}{\partial t} + u_j \frac{\partial u_i}{\partial x_j} = -\frac{1}{\rho} \frac{\partial p}{\partial x_i} + \nu \frac{\partial^2 u_i}{\partial x_j^2} + f_i, \quad \frac{\partial u_i}{\partial x_i} = 0, \tag{1.5}$$

where ρ, ν, and p denote the density, kinematic viscosity, and pressure, respectively, and f_i represents an arbitrary forcing. The VGT can immediately be

seen to contribute to the advection term and the viscous diffusion term in the momentum equation as well as to the continuity equation. Its contribution to pressure is revealed through the pressure Poisson equation, which is given by

$$\frac{1}{\rho}\frac{\partial^2 p}{\partial x_i^2} = 2Q, \tag{1.6}$$

where we have assumed that f_i is solenoidal. This equation reflects how strongly rotational vortex cores, which are associated with large values of Q, typically produce local pressure minima.

The VGT is also critical to the dynamics of kinetic energy, $E = \frac{1}{2}u_i u_i$, which can be expressed as

$$\frac{\partial E}{\partial t} + \frac{\partial T_i}{\partial x_i} = u_i f_i - \Phi, \tag{1.7}$$

where $\frac{\partial T_i}{\partial x_i}$ represents spatial transport and $T_i = \left(E + \frac{p}{\rho}\right) u_i - 2\nu S_{ij} u_j$. Here, $u_i f_i$ (typically) represents the rate of kinetic energy injection by the forcing and $\Phi = 2\nu S_{ij} S_{ij} > 0$ represents the rate of kinetic energy dissipation. This equation shows that the strain-rate tensor is directly responsible for dissipation. However, dissipation is also implicitly tied to the vorticity tensor under appropriate conditions. For example, in homogeneous turbulence, the average dissipation rate can be recast in terms of enstrophy since $\langle Q \rangle = 0$, where $\langle \cdot \rangle$ denotes averaging [21].

The preceding discussion highlights that the strength of the strain-rate tensor, $S^2 = S_{ij} S_{ij}$, and the strength of the vorticity tensor, $\Omega^2 = \Omega_{ij}\Omega_{ij}$, capture salient structural and dynamical features of turbulent flows. The Lagrangian dynamics of S^2 and Ω^2 can be used to glean further insight into the mechanisms that drive turbulence at small scales. Neglecting the forcing term, f_i, they can be expressed as

$$\frac{DS^2}{Dt} = -2S_{ij}S_{ik}S_{jk} + 2S_{ij}\Omega_{ik}\Omega_{jk} - 2S_{ij}\frac{\partial^2 (p/\rho)}{\partial x_i \partial x_j} + \nu\frac{\partial^2 S^2}{\partial x_k^2} - 2\nu\frac{\partial S_{ij}}{\partial x_k}\frac{\partial S_{ij}}{\partial x_k}, \tag{1.8}$$

$$\frac{D\Omega^2}{Dt} = \qquad -4S_{ij}\Omega_{ik}\Omega_{jk} \qquad + \nu\frac{\partial^2 \Omega^2}{\partial x_k^2} - 2\nu\frac{\partial \Omega_{ij}}{\partial x_k}\frac{\partial \Omega_{ij}}{\partial x_k}, \tag{1.9}$$

where $\frac{D}{Dt} = \frac{\partial}{\partial t} + u_k\frac{\partial}{\partial x_k}$ represents the material derivative. Summing these two equations recovers the dynamics of the total velocity gradient strength, $A^2 = S^2 + \Omega^2$. Strain self-amplification amplifies strain rates through the $-2S_{ij}S_{ik}S_{jk}$ term and it is prototypically modeled in terms of strain sheets.

Vortex stretching amplifies vorticity through the $-4S_{ij}\Omega_{ik}\Omega_{jk}$ term and diminishes strain rates through the $+2S_{ij}\Omega_{ik}\Omega_{jk}$ term, and it is prototypically modeled using vortex tubes. On average, both of these mechanisms amplify velocity gradients in three-dimensional turbulence and their contributions are related to one another through the third invariant of the VGT, as expressed in (1.3). For homogeneous turbulence, the constraint that $\langle R \rangle = 0$ [21] implies that the average contribution of strain self-amplification to the amplification of velocity gradients is three times stronger than that of vortex stretching. Moreover, despite the longstanding assumption that vortex stretching predominantly drives the energy cascade, recent evidence suggests that strain self-amplification actually has a stronger overall contribution [22–24].

In this section, we have demonstrated that the symmetry-based decomposition of the VGT permeates countless facets of turbulent flow physics. Therefore, its ubiquitous role in modeling efforts—including in Reynolds-averaged [25], large-eddy [13], and Lagrangian settings [15]—is perhaps unsurprising. However, as discussed in §1.3, it has significant limitations that we aim to address in this thesis.

1.3 Normality-based analysis of velocity gradients

The straining and rotational motions identified by the symmetry-based decomposition of the VGT provide a useful classification of velocity gradients. For example, when $Q \to \frac{1}{2}A^2 > 0$, the local flow can be approximated as rigid-body rotation whereas, when $Q \to -\frac{1}{2}A^2 < 0$, it can be approximated as a potential flow. Nevertheless, in this thesis, we advocate for the consideration of the normality properties of the VGT alongside its symmetry properties. For our purposes, a real-valued second-order tensor, B_{ij}, is called normal if $B_{ij}B_{kj} = B_{ji}B_{jk}$. To motivate our normality-based analysis, we begin this section by illustrating how, alone, the symmetry-based analysis can obscure key features of velocity gradients and local flow structure.

Consider in isolation an arbitrary strain-rate tensor, S_{ij}, which is strictly symmetric and therefore normal. It may be transformed to the strain-rate eigenframe, denoted by $(\cdot)^{\blacksquare}$, as

$$S_{ij}^{\blacksquare} = V_{ik}^{\blacksquare} S_{km} V_{jm}^{\blacksquare} = \begin{bmatrix} \lambda_1 & 0 & 0 \\ 0 & \lambda_2 & 0 \\ 0 & 0 & \lambda_3 \end{bmatrix}, \tag{1.10}$$

where $\lambda_1 > \lambda_2 > \lambda_3$ are the eigenvalues of S_{ij} and incompressibility implies that $\lambda_1 > 0$ and $\lambda_3 = -\lambda_1 - \lambda_2 < 0$. This eigenframe representation emphasizes that the strain-rate tensor can be associated with local stretching and compression in orthogonal directions and has provided key insights into alignment properties of turbulent flows [26–28].

Now, consider in isolation an arbitrary vorticity tensor, $\Omega_{ij} = -\frac{1}{2}\varepsilon_{ijk}\omega_k$, which is strictly antisymmetric and therefore normal. By transforming it into a reference frame, denoted by $(\cdot)^{\bullet}$, where the vorticity vector lies along the $z^{\bullet}$-axis, it may be expressed as

$$\Omega_{ij}^{\bullet} = V_{ik}^{\bullet}\,\Omega_{km}V_{jm}^{\bullet} = \begin{bmatrix} 0 & -\frac{1}{2}\omega_3 & 0 \\ \frac{1}{2}\omega_3 & 0 & 0 \\ 0 & 0 & 0 \end{bmatrix}. \tag{1.11}$$

This representation emphasizes that, in an appropriate reference frame, the vorticity tensor can be associated with rigid-body rotation in the form of a local vortex tube.

These conceptual pictures for the strain-rate and vorticity tensors are useful when considered in isolation; however, velocity gradients typically contain both symmetric and antisymmetric parts. Whereas, in isolation, S_{ij} and Ω_{ij} are normal, summing their contributions can result in a VGT, $A_{ij} = S_{ij} + \Omega_{ij}$, that is non-normal. For example,

$$\underbrace{\begin{bmatrix} 0 & 1 & 0 \\ 1 & 0 & 0 \\ 0 & 0 & 0 \end{bmatrix}}_{S_{ij}} + \underbrace{\begin{bmatrix} 0 & 1 & 0 \\ -1 & 0 & 0 \\ 0 & 0 & 0 \end{bmatrix}}_{\Omega_{ij}} = \underbrace{\begin{bmatrix} 0 & 2 & 0 \\ 0 & 0 & 0 \\ 0 & 0 & 0 \end{bmatrix}}_{A_{ij}} \tag{1.12}$$

demonstrates how summing a normal strain-rate tensor and a normal vorticity tensor can produce a strictly non-normal tensor that represents a state of pure shearing (for which $Q = R = 0$). Furthermore, the reference frames associated with $V_{ij}^{\blacksquare}$ and $V_{ij}^{\bullet}$ do not generally align with each other, which can obfuscate the interaction between S_{ij} and Ω_{ij} and complicate the interpretation of mechanisms like vortex stretching. Therefore, symmetry properties alone cannot reliably distinguish contributions from normal straining, rigid rotation, and a non-normal residual (associated with shearing) to the VGT in a single, unified reference frame.

To address this limitation, Kolář [29, 30] pioneered[1] a 'triple decomposition' of the VGT that identifies contributions from normal straining, rigid rotation, and pure shearing in a 'basic' reference frame. Their approach identifies the basic reference frame by maximizing an interaction scalar over a finite number of sample frames and, although it is typically robust, it can be computationally expensive and yield non-unique solutions. Recently, a more pragmatic approach based on the real Schur form of the VGT was developed [34–36]. This approach identifies a 'principal' reference frame in which the VGT is quasi-triangular for locally rotational points ($\Delta > 0$) and triangular for locally non-rotational points ($\Delta \leq 0$). Some recent investigations [37–40] have also considered the complex Schur form of the VGT, which is always triangular but becomes complex-valued for locally rotational points. This thesis focuses solely on the normality-based decomposition associated with the real Schur form of the VGT.

In the principal frame, denoted by $(\cdot)^*$, the VGT can be expressed as

$$A^*_{ij} = V^{\mathrm{L}}_{ik} A_{km} V^{\mathrm{L}}_{jm} = \underbrace{\begin{bmatrix} \dot{\epsilon}^*_1 & 0 & 0 \\ 0 & \dot{\epsilon}^*_2 & 0 \\ 0 & 0 & \dot{\epsilon}^*_3 \end{bmatrix}}_{S^{\epsilon*}_{ij}} + \underbrace{\begin{bmatrix} 0 & 0 & 0 \\ \dot{\gamma}^*_3 & 0 & 0 \\ \dot{\gamma}^*_2 & \dot{\gamma}^*_1 & 0 \end{bmatrix}}_{A^{\gamma*}_{ij}} + \underbrace{\begin{bmatrix} 0 & -\dot{\varphi}^*_3 & 0 \\ \dot{\varphi}^*_3 & 0 & 0 \\ 0 & 0 & 0 \end{bmatrix}}_{\Omega^{\varphi*}_{ij}}, \tag{1.13}$$

where $S^{\epsilon*}_{ij}$, $A^{\gamma*}_{ij}$, and $\Omega^{\varphi*}_{ij}$ denote the normal straining, pure shearing, and rigid rotation tensors, respectively. These tensors can be expressed in the original coordinate system (as S^{ϵ}_{ij}, A^{γ}_{ij}, and Ω^{φ}_{ij}) using the unitary coordinate transformation, V^{L}_{ij}. The elements of the normal straining tensor represent the real parts of the eigenvalues of the VGT which, for locally rotational points, are ordered such that ϵ^*_3 is the (sole) real eigenvalue of the VGT. This ordering ensures that the vorticity vector associated with rigid rotation, $\omega^{\varphi}_i = -\varepsilon_{ijk}\Omega^{\varphi}_{jk}$, which lies along the z^*-axis, aligns with the local rotation axis, which is given by the real eigenvector of the VGT, v^{R}_i. The strength of rigid rotation about this axis is given by

$$\dot{\varphi}^*_3 = \left|\frac{1}{2}\omega_i v^{\mathrm{R}}_i\right| - \left[\left(\frac{1}{2}\omega_i v^{\mathrm{R}}_i\right)^2 - \lambda^2_{\mathrm{CI}}\right]^{1/2}, \tag{1.14}$$

where λ_{CI} represents the imaginary part of the complex conjugate eigenvalues of the VGT.

[1] While additively decomposing the VGT into straining, rotational, and shearing motions is a relatively recent development, the history of studying the properties of straining and rotational motions is long and rich [31], including important contributions from Cauchy [32] and Stokes [33] (among others) in the 1800s.

The lower quasi-triangular form expressed in (1.13) implies that $\dot{\varphi}_3^* \geq 0$ represents counterclockwise rigid-body rotation about the z^*-axis [34–36, 41, 42]. An equivalent upper quasi-triangular form [43–45] can be expressed as

$$A_{ij}^* = V_{ik}^{\mathrm{U}} A_{km} V_{jm}^{\mathrm{U}} = \underbrace{\begin{bmatrix} \dot{\epsilon}_1^* & 0 & 0 \\ 0 & \dot{\epsilon}_2^* & 0 \\ 0 & 0 & \dot{\epsilon}_3^* \end{bmatrix}}_{S_{ij}^{\epsilon *}} + \underbrace{\begin{bmatrix} 0 & \dot{\gamma}_3^* & \dot{\gamma}_2^* \\ 0 & 0 & \dot{\gamma}_1^* \\ 0 & 0 & 0 \end{bmatrix}}_{A_{ij}^{\gamma *}} + \underbrace{\begin{bmatrix} 0 & 0 & 0 \\ 0 & 0 & \dot{\varphi}_1^* \\ 0 & -\dot{\varphi}_1^* & 0 \end{bmatrix}}_{\Omega_{ij}^{\varphi *}}, \tag{1.15}$$

where, for locally rotational points, ϵ_1^* is the real eigenvalue of the VGT and $\dot{\varphi}_1^* \geq 0$ represents clockwise rigid-body rotation about the x^*-axis. Both (1.13) and (1.15) produce identical contributions from S_{ij}^{ϵ}, A_{ij}^{γ}, and Ω_{ij}^{φ} in the original coordinate system.

As originally formulated, the VGT in the principal frame was identified via a series of rotations of the coordinate axes. However, Kronborg and Hoffman [43] showed that its constituents can be identified and transformed to the original coordinate system directly from the elements of the (ordered) real Schur form of the VGT. This enables efficient computations since the real Schur form can be computed using optimized numerical packages in common programming languages. We have developed an instructional `MATLAB` implementation of this approach, which is available in the Caltech Data Repository and briefly outlined in Algorithm 1.1. In practice, the unitary transformations produced by algorithms that compute the real Schur form may have negative determinants and, therefore, may not strictly reflect proper rotations of the coordinate axes. However, Liu et al. [34] showed that this is inconsequential since the transformations can always be modified to ensure that they represent proper rotations. The modification flips the signs of $\dot{\gamma}_1^*$ and $\dot{\gamma}_2^*$ in (1.13) and $\dot{\gamma}_2^*$ and $\dot{\gamma}_3^*$ in (1.15), but it does not affect the representations of S_{ij}^{ϵ}, A_{ij}^{γ}, and Ω_{ij}^{φ} in the original coordinate system.

In general, the coordinate axes of the principal frame do not align with those of the strain-rate eigenframe or with the vorticity vector. Figure 1.1 demonstrates this misalignment for a sample VGT given by

$$A_{ij}^* = \underbrace{\begin{bmatrix} -1 & 0 & 0 \\ 0 & -1 & 0 \\ 0 & 0 & 2 \end{bmatrix}}_{S_{ij}^{\epsilon *}} + \underbrace{\begin{bmatrix} 0 & 0 & 0 \\ 0 & 0 & 0 \\ 2 & -2 & 0 \end{bmatrix}}_{A_{ij}^{\gamma *}} + \underbrace{\begin{bmatrix} 0 & -1 & 0 \\ 1 & 0 & 0 \\ 0 & 0 & 0 \end{bmatrix}}_{\Omega_{ij}^{\varphi *}}, \tag{1.16}$$

Algorithm 1.1: Outline for computing the normality-based decomposition of the VGT via its real Schur form, following the formulation of Kronborg and Hoffman [43]. We compute the ordered real Schur form using the `schur` and `ordschur` functions in `MATLAB`. The tensor $\tilde{A}^*_{ij}$ is upper quasi-triangular and, while $\tilde{A}^*_{ij}$ and $\tilde{V}^*_{ij}$ need not strictly reflect the form expressed in (1.15), the output tensors in the original coordinate system (S^ϵ_{ij}, A^γ_{ij}, and Ω^φ_{ij}) are identical to those produced by (1.13) and (1.15).

Input: A_{ij}

Output: S^ϵ_{ij}, A^γ_{ij}, Ω^φ_{ij}

$\left[\tilde{V}^U_{ij}, \tilde{A}^*_{ij}\right] \leftarrow \texttt{orderedRealSchurForm}\left(A_{ij}\right)$ `// s.t.` $\tilde{A}^*_{11}$ `is real eigenvalue`

$S^\epsilon_{ij} \leftarrow \tilde{V}^U_{ki} \begin{bmatrix} \tilde{A}^*_{11} & 0 & 0 \\ 0 & \tilde{A}^*_{22} & 0 \\ 0 & 0 & \tilde{A}^*_{33} \end{bmatrix} \tilde{V}^U_{mj}$

$\dot{\varphi}^*_1 \leftarrow \texttt{min}\left(\texttt{abs}\left(\tilde{A}^*_{23}\right), \texttt{abs}\left(\tilde{A}^*_{32}\right)\right)$

$\Omega^\varphi_{ij} \leftarrow \tilde{V}^U_{ki} \begin{bmatrix} 0 & 0 & 0 \\ 0 & 0 & \texttt{sign}\left(\tilde{A}^*_{23}\right)\dot{\varphi}^*_1 \\ 0 & \texttt{sign}\left(\tilde{A}^*_{32}\right)\dot{\varphi}^*_1 & 0 \end{bmatrix} \tilde{V}^U_{mj}$

$A^\gamma_{ij} \leftarrow A_{ij} - S^\epsilon_{ij} - \Omega^\varphi_{ij}$

return S^ϵ_{ij}, A^γ_{ij}, Ω^φ_{ij}

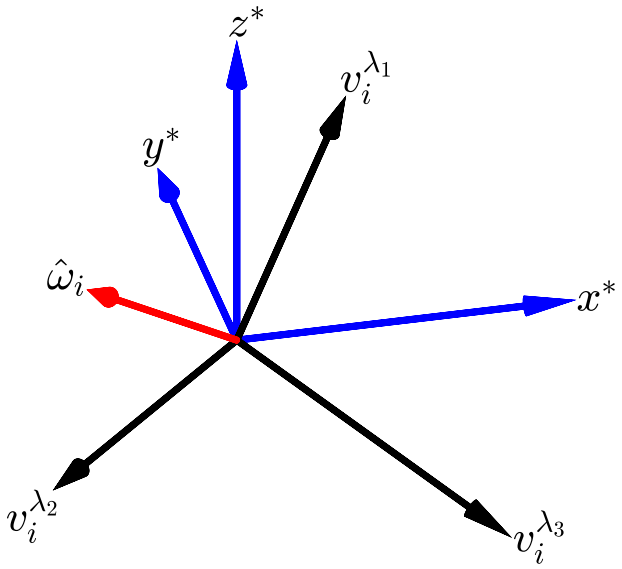

Figure 1.1: Misalignment of the coordinate axes of the principal frame (blue), the coordinate axes of the strain-rate eigenframe (black), and the unit vorticity vector (red) for the VGT in (1.16).

which is of the form in (1.13). If the contribution from $A_{ij}^{\gamma*}$ were removed, this VGT would consist of only normal straining and rigid rotation. As a result, the principal frame would align with the strain-rate eigenframe and the vorticity vector would align with the z^*-axis. In fact, these alignment properties hold for any VGT that does not include a contribution from $A_{ij}^{\gamma*}$. Therefore, the non-normal contribution of shearing is responsible for (i) the misalignment of the principal frame and the strain-rate eigenframe and (ii) the misalignment of the vorticity vector with the local rotation axis.

The normality-based decomposition of the VGT addresses the limitations of the symmetry-based decomposition discussed at the beginning of this section in a principled yet pragmatic manner. Using the form of the VGT in the principal frame, it identifies contributions from normal straining, which is symmetric and normal, rigid rotation, which is antisymmetric and normal, and pure shearing, which is strictly non-normal. It represents a refinement of the symmetry-based decomposition since $S_{ij} = S_{ij}^{\epsilon} + S_{ij}^{\gamma}$ and $\Omega_{ij} = \Omega_{ij}^{\varphi} + \Omega_{ij}^{\gamma}$, where $S_{ij}^{\gamma} = \frac{1}{2}\left(A_{ij}^{\gamma} + A_{ij}^{\gamma}\right)$ represents the (symmetric) shear straining tensor and $\Omega_{ij}^{\gamma} = \frac{1}{2}\left(A_{ij}^{\gamma} - A_{ij}^{\gamma}\right)$ represents the (antisymmetric) shear vorticity tensor. As depicted in Figure 1.2, S_{ij}^{ϵ}, Ω_{ij}^{φ}, and A_{ij}^{γ} can conceptually be associated with local stretching/compression, local vortex tubes, and local shear layers, respectively[2]. Distinguishing these local features resolves the ambiguity in the interaction of S_{ij} and Ω_{ij} and, thereby, enhances the structural expressivity of the symmetry-based decomposition. In fact, the form of the VGT in the principal frame reveals that the sum $S_{ij}^{\epsilon} + \Omega_{ij}^{\varphi}$ is normal and, therefore, does not produce a non-normal residual associated with shearing. Moreover, the vorticity fields associated with rigid rotation and shearing have been shown to organize into tube-like and sheet-like vortical flow structures, respectively [34, 35, 46–50]. This highlights how the normality-based decomposition of the VGT can glean insight into the surrounding turbulence structure in a manner that the symmetry-based decomposition cannot.

1.4 Overview of thesis

A central aim of this thesis is to comprehensively identify how the expressivity of the normality-based decomposition of the VGT can enhance our ability

[2] In §4.A1, we illustrate these associations using Burgers vortex layers and tubes, which are prototypical models of stretched shear layers and stretched vortices, respectively. The latter can be crudely described as a rigidly rotating inner vortex core with a shear annulus wrapped around it.

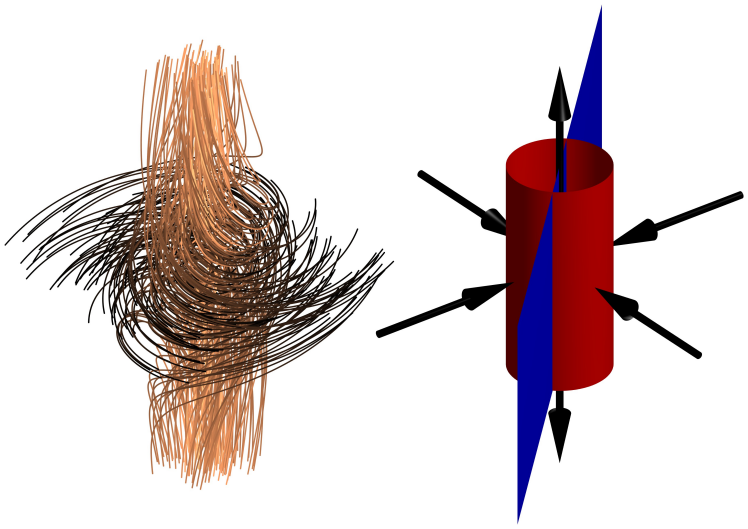

Figure 1.2: Depictions of fluid particle trajectories (left) and normality-based constituents (right) for a spatially linear velocity field undergoing vortex stretching. The trajectories progress from darker to lighter colors. The black arrows, red vortex tube, and blue shear layer correspond to normal straining, rigid rotation, and pure shearing, respectively.

to understand and model turbulent flows. To achieve this goal, we develop theoretical insights into the normality-based analysis, formulate normality-based frameworks that capture key flow features, and apply these frameworks to a broad range of turbulent flows. In Chapter 2, we tailor the normality-based analysis to characterize velocity gradients in a head-on collision between two vortex rings. Our results provide novel insight into the instability mechanism governing transition and the behavior of the resulting turbulent cloud. In Chapter 3 we perform a focused normality-based analysis of the strength of velocity gradients in wall-bounded turbulent flows, including channels and boundary layers. Our results identify distinguishing features of different flow regimes and remarkable statistical collapses across all flows. In Chapter 4, we develop a normality-based analysis of multiscale velocity gradients and interscale energy transfer. Our results provide novel insight into mechanisms underlying the energy cascade and the performance of closure models for large-eddy simulation. Finally, in Chapter 5, we summarize the contributions of each chapter and discuss implications of our work for future research directions.

The notation used in our normality-based analyses varies across Chapters 2, 3, and 4, which each represent a distinct published contribution. A commonality across all chapters is that ϵ, γ, and φ correspond to normal straining, pure shearing, and rigid rotation, respectively.

References

[1]Feynman, R.P., Leighton, R.B., and Sands, M. The Feynman lectures on physics. Vol. I (Addison–Wesley, 1963) Chap. 3-7.

[2]Lemarié-Rieusset, P.G. The Navier-Stokes problem in the 21st century. 2nd ed. (Chapman and Hall/CRC, 2023).

[3]Bruno, R. and Carbone, V. The solar wind as a turbulence laboratory. *Living Rev. Solar Phys.* **10**, 2 (2013).

[4]Dauxois, T., Peacock, T., Bauer, P., Caulfield, C.P., Cenedese, C., Gorlé, C., Haller, G., Ivey, G.N., Linden, P.F., Meiburg, E., Pinardi, N., Vriend, N.M., and Woods, A.W. Confronting Grand Challenges in environmental fluid mechanics. *Phys. Rev. Fluids* **6**, 020501 (2021).

[5]Jordan, P. and Colonius, T. Wave packets and turbulent jet noise. *Annu. Rev. Fluid Mech.* **45**, 173–195 (2013).

[6]Chung, D., Hutchins, N., Schultz, M.P., and Flack, K.A. Predicting the drag on rough surfaces. *Annu. Rev. Fluid Mech.* **53**, 439–471 (2021).

[7]Ku, D.N. Blood flow in arteries. *Annu. Rev. Fluid Mech.* **29**, 399–434 (1997).

[8]Ma, Y., Cheng, W., Huang, S., Schmitt, F.G., Lin, X., and Huang, Y. Hidden turbulence in van Gogh's *The Starry Night*. *Phys. Fluids* **36**, 095140 (2024).

[9]Kolmogorov, A.N. The local structure of turbulence in incompressible viscous fluid for very large Reynolds numbers. *Dokl. Akad. Nauk SSSR* **30**, 301–305, reprinted in *Proc. R. Soc. Lond.* A **434**, 9–13. (1941).

[10]Kolmogorov, A.N. A refinement of previous hypotheses concerning the local structure of turbulence in a viscous incompressible fluid at high Reynolds number. *J. Fluid Mech.* **13**, 82–85 (1962).

[11]Oboukhov, A.M. Some specific features of atmospheric tubulence. *J. Fluid Mech.* **13**, 77–81 (1962).

[12]Sreenivasan, K.R. and Antonia, R.A. The phenomenology of small-scale turbulence. *Annu. Rev. Fluid Mech.* **29**, 435–472 (1997).

[13]Meneveau, C. and Katz, J. Scale-invariance and turbulence models for large-eddy simulation. *Annu. Rev. Fluid Mech.* **32**, 1–32 (2000).

[14]Wallace, J.M. Twenty years of experimental and direct numerical simulation access to the velocity gradient tensor: what have we learned about turbulence?, *Phys. Fluids* **21**, 021301 (2009).

[15]Meneveau, C. Lagrangian dynamics and models of the velocity gradient tensor in turbulent flows. *Annu. Rev. Fluid Mech.* **43**, 219–245 (2011).

[16]Johnson, P.L. and Wilczek, M. Multiscale velocity gradients in turbulence. *Annu. Rev. Fluid Mech.* **56**, 463–490 (2024).

[17]Perry, A.E. and Fairlie, B.D. Critical points in flow patterns. *Adv. Geophys.* **18**, 299–315 (1975).

[18]Perry, A.E. and Chong, M.S. A description of eddying motions and flow patterns using critical-point concepts. *Annu. Rev. Fluid Mech.* **19**, 125–155 (1987).

[19]Chong, M.S., Perry, A.E., and Cantwell, B.J. A general classification of three-dimensional flow fields. *Phys. Fluids A* **2**, 765–777 (1990).

[20]Hunt, J.C.R., Wray, A.A., and Moin, P. Eddies, streams, and convergence zones in turbulent flows. In Proceedings of the 1988 Summer Program (Center for Turbulence Research, 1988), pp. 193–208.

[21]Betchov, R. An inequality concerning the production of vorticity in isotropic turbulence. *J. Fluid Mech.* **1**, 497–504 (1956).

[22]Carbone, M. and Bragg, A.D. Is vortex stretching the main cause of the turbulent energy cascade?, *J. Fluid Mech.* **883**, R2 (2020).

[23]Johnson, P.L. Energy transfer from large to small scales in turbulence by multiscale nonlinear strain and vorticity interactions. *Phys. Rev. Lett.* **124**, 104501 (2020).

[24]Johnson, P.L. On the role of vorticity stretching and strain self-amplification in the turbulence energy cascade. *J. Fluid Mech.* **922**, A3 (2021).

[25]Durbin, P.A. Some recent developments in turbulence closure modeling. *Annu. Rev. Fluid Mech.* **50**, 77–103 (2018).

[26]Ashurst, W.T., Kerstein, A.R., Kerr, R.M., and Gibson, C H. Alignment of vorticity and scalar gradient with strain rate in simulated Navier–Stokes turbulence. *Phys. Fluids* **30**, 2343–2353 (1987).

[27]Ballouz, J.G. and Ouellette, N.T. Tensor geometry in the turbulent cascade. *J. Fluid Mech.* **835**, 1048–1064 (2018).

[28]Tom, J., Carbone, M., and Bragg, A.D. Exploring the turbulent velocity gradients at different scales from the perspective of the strain-rate eigenframe. *J. Fluid Mech.* **910**, A24 (2021).

[29]Kolář, V. 2D velocity-field analysis using triple decomposition of motion. In Proceedings of the 15th Australasian Fluid Mechanics Conference (The University of Sydney, 2004), AFMC00017.

[30]Kolář, V. Vortex identification: new requirements and limitations. *Intl J. Heat Fluid Flow* **28**, 638–652 (2007).

[31]Truesdell, C. and Toupin, R. The classical field theories. In *Handbuch der Physik*, Vol. 3/1 (Springer, 1960), pp. 226–858.

[32]Cauchy, A.-L. Mémoire sur les dilatations, les condensations et les rotations produits par un changement de forme dans un système de points matériels. *Oeuvres* **12**, 343–377 (1841).

[33]Stokes, G.G. On the theories of the internal friction of fluids in motion, and of the equilibrium and motion of elastic solids. *Trans. Camb. Phil. Soc.* **8**, 287–319 (1845).

[34]Liu, C., Gao, Y., Tian, S., and Dong, X. Rortex—a new vortex vector definition and vorticity tensor and vector decompositions. *Phys. Fluids* **30**, 035103 (2018).

[35]Gao, Y. and Liu, C. Rortex and comparison with eigenvalue-based vortex identification criteria. *Phys. Fluids* **30**, 085107 (2018).

[36]Gao, Y. and Liu, C. Rortex based velocity gradient tensor decomposition. *Phys. Fluids* **31**, 011704 (2019).

[37]Keylock, C.J. The Schur decomposition of the velocity gradient tensor for turbulent flows. *J. Fluid Mech.* **848**, 876–905 (2018).

[38]Keylock, C.J. Turbulence at the Lee bound: maximally non-normal vortex filaments and the decay of a local dissipation rate. *J. Fluid Mech.* **881**, 283–312 (2019).

[39]Keylock, C.J. The role of normal and non-normal contributions to enstrophy production in the near-wall region of a turbulent channel flow. *J. Fluid Mech.* **1006**, A3 (2025).

[40]Beaumard, P., Buxton, O.R.H., and Keylock, C.J. The importance of non-normal contributions to velocity gradient tensor dynamics for spatially developing, inhomogeneous, turbulent flows. *J. Turbul.* **20**, 577–598 (2019).

[41]Das, R. and Girimaji, S.S. Revisiting turbulence small-scale behavior using velocity gradient triple decomposition. *New J. Phys.* **22**, 063015 (2020).

[42]Arun, R. and Colonius, T. Velocity gradient analysis of a head-on vortex ring collision. *J. Fluid Mech.* **982**, A16 (2024).

[43]Kronborg, J. and Hoffman, J. The triple decomposition of the velocity gradient tensor as a standardized real Schur form. *Phys. Fluids* **35**, 031703 (2023).

[44]Arun, R. and Colonius, T. Velocity gradient partitioning in turbulent flows. *J. Fluid Mech.* **1000**, R5 (2024).

[45]Arun, R., Kamal, M., Colonius, T., and Johnson, P.L. Normality-based analysis of multiscale velocity gradients and energy transfer in direct and large-eddy simulations of isotropic turbulence. *J. Fluid Mech.* **1021**, A47 (2025).

[46]Liu, C., Gao, Y., Dong, X., Wang, Y., Liu, J., Zhang, Y., Cai, X., and Gui, N. Third generation of vortex identification methods: Omega and Liutex/Rortex based systems. *J. Hydrodyn.* **31**, 205–223 (2019).

[47]Haller, G. Can vortex criteria be objectivized?, *J. Fluid Mech.* **908**, A25 (2021).

[48]Nagata, R., Watanabe, T., Nagata, K., and da Silva, C.B. Triple decomposition of velocity gradient tensor in homogeneous isotropic turbulence. *Comput. Fluids* **198**, 104389 (2020).

[49]Watanabe, T., Tanaka, K., and Nagata, K. Characteristics of shearing motions in incompressible isotropic turbulence. *Phys. Rev. Fluids* **5**, 072601 (2020).

[50]Enoki, R., Watanabe, T., and Nagata, K. Statistical properties of shear and nonshear velocity components in isotropic turbulence and turbulent jets. *Phys. Rev. Fluids* **8**, 104602 (2023).

Chapter 2

VELOCITY GRADIENT ANALYSIS OF A HEAD-ON VORTEX RING COLLISION

This chapter consists of the following published journal article.

[1]**Arun, R.** and Colonius, T. Velocity gradient analysis of a head-on vortex ring collision. *J. Fluid Mech.* **982**, A16 (2024).

Abstract

We simulate the head-on collision between vortex rings with circulation Reynolds numbers of 4000 using an adaptive, multiresolution solver based on the lattice Green's function. The simulation fidelity is established with integral metrics representing symmetries and discretization errors. Using the velocity gradient tensor and structural features of local streamlines, we characterize the evolution of the flow with a particular focus on its transition and turbulent decay. Transition is excited by the development of the elliptic instability, which grows during the mutual interaction of the rings as they expand radially at the collision plane. The development of antiparallel secondary vortex filaments along the circumference mediates the proliferation of small-scale turbulence. During turbulent decay, the partitioning of the velocity gradients approaches an equilibrium that is dominated by shearing and agrees well with previous results for forced isotropic turbulence. We also introduce new phase spaces for the velocity gradients that reflect the interplay between shearing and rigid rotation and highlight geometric features of local streamlines. In conjunction with our other analyses, these phase spaces suggest that, while the elliptic instability is the predominant mechanism driving the initial transition, its interplay with other mechanisms, e.g. the Crow instability, becomes more important during turbulent decay. Our analysis also suggests that the geometry-based phase space may be promising for identifying the effects of the elliptic instability and other mechanisms using the structure of local streamlines. Moving forward, characterizing the organization of these mechanisms within vortices and universal features of velocity gradients may aid in modeling turbulent flows.

2.1 Introduction

2.1.1 Vortex rings

Vortex rings are ubiquitous flow phenomena in both applied and theoretical settings, with applications including sound generation, transport, mixing, and vortex interactions [1]. In geophysical settings, vortex rings can be used to model entrainment and dispersion in particle clouds [2]. They play important roles in the initial jets of volcanic eruptions [3] and the transport of contaminated sediments disposed of in open-water settings [4]. In biomechanical settings, vortex rings have been observed in the motions of blood in the human heart [5] and in the propulsive motion of oblate medusan jellyfish [6]. Remarkably, separated vortex rings augment dandelion seed dispersal by prolonging flight through drag enhancement [7]. In aerodynamic settings, vortex rings are responsible for the so-called vortex ring state, which negatively impacts lift in helicopters [8] and the performance of offshore wind turbines [9]. In experimental and numerical settings, the formation and pinch-off of vortex rings are of particular interest in jet flows involving nozzles and orifices [10–14].

Vortex rings are also associated with complex instabilities and dynamics that relate more generally to the sustenance of turbulence. Flow instabilities in vortex rings depend primarily on the core vorticity distribution, the circulation Reynolds number ($Re_\Gamma = \Gamma/\nu$), and the slenderness ratio ($\delta = a/R$) [15]. Here, Γ is the circulation, ν is the kinematic viscosity, a is the core radius, and R is the ring radius. We focus on the evolution of thin-cored vortex rings with Gaussian core vorticity profiles, no swirl, and centroids (Z) that propagate along the z-axis. In cylindrical coordinates (r, θ, z), this initial vorticity profile is written as

$$\omega_\theta(r, z; t = 0) = \pm \frac{\Gamma_0}{\pi a_0^2} \exp\left(-\frac{(z - Z_0)^2 + (r - R_0)^2}{a_0^2}\right), \tag{2.1}$$

where subscripts $(\cdot)_0$ denote parameter values at $t = 0$ and the sign of ω_θ dictates the propagation direction. Since Gaussian vortex rings only satisfy the governing equations with infinitesimal core thickness, they initially undergo a rapid period of equilibration in which vorticity is redistributed throughout the core [15–17]. Following instability growth, transition is often marked by the development of secondary vorticity in a halo around the core vorticity [17–19]. During turbulent decay, the shedding of secondary vortex structures to the wake can result in a stepwise decay in circulation [19, 20].

Stability analyses of thin vortex rings are often (classically) formulated in terms of asymptotic expansions in δ [21–23]. Infinitesimally thin vortex rings ($\delta \to 0$) are neutrally stable [1]. For rings with finite thickness ($\delta > 0$), the curvature instability occurs at first order in δ and the elliptic instability occurs at second order in δ. The curvature and elliptic instabilities occur at short wavelengths and arise due to parametric resonance between Kelvin waves with core azimuthal wavenumbers separated by one and two, respectively [23, 24]. The curvature instability is attributed to a dipole field produced by the vortex ring curvature [23, 25, 26]. By contrast, the elliptic instability is attributed to a quadrupole field generated by straining induced by the ring or some external source [23, 25, 27].

This elliptic instability acts to break up elliptic streamlines and is key to the development of three-dimensional transitional and turbulent flows [28]. In the context of vortex rings (or, more generally, strained vortices), it is sometimes called the Moore–Saffman–Tsai–Widnall (MSTW) instability [23, 29] based on the initial investigations of Moore and Saffman [30] and Tsai and Widnall [31]. The elliptic instability dominates the curvature instability for thin Gaussian vortex rings without swirl. However, the curvature instability becomes increasingly important for vortex rings with increasing Re_Γ and decreasing δ, as well as in vortex rings with swirl [24, 26].

While interesting in their own right, thin vortex rings often form canonical building blocks of more complex turbulent flows. Modified vortex geometries, such as elliptic vortex rings [32, 33] and trefoil knots [34, 35], provide alternative means of probing vortex dynamics and interactions. Collisions between vortex rings and other vortex rings, walls, and free surfaces are also commonly studied to investigate mechanisms underlying the turbulent cascade and the generation of small scales (see Mishra et al. [36] for a review). These mechanisms can be characterized using a variety of collision geometries, including head-on collisions [36–39], inclined collisions [40–42], and axis-offset collisions [43–45], among others. Boundary layers play an important role in vortex–wall interactions (e.g. by causing rebounding events) [46] and interactions with free surfaces can often be understood in terms of image vortices [47].

Here, we focus on head-on collisions between identical vortex rings of opposite circulation, which have been noted for their rapid enstrophy production [48–50]. They have been classically studied in the contexts of the formation

of smaller rings through vortex reconnection and the formation of turbulent clouds at high Re_Γ [51–53]. Many recent investigations have focused particularly on the mechanisms (e.g. instabilities) underlying these transitional and turbulent processes [36, 38, 39].

For the head-on vortex ring collisions under consideration, the elliptic instability competes and interacts with the longer-wavelength Crow instability. The Crow instability [54] is associated with the mutual interaction of perturbed counter-rotating vortices, which, in the linear regime, locally displaces the vortices without modifying their core structures [55]. Mishra et al. [36] provides a focused review of vortex ring collisions in the context of the these instabilities. For collisions at relatively low Reynolds numbers, the Crow instability can lead to the pinch-off of secondary vortex rings via local reconnections. At higher Reynolds numbers, the elliptic instability favors rapid disintegration of the vortex rings into a turbulent cloud.

McKeown et al. [39] proposed that iterative elliptic instabilities between successive generations of antiparallel vortices can mediate the turbulent cascade in head-on vortex ring collisions. Mishra et al. [36] also observed that the elliptic instability tends to dominate at high Re_Γ, although this behavior is also sensitive to the slenderness ratio and vorticity distribution. In a different configuration involving symmetrically perturbed antiparallel vortices, Yao and Hussain [56] attributed the turbulent cascade at high Re_Γ to an avalanche of successive vortex reconnections. In general, Ostilla-Mónico et al. [57] found that collisions between counter-rotating vortices are indeed highly sensitive to the geometry of their configuration. They particularly found that the mechanisms mediating the cascade bear resemblance to the reconnection scenario [56] when the vortices are nearly perpendicular, whereas they are more reminiscent of the iterative elliptic instability scenario [39] when the vortices are more acutely aligned. These recent works share two common themes: (i) that the mode of transition and the formation of a cascade are sensitive to the details of the initial flow configuration, and (ii) that the interplay between relevant instabilities is simultaneously important to the flow physics and difficult to capture.

2.1.2 Velocity gradients and vortices

The elliptic instability, which typically dominates head-on collisions between the vortex rings of interest at high Re_Γ [36, 39], is associated with elliptic streamlines [28]. This generic feature of strained vortical flows can be used to characterize the elliptic instability, which is typically difficult to discern in the complex interactions of multiscale vortices [36, 57]. Given the inherent complexity of turbulent flows, the geometry of local streamlines provides a relatively simple and interpretable means for characterizing flow features (e.g. vortices).

The instantaneous trajectory of a materially advecting fluid particle follows the streamlines, which are frame dependent. At a critical point, e.g. in a frame advecting with the particle, the velocity gradient tensor (VGT), $\boldsymbol{A} = \boldsymbol{\nabla u}$, determines, to linear order, the local structure of streamlines [58–60]. The scale-invariant shape of local streamlines is captured by normalizing the VGT as $\tilde{\boldsymbol{A}} = \boldsymbol{A}/A$ [61, 62], where $A = \|\boldsymbol{A}\|_{\mathrm{F}} = \mathrm{tr}(\boldsymbol{A}^{\mathrm{T}}\boldsymbol{A})^{1/2}$ is the Frobenius norm of the VGT, $(\cdot)^{\mathrm{T}}$ represents the transpose and, unless otherwise stated, non-bold versions of bold tensor quantities represent their Frobenius norms. This normalized VGT has been used to investigate the scalings, forcings, and non-local features of the VGT dynamics [62–64] and a similar analysis of vorticity gradients has been used to classify the geometry of local vortex lines [65].

The principal invariants of $\tilde{\boldsymbol{A}}$ instantaneously characterize local streamline topologies and geometries [60, 62, 63, 66]. They are given by

$$p_A = -\mathrm{tr}\left(\tilde{\boldsymbol{A}}\right), \quad q_A = \frac{1}{2}\left(\mathrm{tr}\left(\tilde{\boldsymbol{A}}\right)^2 - \mathrm{tr}\left(\tilde{\boldsymbol{A}}^2\right)\right), \quad r_A = -\det\left(\tilde{\boldsymbol{A}}\right), \tag{2.2}$$

where $\mathrm{tr}(\cdot)$ and $\det(\cdot)$ represent the trace and determinant, respectively. For incompressible flows ($p_A = 0$), four classes of local streamline topologies are separated by degenerate geometries in the $q_A - r_A$ plane. Using the invariants of $\tilde{\boldsymbol{A}}$ is advantageous compared with using the invariants of $\boldsymbol{A}$ since the $q_A - r_A$ plane is a bounded phase space and it provides a more complete representation of streamline geometries [62, 63, 66]. For example, the aspect ratio of purely elliptic local streamlines ($q_A > 0$ and $r_A = 0$) is completely characterized by q_A, but not by $Q = A^2 q_A$. However, while the $q_A - r_A$ plane efficiently characterizes local streamline geometries at critical points, additional parameters are required to fully describe all geometries [63].

Following Das and Girimaji [66], we consider the local streamline geometry in

the context of the modes of deformation of a fluid parcel: extensional straining, (symmetric and antisymmetric) shearing, and rigid rotation. The well-known Cauchy–Stokes decomposition of the VGT, $\tilde{\boldsymbol{A}} = \tilde{\boldsymbol{S}} + \tilde{\boldsymbol{W}}$, disambiguates contributions from the symmetric strain rate tensor, $\tilde{\boldsymbol{S}} = (\tilde{\boldsymbol{A}} + \tilde{\boldsymbol{A}}^{\mathrm{T}})/2$, and the antisymmetric vorticity tensor, $\tilde{\boldsymbol{W}} = (\tilde{\boldsymbol{A}} - \tilde{\boldsymbol{A}}^{\mathrm{T}})/2$. It has enabled insightful characterizations of the VGT dynamics from the perspective of the strain rate eigenframe [67]. However, it does not disambiguate symmetric shearing from extensional straining in $\tilde{\boldsymbol{S}}$ or antisymmetric shearing from rigid rotation in $\tilde{\boldsymbol{W}}$. This limitation motivated the development of the triple decomposition of the VGT [68], which disambiguates all three fundamental modes of deformation.

Kolář [68, 69] originally formulated the triple decomposition of the VGT by identifying a 'basic' reference frame in which motions associated with elongation, rigid rotation, and pure shearing can be isolated. However, identifying a basic reference frame requires a challenging pointwise optimization problem, the solution of which is typically approximated over a finite number of frames [68, 70]. More recently, Gao and Liu [71, 72] introduced a unique triple decomposition, based on a related vorticity tensor decomposition [73, 74], that is more computationally practical than that of Kolář [68, 69]. This triple decomposition is formally performed in a local 'principal' coordinate system (x^*, y^*, z^*), which is related to the global coordinate system (x, y, z) by an orthogonal transformation. In this principal frame, denoted by $(\cdot)^*$, the triple decomposition is given in normalized form by

$$\tilde{\boldsymbol{A}}^* = \underbrace{\begin{bmatrix} \dot{\epsilon}_{x^*} & 0 & 0 \\ 0 & \dot{\epsilon}_{y^*} & 0 \\ 0 & 0 & \dot{\epsilon}_{z^*} \end{bmatrix}}_{\dot{\boldsymbol{\epsilon}}^*} + \underbrace{\begin{bmatrix} 0 & 0 & 0 \\ \dot{\gamma}_{z^*} & 0 & 0 \\ \dot{\gamma}_{y^*} & \dot{\gamma}_{x^*} & 0 \end{bmatrix}}_{\dot{\boldsymbol{\gamma}}^*} + \underbrace{\begin{bmatrix} 0 & -\dot{\varphi}_{z^*} & 0 \\ \dot{\varphi}_{z^*} & 0 & 0 \\ 0 & 0 & 0 \end{bmatrix}}_{\dot{\boldsymbol{\varphi}}^*}. \tag{2.3}$$

Here, $\dot{\boldsymbol{\epsilon}}^*$, $\dot{\boldsymbol{\gamma}}^*$, and $\dot{\boldsymbol{\varphi}}^*$ represent the normal straining, pure shearing, and rigid body rotation tensors, respectively. Their constituents can be directly identified from the components of the VGT in the principal frame [66, 71, 72]. Their representations in the global coordinates ($\dot{\boldsymbol{\epsilon}}$, $\dot{\boldsymbol{\gamma}}$, and $\dot{\boldsymbol{\varphi}}$) can subsequently be recovered by inverting (i.e. transposing) the original orthogonal transformation [74].

The components of the normal straining tensor represent the real parts of the eigenvalues of $\tilde{\boldsymbol{A}}$, which are identical to those of $\tilde{\boldsymbol{A}}^*$. For points with rotational local streamlines, $\tilde{\boldsymbol{A}}$ has a pair of complex eigenvalues and the real eigenvector

defines the local rotation axis. In this case, the transformation to the principal frame is identified by (i) using a real Schur decomposition to align the z^*-axis with the real eigenvector of the VGT and (ii) orienting the $x^* - y^*$ plane to minimize the local rotational speed [66, 73]. One advantage of (2.3) is that it provides representations of the strength ($2\dot{\varphi}_{z^*}$) and the axis (z^*) of rigid rotation that are Galilean invariant [75]. Unlike the rotational case, the VGT has only real eigenvalues when the local streamline geometry is non-rotational ($\dot{\boldsymbol{\varphi}}^* = \mathbf{0}$). In this case, the principal frame is identified by using a Schur decomposition to transform the VGT into a triangular tensor. The modes of deformation are then isolated by decomposing this transformed tensor into a normal, diagonal tensor representing normal straining and a non-normal, strictly triangular tensor representing pure shearing [66, 76].

The triple decomposition enables refined analyses of the influences of fundamental constituents of the VGT. For example, the original triple decomposition [68] has been used to show that lifetimes of fundamental flow structures at macroscopic scales (where viscosity can be neglected) can be related to stability of rigid rotation, linear instability of pure shearing, and exponential instability of irrotational straining [77]. At small scales, the more recent triple decomposition [71, 72] has been used to show that pure shearing is typically the dominant contributor to energy dissipation [78] and intermittency [66] in turbulent flows. Further, the symmetric and antisymmetric components of $\dot{\boldsymbol{\gamma}}^*$ are given by $\dot{\boldsymbol{\gamma}}^*_S = \left(\dot{\boldsymbol{\gamma}}^* + \dot{\boldsymbol{\gamma}}^{*\mathrm{T}}\right)/2$ and $\dot{\boldsymbol{\gamma}}^*_W = \left(\dot{\boldsymbol{\gamma}}^* - \dot{\boldsymbol{\gamma}}^{*\mathrm{T}}\right)/2$, respectively. In this manner, the triple decomposition is more refined than the Cauchy–Stokes decomposition since $\tilde{\boldsymbol{S}}^* = \dot{\boldsymbol{\epsilon}}^* + \dot{\boldsymbol{\gamma}}^*_S$ and $\tilde{\boldsymbol{W}}^* = \dot{\boldsymbol{\varphi}}^* + \dot{\boldsymbol{\gamma}}^*_W$ [66, 72]. As described in detail by Das and Girimaji [66], the triple decomposition also enables a natural characterization of local streamline topologies and geometries. Similar topological analyses of vortical flow features have also been proposed [79], but we focus on the triple decomposition for the advantages outlined herein.

The ability of the triple decomposition to capture local streamline structure in terms of fundamental modes of deformation has guided efforts to define improved vortex criteria. There are an abundance of criteria to identify vortices that are based on various features (e.g. eigenvalues) of the VGT and that adopt various philosophies of what constitutes a vortex [80–84]. Debates surrounding these criteria primarily involve their (i) philosophical underpinnings, (ii) threshold sensitivities, and (iii) observational invariances.

Regarding (i), the Cauchy–Stokes decomposition underlies many common symmetry-based vortex criteria, including the Q [85] and λ_2 [86] criteria. Local streamline topology underlies many common geometry-based vortex criteria, including the Δ [60] and λ_{CI} [80] criteria. Like the geometry-based methods, and unlike the symmetry-based methods, the rigid vorticity criterion ($\dot{\varphi}_{z^*} > 0$) [87] captures all rotational local streamline geometries under the assumption that rigid rotation is an essential ingredient of a vortex [66, 83]. The philosophical distinction between symmetry-based and geometry-based criteria also underlies the so-called 'disappearing vortex problem' in which, fixing the VGT configuration and strain rate, increasing only the vorticity magnitude can remove a geometry-based vortex from the flow [80, 88, 89]. However, we here adopt the geometry-based viewpoint since, unlike vorticity, rigid rotation persistently underlies rotational local streamline topologies in all inertial frames. This interpretation in terms of local streamline topology has the potential to elucidate connections to related (e.g. elliptic) instabilities.

Regarding (ii), the Omega (Ω) class of vortex criteria [90–93] is advantageous since it uses quantities that are bounded and less threshold sensitive than the aforementioned methods. Regarding (iii), whereas most common vortex criteria are Galilean invariant, they are typically not objective since they are not preserved in rotating reference frames [81, 82]. However, the objectivized $\dot{\varphi}_{z^*}$ [94] and objectivized Ω [95] criteria, which are formulated by replacing $\tilde{\boldsymbol{W}}$ with its deviation from its global spatial mean, remain invariant in these reference frames. Moreover, they are among the only compatible (i.e. self-consistent) objectivized vortex criteria out of the modifications commonly associated with the vortex criteria we have discussed [84]. This advantage enhances the experimental verifiability and clarifies the physical significance of visualizations of the corresponding vortex structures.

Synthesizing the advantages of the geometry-based vortex definitions and the Ω class of vortex criteria, we identify vortices using the Ω_r method in the present investigation. This criterion is formulated in terms of the quantity

$$\Omega_r = \frac{(\boldsymbol{\omega} \cdot \boldsymbol{e}_{z^*})^2}{2\,(\boldsymbol{\omega} \cdot \boldsymbol{e}_{z^*})^2 - 4\lambda_{\mathrm{CI}}^2 + 4\varepsilon_{\mathrm{vort}}}, \tag{2.4}$$

where λ_{CI} is the imaginary part of the complex eigenvalues of $\boldsymbol{A}$, $\boldsymbol{e}_{z^*}$ is the unit vector along the z^*-axis, and $\varepsilon_{\mathrm{vort}}$ is a numerical threshold used to prevent division by zero. Vortices are theoretically identified as spatially connected

regions satisfying $\Omega_r > 0.5$ when $\varepsilon_{\text{vort}} = 0$. In practice, however, vortices are identified using a small $\varepsilon_{\text{vort}} > 0$ and $\Omega_r \geq 0.52$ [83] to e.g. remove weak vortices.

2.1.3 Contributions

In this paper, we utilize the advantageous properties of geometry-based analyses of the VGT to efficiently characterize turbulence initiated by a vortex ring collision. We use the adaptive, multiresolution computational techniques discussed in §2.2 to perform a direct numerical simulation of this flow at $Re_{\Gamma_0} = 4000$. In §2.3, we establish the fidelity of our simulation and we visualize and discuss the various regimes of its evolution. In §2.4, we analyze the partitioning of the velocity gradients to characterize these regimes in terms of the modes of deformation. In §2.5, we introduce a geometry-based phase space that characterizes the action of the elliptic instability and its interplay with other mechanisms driving the turbulent flow. Our analyses reveal statistical features of the VGT that are similar to those of previous simulations. They also provide tools with the potential to help disentangle mechanisms underlying vortex interactions during transition and turbulent decay. Finally, we summarize our results in the context of previous works and highlight promising future research prospects in §2.6.

2.2 Methods

2.2.1 Computational method

To efficiently simulate a turbulent vortex ring collision, we adopt a recently developed multiresolution solver for viscous, incompressible flows on unbounded domains [96–99]. Yu et al. [99] provide a detailed discussion of the formulation, properties, and performance of the method. We summarize the key advantages of the solver here and expound the computational formulation in Appendix 2.A1. The advantages we discuss allow us to simulate a relatively high Reynolds number vortex ring collision at a relatively low computational cost.

The Navier–Stokes equations (NSE) are spatially discretized onto a staggered Cartesian grid using a second-order-accurate finite-volume scheme that endows discrete operators with useful properties (i) [96]. Discrete differential operators are constructed to mimic the symmetry, orthogonality, and integration properties of their continuous counterparts. They also commute with

the Laplacian and integrating factor operators, as defined in Appendix 2.A1. Furthermore, the discretization of the nonlinear term in the momentum equations preserves relevant (e.g. energy) conservation properties in the absence of viscosity. Together, the mimesis, commutativity, and conservation properties of the discretization scheme facilitate fast, stable, high-fidelity simulations of turbulent flows.

The computational methods we employ also have high parallel efficiency (ii) and linear algorithmic complexity (iii). The computational efficiency of the flow solver is primarily centered around solving the discrete pressure Poisson equation on a formally unbounded grid using the lattice Green's function (LGF) [96, 100, 101]. The Poisson equation is obtained by taking the divergence of the NSE in rotational form, such that the source term is $\boldsymbol{\nabla} \cdot \boldsymbol{r}$, where $\boldsymbol{r} = \boldsymbol{u} \times \boldsymbol{\omega}$ is the Lamb vector. By considering flows with at least exponentially decaying far-field vorticity, the approximate support of this source field can be captured using a finite computational domain. Given a source cutoff threshold, the finite domain is adaptively truncated to capture only the regions relevant to the Poisson problem. Solving the Poisson problem over this domain involves the convolution of the LGF with the source field. The flow solver achieves (ii) and (iii) by efficiently evaluating this convolution via a fast multipole method [100] that compresses the kernel using polynomial interpolation. This method is accelerated by exploiting the efficiency of fast Fourier transforms on a block-structured Cartesian grid.

In addition to spatially adapting the extent of the computational domain, adaptive multiresolution discretization (iv) is achieved by using adaptive mesh refinement (AMR) to reduce the number of degrees of freedom required for solutions. As discussed previously [97, 99], the present AMR framework is carefully constructed to preserve the desirable operator properties (i) and augment the efficiencies (ii, iii) associated with the uniform-grid framework [96, 100]. In the AMR framework, the computational grid is partitioned into multiple levels, each with double the resolution in each direction as the previous level. The spatial regions associated with each level are non-overlapping, except for extended regions that are used to compute a combined source term that includes a correction induced by the difference between the coarse-grid and fine-grid partial solutions. As formulated in Appendix 2.A1, a region is refined when its combined source exceeds a threshold and it is coarsened when

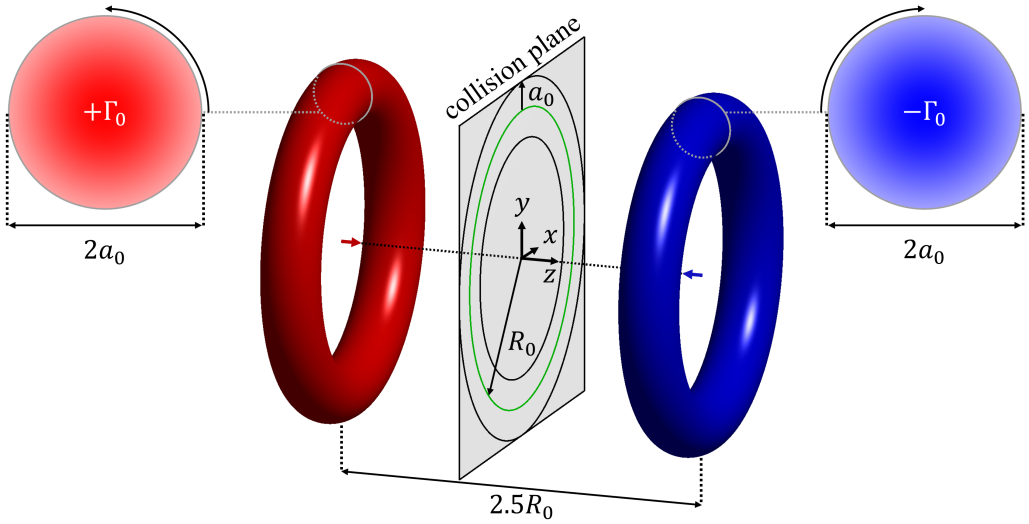

Figure 2.1: Initial geometry of the flow configuration used to simulate the head-on collision between vortex rings. The shading of the vortex cores reflects their Gaussian vorticity profiles.

its combined source falls below a smaller threshold. As shown in §2.3.1 (see Table 2.1), this AMR formulation drastically reduces the number of computational cells required to capture a head-on vortex ring collision compared with a fixed-resolution scheme.

2.2.2 Vortex ring collision simulation

As depicted in Figure 2.1, we consider a flow configuration in which the vortex rings are initialized with opposing circulations such that they propagate toward one another along the z-axis and meet at the collision plane at $z = 0$. The rings are initialized a distance $L_z = 2.5R_0$ apart, which is sufficiently large to mitigate their mutual influence during the most vigorous period of equilibration. Both rings are initialized with Gaussian vorticity distributions (2.1) such that $Re_{\Gamma_0} = 4000$ and $\delta_0 = 0.2$. Unless otherwise stated, we use the initial circulation, $\Gamma_0 = 1$, and radius, $R_0 = 1$, of each ring to non-dimensionalize all variables. To excite transition, we randomly perturb the radii of the vortex rings using the first 32 Fourier modes in θ, which are prescribed random phases and uniform magnitudes, $R_{\text{pert}} = 5 \times 10^{-4}$. Consistent with previous tests [99], these initial perturbations are sufficiently large to dominate perturbations incurred by discretization errors.

The computational mesh we use has $N_{\text{level}} = 2$ levels of refinement beyond the base level such that the ratio of the coarsest-grid spacing to the finest-grid

spacing is $\Delta x_{\text{base}}/\Delta x_{\text{fine}} = 4$. Based on preliminary simulations of turbulent vortex rings [96] and vortex ring collisions [99], we select $a_0/\Delta x_{\text{base}} = 5$ and $\Delta t/\Delta x_{\text{fine}} = 0.35$ to ensure the flow is well resolved throughout the simulation. Finally, parameters controlling the spatial and mesh refinement thresholds are chosen as discussed in Appendix 2.A1.

2.2.3 Simulation integral metrics

We track the evolution and fidelity of the simulation using integral metrics associated with incompressible flows [96]. Particularly, we compute the hydrodynamic impulse, helicity, vortical kinetic energy, and enstrophy of the flow, which are denoted by $\boldsymbol{I}_V$, H, K_V, and E, respectively. These integrals are formally evaluated on an unbounded domain, but we evaluate them using the finite AMR grid as

$$\begin{aligned} \boldsymbol{I}_V(t) &= \int_{V(t)} (\boldsymbol{x} \times \boldsymbol{\omega}) dV, \quad H(t) = \int_{V(t)} (\boldsymbol{u} \cdot \boldsymbol{\omega}) dV, \\ K_V(t) &= \int_{V(t)} \boldsymbol{u} \cdot (\boldsymbol{x} \times \boldsymbol{\omega}) dV, \quad E(t) = \frac{1}{2} \int_{V(t)} |\boldsymbol{\omega}|^2 \quad dV, \end{aligned} \tag{2.5}$$

where $V(t)$ is the time-varying AMR grid. The impulse is the appropriate measure of momentum since it converges for flows on unbounded domains with compact vorticity. The vortical kinetic energy can also be expressed as $K_V = K + K_{\partial V}$, where K represents the kinetic energy and $K_{\partial V}$ is a correction term based on the flow at the boundary of the grid, $\partial V(t)$. These metrics can be expressed as

$$K(t) = \frac{1}{2} \int_{V(t)} |\boldsymbol{u}|^2 \, dV, \quad K_{\partial V}(t) = \int_{\partial V(t)} \boldsymbol{x} \cdot \left((\boldsymbol{u}\boldsymbol{u}) \cdot \boldsymbol{n} - \frac{1}{2} |\boldsymbol{u}|^2 \boldsymbol{n} \right) dS, \tag{2.6}$$

where $\boldsymbol{n}$ is the normal vector of ∂V [102]. For vanishing far-field velocity, $K_{\partial V}$ vanishes on unbounded domains and, for the present grid, we make use of the smallness of $K_{\partial V}$ when analyzing dissipation.

In the absence of non-conservative external body forces, the hydrodynamic impulse is conserved for incompressible flows on unbounded domains [103]. The helicity would also be conserved in the absence of viscosity, and it is useful for assessing simulation fidelity as the vortex rings initially approach the collision plane since the evolution of the flow is dominated by inviscid effects. These integral metrics initially evaluate to $\boldsymbol{I}_V(0) = \boldsymbol{0}$ and $H(0) = 0$ due to the spatial symmetries of the initial flow configuration. These initial symmetries hold to the extent that the vorticity is well captured and the contributions

of the random perturbations used to excite instability growth are negligible. As the flow evolves, subsequent deviations from these initial values reflect the degree to which the corresponding initial symmetries are broken.

The enstrophy and the kinetic energy provide a more detailed picture of simulation fidelity during transition and turbulent decay, when viscous dissipation at small scales becomes relevant. For unsteady, incompressible flows on unbounded domains, the dissipation governs the decay rate of kinetic energy and can be expressed in terms of the enstrophy. Comparing these integrals is useful for characterizing (i) the degree to which small-scale features are resolved during peak dissipation and (ii) the flux of kinetic energy out of the finite computational domain [17]. We therefore introduce effective Reynolds numbers, which are given by

$$\frac{Re_S^{\text{eff}}(t)}{Re_{\Gamma_0}} = -\frac{\Phi_S(t)}{dK/dt}, \qquad \frac{Re_W^{\text{eff}}(t)}{Re_{\Gamma_0}} = -\frac{\Phi_W(t)}{dK/dt}, \tag{2.7}$$

where Φ_S is the volume-integrated dissipation and $\Phi_W = 2E/Re_{\Gamma_0}$ is its enstrophy-based counterpart [104]. Here, we differentiate K instead of K_V when computing the effective Reynolds numbers to prevent amplification of the noise associated with adaptations in the computational domain, to which K_V is more sensitive. This is justified since K and K_V are nearly identical throughout the present simulations (see Figure 2.2). The ratio Re_S^{eff} is useful for assessing spatial resolution since the dissipation can vary significantly during transition and turbulent decay. The corresponding Kolmogorov scale, $\eta = (\nu^3/\Phi_S)^{1/4}$, can also be used to validate the selected grid spacings. The difference between Re_S^{eff} and Re_W^{eff} reflects the relative significance of the acceleration of the flow on ∂V through the boundary integral in the Bobyleff–Forsyth formula [104]. Together, the error metrics defined in this section comprehensively characterize the fidelity of the simulation as its flow structures evolve and the computational domain adapts accordingly.

2.3 Evolution of integral metrics and vortical structures

2.3.1 Evolution of integral metrics

Figure 2.2 shows the evolution of the integral metrics from §2.2.3 over the course of the simulation. In the subsequent analysis, we reference the various regimes of flow development with respect to the time, $t^* = 14.77$, at which maximum dissipation is attained. Table 2.1 qualitatively characterizes

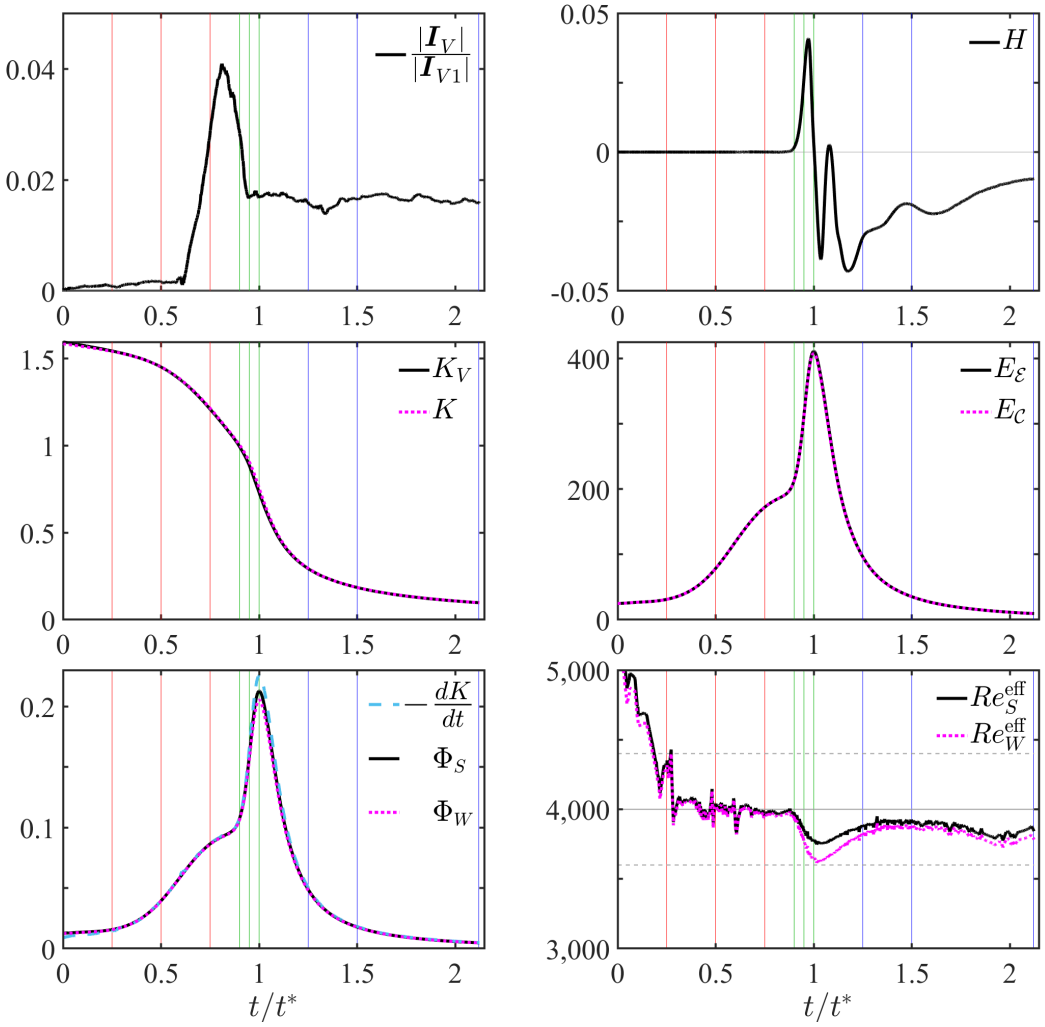

Figure 2.2: Temporal evolution of the integral metrics defined in §2.2.3 over the course of the simulation. The vertical lines correspond to the reference times in Table 2.1 and they are colored accordingly. The horizontal lines in the Re^{eff} panel represent Re_{Γ_0} (solid) with 10% margins (dashed). The impulse magnitude is normalized by that of each vortex ring in isolation, $|\boldsymbol{I}_{V1}| \approx 1.02\pi \approx 3.204$. The enstrophies $E_\mathcal{E}$ and $E_\mathcal{C}$ are computed using vorticities located at the edges and centers, respectively, of the computational cells.

the state of the simulation at each reference time we consider for the initial, transitional, and turbulent regimes of the simulation.

The initial evolution of the flow involves a rapid period of equilibration ($t \lesssim 0.25t^*$) and the propagation of the equilibrated rings towards the collision plane ($0.25t^* \lesssim t \lesssim 0.50t^*$). The interaction of the rings accelerates their radial expansion ($0.50t^* \lesssim t \lesssim 0.75t^*$) and the elliptic instability eventually emerges along the expanding rings ($0.75t^* \lesssim t \lesssim 0.90t^*$). Appendix 2.A2

Regime of evolution	t/t^*	$\bar{R}_p$	V	ϕ_0 (%)	ϕ_1 (%)	ϕ_2 (%)
Post-equilibration vortex rings	0.25	1.18	201	80.9	13.8	5.3
Vortex boundary merger	0.50	2.01	243	76.6	18.5	4.9
Enhanced radial expansion	0.75	3.58	356	80.6	15.7	3.7
Formation of secondary vortices	0.90	4.51	408	76.6	20.0	3.4
Interaction of secondary vortices	0.95	4.77	421	72.0	24.1	3.9
Proliferation of small scales	1.00	4.97	445	63.8	30.9	5.3
Early turbulent decay	1.25	5.38	507	61.4	30.8	7.8
Intermediate turbulent decay	1.50	5.60	531	66.7	26.7	6.6
Late turbulent decay	2.12	5.82	564	72.1	26.8	1.1

Table 2.1: Reference times used to analyze the initial (red), transitional (green), and turbulent (blue) regimes of the present vortex ring collision, where $t^* = 14.77$ is the time of maximum dissipation. Here, $\bar{R}_p$ represents the mean vortex ring radius (see Appendix 2.A2), V is the volume of the computational domain, and ϕ_k is the fraction of V occupied by level k of the AMR grid, which has grid spacing $\Delta x_k = \Delta x_{\text{base}}/2^k$ with $\Delta x_{\text{base}} = 0.04$.

supports the importance of the elliptic instability during the early stages of transition. Subsequently, the flow transitions to turbulence ($0.90t^* \lesssim t \lesssim t^*$) and rapidly produces small-scale flow structures. Following transition, the flow undergoes turbulent decay for the remainder of the simulation (i.e. for $t \gtrsim t^*$). See §2.3.2 for visualizations of the flow at the reference times from Table 2.1 associated with each of these regimes of evolution.

As the vortex rings initially propagate towards the collision plane ($t \lesssim 0.50t^*$), the kinetic energy decays slowly and the enstrophy and dissipation are relatively small. The effective Reynolds numbers rapidly adjust to the value of Re_{Γ_0} during the initial equilibration period ($t \lesssim 0.25t^*$) and remain roughly constant as the equilibrated rings approach the collision plane ($0.25t^* \lesssim t \lesssim 0.50t^*$). The helicity is well conserved in this regime since the flow evolves in a nearly inviscid fashion. Further, the impulse is initially small and grows relatively slowly during this period. These results suggest that the symmetries associated with the handedness and momentum distribution of the flow are well preserved in the initial regime of evolution.

As the rings expand radially at the collision plane ($0.50t^* \lesssim t \lesssim 0.75t^*$) and the elliptic instability emerges ($0.75t^* \lesssim t \lesssim 0.90t^*$), the kinetic energy decays more rapidly and the dissipation grows. During these periods, the helicity symmetry remains well preserved and the effective Reynolds numbers remain

relatively constant near Re_{Γ_0}, suggesting that the flow is well resolved. However, the impulse magnitude varies more rapidly in time due to the rapid radial expansion of the rings. In following the expanding vortical flow at the collision plane, the adaptations of the domain break the symmetry[1] associated with impulse integral more significantly than during the initial evolution of the rings. The resulting growth in $|\boldsymbol{I}_V|$ is primarily attributed to its component in the z direction, along which the domain is compressed as the flow concentrates about the collision plane.

As the flow transitions to turbulence ($0.90t^* \lesssim t \lesssim t^*$), the kinetic energy decays even more rapidly and the dissipation approaches its maximum value. Due to the proliferation of small-scale flow structures during this period, the effective Reynolds numbers drop to their minimum values at $t \approx t^*$, when the flow is most difficult to resolve. The increased difference between Re_S^{eff} and Re_W^{eff} reflects that the acceleration of the flow near ∂V is more relevant at this time. The rapid generation of small-scale flow structures also implies that viscosity plays a more important role in this regime. Correspondingly, the helicity begins to vary in time in this regime, reaching its maximum rate of change at the time of peak dissipation. Its variations reflect that vortex lines in the flow undergo rapid topological changes during transition. By contrast, the impulse magnitude decays to a roughly constant value as the radial expansion of the rings slows in this transitional regime.

During the turbulent decay of the flow ($t \gtrsim t^*$), the kinetic energy becomes small and the dissipation decays rapidly, eventually falling below its initial value (at $t \approx 1.62t^*$). The dissipation matches the kinetic energy decay rate more closely for this regime than for transition. Further, as the turbulence develops, the effective Reynolds numbers agree well with one another and, to a lesser extent, with Re_{Γ_0}. These features reflect, respectively, that the acceleration near ∂V is less significant and that the small scales are relatively well resolved, especially with respect to the transitional period. The helicity variations in this turbulent regime also eventually slow relative to those observed during transition. Similarly, the impulse remains roughly constant around its value at $t = t^*$. Whereas the z component dominates the impulse magnitude during the radial expansion of the rings, all impulse components have similar magnitudes in this turbulent regime.

[1] This symmetry-breaking effect should be interpreted as an artifact of the adaptive numerical scheme and not the result of a physical mechanism.

The evolution of the integral metrics characterizes the various regimes of the flow and supports the fidelity of our simulation. For example, the helicity is well conserved during the nearly inviscid evolution of the vortex rings and its subsequent variations are relatively small in magnitude. Further, the variations in the impulse magnitude throughout the simulation remain less than 5% of the impulse associated with each vortex ring in isolation. These results indicate that the symmetries associated with the handedness and momentum distribution of the flow also remain well preserved in the appropriate regimes of the simulation.

Our dissipation analysis also suggests that the small-scale flow structures remain reasonably well resolved throughout the entire simulation. After equilibration, the maximum relative deviation in Re_S^{eff} from Re_{Γ_0} is roughly 6.5% and it occurs around $t \approx t^*$. This relative deviation is similar to that of a previous simulation of a single vortex ring at $Re_{\Gamma_0} = 7500$ using a finite computational grid [17]. Moreover, it is considerably smaller during the approach and radial expansion of the rings and, to a lesser extent, during turbulent decay. Even during peak dissipation, when the Kolmogorov scale is smallest, the finest grid has acceptable resolution since $\Delta x_{\text{fine}}/\eta \approx 3.42$. Altogether, these results suggest that our simulation is well resolved and support our analysis of the mechanisms underlying transition and turbulent decay.

2.3.2 Evolution of vortical flow structures

For the present simulation, we identify vortices using the Ω_r criterion [83] with a numerical threshold of $\varepsilon_{\text{vort}} = 0.04$. This criterion provides connections to the triple decomposition of the VGT and the structure of local streamlines. Due to the well-preserved symmetries of the flow, the global spatial mean of the vorticity tensor is nearly zero and, hence, the Ω_r criterion is nearly objective [95] for the present simulation. We specifically visualize the flow using $\Omega_r = 0.52$ and $\Omega_r = 0.93$ to investigate the structures of the vortex boundaries and the vortex cores, respectively. We color these structures using $\cos\theta^*$, where θ^* is the angle between the z^*-axis and the z-axis. This color scheme enables the identification of antiparallel vortices along the z-axis, which play an important role in mediating transition and generating small-scale flow structures in the present vortex ring collision. In Figure 2.3, we visualize the vortical structures in the flow at each reference time from Table 2.1.

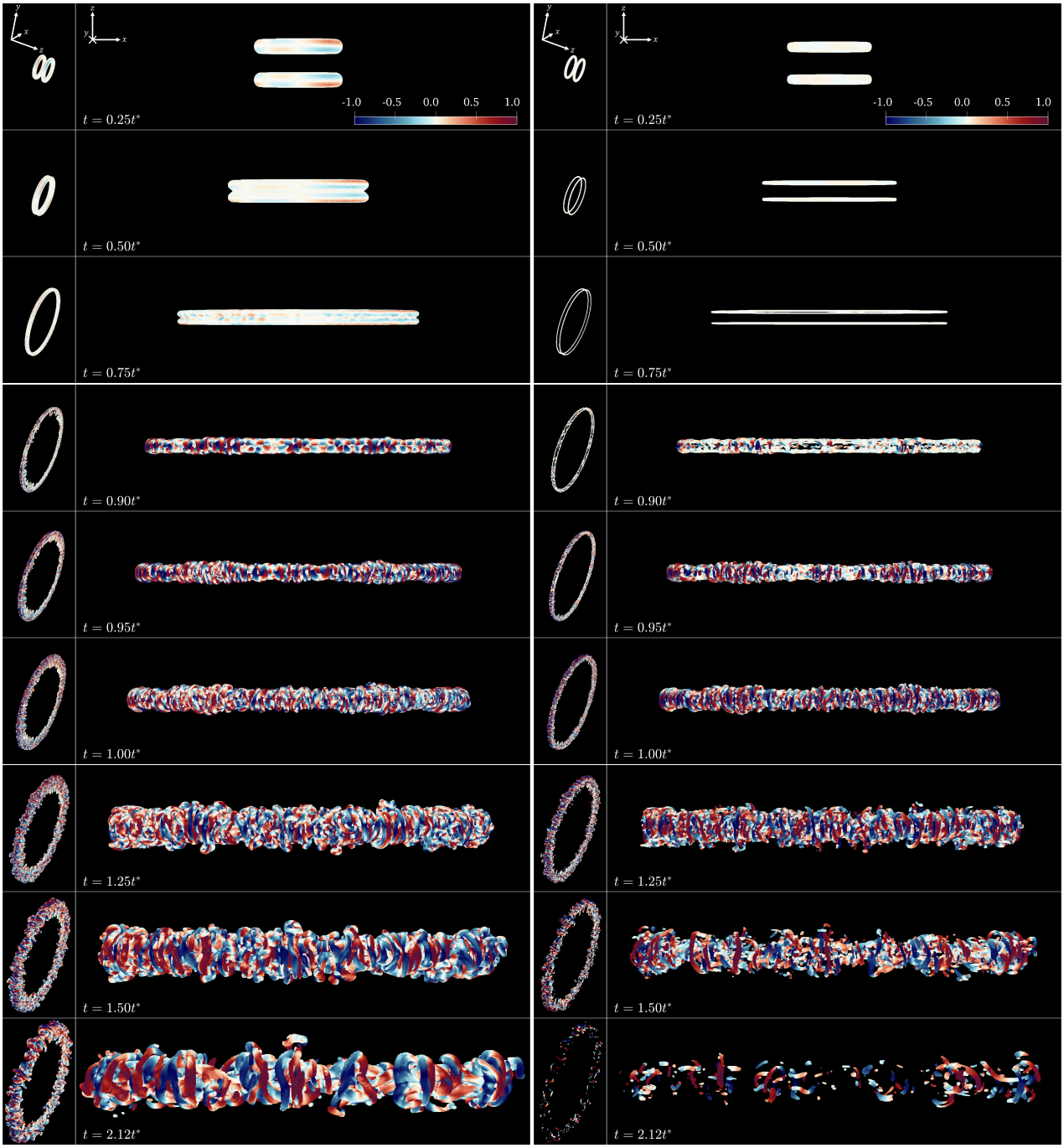

Figure 2.3: Visualizations of the vortex boundaries ($\Omega_r = 0.52$, left side) and vortex cores ($\Omega_r = 0.93$, right side), colored by $\cos\theta^*$, for each reference time from Table 2.1. A movie depicting the evolution of the vortex boundaries from the auxiliary viewpoint (leftmost column) is provided as supplementary material available at https://doi.org/10.1017/jfm.2024.90.

During the initial evolution of the flow, the equilibrated vortex rings approach the collision plane and expand radially due to their mutual interaction. In this regime, the thinning of the vortex boundaries and cores illustrates the mechanisms driving the shift from a rigid-rotation-dominated regime to a shearing-dominated regime. Further, the visualizations at $t = 0.75t^*$ depict the emergence of the short-wave elliptic instability, which is consistent with previous vortex ring collision simulations in similar parameter regimes [36, 39].

The transitional regime of the flow is marked by the development of secondary vortex filaments and the subsequent generation of small-scale vortical flow structures. At $t = 0.90t^*$, the visualizations show the development of secondary vortical structures around the circumference of the collision. These structures consist of antiparallel vortex filament pairs that arise in regions where the elliptic instability drives local interactions between the rings. This behavior supports the notion that the elliptic instability mediates the initial transition of the rings, leading to the development of secondary vortical structures. The antiparallel secondary filaments become increasingly densely-packed as transition progresses and they mediate the proliferation of small-scale vortical flow structures, e.g. as observed at $t = t^*$.

In Appendix 2.A2, we decompose the flow into azimuthal Fourier modes to characterize the wavenumbers of the perturbations that dominate transition. Our analysis confirms that the short-wave elliptic instability, with wavelength of the order of the core radius, mediates the initial stages of transition. We further show that, at $t = t^*$, the most prominent antiparallel vortices occur at the second harmonic of an originally dominant perturbation. Taken together, our visualizations and perturbation analysis are consistent with the initial stages of the iterative elliptic instability pathway, which is driven by subsequent generations of antiparallel vortex filaments [39].

During the turbulent decay of the flow, the geometric features of the vortex boundaries remain similar at each reference time. However, as energy is dissipated, the smallest-scale vortices are progressively destroyed and the vortical flow structures grow larger in time. The structures of the vortex cores and boundaries reinforce the importance of the interactions between the secondary vortex filaments in mediating the evolution of the turbulent flow. The vortex boundaries also show the formation and ejection of vortex rings from the turbulent cloud resulting from the collision. These ejections, which are a hall-

mark of the Crow instability, often occur in regions where antiparallel vortex filaments interact and are of similar size to those filaments. This observation provides further evidence of the interplay between the elliptic and Crow instabilities driven by interacting vortex filaments around the turbulent cloud [36, 57]. In what follows, we develop machinery to probe these mechanisms in the context of features of the velocity gradients, with a particular emphasis on characterizing the action of the elliptic instability among other mechanisms.

2.4 Partitioning of velocity gradients

Here, we investigate the partitioning of the velocity gradients to characterize the evolution of the flow in the context of the fundamental modes of deformation. We first consider volumetric weighted averages of the relative contributions of various constituents of $\tilde{\boldsymbol{A}}$ to the strength of the velocity gradients. These averages may be expressed as

$$\left\langle \xi \right\rangle_{A^2} = \frac{\int_{V(t)} A^2 \xi \, dV}{\int_{V(t)} A^2 \; dV}, \tag{2.8}$$

where $\xi \in \{\tilde{S}^2, \tilde{W}^2\}$ for the Cauchy–Stokes decomposition and $\xi \in \{\dot{\epsilon}^2, \dot{\gamma}^2, \dot{\varphi}^2, 2\dot{\boldsymbol{\varphi}}\!:\!\dot{\boldsymbol{\gamma}}\}$ for the triple decomposition. Here, we have used that the Frobenius inner product, denoted by :, of a symmetric tensor with an antisymmetric tensor is zero and that $\dot{\gamma}_W^2 = \dot{\gamma}_S^2 = \dot{\gamma}^2/2$. The shear–rotation correlation term, $2\dot{\boldsymbol{\varphi}}\!:\!\dot{\boldsymbol{\gamma}} = 2\dot{\varphi}_{z^*}\dot{\gamma}_{z^*} > 0$, reflects the presence of shearing in the plane of rigid rotation. All of the relative contributions discussed are unitarily invariant and, thus, they apply to both the principal coordinates and the global coordinates. Figure 2.4 shows how these relative contributions evolve during the simulation for both decompositions of $\tilde{\boldsymbol{A}}$.

Consistent with the equivalence of Φ_S and Φ_W for incompressible flows on unbounded domains [104], $\left\langle \tilde{S}^2 \right\rangle_{A^2} \approx \left\langle \tilde{W}^2 \right\rangle_{A^2} \approx 0.50$ for the present simulations. The largest deviations from this balance occur during equilibration ($t \lesssim 0.25t^*$) and around the time of peak dissipation ($t \approx t^*$). These deviations are consistent with the behavior of the effective Reynolds numbers in Figure 2.2 and their smallness further validates the ability of the finite computational grid to approximate a formally unbounded flow. However, since $\left\langle \tilde{S}^2 \right\rangle_{A^2}$ and $\left\langle \tilde{W}^2 \right\rangle_{A^2}$ remain relatively constant throughout the simulation, they provide limited information about the nature of the velocity gradients as the flow progresses through its initial, transitional, and turbulent regimes.

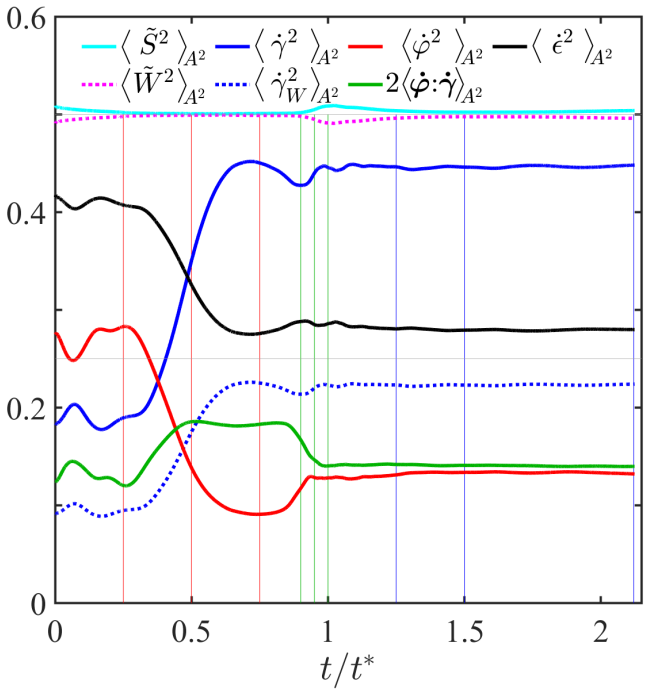

Figure 2.4: Relative contributions of the constituents of the Cauchy–Stokes decomposition and the triple decomposition to A^2. The vertical lines correspond to the reference times in Table 2.1 and they are colored accordingly.

Compared with the constituents of the Cauchy–Stokes decomposition, the constituents of the triple decomposition show more pronounced variations associated with the different regimes of evolution. For the initial Gaussian vorticity profiles, the contribution of rigid rotation to the enstrophy dominates the contribution of antisymmetric shearing. During equilibration ($t \lesssim 0.25t^*$), the fluctuations in all contributions of the triple decomposition constituents reflect the redistribution of velocity gradients in the cores of the vortex rings. As the equilibrated rings approach the collision plane and spread ($0.25t^* \lesssim t \lesssim 0.75t^*$), $\left\langle \dot{\epsilon}^2 \right\rangle_{A^2}$ and $\left\langle \dot{\varphi}^2 \right\rangle_{A^2}$ decrease and $\left\langle \dot{\gamma}^2 \right\rangle_{A^2}$ and $2\left\langle \dot{\boldsymbol{\varphi}} : \dot{\boldsymbol{\gamma}} \right\rangle_{A^2}$ increase. As the elliptic instability emerges, these contributions level off in a regime where antisymmetric shearing dominates rigid rotation and shear–rotation correlations are enhanced. The subsequent development of the elliptic instability ($0.75t^* \lesssim t \lesssim 0.90t^*$) is marked by slight rebounds in the contributions of $\left\langle \dot{\varphi}^2 \right\rangle_{A^2}$ and $\left\langle \dot{\gamma}^2 \right\rangle_{A^2}$. These rebounds are associated with the emergence of secondary vortex filaments and, hence, the nonlinear evolution of the elliptic instability. The transition to turbulence ($0.90t^* \lesssim t \lesssim t^*$), which is associated with the generation of small scales and enhanced dissipation, is marked by a decrease in the contribution of $2\left\langle \dot{\boldsymbol{\varphi}} : \dot{\boldsymbol{\gamma}} \right\rangle_{A^2}$.

Constituent	$\left\langle \dot{\epsilon}^2 \right\rangle_{A^2}$	$\left\langle \dot{\gamma}^2 \right\rangle_{A^2}$	$\left\langle \dot{\varphi}^2 \right\rangle_{A^2}$	$2\left\langle \dot{\boldsymbol{\varphi}}{:}\dot{\boldsymbol{\gamma}} \right\rangle_{A^2}$
Present vortex ring collision	28.0 %	44.6 %	13.3 %	14.1 %
Forced isotropic turbulence [66]	24 %	52 %	11 %	13 %

Table 2.2: Comparison of the equilibrium partitioning of the velocity gradients for the present vortex ring collision with the partitioning computed for forced isotropic turbulence [66]. Here, the equilibrium partitioning is computed as the mean over the turbulent decay regime ($t \gtrsim t^*$) and it is insensitive to the length of the averaging interval.

Remarkably, even though the flow is not stationary during turbulent decay, the relative contributions of the constituents of the triple decomposition to the strength of the velocity gradients remain roughly constant after transition. Further, as summarized in Table 2.2, these 'equilibrium' relative contributions are similar to those computed by Das and Girimaji [66] for forced isotropic turbulence at high Taylor-scale Reynolds numbers. This agreement suggests that the velocity gradient partitioning may encode a relatively common balance in unbounded, incompressible turbulence with appropriate symmetries. In this balance, shearing makes the largest contribution to the velocity gradients and rigid rotation makes the smallest contribution.

Beyond the strength of velocity gradients, it is also useful to examine the interplay between the modes of deformation in the context of vortical flow structures. Here, we introduce a new phase space defined by the relative contributions of $\left\langle \dot{\gamma}_W^2 \right\rangle_{A^2}$, $\left\langle \dot{\varphi}^2 \right\rangle_{A^2}$, and (implicitly) $2\left\langle \dot{\boldsymbol{\varphi}}{:}\dot{\boldsymbol{\gamma}} \right\rangle_{A^2}$ to $\left\langle \tilde{W}^2 \right\rangle_{A^2}$. The upper bound of this phase space is found by maximizing $\left\langle \dot{\varphi}^2 \right\rangle_{A^2} / \left\langle \tilde{W}^2 \right\rangle_{A^2}$, which occurs when $2\left\langle \dot{\boldsymbol{\varphi}}{:}\dot{\boldsymbol{\gamma}} \right\rangle_{A^2} / \left\langle \tilde{W}^2 \right\rangle_{A^2} = 0$. The bottom boundary is found by minimizing $\left\langle \dot{\varphi}^2 \right\rangle_{A^2} / \left\langle \tilde{W}^2 \right\rangle_{A^2}$, which occurs when $2\left\langle \dot{\boldsymbol{\varphi}}{:}\dot{\boldsymbol{\gamma}} \right\rangle_{A^2} / \left\langle \tilde{W}^2 \right\rangle_{A^2} = 2\sqrt{\left\langle \dot{\varphi}^2 \right\rangle_{A^2} \left\langle \dot{\gamma}_W^2 \right\rangle_{A^2}} / \left\langle \tilde{W}^2 \right\rangle_{A^2}$. Correspondingly, these boundaries may be expressed as

$$\left(1 - \sqrt{\frac{\left\langle \dot{\gamma}_W^2 \right\rangle_{A^2}}{\left\langle \tilde{W}^2 \right\rangle_{A^2}}}\right)^2 \leq \frac{\left\langle \dot{\varphi}^2 \right\rangle_{A^2}}{\left\langle \tilde{W}^2 \right\rangle_{A^2}} \leq 1 - \frac{\left\langle \dot{\gamma}_W^2 \right\rangle_{A^2}}{\left\langle \tilde{W}^2 \right\rangle_{A^2}}, \tag{2.9}$$

$$\Updownarrow \qquad\qquad \Updownarrow$$

$$-2\left(\frac{\left\langle \dot{\gamma}_W^2 \right\rangle_{A^2}}{\left\langle \tilde{W}^2 \right\rangle_{A^2}} - \sqrt{\frac{\left\langle \dot{\gamma}_W^2 \right\rangle_{A^2}}{\left\langle \tilde{W}^2 \right\rangle_{A^2}}}\right) \geq \frac{2\left\langle \dot{\boldsymbol{\varphi}}{:}\dot{\boldsymbol{\gamma}} \right\rangle_{A^2}}{\left\langle \tilde{W}^2 \right\rangle_{A^2}} \geq 0, \tag{2.10}$$

highlighting that lower and upper bounds of the rigid rotation contribution correspond to the upper and lower bounds, respectively, of the shear–rotation cor-

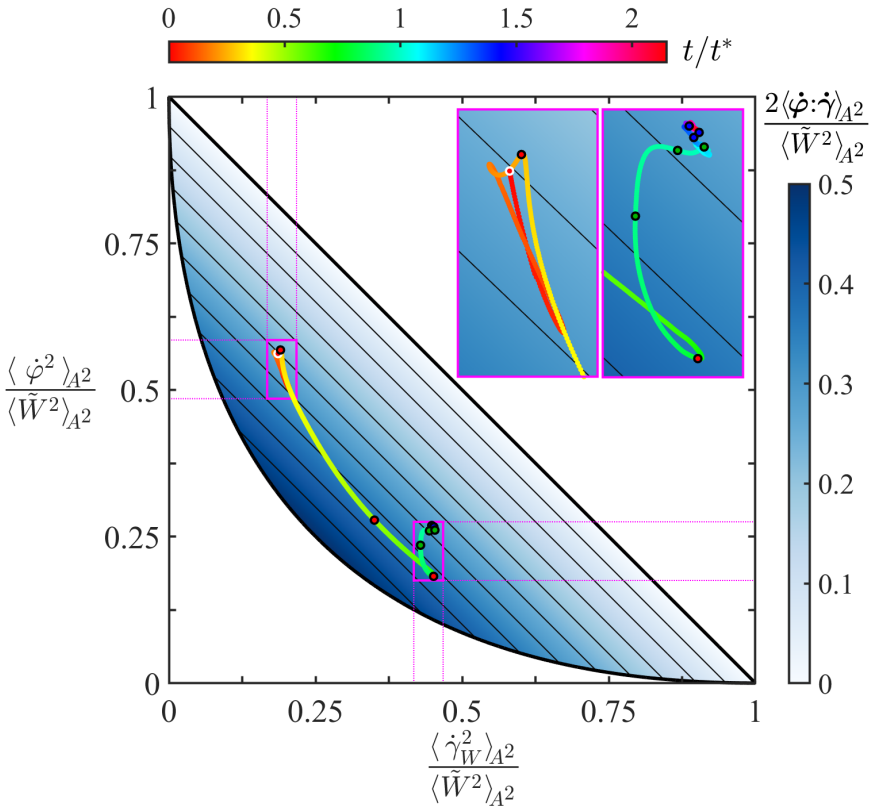

Figure 2.5: Shear–rotation phase space trajectory of the flow, highlighting the evolution during equilibration (left inset) and transition and turbulent decay (right inset). The contours represent increments of 0.05 in the color scale. The white circle marks the initial condition and the fill colors of the black circles correspond to the reference times they represent from Table 2.1.

relation contribution. The maximum value of $2\left\langle\dot{\boldsymbol{\varphi}}:\dot{\boldsymbol{\gamma}}\right\rangle_{A^2}/\left\langle\tilde{W}^2\right\rangle_{A^2}$ varies along the lower boundary of this phase space to ensure that the relative contributions sum to unity. The global maximum occurs when $2\dot{\boldsymbol{\varphi}}:\dot{\boldsymbol{\gamma}}/\tilde{W}^2 = 0.5$ or, equivalently, $\dot{\varphi}^2/\tilde{W}^2 = \dot{\gamma}_W^2/\tilde{W}^2 = 0.25$ at all points, which corresponds to the (pointwise) maximum of $2\dot{\boldsymbol{\varphi}}:\dot{\boldsymbol{\gamma}} = (\sqrt{2}+1)^{-1}$ reported by Das and Girimaji [66]. This maximum corresponds to local streamlines in the principal frame for which shearing occurs exclusively in the plane of rigid rotation.

Figure 2.5 depicts the trajectory of the flow in this shear–rotation phase space and elucidates how the relationships between the constituents of enstrophy associated with the triple decomposition evolve in time. Following rapid variations during equilibration, the trajectory returns to a position in phase space similar to that of the initial condition at $t \approx 0.25t^*$. The trajectory then undergoes a shift across the phase space as the equilibrated rings approach the

collision plane and spread radially ($0.25t^* \lesssim t \lesssim 0.75t^*$). This shift from a rigid-rotation-dominated regime to a shearing-dominated regime is associated with an enhanced contribution from $2\left\langle \dot{\boldsymbol{\varphi}}{:}\dot{\boldsymbol{\gamma}} \right\rangle_{A^2} / \left\langle \tilde{W}^2 \right\rangle_{A^2}$. The development of the elliptic instability ($0.75t^* \lesssim t \lesssim 0.90t^*$) and transition ($0.90t^* \lesssim t \lesssim t^*$) are associated with a shift in the direction of the trajectory towards smaller contributions of $2\left\langle \dot{\boldsymbol{\varphi}}{:}\dot{\boldsymbol{\gamma}} \right\rangle_{A^2} / \left\langle \tilde{W}^2 \right\rangle_{A^2}$. During turbulent decay ($t \gtrsim t^*$), the trajectory remains roughly fixed in the phase space and very close to its position at $t = t^*$.

Considering this phase space trajectory in the context of the dissipation (see Figure 2.2) reveals that, while the initial growth in dissipation is associated with enhanced shear–rotation correlations, its subsequent enhancement during transition is associated with a reduction in shear–rotation correlations. In Appendix 2.A3, we reexamine the visualizations from Figure 2.3 in terms of the shear–rotation correlations in the flow to highlight their relationship to the vortical flow structures. In §2.5, we interpret the effects of these shear–rotation correlations using a new, related phase space, based on local streamline geometry, to characterize the elliptic instability and other mechanisms.

2.5 Statistical geometry of local streamlines

2.5.1 Phase space transformations

The elliptic instability is associated with the resonance of the vortical flow with the underlying strain field and acts to break up elliptic streamlines. Consistent with this picture, we introduce a new geometry-based phase space that captures local flow features that (i) are conducive to the elliptic instability and (ii) characterize its action.

To address (i), we consider the angle, θ_ω, between the vorticity vectors associated with antisymmetric shearing and rigid rotation, which is given by

$$\theta_\omega = \cos^{-1}\left(\sqrt{\frac{\left(\dot{\boldsymbol{\varphi}}{:}\dot{\boldsymbol{\gamma}}\right)^2}{\dot{\varphi}^2 \dot{\gamma}_W^2}} \right). \tag{2.11}$$

Our emphasis on shearing is consistent with the classical models of strained vortices used to characterize the elliptic instability [28]. Since decreasing θ_ω corresponds to increasing the alignment between shearing and rigid rotation, it can be associated with conditions conducive to the elliptic instability.

To address (ii), we consider the aspect ratio, ζ, of the elliptic component of

rotational local streamlines in the plane of rigid rotation, which is given by

$$\zeta = \sqrt{1-e^2} = \sqrt{\frac{\dot{\varphi}^2}{\dot{\varphi}^2 + 2\dot{\boldsymbol{\varphi}}{:}\dot{\boldsymbol{\gamma}}}}, \tag{2.12}$$

where e represents the eccentricity of an ellipse with aspect ratio ζ. This aspect ratio characterizes the scale-invariant geometry of the local streamlines in the plane of rigid rotation. As such, it can be used alongside θ_ω to characterize the action of the elliptic instability by identifying how alignment between shearing and rigid rotation affects local streamline geometry.

The present shear–rotation and geometry-based phase spaces can be understood through nonlinear transformations of the $q_A - r_A$ phase space. The transformations we derive express the relative contributions of the triple decomposition to the velocity gradients using q_A and r_A, and they represent the inverse transformations to those presented by Das and Girimaji [66]. However, an additional parameter, θ_ω, is generally required to evaluate our transformations. This extra parameter demonstrates that the invariants of $\tilde{\boldsymbol{A}}$ alone cannot generally characterize the relative contributions of the constituents of the triple decomposition to the velocity gradients.

For rotational local streamlines, the transformations are given by

$$\begin{aligned}
\dot{\epsilon}^2 &= \frac{\left(-3\times 2^{2/3} q_A + 3^{2/3}\left(2\sqrt{3\Delta} + 9|r_A|\right)^{2/3}\right)^2}{6^{5/3}\left(2\sqrt{3\Delta} + 9|r_A|\right)^{2/3}}, \qquad \dot{\gamma}^2 = 2\dot{\gamma}_W^2 = 1 - 2\dot{\epsilon}^2 - 2q_A \ , \\
\dot{\varphi}^2 &= \left(-\sqrt{\dot{\gamma}_W^2}\cos\theta_\omega + \sqrt{1-\dot{\epsilon}^2 - \dot{\gamma}_W^2\left(2-\cos^2\theta_\omega\right)}\right)^2, \quad 2\dot{\boldsymbol{\varphi}}{:}\dot{\boldsymbol{\gamma}} = 2\sqrt{\dot{\varphi}^2\dot{\gamma}_W^2}\cos\theta_\omega,
\end{aligned} \tag{2.13}$$

where $\Delta = q_A^3 + \frac{27}{4} r_A^2$ is proportional to the discriminant of the characteristic equation of $\tilde{\boldsymbol{A}}$. In this case, $\dot{\epsilon}^2$ and $\dot{\gamma}^2$ can be determined directly from q_A and r_A and $\dot{\varphi}^2$, $2\dot{\boldsymbol{\varphi}}{:}\dot{\boldsymbol{\gamma}}$, and ζ can be determined if θ_ω is known. For non-rotational local streamlines, the transformations are given by

$$\dot{\epsilon}^2 = -2q_A, \quad \dot{\gamma}^2 = 1 - \dot{\epsilon}^2, \quad \dot{\varphi}^2 = 0, \tag{2.14}$$

which can be determined directly from a single parameter, q_A. The rotational and non-rotational transformations are continuous with one another at their boundary ($\Delta = 0$) and they are both symmetric about the q_A-axis. However, the aspect ratio is only well defined for $\Delta > 0$, consistent with our focus on rotational local streamlines.

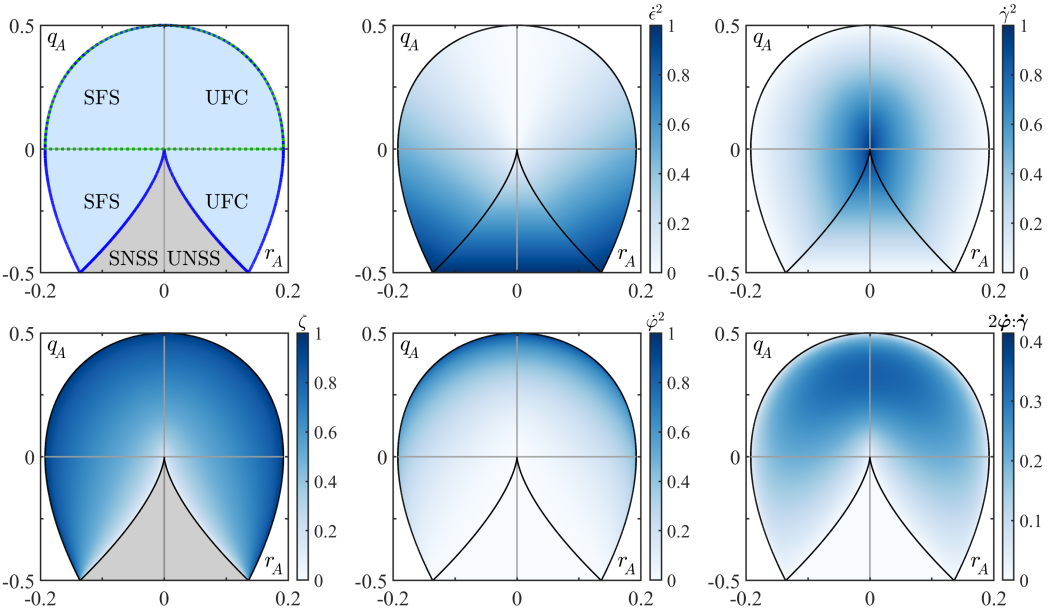

Figure 2.6: The $q_A - r_A$ phase space (top left) and the variations in $\dot{\epsilon}^2$, $\dot{\gamma}^2$, $\dot{\varphi}^2$, $2\dot{\boldsymbol{\varphi}} : \dot{\boldsymbol{\gamma}}$, and ζ in this space when $\theta_\omega = 43.57°$ is held constant. The top left panel shows the boundaries corresponding to the symmetry-based (dotted green) and the geometry-based (solid blue) vortex criteria (see §2.1.2). It also labels the four classes of non-degenerate local streamline topologies: stable-focus–stretching (SFS), unstable-focus–compression (UFC), stable-node–saddle-saddle (SNSS), and unstable-node–saddle-saddle (UNSS).

In Figure 2.6, we illustrate how $\dot{\epsilon}^2$, $\dot{\gamma}^2$, $\dot{\varphi}^2$, $2\dot{\boldsymbol{\varphi}}{:}\dot{\boldsymbol{\gamma}}$, and ζ vary within the $q_A - r_A$ phase space. In this phase space, the rotational geometries are externally bounded by $3\sqrt{3}|r_A| = (1 + q_A)(1 - 2q_A)^{1/2}$ and the non-rotational geometries are externally bounded by $q_A = -\frac{1}{2}$. For the rotational geometries, we display $\dot{\varphi}^2$, $2\dot{\boldsymbol{\varphi}} : \dot{\boldsymbol{\gamma}}$, and ζ for $\theta_\omega = 43.57°$, which corresponds to the mean value at $t = 1.25t^*$ (see Figure 2.8) and approximates the equilibrium value during turbulent decay. We document how each of these quantities varies with θ_ω in the $q_A - r_A$ phase space in Appendix 2.A4.

Figure 2.6 shows that, generically, the contribution of pure shearing ($\dot{\gamma}^2$) tends to dominate the velocity gradients near the origin of the $q_A - r_A$ plane. The contribution of normal straining ($\dot{\epsilon}^2$) grows large when the velocity gradients are dominated by the strain rate tensor. By contrast, for rotational geometries, the contribution of rigid rotation ($\dot{\varphi}^2$) grows large near the external boundary in regions where the vorticity tensor dominates. The contribution of shear–rotation correlations ($2\dot{\boldsymbol{\varphi}} : \dot{\boldsymbol{\gamma}}$) grows largest in the intermediate region of the phase space and it decays near the discriminant line and the external boundary.

The aspect ratio ζ is unity along the external boundary and it decays to zero at the discriminant line.

The elliptic instability, which is relevant in strained vortical flows, is expected to be most active for an intermediate range of aspect ratios. Further, vortex stretching and squeezing, which are known to play important roles in turbulent flows, can most readily be associated with the SFS and UFC streamline topologies, respectively [105]. In the corresponding regions in the $q_A - r_A$ plane, the transformations in Figure 2.6 suggest that the interplay between shearing and rotation is pertinent to these fundamental turbulent processes. Within this context, the transformations have the potential to characterize the role of the elliptic instability, among other mechanisms, in mediating such processes. In what follows, we investigate this premise by analyzing the evolution of the velocity gradient distributions in the $q_A - r_A$, shear–rotation, and $\zeta - \theta_\omega$ phase spaces.

2.5.2 Phase space distributions

The joint probability density functions (p.d.f.s) of the normalized velocity gradients in the phase spaces we investigate encode information about the local streamline geometries. Although these phase spaces are related to one another, the choice of phase space plays an important role in interpreting the statistical distributions of the flow. In the $q_A - r_A$ phase space, incompressible turbulent flows often follow a near-universal teardrop-like distribution about the origin [62, 63]. The shear–rotation phase space highlights the distribution of rotational streamline geometries and it characterizes the interplay of rigid rotation and antisymmetric shearing. The $\zeta - \theta_\omega$ phase space also considers rotational streamline geometries and it characterizes the flow in terms of geometric features of local streamlines that are associated with the elliptic instability.

Figure 2.7 shows the $q_A - r_A$ and the shear–rotation phase space distributions at reference times, selected from Table 2.1, that pertain to the development of the elliptic instability, transition, and turbulent decay. As the elliptic instability emerges ($t \approx 0.75t^*$), the velocity gradients are concentrated near the q_A-axis. Since $2\left\langle \dot{\boldsymbol{\varphi}} : \dot{\boldsymbol{\gamma}} \right\rangle_{A^2}$ is relatively large around this time, the rotational regions of the flow are concentrated near the bottom boundary of the shear–rotation phase space, particularly near the location where $2\left\langle \dot{\boldsymbol{\varphi}} : \dot{\boldsymbol{\gamma}} \right\rangle_{A^2}$ is maximized.

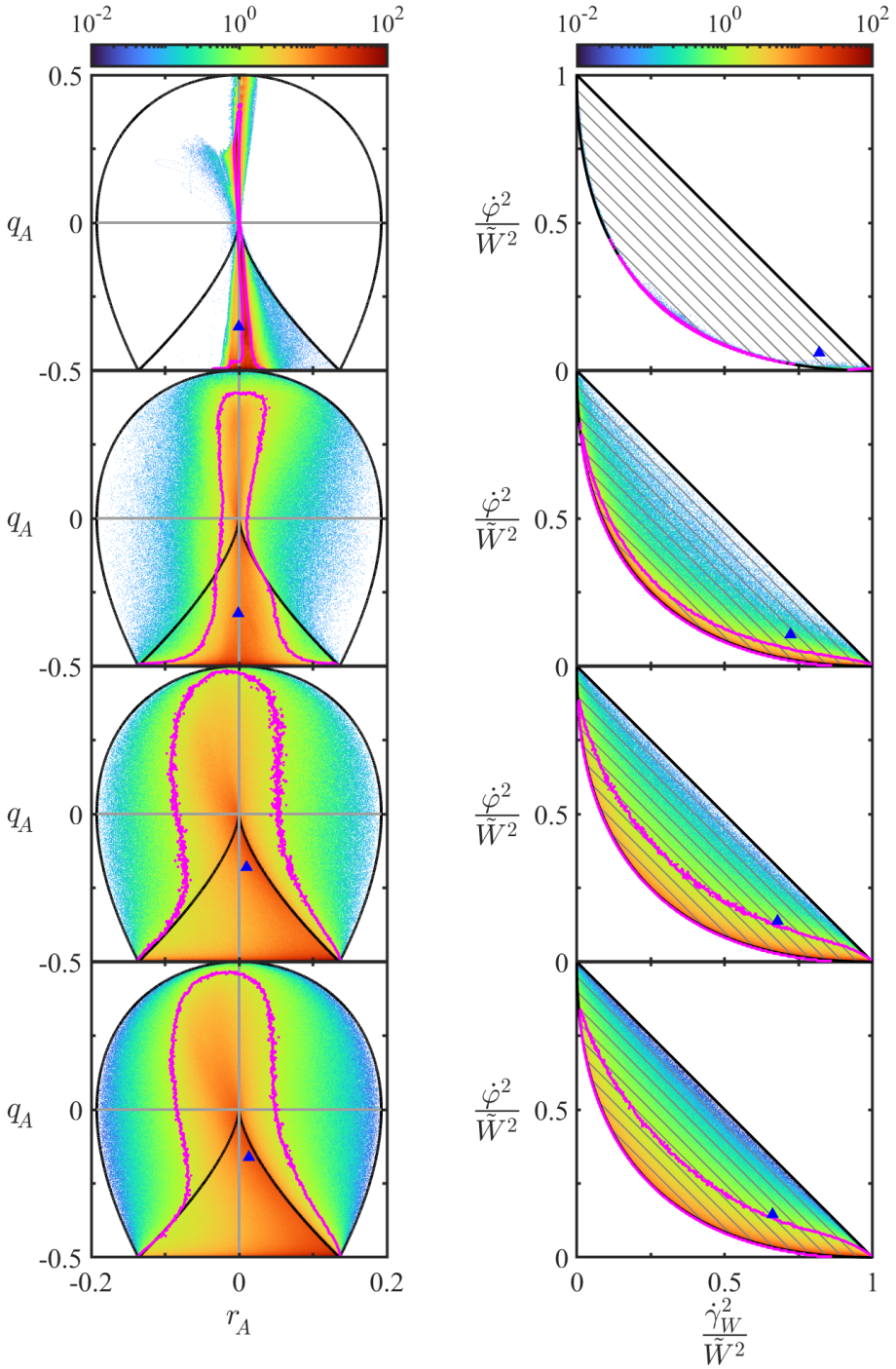

Figure 2.7: Joint p.d.f.s of the velocity gradients satisfying $A^2/\max(A^2) \geq 0.1\%$ in the $q_A - r_A$ phase space (left) and $W^2/\max(W^2) \geq 0.1\%$ in the shear–rotation phase space (right) at times $t = 0.75t^*$, $0.90t^*$, $1.00t^*$, and $1.25t^*$ (from top to bottom). The blue triangles represent the centroids of the distributions and the magenta contours represent the p.d.f. levels for which 90% of the flow (by volume) resides at higher p.d.f. levels. These contours are smoothed by using coarser p.d.f. bins to ensure that they roughly enclose the regions with higher p.d.f. levels.

As the flow transitions ($t \approx 0.90t^*$), the distribution remains centered about the q_A-axis but it expands towards larger $|r_A|$ as it begins to fill the $q_A - r_A$ phase space. Similarly, the p.d.f. in the shear–rotation phase space begins extending away from the bottom boundary of the phase space, although its bulk remains concentrated at the boundary. The broadening p.d.f.s represent the generation of more diverse local streamline topologies (see Figure 2.6), which is consistent with the formation of more complex vortical structures (see Figure 2.3).

At the time of peak dissipation ($t \approx t^*$), the distributions populate nearly all of the area in both the phase spaces. During the subsequent turbulent decay (as shown for $t \approx 1.25t^*$), the flow approaches its equilibrium distributions in both phase spaces, which remain similar to the distributions for $t \approx t^*$. In the $q_A - r_A$ phase space, the equilibrium p.d.f. above the r_A-axis is concentrated slightly left of the q_A-axis. This slight preference of the SFS topology is consistent with the typical presence of positive vortex stretching in regions of turbulent flows with rotational geometries. Below the r_A-axis, the p.d.f. is concentrated along the discriminant line for $r_A > 0$. The equilibrium distribution of our vortex ring collision in this phase space is similar to the near-universal teardrop-like shapes reported previously for forced isotropic turbulence [62, 63]. This similarity suggests that, in addition to the velocity gradient partitioning (see Table 2.2), the teardrop-like distribution may be more broadly applicable to incompressible flows with appropriate symmetries.

The p.d.f.s in the shear–rotation phase space evolve similarly to those in the $q_A - r_A$ phase space (e.g. by broadening) and specifically highlight rotational geometries. However, the difference between vortex stretching and squeezing, which is encoded in the sign of the real eigenvalue of the VGT, cannot be distinguished in this phase space since its constituents are non-negative. The high concentration of the p.d.f.s near the lower corner of this phase space, representing the origin of the $q_A - r_A$ phase space, shifts the centroids accordingly and highlights the importance of shearing in the generation and evolution of turbulent flows. The equilibrium distribution remains relatively concentrated about the lower boundary of this phase space, including regions where $2\left\langle \dot{\boldsymbol{\varphi}} : \dot{\boldsymbol{\gamma}} \right\rangle_{A^2}$ is relatively large. This behavior highlights the potential for the elliptic instability to be active during turbulent decay, but the breadth of the distribution suggests it may not be a completely dominant mechanism

driving turbulent flow in rotational regions.

To further investigate the evolution of the flow in the context of the elliptic instability, we again consider the relationship between the $\zeta - \theta_\omega$ and shear–rotation phase spaces. Using θ_ω and ζ, the constituents of the shear–rotation phase space and the corresponding shear–rotation correlation term and vortex identification criterion are given by

$$\begin{aligned} \frac{\dot{\varphi}^2}{\tilde{W}^2} &= \frac{4\zeta^4 \cos^2\theta_\omega}{1 + \left(-2 + 4\cos^2\theta_\omega\right)\zeta^2 + \zeta^4}, \quad \frac{\dot{\gamma}_W^2}{\tilde{W}^2} = \frac{\left(1-\zeta^2\right)^2}{1 + \left(-2 + 4\cos^2\theta_\omega\right)\zeta^2 + \zeta^4}, \\ \frac{2\dot{\boldsymbol{\varphi}}{:}\dot{\boldsymbol{\gamma}}}{\tilde{W}^2} &= \frac{4\zeta^2 \cos^2\theta_\omega \left(1-\zeta^2\right)}{1 + \left(-2 + 4\cos^2\theta_\omega\right)\zeta^2 + \zeta^4}, \quad \Omega_r = \left(1 + \left(1 - \sqrt{\frac{\dot{\varphi}^2}{\tilde{W}^2}}\right)^2\right)^{-1}. \end{aligned} \tag{2.15}$$

Figure 2.8 shows the p.d.f.s of the velocity gradients alongside the distributions of $2\dot{\boldsymbol{\varphi}}{:}\dot{\boldsymbol{\gamma}}/\tilde{W}^2$ and Ω_r in the geometry-based phase space at the same times as those in Figure 2.7.

As the elliptic instability emerges ($t \approx 0.75t^*$), the p.d.f. is highly concentrated at small values of θ_ω over a broad range of ζ. This distribution is consistent with the enhancement of $2\left\langle \dot{\boldsymbol{\varphi}}{:}\dot{\boldsymbol{\gamma}} \right\rangle_{A^2}$ around this time (see Figure 2.4) and reflects conditions conducive to the elliptic instability. The centroid of the distribution is located around $\zeta \approx 0.5$, which suggests that rotational streamlines with this aspect ratio may be particularly susceptible to these conditions.

During transition ($t \approx 0.90t^*$), the distribution broadens to a much larger range of θ_ω and, at the high end of this range, ζ becomes increasingly correlated with θ_ω. This broadening reflects the diversification of rotational local streamline topologies to include those for which shearing and rigid rotation are not well aligned. However, despite this broadening, the p.d.f. is still concentrated at small θ_ω. This behavior is consistent with the importance of the elliptic instability during transition (see Appendix 2.A2).

During turbulent decay ($t \gtrsim t^*$), the features of the p.d.f. are relatively invariant in time. In the equilibrium distribution (approximated at $t \approx 1.25t^*$), the centroid is located around $\theta_\omega \approx 44°$, which is considerably larger than its value ($\theta_\omega \approx 3°$) at $t = 0.75t^*$. Further, the 90% contour of the p.d.f. spans nearly the entire range of θ_ω and highlights a well-defined sharpening in the correlation of ζ with θ_ω with increasing θ_ω. The upper limit $(\theta_\omega, \zeta) = (90°, 1)$

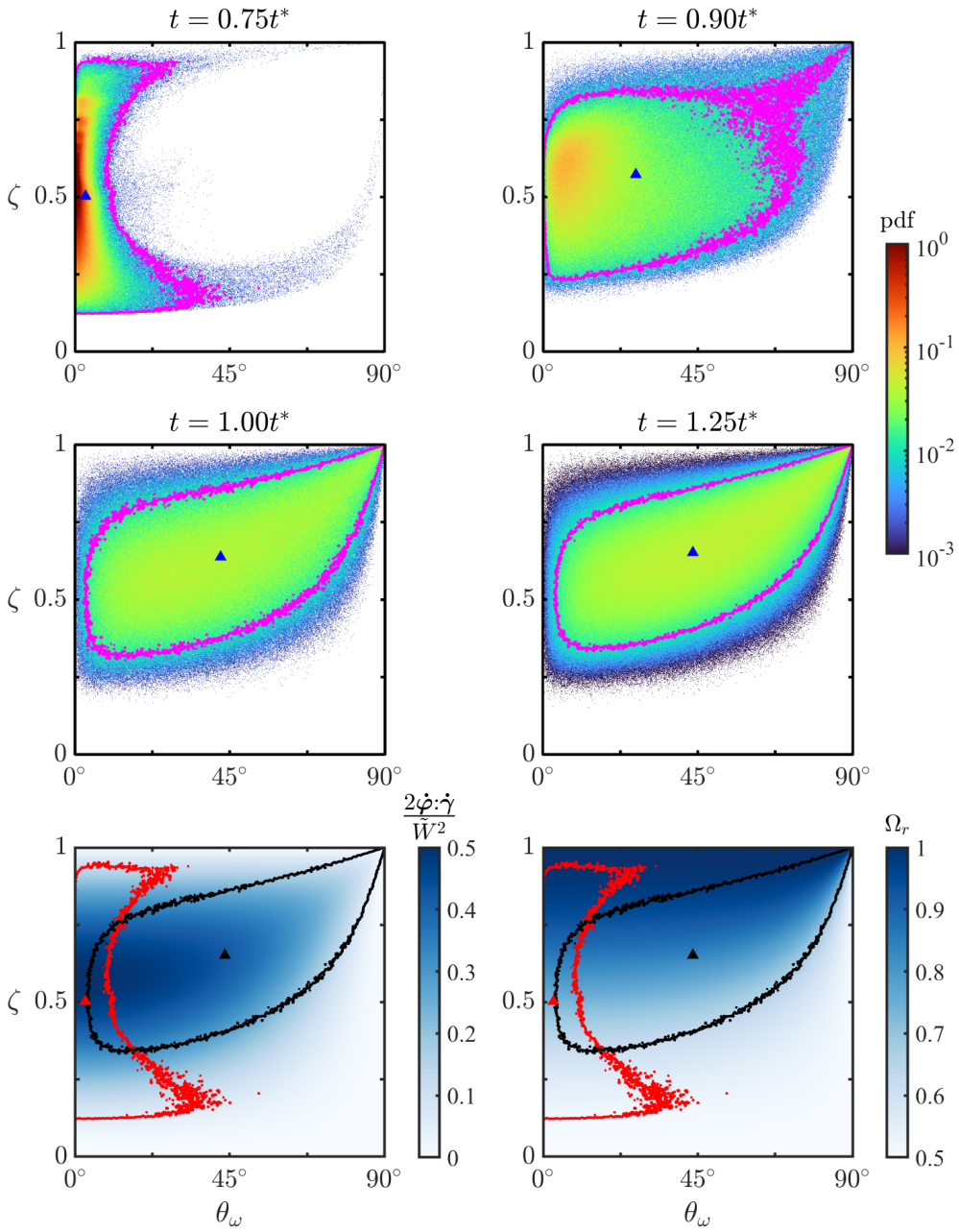

Figure 2.8: Joint p.d.f.s (top and middle) of the velocity gradients in the $\zeta - \theta_\omega$ phase space at the same times, at the same points, and in the same style as those in Figure 2.7. The bottom plots superimpose the 90% contours and centroids for $t = 0.75t^*$ (red) and $t = 1.25t^*$ (black) on $2\dot{\boldsymbol{\varphi}}{:}\dot{\boldsymbol{\gamma}}/\tilde{W}^2$ (left) and on Ω_r (right), as given by (2.15).

corresponds to circular local streamlines in the plane of rigid rotation subject to out-of-plane shearing.

The shifts in the centroid and the 90% contour support the hypothesis that, while the elliptic instability still plays a role in the turbulent regime, other mechanisms also contribute significantly to the local flow structure. Specifically, they suggest that, in addition to the breakup of elliptic streamlines via the elliptic instability, the deformation of vortices, e.g. through the action of the Crow instability, may play an important role during turbulent decay. As discussed in Appendix 2.A3, the partitioning of shear–rotation correlations between the cores and boundaries of vortices in the flow (see Figure 2.12) provides an interesting opportunity for analyzing these mechanisms. Given current challenges in disentangling the elliptic and Crow instabilities in turbulent flows [36, 57], the present geometry-based $(\zeta - \theta_\omega)$ phase space has the potential to help distinguish flow features associated with these ubiquitous mechanisms.

Altogether, the results in this section reinforce the notion that the elliptic instability is the dominant mechanism mediating the transition of the present vortex ring collision. They also support the notion that, after transition, the elliptic instability is no longer a strictly dominant mechanism underlying the turbulent decay of the flow. The results point to increased contributions from rotational geometries with out-of-plane shearing, which may reflect interactions associated with mechanisms like the Crow instability. The results also highlight the ability of the new shear–rotation and geometry-based phases spaces to characterize the relative contributions of different modes of deformation and rotational features of local streamlines, respectively.

2.6 Concluding remarks

We use a recently developed adaptive, multiresolution numerical scheme based on the LGF to efficiently simulate the head-on collision between two vortex rings at a relatively high Reynolds number ($Re_{\Gamma_0} = 4000$). The fidelity of this simulation is confirmed using various integral metrics that reflect the symmetries, conservation properties, and discretization errors of the flow. We provide a detailed analysis of the initial evolution, transition, and turbulent decay of the flow to elucidate flow features that are pertinent to the mechanisms driving its evolution, e.g. the elliptic instability.

Our visualizations of vortex structures enable qualitative characterizations of the various regimes through which the flow evolves. They depict the short-wave elliptic instability as the mechanism driving the initial transition of the rings as they merge at the collision plane. Consistent with previous studies [36, 39], late transition and (to a lesser extent) turbulent decay are mediated by antiparallel secondary vortex filaments that arise from local interactions associated with the elliptic instability. We confirm that the elliptic instability dominates transition by analyzing the scales of dominant wave-like perturbations in that regime. During turbulent decay, we observe local ejections of vortex rings in regions where antiparallel vortex filaments interact. This observation supports the notion that interplay between the elliptic and Crow instabilities can impact vortex interactions, consistent with previous findings [36, 57].

Our analysis of the flow centers around using the triple decomposition of the VGT to characterize the contributions of axial straining, shearing, rigid rotation, and shear–rotation correlations to the velocity gradients. The mutual interaction of the rings is marked by the development of shearing-dominated vorticity and enhanced shear–rotation correlations, reflecting conditions conducive to the elliptic instability. These conditions are consistent with the initial elliptic instability observed in our visualizations and previously in similar configurations [36, 39]. During turbulent decay, the relative contributions of the different modes of deformation to the velocity gradient strength (which is not stationary) are roughly invariant in time, suggesting an equilibrium partitioning of the VGT. This equilibrium partitioning is remarkably similar to the partitioning observed for forced isotropic turbulence [66], suggesting that it may provide a broadly applicable avenue for modeling incompressible flows with appropriate symmetries.

During the transition and turbulent decay of the flow, we also consider instantaneous distributions of the velocity gradients in various phase spaces. The broadening of the phase space distributions in these regimes reflects the generation of more diverse local streamline topologies. The distributions in the $q_A - r_A$ phase space show that the present vortex ring collision produces velocity gradients that follow the near-universal teardrop-like distribution observed previously for forced isotropic turbulence [62, 63]. In addition to the $q_A - r_A$ phase space, we introduce the shear–rotation phase space to characterize the

interplay of shearing and rigid rotation in rotational settings and highlight the role of their correlations during transition and turbulent decay.

Finally, we introduce a geometry-based $(\zeta - \theta_\omega)$ phase space to further characterize the action of the elliptic instability (and other mechanisms) during transition and turbulent decay. As the rings interact, the emergence of the elliptic instability spurring transition is associated with the alignment of shearing and rigid rotation ($\theta_\omega \approx 3°$). In this regime, the elliptic local streamlines in the plane of rigid rotation have aspect ratios centered about $\zeta \approx 0.5$. During late transition and turbulent decay, the generation and interaction of secondary vortical structures broadens the distribution to include larger θ_ω, and the equilibrium distribution is ultimately centered near $\theta \approx 44°$. In this regime, regions with high θ_ω and high ζ become increasingly correlated as they approach $(\theta_\omega, \zeta) = (90°, 1)$. In conjunction with our visualizations, these results suggest that proximity to vortex cores and boundaries may be a useful tool for modeling the interplay between mechanisms such as the elliptic and Crow instabilities. As a whole, the geometry-based phase space we introduce has the potential to help distinguish effects associated with the elliptic instability (small θ_ω) and other mechanisms, which is an ongoing challenge for turbulent flows driven by interacting vortex filaments [36, 57].

Moving forward, the VGT phase spaces we introduce may provide a useful setting for analyzing a broad class of turbulent flows. For vortex ring collisions, analyzing regimes where the Crow instability dominates the elliptic instability would clarify the extent to which the phase spaces can disambiguate these mechanisms. More generally, it would also be useful to identify the conditions under which (i) the equilibrium partitioning of the VGT [66] and (ii) the teardrop-like distribution in the $q_A - r_A$ phase space [62, 63] are applicable. The present VGT analyses are limited by the local, instantaneous nature of the streamline geometries under consideration. It would be interesting to generalize these analyses to capture features that are non-local and that persist in time.

Supplementary data: Supplementary movies are available at https://doi.org/10.1017/jfm.2024.90.

Acknowledgements: The authors gratefully acknowledge B. Dorschner and K. Yu for their extensive guidance on the computations.

Funding: R.A. was supported by the Department of Defense (DoD) through the National Defense Science & Engineering Graduate (NDSEG) Fellowship Program. This work used the Extreme Science and Engineering Discovery Environment (XSEDE, Towns et al. [106]), which is supported by National Science Foundation grant number ACI-1548562. Specifically, it used the Bridges-2 system, which is supported by NSF award number ACI-1928147, at the Pittsburgh Supercomputing Center (PSC).

2.A1 Computational formulation

Here, we briefly document the adaptive computational framework. We refer to Yu et al. [99] for a detailed description of the framework and a discussion of its novel aspects.

The non-dimensional, incompressible NSE are given by

$$\partial_t \boldsymbol{u} + (\boldsymbol{u} \cdot \nabla)\boldsymbol{u} = -\nabla p + \frac{1}{Re}\nabla^2 \boldsymbol{u}, \quad \nabla \cdot \boldsymbol{u} = 0, \tag{2.16}$$

where $\boldsymbol{u} = (u, v, w)$ is the velocity, p is the pressure, t denotes time, and Re is the Reynolds number. We focus particularly on the class of unbounded flows obeying the following far-field boundary conditions: $\boldsymbol{u}(\boldsymbol{x}, t) \to \boldsymbol{0}$, $p(\boldsymbol{x}, t) \to p_\infty$, and $\boldsymbol{\omega}(\boldsymbol{x}, t) \to \boldsymbol{0}$ (exponentially) as $|\boldsymbol{x}| \to \infty$. These boundary conditions differ slightly from the more generic (time-varying) free-stream conditions considered by Liska and Colonius [96]. For the present simulations, variables are non-dimensionalized using the initial radius and circulation of each vortex ring (R_0 and Γ_0, respectively) and Re is given by the initial circulation Reynolds number (Re_{Γ_0}).

The NSE are spatially discretized on the composite grid, which contains a series of uniform staggered Cartesian meshes with increasing resolution. Figure 2.9 depicts the locations of various vector and scalar flow variables on the cells of these meshes. We use $\mathcal{Q} \in \{\mathcal{C}, \mathcal{F}, \mathcal{E}, \mathcal{V}\}$ to denote operations that are constrained to the corresponding locations on the cells. The semi-discrete NSE on the composite grid are given by

$$\frac{d\boldsymbol{u}}{dt} - \boldsymbol{N}(\boldsymbol{u}) = -\boldsymbol{G}p_{\mathsf{tot}} + \frac{1}{Re}\boldsymbol{L}_{\mathcal{F}}\boldsymbol{u}, \quad \boldsymbol{D}\boldsymbol{u} = 0, \tag{2.17}$$

where we represent discretized variables and operators using sans-serif symbols, which are bold in vector settings and non-bold in scalar settings. Here, $\boldsymbol{G}$, $\boldsymbol{D}$, $\boldsymbol{L}$, and $\boldsymbol{N}$ represent the discrete forms of the gradient, divergence, Laplace,

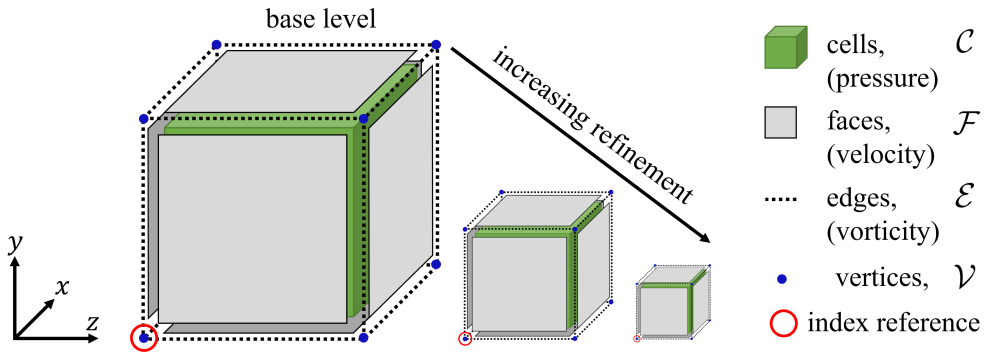

Figure 2.9: Unit cells of the staggered Cartesian grid at the base and refinement levels of the mesh, showing the locations of relevant flow variables.

and nonlinear operators, respectively. We have used the rotational form of the convective term in (2.17) such that $p_{\text{tot}} = p + \frac{1}{2}|\boldsymbol{u}|^2$ discretely represents the total pressure perturbation and $\boldsymbol{N}(\boldsymbol{u}) = \boldsymbol{r}$ discretely represents the Lamb vector, $\boldsymbol{r} = \boldsymbol{u} \times \boldsymbol{\omega}$.

The semi-discrete momentum equations, subject to the continuity constraint, are integrated in time using the IF-HERK method [96, 99]. This method combines an integrating factor (IF) technique for the viscous term with a half-explicit Runge-Kutta (HERK) technique for the convective term. In the HERK time-stepping scheme [96, 99, 107], the task of integrating (2.17) at each time step is subdivided into N_{stage} stages. Using a block lower–upper (LU) decomposition and the mimesis and commutativity properties of the relevant operators, the subproblem associated with stage i of the HERK scheme is formulated on the composite grid as

$$L_{\mathcal{C}} p_{\text{tot}}^i = f^i = \boldsymbol{D}\boldsymbol{r}^i, \quad \boldsymbol{u}^i = \boldsymbol{H}_{\mathcal{F}}^i \left(\boldsymbol{r}^i - \boldsymbol{G} p_{\text{tot}}^i \right). \tag{2.18}$$

Here, $\boldsymbol{H}$ represents the IF operator and $f = \boldsymbol{D}\boldsymbol{r}$ approximately represents the divergence of the Lamb vector. For brevity, we omit the exact dependencies of $\boldsymbol{r}^i$ on various flow variables from stages 1 to i of the HERK scheme. We refer to the formulation in §2.4 of Yu et al. [99] for these details and for the corresponding Butcher tableau.

While the discrete operators in (2.17) and (2.18) are formally defined on the unbounded composite grid, they are practically applied to the finite subset representing the AMR grid. The operator $R_{\mathcal{Q}}$ restricts variables from the composite grid $(\cdot)$ to the AMR grid as $\widehat{(\cdot)} = R_{\mathcal{Q}}(\,\cdot\,)$. In the other direction,

the operator $P_{\mathcal{Q}}$ approximates variables on the composite grid using the values on the AMR grid as $(\cdot) \approx P_{\mathcal{Q}}\widehat{(\cdot)}$. Using these operators, solutions to the subproblems associated with each stage of the HERK formulation in (2.18) can be approximated on the AMR grid.

The two steps of each subproblem in (2.18) involve (i) solving the discrete pressure Poisson equation and (ii) applying the IF to recover the velocity. The solution to the pressure Poisson equation on the AMR grid can be expressed as

$$\widehat{p^i_{\text{tot}}} = R_{\mathcal{C}}\mathcal{G}_{\mathcal{C}} * f^i = R_{\mathcal{C}}L_{\mathcal{C}}^{-1}f^i \approx R_{\mathcal{C}}L_{\mathcal{C}}^{-1}P_{\mathcal{C}}\widehat{f^i}, \tag{2.19}$$

where $\mathcal{G}_{\mathcal{C}}$ is the LGF and $*$ represents the discrete convolution. We efficiently evaluate (2.19) using a fast multipole method [97, 100] that accelerates solutions by incorporating summation techniques based on the fast Fourier transform. This method is key to enabling the linear algorithmic complexity and high parallel efficiency of the flow solver. The application of the IF operator can similarly be expressed as

$$\widehat{\boldsymbol{u}^i} = \boldsymbol{R}_{\mathcal{F}}\boldsymbol{H}^i_{\mathcal{F}}\left(\boldsymbol{r}^i - \boldsymbol{G}p^i_{\text{tot}}\right) \approx \boldsymbol{R}_{\mathcal{F}}\boldsymbol{H}^i_{\mathcal{F}}\boldsymbol{P}_{\mathcal{F}}\left(\widehat{\boldsymbol{r}^i} - \widehat{\boldsymbol{G}p^i_{\text{tot}}}\right), \tag{2.20}$$

where $\widehat{\boldsymbol{G}p^i_{\text{tot}}} = \boldsymbol{R}_{\mathcal{C}}\boldsymbol{G}p^i_{\text{tot}}$. The application of the IF operator represents a convolution with an exponentially decaying kernel and it can also be evaluated using fast LGF techniques [96, 99].

At each time step, the simulation adapts the extent of the AMR grid and adaptively refines regions within the AMR grid according to the spatial adaptivity and mesh refinement criteria, respectively. The spatial adaptivity criterion sets the boundaries of the AMR grid to capture regions where the source of the pressure Poisson equation exceeds a threshold, $\varepsilon_{\text{adapt}}$, relative to its maximum value in the domain. In other words, the AMR grid is adaptively truncated to capture the subset of the unbounded domain satisfying

$$|f(\boldsymbol{x}, t)| < \varepsilon_{\text{adapt}}\|f\|_\infty(t), \tag{2.21}$$

where $\varepsilon_{\text{adapt}} = 10^{-6}$ for the present simulation. One caveat is that the IF convolution involves a velocity source that decays slower than vorticity. Correspondingly, its evaluation requires the velocity field in a slightly extended domain based on a cutoff distance that is selected to capture the IF kernel with high accuracy. For the present simulation, the initial rectangular domain

is large enough to contain as a subset the domain satisfying the adaptivity criterion (2.21).

At each level k of the AMR grid, the mesh refinement criteria are formulated in terms of a combined source, $f_k(t)$, which includes the source of the pressure Poisson equation and a correction term. The correction term accounts for the differences between the partial solutions on the coarse and fine grids and it is evaluated using an extended region that can overlap with neighboring levels. We refer to Yu et al. [99] for the details of its formulation and implementation, which we omit for brevity. Using the combined source, a region is refined or coarsened when

$$f_k(\boldsymbol{x}, t) > \alpha^{N_{\text{level}}-k} f_{\max}(t) \quad \text{or} \quad f_k(\boldsymbol{x}, t) < \beta\alpha^{N_{\text{level}}-k} f_{\max}(t), \tag{2.22}$$

respectively, where $\alpha \in (0, 1)$ and $\beta \in (0, 1)$ and we select $\alpha = 0.125$ and $\beta = 0.875$ for the present simulation. In these criteria, the combined source is evaluated relative to its maximum blockwise root-mean-square (BRMS) value computed over all blocks and previous times, which is expressed as

$$f_{\max}(t) = \max_{\tau<t} \text{BRMS}\left(f_k(\boldsymbol{x}, \tau)\right). \tag{2.23}$$

2.A2 Instability development during transition

Whereas the short-wave elliptic instability has a wavelength of the order of the vortex core radius, $a(t)$, the long-wave Crow instability occurs at wavelengths much larger than $a(t)$ [36, 39, 55]. Here, we track the development of wave-like instabilities around the azimuth of the ring at the reference times from Table 2.1 associated with the transition to turbulence. Figure 2.10 shows closeups of the vortical flow structures at these times from the auxiliary viewpoint in Figure 2.3.

The dominant scales of the wave-like perturbations are identified by decomposing the flow into azimuthal Fourier modes, which are denoted using $\hat{(\cdot)}$ and have corresponding wavenumbers m. To obtain these Fourier modes, we linearly interpolate the flow at the finest level of the AMR grid to a uniform cylindrical grid. This uniform grid is discretized into $N_\theta = 1001$ points in the azimuthal direction and it has spacings, $\Delta r_{\text{uni}} = \Delta z_{\text{uni}} = 0.01$, that are consistent with that of the finest level, $\Delta x_{\text{fine}} = 0.01$. In the following analysis, we limit our consideration to (r, z) pairs for which $\langle\omega_z^2\rangle_\theta$ exceeds 10% of $\max_{r,z}\langle\omega_z^2\rangle_\theta$, where $\langle\cdot\rangle_\theta$ denotes azimuthal averaging.

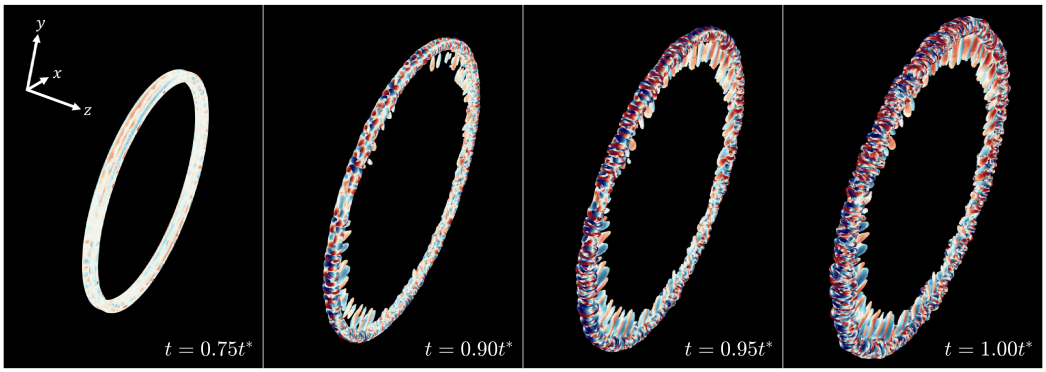

Figure 2.10: Magnified versions of the auxiliary viewpoints in Figure 2.3 at the reference times associated with instability growth and transition.

As depicted in Figure 2.11, we characterize instability development using two flow variables. First, following previous studies [36, 39], we approximate the positions, $\boldsymbol{X}^+$ and $\boldsymbol{X}^-$, of the vortex cores by identifying the locations of the pressure minima for $z > 0$ and $z < 0$, respectively. The radial perturbations of these cores, $R_p^+(\theta)$ and $R_p^-(\theta)$, about their mean radial positions, $\bar{R}_p^+$ and $\bar{R}_p^-$, characterize the interactions between the rings. We measure the strength of the vortex core perturbations using $|\hat{R}_p| = [(|\hat{R}_p^+|^2 + |\hat{R}_p^-|^2)/2]^{1/2}$. Second, we consider ω_z since it captures the antiparallel vortex structures that develop around the ring during transition. The Fourier coefficient amplitudes of the corresponding perturbations, $|\hat{\omega}_z|$, are colored according to their displacement from average vortex ring radius, $\bar{R}_p = (\bar{R}_p^+ + \bar{R}_p^-)/2$.

To characterize the wavelengths of the dominant perturbations in terms of the elliptic and Crow instabilities, we estimate the core radii, a^+ and a^-, of the vortex rings at each reference time. Following McKeown et al. [39], we fit a two-dimensional Gaussian function to the vortex core profiles, $\langle\omega_\theta\rangle_\theta$, for each ring. However, whereas McKeown et al. [39] estimated the core radii by averaging the standard deviations of the Gaussian fits, $\sigma_{\min}^\pm$ and $\sigma_{\max}^\pm$, we instead estimate the core radii as $a^\pm = [(\sigma_{\min}^\pm)^2 + (\sigma_{\max}^\pm)^2]^{1/2}$. Our estimates produce core radii that are consistent with the definition in (2.1) for Gaussian vortex rings. Hence, we correctly identify $a_0 = 0.2$ for the initial condition, which is larger than the alternate core radius definition [39, 57] by a factor of $\sqrt{2}$. We compute the average slenderness ratio of the vortex rings as $\delta = (\delta^+ + \delta^-)/2$, where $\delta^\pm = a^\pm/\bar{R}_p^\pm$. This definition is consistent with the Gaussian fits we consider since the radial locations of their centroids coincide with $\bar{R}_p^\pm$ to within 0.38%. The average ratio of the perturbation wavelength to the core

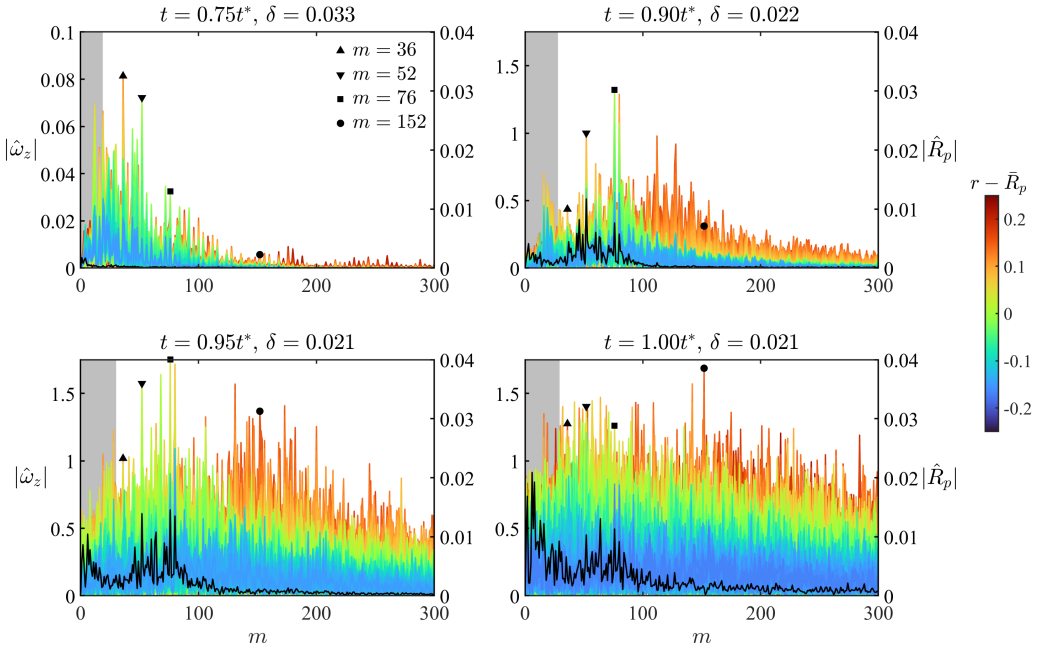

Figure 2.11: Fourier coefficient amplitudes: $|\hat{\omega}_z|$ (colored by radial displacement from $\bar{R}_p$) and $|\hat{R}_p|$ (black). At each of the reference times shown, δ represents the average slenderness ratio of the vortex rings. The values of $|\hat{\omega}_z|$ at wavenumbers pertinent to instability development are marked by symbols and the shaded regions represent wavenumbers for which $C > 10$.

thickness can be expressed as $C = (C^+ + C^-)/2$, where $C^\pm = 2\pi/m\delta^\pm$. Here, we loosely associate $C > 10$ and $C < 10$ with the Crow and elliptic instabilities, respectively.

At $t = 0.75t^*$, the wavenumber ($m = 36$) of the largest $\hat{\omega}_z$ perturbation corresponds to $C = 5.08$. A similar value, $C = 5.38$, is obtained at $t = 0.90t^*$ for the $m = 52$ perturbation. However, $m = 76$ represents the largest perturbation at both $t = 0.90t^*$ and $t = 0.95t^*$, for which $C = 3.68$ and 3.97, respectively. At each of these times, the dominant short-wave perturbations are of the order of the core thickness. This result suggests that the corresponding development of secondary antiparallel vortex filaments (see Figure 2.10) can be associated with the development of the elliptic instability.

The vortex core perturbations further support the notion that the elliptic instability is the dominant mechanism in the transitional regime. The perturbations at $t = 0.75t^*$ are too small, relative to $\Delta r_{\text{uni}} = 0.01$, to resolve. The dominant core perturbations are resolved for $t = 0.90t^*$ and $t = 0.95t^*$ and, consistent with the vorticity perturbations, they are largest at $m = 52$ and

$m = 76$. For both $\hat{\omega}_z$ and $\hat{R}_p$, we also observe prominent perturbations at $m = 80$, but we do not speculate on their source.

For a similar vortex ring collision with $Re_{\Gamma_0} = 3500$ and $\delta_0 = 0.1$, Mishra et al. [36] attributed the growth of the $m = 40$ mode to the elliptic instability in a regime where $2\pi R_p(t)/m \approx 0.2 - 0.4$. Employing a crude volume-conserving approximation for the vortex cores [36, 39], the core radii can be modeled as $a^{\pm} = a_0\sqrt{R_0/R_p^{\pm}}$, which suggests that $C \approx 2.26 - 6.38$ in that regime. Hence, the scales of the dominant perturbations relative to the core thickness in the present case are consistent with those previously attributed to the elliptic instability in a similar collision.

At $t = t^*$, we remarkably observe that the dominant $\hat{\omega}_z$ perturbation occurs at $m = 152$, which is the second harmonic of the $m = 76$ perturbation that governed the generation of secondary vorticity. This observation suggests that the elliptic instability retains an important role in mediating the production of subsequent generations of vortical structures at progressively smaller scales. It thus qualitatively supports the initial stages of iterative elliptic instability scenario leading to the generation of turbulence [39]. Identifying the later stages of this pathway would require a more refined analysis of the orientation of each generation of vortices relative to previous generations.

Although perturbations for which $C > 10$ are non-negligible, their signatures in $\hat{\omega}_z$ are not as prominent as those for which $C < 10$. This observation supports the notion that the Crow instability plays a secondary role to the elliptic instability in the transitional regime, consistent with previous studies in similar configurations [36, 39]. Nevertheless, especially as the flow becomes turbulent, the broadening range of active scales obscures the interplay between these mechanisms. As this occurs, the vortex core perturbations gain significant energy at lower wavenumbers ($C > 10$), indicating that long-wave mechanisms like the Crow instability may become important. Altogether, while relatively limited, the present analysis of instability development confirms the preeminence of the elliptic instability during transition and supports our interpretation of the corresponding velocity gradients.

2.A3 Shear–rotation correlations and vortical flow structures

The visualizations in Figure 2.3 help identify antiparallel vortex filaments and interactions between vortices, but the comparisons between the vortex bound-

ary ($\Omega_r = 0.52$) and core ($\Omega_r = 0.93$) structures provide relatively little information. In Figure 2.12, we visualize the same vortex structures but instead color them using $2\dot{\boldsymbol{\varphi}}{:}\dot{\boldsymbol{\gamma}}/\tilde{W}^2$ to probe how conditions conducive to the elliptic instability are structured throughout the vortices in the flow.

As the vortex boundaries merge and expand radially, the shear–rotation correlations are relatively large at the collision plane and the outer boundaries in z and they are relatively small at the inner and outer boundaries in the radial direction. This structuring illustrates how shear–rotation correlations are especially enhanced in regions where the vortex boundaries become thinner, corresponding to the shift from a rigid-rotation-dominated regime to a shearing-dominated regime. During transition, the secondary vortex filaments are initially associated with relatively high and low shear–rotation correlations near their boundaries and cores, respectively. As the turbulence develops, this structuring of $2\dot{\boldsymbol{\varphi}} : \dot{\boldsymbol{\gamma}}/\tilde{W}^2$ within the vortices remains similar to that of the secondary vortices mediating transition.

This persistent partitioning opens up an interesting possibility of analyzing the action of various mechanisms (e.g. the elliptic and Crow instabilities) in turbulent flows based on their proximity to vortex cores. For example, the phase space transformations in §2.5 can be used to characterize local streamline geometries throughout vortices using the structure of the shear–rotation correlations. Consistent with the transformations depicted in Figure 2.8, our results suggest that local streamlines are more elliptic near vortex boundaries and more circular near vortex cores. This conceptual picture is consistent with the notion that the breakup and displacement of vortex core structures can be loosely associated with the elliptic and Crow instabilities, respectively.

2.A4 Effect of shear–rotation alignment

Here, we characterize the effect of the alignment between shearing and rigid rotation, as measured by θ_ω, on the phase space transformations associated with rotational local streamline geometries. Figure 2.13 depicts how the corresponding transformations vary with θ_ω in the $q_A - r_A$ phase space. When $\theta_\omega = 90°$, shearing and rigid rotation occur in orthogonal planes. In this case, $2\dot{\boldsymbol{\varphi}}{:}\dot{\boldsymbol{\gamma}} = 0$, $\zeta = 1$, and the region where $\dot{\varphi}^2$ dominates A^2 extends the furthest from the external boundary of the phase space. When $\theta_\omega = 45°$, the regions where $\dot{\varphi}^2$ and ζ are large concentrate more sharply near the external bound-

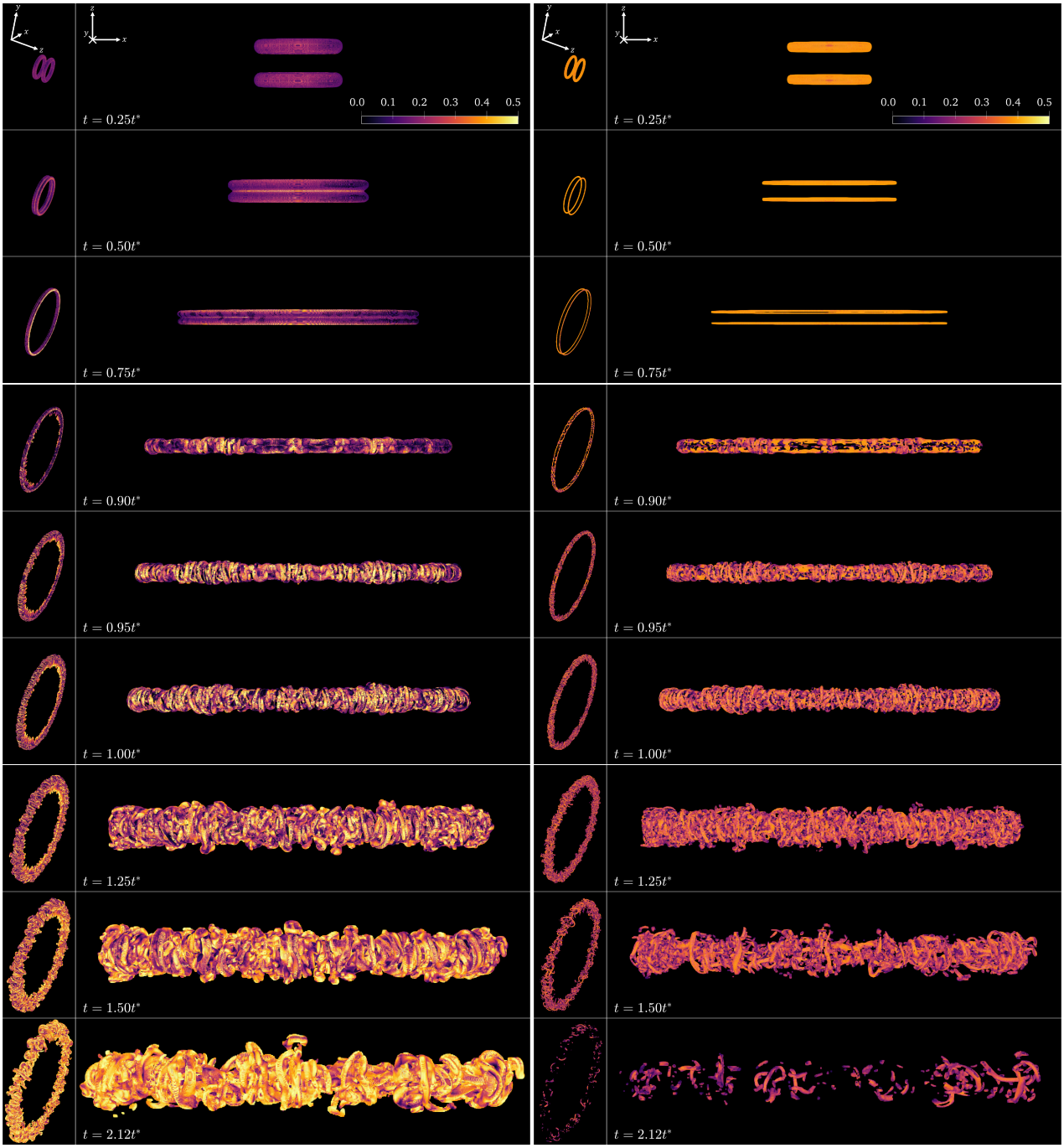

Figure 2.12: Visualizations of the vortex boundaries ($\Omega_r = 0.52$, left side) and vortex cores ($\Omega_r = 0.93$, right side), colored by $2\dot{\boldsymbol{\varphi}}{:}\dot{\boldsymbol{\gamma}}/\tilde{W}^2$, for each reference time from Table 2.1. A movie depicting the evolution of the vortex boundaries from the auxiliary viewpoint (leftmost column) is provided as supplementary material.

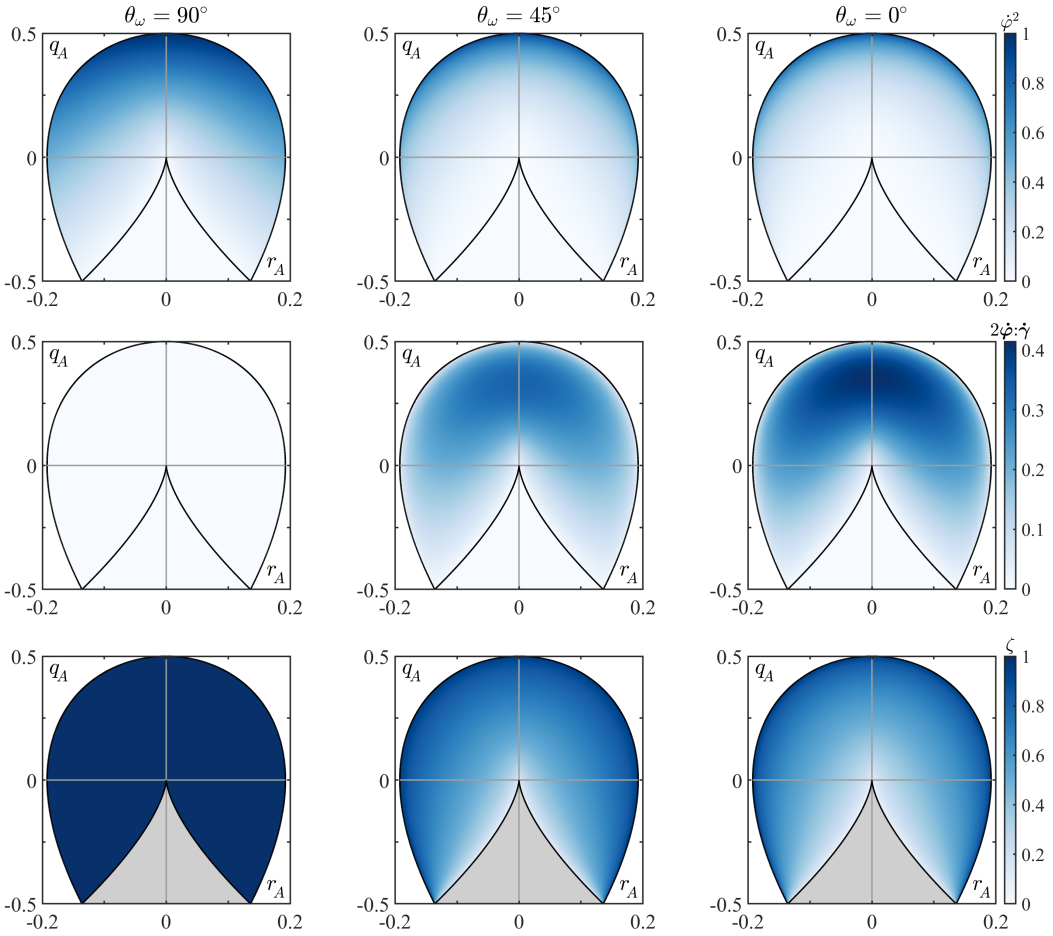

Figure 2.13: Transformations to $\dot{\varphi}^2$, $2\dot{\boldsymbol{\varphi}}{:}\dot{\boldsymbol{\gamma}}$, and ζ from the $q_A - r_A$ phase space for various alignment angles, θ_ω. The plots are in the same style as those in Figure 2.6.

ary and $2\dot{\boldsymbol{\varphi}}{:}\dot{\boldsymbol{\gamma}}$ grows in the intermediate region between the boundaries of the rotational geometries. The concentration of $\dot{\varphi}^2$ and ζ and the amplification of $2\dot{\boldsymbol{\varphi}}{:}\dot{\boldsymbol{\gamma}}$ are most extreme when $\theta_\omega = 0°$. In this case, the peak contribution of $2\dot{\boldsymbol{\varphi}}{:}\dot{\boldsymbol{\gamma}}$ is $(\sqrt{2}+1)^{-1}$ [66] and, for all $\theta_\omega < 90°$, it occurs when $r_A = 0$. The location of this maximum approaches $q_A \to \frac{1}{4}$ as $\theta_\omega \to 90°$ and $q_A \to \frac{1}{2\sqrt{2}}$ as $\theta_\omega \to 0°$. The qualitative features of the distributions vary more significantly from $\theta_\omega = 90°$ to $\theta_\omega = 45°$ than they do from $\theta_\omega = 45°$ to $\theta_\omega = 0°$.

References

[1]Shariff, K. and Leonard, A. Vortex rings. *Annu. Rev. Fluid Mech.* **24**, 235–279 (1992).

[2]Bush, J.W.M., Thurber, B.A., and Blanchette, F. Particle clouds in homogeneous and stratified environments. *J. Fluid Mech.* **489**, 29–54 (2003).

[3]Taddeucci, J., Alatorre-Ibarguengoitia, M.A., Palladino, D.M., Scarlato, P., and Camaldo, C. High-speed imaging of Strombolian eruptions: gas-pyroclast dynamics in initial volcanic jets. *Geophys. Res. Lett.* **42**, 6253–6260 (2015).

[4]Ruggaber, G.J. Dynamics of particle clouds related to open-water sediment disposal. PhD Thesis (Massachusetts Institute of Technology, Cambridge, MA, 2000).

[5]Arvidsson, P.M., Kovács, S.J., Töger, J., Borgquist, R., Heiberg, E., Carlsson, M., and Arheden, H. Vortex ring behavior provides the epigenetic blueprint for the human heart. *Sci. Rep.* **6**, 22021 (2016).

[6]Dabiri, J.O. Flow patterns generated by oblate medusan jellyfish: field measurements and laboratory analyses. *Journal Exp. Biol.* **208**, 1257–1265 (2005).

[7]Cummins, C., Seale, M., Macente, A., Certini, D., Mastropaolo, E., Viola, I.M., and Nakayama, N. A separated vortex ring underlies the flight of the dandelion. *Nature* **562**, 414–418 (2018).

[8]Johnson, W. Model for vortex ring state influence on rotorcraft flight dynamics. Tech. rep. NASA/TP-2005-213477 (National Aeronautics and Space Administration, 2005).

[9]Kyle, R., Lee, Y.C., and Früh, W. Propeller and vortex ring state for floating offshore wind turbines during surge. *Renewable Energy* **155**, 645–657 (2020).

[10]Gharib, M., Rambod, E., and Shariff, K. A universal time scale for vortex ring formation. *J. Fluid Mech.* **360**, 121–140 (1998).

[11]Mohseni, K., Ran, H., and Colonius, T. Numerical experiments on vortex ring formation. *J. Fluid Mech.* **430**, 267–282 (2001).

[12]Krueger, P.S. and Gharib, M. The significance of vortex ring formation to the impulse and thrust of a starting jet. *Phys. Fluids* **15**, 1271–1281 (2003).

[13]O'Farrell, C. and Dabiri, J.O. Pinch-off of non-axisymmetric vortex rings. *J. Fluid Mech.* **740**, 61–96 (2014).

[14]Limbourg, R. and Nedić, J. Formation of an orifice-generated vortex ring. *J. Fluid Mech.* **913**, A29 (2021).

[15]Balakrishna, N., Mathew, J., and Samanta, A. Inviscid and viscous global stability of vortex rings. *J. Fluid Mech.* **902**, A9 (2020).

[16]Shariff, K., Verzicco, R., and Orlandi, P. A numerical study of three-dimensional vortex ring instabilities: viscous corrections and early nonlinear stage. *J. Fluid Mech.* **279**, 351–375 (1994).

[17]Archer, P.J., Thomas, T.G., and Coleman, G.N. Direct numerical simulation of vortex ring evolution from the laminar to the early turbulent regime. *J. Fluid Mech.* **598**, 201–226 (2008).

[18]Dazin, A., Dupont, P., and Stanislas, M. Experimental characterization of the instability of the vortex rings. Part II: non-linear phase. *Exp. Fluids* **41**, 401–413 (2006).

[19]Bergdorf, M., Koumoutsakos, P., and Leonard, A. Direct numerical simulations of vortex rings at $Re_\Gamma = 7500$. *J. Fluid Mech.* **581**, 495–505 (2007).

[20]Weigand, A. and Gharib, M. On the decay of a turbulent vortex ring. *Phys. Fluids* **6**, 3806–3808 (1994).

[21]Widnall, S.E., Bliss, D.B., and Tsai, C. The instability of short waves on a vortex ring. *J. Fluid Mech.* **66**, 35–47 (1974).

[22]Widnall, S.E. and Tsai, C. The instability of the thin vortex ring of constant vorticity. *Phil. Trans. R. Soc. Lond. A* **287**, 273–305 (1977).

[23]Fukumoto, Y. and Hattori, Y. Curvature instability of a vortex ring. *J. Fluid Mech.* **526**, 77–115 (2005).

[24]Hattori, Y., Blanco-Rodríguez, F.J., and Le Dizès, S. Numerical stability analysis of a vortex ring with swirl. *J. Fluid Mech.* **878**, 5–36 (2019).

[25]Blanco-Rodríguez, F.J., Le Dizès, S., Selçuk, C., Delbende, I., and Rossi, M. Internal structure of vortex rings and helical vortices. *J. Fluid Mech.* **785**, 219–247 (2015).

[26]Blanco-Rodríguez, F.J. and Le Dizès, S. Curvature instability of a curved Batchelor vortex. *J. Fluid Mech.* **814**, 397–415 (2017).

[27]Blanco-Rodríguez, F.J. and Le Dizès, S. Elliptic instability of a curved Batchelor vortex. *J. Fluid Mech.* **804**, 224–247 (2016).

[28]Kerswell, R.R. Elliptical instability. *Annu. Rev. Fluid Mech.* **34**, 83–113 (2002).

[29]Chang, C. and Llewellyn Smith, S.G. Density and surface tension effects on vortex stability. Part 2. Moore–Saffman–Tsai–Widnall instability. *J. Fluid Mech.* **913**, A15 (2021).

[30]Moore, D.W. and Saffman, P.G. The instability of a straight vortex filament in a strain field. *Proc. R. Lond. Soc. A* **346**, 413–425 (1975).

[31]Tsai, C. and Widnall, S.E. The stability of short waves on a straight vortex filament in a weak externally imposed strain field. *J. Fluid Mech.* **73**, 721–733 (1976).

[32]Cheng, M., Lou, J., and Lim, T.T. Evolution of an elliptic vortex ring in a viscous fluid. *Phys. Fluids* **28**, 037104 (2016).

[33]Cheng, M., Lou, J., and Lim, T.T. Collision and reconnection of viscous elliptic vortex rings. *Phys. Fluids* **31**, 067107 (2019).

[34]Zhao, X., Yu, Z., Chapelier, J., and Scalo, C. Direct numerical and large-eddy simulation of trefoil knotted vortices. *J. Fluid Mech.* **910**, A31 (2021).

[35]Yao, J., Yang, Y., and Hussain, F. Dynamics of a trefoil knotted vortex. *J. Fluid Mech.* **923**, A19 (2021).

[36]Mishra, A., Pumir, A., and Ostilla-Mónico, R. Instability and disintegration of vortex rings during head-on collisions and wall interactions. *Phys. Rev. Fluids* **6**, 104702 (2021).

[37]Cheng, M., Lou, J., and Lim, T.T. Numerical simulation of head-on collision of two coaxial vortex rings. *Fluid Dyn. Res.* **50**, 065513 (2018).

[38]McKeown, R., Ostilla-Mónico, R., Pumir, A., Brenner, M.P., and Rubinstein, S.M. Cascade leading to the emergence of small structures in vortex ring collisions. *Phys. Rev. Fluids* **3**, 124702 (2018).

[39]McKeown, R., Ostilla-Mónico, R., Pumir, A., Brenner, M.P., and Rubinstein, S.M. Turbulence generation through an iterative cascade of the elliptical instability. *Sci. Adv.* **6**, eaaz2717 (2020).

[40]Kida, S., Takaoka, M., and Hussain, F. Collision of two vortex rings. *J. Fluid Mech.* **230**, 583–646 (1991).

[41]Yao, J. and Hussain, F. On singularity formation via viscous vortex reconnection. *J. Fluid Mech.* **888**, R2 (2020).

[42]Yao, J. and Hussain, F. Separation scaling for viscous vortex reconnection. *J. Fluid Mech.* **900**, R4 (2020).

[43]Zawadzki, I. and Aref, H. Mixing during vortex ring collision. *Phys. Fluids A* **3**, 1405–1410 (1991).

[44]Smith, G.B. and Wei, T. Small-scale structure in colliding off-axis vortex rings. *J. Fluid Mech.* **259**, 281–290 (1994).

[45]Nguyen, V.L., Phan, T.T., Duong, V.D., and Le, N.T.P. Turbulent energy cascade associated with viscous reconnection of two vortex rings. *Phys. Fluids* **33**, 085117 (2021).

[46]Walker, J.D.A., Smith, C.R., Cerra, A.W., and Doligalski, T.L. The impact of a vortex ring on a wall. *J. Fluid Mech.* **181**, 99–140 (1987).

[47]Archer, P.J., Thomas, T.G., and Coleman, G.N. The instability of a vortex ring impinging on a free surface. *J. Fluid Mech.* **642**, 79–94 (2010).

[48]Lu, L. and Doering, C.R. Limits on enstrophy growth for solutions of the three-dimensional Navier-Stokes equations. *Indiana Univ. Math. J.* **57**, 2693–2727 (2008).

[49]Ayala, D. and Protas, B. Extreme vortex states and the growth of enstrophy in three-dimensional incompressible flows. *J. Fluid Mech.* **818**, 772–806 (2017).

[50]Kang, D., Yun, D., and Protas, B. Maximum amplification of enstrophy in three-dimensional Navier–Stokes flows. *J. Fluid Mech.* **893**, A22 (2020).

[51]Oshima, Y. Head-on collision of two vortex rings. *J. Phys. Soc. Jpn.* **44**, 328–331 (1978).

[52]Lim, T. and Nickels, T. Instability and reconnection in the head-on collision of two vortex rings. *Nature* **357**, 225–227 (1992).

[53]Chu, C., Wang, C., Chang, C., Chang, R., and Chang, W. Head-on collision of two coaxial vortex rings: experiment and computation. *J. Fluid Mech.* **296**, 39–71 (1995).

[54]Crow, S.C. Stability theory for a pair of trailing vortices. *AIAA J.* **8**, 2172–2179 (1970).

[55]Leweke, T., Le Dizès, S., and Williamson, C.H.K. Dynamics and instabilities of vortex pairs. *Annu. Rev. Fluid Mech.* **48**, 507–541 (2016).

[56]Yao, J. and Hussain, F. A physical model of turbulence cascade via vortex reconnection sequence and avalanche. *J. Fluid Mech.* **883**, A51 (2020).

[57]Ostilla-Mónico, R., McKeown, R., Brenner, M.P., Rubinstein, S.M., and Pumir, A. Cascades and reconnection in interacting vortex filaments. *Phys. Rev. Fluids* **6**, 074701 (2021).

[58]Perry, A.E. and Fairlie, B.D. Critical points in flow patterns. *Adv. Geophys.* **18**, 299–315 (1975).

[59]Perry, A.E. and Chong, M.S. A description of eddying motions and flow patterns using critical-point concepts. *Annu. Rev. Fluid Mech.* **19**, 125–155 (1987).

[60]Chong, M.S., Perry, A.E., and Cantwell, B.J. A general classification of three-dimensional flow fields. *Phys. Fluids A* **2**, 765–777 (1990).

[61]Girimaji, S.S. and Speziale, C.G. A modified restricted Euler equation for turbulent flows with mean velocity gradients. *Phys. Fluids* **7**, 1438–1446 (1995).

[62]Das, R. and Girimaji, S.S. On the Reynolds number dependence of velocity-gradient structure and dynamics. *J. Fluid Mech.* **861**, 163–179 (2019).

[63]Das, R. and Girimaji, S.S. Characterization of velocity-gradient dynamics in incompressible turbulence using local streamline geometry. *J. Fluid Mech.* **895**, A5 (2020).

[64]Das, R. and Girimaji, S.S. The effect of large-scale forcing on small-scale dynamics of incompressible turbulence. *J. Fluid Mech.* **941**, A34 (2022).

[65]Sharma, B., Das, R., and Girimaji, S.S. Local vortex line topology and geometry in turbulence. *J. Fluid Mech.* **924**, A13 (2021).

[66]Das, R. and Girimaji, S.S. Revisiting turbulence small-scale behavior using velocity gradient triple decomposition. *New J. Phys.* **22**, 063015 (2020).

[67]Tom, J., Carbone, M., and Bragg, A.D. Exploring the turbulent velocity gradients at different scales from the perspective of the strain-rate eigenframe. *J. Fluid Mech.* **910**, A24 (2021).

[68]Kolář, V. Vortex identification: new requirements and limitations. *Intl J. Heat Fluid Flow* **28**, 638–652 (2007).

[69]Kolář, V. 2D velocity-field analysis using triple decomposition of motion. In Proceedings of the 15th Australasian Fluid Mechanics Conference (The University of Sydney, 2004), AFMC00017.

[70]Nagata, R., Watanabe, T., Nagata, K., and da Silva, C.B. Triple decomposition of velocity gradient tensor in homogeneous isotropic turbulence. *Comput. Fluids* **198**, 104389 (2020).

[71]Gao, Y. and Liu, C. Rortex and comparison with eigenvalue-based vortex identification criteria. *Phys. Fluids* **30**, 085107 (2018).

[72]Gao, Y. and Liu, C. Rortex based velocity gradient tensor decomposition. *Phys. Fluids* **31**, 011704 (2019).

[73]Liu, C., Gao, Y., Tian, S., and Dong, X. Rortex—a new vortex vector definition and vorticity tensor and vector decompositions. *Phys. Fluids* **30**, 035103 (2018).

[74]Gao, Y., Yu, Y., Liu, J., and Liu, C. Explicit expressions for Rortex tensor and velocity gradient tensor decomposition. *Phys. Fluids* **31**, 081704 (2019).

[75]Wang, J., Wan, M., Chen, S., and Chen, S. Kinetic energy transfer in compressible isotropic turbulence. *J. Fluid Mech.* **841**, 581–613 (2018).

[76]Keylock, C.J. The Schur decomposition of the velocity gradient tensor for turbulent flows. *J. Fluid Mech.* **848**, 876–905 (2018).

[77]Hoffman, J. Energy stability analysis of turbulent incompressible flow based on the triple decomposition of the velocity gradient tensor. *Phys. Fluids* **33**, 081707 (2021).

[78]Wu, Y., Zhang, W., Wang, Y., Zou, Z., and Chen, J. Energy dissipation analysis based on velocity gradient tensor decomposition. *Phys. Fluids* **32**, 035114 (2020).

[79]Nakayama, K. Topological features and properties associated with development/decay of vortices in isotropic homogeneous turbulence. *Phys. Rev. Fluids* **2**, 014701 (2017).

[80]Chakraborty, P., Balachandar, S., and Adrian, R.J. On the relationships between local vortex identification schemes. *J. Fluid Mech.* **535**, 189–214 (2005).

[81]Epps, B.P. Review of vortex identification methods. In 55th AIAA Aerospace Sciences Meeting (Grapevine, Texas, 2017), 2017-0989.

[82]Günther, T. and Theisel, H. The state of the art in vortex extraction. *Comput. Graphics Forum* **37**, 149–173 (2018).

[83]Liu, C., Gao, Y., Dong, X., Wang, Y., Liu, J., Zhang, Y., Cai, X., and Gui, N. Third generation of vortex identification methods: Omega and Liutex/Rortex based systems. *J. Hydrodyn.* **31**, 205–223 (2019).

[84]Haller, G. Can vortex criteria be objectivized?, *J. Fluid Mech.* **908**, A25 (2021).

[85]Hunt, J.C.R., Wray, A.A., and Moin, P. Eddies, streams, and convergence zones in turbulent flows. In Proceedings of the 1988 Summer Program (Center for Turbulence Research, 1988), pp. 193–208.

[86]Jeong, J. and Hussain, F. On the identification of a vortex. *J. Fluid Mech.* **285**, 69–94 (1995).

[87]Tian, S., Gao, Y., Dong, X., and Liu, C. Definitions of vortex vector and vortex. *J. Fluid Mech.* **849**, 312–339 (2018).

[88]Kolář, V. and Šístek, J. Consequences of the close relation between Rortex and swirling strength. *Phys. Fluids* **32**, 091702 (2020).

[89]Kolář, V. and Šístek, J. Disappearing vortex problem in vortex identification: non-existence for selected criteria. *Phys. Fluids* **34**, 071704 (2022).

[90]Liu, C., Wang, Y., Yang, Y., and Duan, Z. New omega vortex identification method. *Sci. China Phys., Mech. Astron.* **59**, 684711 (2016).

[91]Dong, X., Wang, Y., Chen, X., Dong, Y., Zhang, Y., and Liu, C. Determination of epsilon for Omega vortex identification method. *J. Hydrodyn.* **30**, 541–548 (2018).

[92]Dong, X., Gao, Y., and Liu, C. New normalized Rortex/vortex identification method. *Phys. Fluids* **31**, 011701 (2019).

[93]Liu, C., Gao, Y., Dong, X., Wang, Y., Liu, J., Zhang, Y., Cai, X., and Gui, N. Third generation of vortex identification methods: Omega and Liutex/Rortex based systems. *J. Hydrodyn.* **31**, 205–223 (2019).

[94]Liu, J., Gao, Y., and Liu, C. An objective version of the Rortex vector for vortex identification. *Phys. Fluids* **31**, 065112 (2019).

[95]Liu, J., Gao, Y., Wang, Y., and Liu, C. Objective Omega vortex identification method. *J. Hydrodyn.* **31**, 455–463 (2019).

[96]Liska, S. and Colonius, T. A fast lattice Green's function method for solving viscous incompressible flows on unbounded domains. *J. Comput. Phys* **316**, 360–384 (2016).

[97]Dorschner, B., Yu, K., Mengaldo, G., and Colonius, T. A fast multi-resolution lattice Green's function method for elliptic difference equations. *J. Comput. Phys.* **407**, 109270 (2020).

[98]Yu, K. Multi-resolution lattice Green's function method for high Reynolds number external flows. PhD Thesis (California Institute of Technology, Pasadena, CA, 2021).

[99]Yu, K., Dorschner, B., and Colonius, T. Multi-resolution lattice Green's function method for incompressible flows. *J. Comput. Phys.* **459**, 110845 (2022).

[100]Liska, S. and Colonius, T. A parallel fast multipole method for elliptic difference equations. *J. Comput. Phys.* **278**, 76–91 (2014).

[101]Liska, S. Fast lattice Green's function methods for viscous incompressible flows on unbounded domains. PhD Thesis (California Institute of Technology, Pasadena, CA, 2016).

[102]Wu, J., Ma, H., and Zhou, M. Vortical Flows. (Springer, 2015).

[103]Saffman, P.G. Vortex dynamics. (Cambridge University Press, 1993).

[104]Serrin, J. Mathematical principles of classical fluid mechanics. In *Handbuch der Physik*, Vol. 8/1 (Springer, 1959), pp. 125–263.

[105]Lopez, J.M. and Bulbeck, C.J. Behavior of streamwise rib vortices in a three-dimensional mixing layer. *Phys. Fluids A* **5**, 1694–1702 (1993).

[106]Towns, J., Cockerill, T., Dahan, M., Foster, I., Gaither, K., Grimshaw, A., Hazlewood, V., Lathrop, S., Lifka, D., Peterson, G.D., Roskies, R., Scott, J.R., and N., Wilkins-Diehr XSEDE: accelerating scientific discovery. *Comput. Sci. Eng.* **16**, 62–74 (2014).

[107]Brasey, V. and Hairer, E. Half-explicit Runge–Kutta methods for differential-algebraic systems of index 2. *SIAM J. Numer. Anal.* **30**, 538–552 (1993).

Chapter 3

VELOCITY GRADIENT PARTITIONING IN TURBULENT FLOWS

This chapter consists of the following published journal article.

[1] **Arun, R.** and Colonius, T. Velocity gradient partitioning in turbulent flows. *J. Fluid Mech.* **1000**, R5 (2024).

Abstract

The velocity gradient tensor can be decomposed into normal straining, pure shearing, and rigid rotation tensors, each with distinct symmetry and normality properties. We partition the strength of turbulent velocity gradients based on the relative contributions of these constituents in several canonical flows. These flows include forced isotropic turbulence, turbulent channels, and turbulent boundary layers. For forced isotropic turbulence, the partitioning is in excellent agreement with previous results. For wall-bounded turbulence, the partitioning collapses onto the isotropic partitioning far from the wall, where the mean shearing is relatively weak. By contrast, the near-wall partitioning is dominated by shearing. Between these two regimes, the partitioning collapses well at sufficiently high friction Reynolds numbers and its variations in the buffer layer and the log-law region can be reasonably modeled as a function of the mean shearing strength. Altogether, our results highlight the expressivity and broad applicability of the velocity gradient partitioning as advantages for turbulence modeling.

3.1 Introduction

Identifying universal features of turbulent flows is a longstanding motif in turbulence modeling. Kolmogorov's local isotropy and similarity hypotheses [1] and their refinements [2, 3] suggest that small-scale flow statistics are approximately isotropic at sufficiently high Reynolds numbers, irrespective of the flow structure at large scales. Velocity gradients provide a useful testbed for investigating these hypotheses since they describe fundamental statistical and structural features of small-scale turbulence [4, 5]. For example, Johnson et al. [6] found support for the local isotropy hypothesis sufficiently far from the wall in a turbulent channel using velocity gradient statistics related to vortex stretching. Aiming to inform turbulence modeling efforts, the present study evaluates velocity gradient statistics in various wall-bounded flows relative to their isotropic values using a recently developed normality-based analysis.

Decomposing the velocity gradient tensor (VGT) based on its symmetry and normality properties distinguishes contributions from three distinct modes of deformation. These modes of deformation are normal straining, rigid rotation, and pure shearing. Originally, these modes were determined by applying a 'triple decomposition' of the VGT in a 'basic' reference frame where the effects of pure shearing can be extracted as a purely asymmetric tensor [7]. While identifying such a frame originally required solving challenging pointwise optimization problems, more computationally practical approaches based on the real Schur decomposition of the VGT have been developed recently [8–10]. We adopt this more recent normality-based triple decomposition, which identifies normal straining as symmetric and normal, rigid rotation as antisymmetric and normal, and pure shearing as strictly non-normal. A complex Schur decomposition has also been used [11], but its relationship to basic reference frames in physical space is less clear [12].

Partitioning the strength of the VGT based on its triple decomposition provides an expressive description of flow features. For example, the contribution of rigid rotation has been used to identify vortices [8, 9, 13] and that of shearing has been found to leave a strong imprint on extreme velocity gradients associated with intermittency [14]. The interplay between shearing and rigid rotation has been used to characterize the transition and turbulent decay of colliding vortex rings mediated by the elliptic instability [15]. The original triple decomposition of the VGT [7] has also been used to analyze the statis-

tical and structural imprint of turbulent shearing [16–18]. A theme of these works is the association of shearing with sheet-like vorticity and rigid rotation with tube-like vorticity.

Das and Girimaji [14] showed that the velocity gradients in forced isotropic turbulence converge to a specific partitioning at high Taylor-scale Reynolds numbers. More recently, Arun and Colonius [15] found that the decaying turbulent cloud produced by a vortex ring collision follows a similar partitioning. However, the spatial development in flows such as wakes, axisymmetric jets, and mixing layers has been associated with enhanced contributions of non-normal velocity gradients [19].

Using the normality-based triple decomposition, we partition the strength of velocity gradients in forced isotropic turbulence, turbulent channels, and turbulent boundary layers. The partitioning framework is presented in §3.2 and the turbulence datasets we analyze are reported in §3.3. We establish the isotropic partitioning in §3.4 and thereafter discuss how the partitioning is modified for wall-bounded turbulence in §3.5, emphasizing the role of the mean shearing and the friction Reynolds number.

3.2 Partitioning framework

The VGT, $\boldsymbol{A} = \boldsymbol{\nabla u}$, can be expressed in its principal reference frame, denoted by $(\cdot)^*$, as $\boldsymbol{A}^* = \boldsymbol{Q}\boldsymbol{A}\boldsymbol{Q}^{\mathrm{T}}$, where $\boldsymbol{Q}$ is unitary and $(\cdot)^{\mathrm{T}}$ represents the transpose. In this frame, the VGT is quasi-triangular and it can be decomposed as

$$\boldsymbol{A}^* = \underbrace{\begin{bmatrix} \dot{\epsilon}_1^* & 0 & 0 \\ 0 & \dot{\epsilon}_2^* & 0 \\ 0 & 0 & \dot{\epsilon}_3^* \end{bmatrix}}_{\boldsymbol{A}_\epsilon^*} + \underbrace{\begin{bmatrix} 0 & 0 & 0 \\ 0 & 0 & \dot{\varphi}_1^* \\ 0 & -\dot{\varphi}_1^* & 0 \end{bmatrix}}_{\boldsymbol{A}_\varphi^*} + \underbrace{\begin{bmatrix} 0 & \dot{\gamma}_3^* & \dot{\gamma}_2^* \\ 0 & 0 & \dot{\gamma}_1^* \\ 0 & 0 & 0 \end{bmatrix}}_{\boldsymbol{A}_\gamma^*}, \tag{3.1}$$

where $\boldsymbol{A}_\epsilon^*$, $\boldsymbol{A}_\varphi^*$, and $\boldsymbol{A}_\gamma^*$ denote the normal straining, rigid rotation, and pure shearing tensors, respectively. These tensors can be determined and transformed to the original coordinate system using the ordered real Schur decomposition of $\boldsymbol{A}$ [12].

Correspondingly, the strength of the velocity gradients can be expressed as

$$A^2 = \mathrm{tr}\left(\boldsymbol{A}^{\mathrm{T}}\boldsymbol{A}\right) = \underbrace{\mathrm{tr}\left(\boldsymbol{A}_\epsilon^{\mathrm{T}}\boldsymbol{A}_\epsilon\right)}_{A_\epsilon^2} + \underbrace{\mathrm{tr}\left(\boldsymbol{A}_\varphi^{\mathrm{T}}\boldsymbol{A}_\varphi\right)}_{A_\varphi^2} + \underbrace{\mathrm{tr}\left(\boldsymbol{A}_\gamma^{\mathrm{T}}\boldsymbol{A}_\gamma\right)}_{A_\gamma^2} + \underbrace{2\mathrm{tr}\left(\boldsymbol{A}_\varphi^{\mathrm{T}}\boldsymbol{A}_\gamma\right)}_{A_{\varphi\gamma}^2}, \tag{3.2}$$

where $\mathrm{tr}(\cdot)$ represents the trace. The first three terms represent the strengths of the constituents in (3.1) and the last term represents the interaction between shearing and rigid rotation. The velocity gradient partitioning is defined in terms of the relative contributions of these constituents to A^2. In normalized form, these contributions are bounded as $A_\epsilon^2/A^2 \in [0,1]$, $A_\varphi^2/A^2 \in [0,1]$, $A_\gamma^2/A^2 \in [0,1]$, and $A_{\varphi\gamma}^2/A^2 \in [0,(\sqrt{2}+1)^{-1}]$ [14].

Ensemble averaging can be used to characterize the statistical relevance of the contributions in this partitioning. We define the averaged partitioning as

$$\langle A_\zeta^2 \rangle_{A^2} = \langle A_\zeta^2 \rangle \big/ \langle A^2 \rangle, \quad \zeta \in \{\epsilon, \varphi, \gamma, \varphi\gamma\}, \tag{3.3}$$

where $\langle(\cdot)\rangle$ denotes averaging over homogeneous spatial directions and time. The present study focuses on this averaged partitioning, which can be used to characterize contributions to enstrophy and dissipation [14, 15].

The practical relevance of the partitioning is tied, in part, to its ability to inform modeling efforts, including for non-canonical flows. Some modeling paradigms, such as large-eddy simulations (LES) and Lagrangian approaches, operate on the basis of the total velocity. Other paradigms, such as the Reynolds-averaged Navier–Stokes (RANS) equations and input-output analyses, operate on the basis of the velocity fluctuations. In these contexts, it is therefore important to distinguish the partitioning of the total velocity gradients from the partitioning of the velocity gradient fluctuations, which we denote as $\langle A_\zeta^2 \rangle_{A^2}$ and $\langle A_\zeta^2 \rangle'_{A^2}$, respectively. This distinction is particularly relevant since the normality-based triple decomposition does not generally commute with filtering or averaging operations. Physically, the modes of deformation for the total partitioning reflect what a fluid parcel would actually experience. By contrast, the modes for the fluctuation partitioning reflect what it would experience if advected only by the velocity fluctuations. We consider both the total partitioning and the fluctuation partitioning for the wall-bounded flows in the present study.

3.3 Turbulence datasets

As summarized in Table 3.1, we analyze the partitioning in several well-validated turbulence datasets obtained from direct numerical simulations. These datasets include forced isotropic turbulence (FIT315 and FIT610) and wall-bounded turbulence (Ch0186, Ch1000, BL0729, and BL1024) over a broad range of Reynolds numbers. Cases FIT610 and Ch1000 are obtained from the

Case	Configuration	Reynolds number	Grid size	N_t	Reference
FIT315	Forced isotropic	$Re_\lambda \approx 315$	$(1024, 1024, 1024)$	67	Cardesa et al. [20]
FIT610	Forced isotropic	$Re_\lambda \approx 610$	$(4096, 4096, 4096)$	1	Yeung et al. [21]
Ch0186	Channel	$Re_\tau \approx 186$	$(32, 129, 32)$	55 925	Arun et al. [22]
Ch1000	Channel	$Re_\tau \approx 1000$	$(2048, 512, 1536)$	40	Graham et al. [23]
BL0729	Boundary layer	$Re_\tau \approx 292{-}729$	$(2049, 90, 256)$	10 000	Towne et al. [24]
BL1024	Boundary layer	$Re_\tau \approx 481{-}1024$	$(4097, 90, 512)$	1500	Towne et al. [24]

Table 3.1: Turbulence datasets considered in the present analyses. Taylor-scale and friction Reynolds numbers are denoted by Re_λ and Re_τ, respectively, and N_t denotes the number of snapshots. The grid sizes correspond to the streamwise (x), wall-normal (y), and spanwise (z) directions, respectively.

Johns Hopkins Turbulence Databases [25] and Ch0186 represents a minimal flow unit for near-wall turbulence [26]. The references in Table 3.1 provide further computational details and validation for each dataset.

We establish the isotropic partitioning using FIT610 and test its sensitivity to Re_λ using FIT315. The snapshots for FIT315 are spaced roughly one integral time unit apart and N_t is selected to produce a similar number of samples to FIT610. We use Ch1000 to characterize the partitioning in a turbulent channel at a moderate Re_τ. Its snapshots are spaced roughly 0.65 eddy turnover time units apart and they span roughly one flow-through time unit [23]. Case Ch0186 allows us to investigate how the wall-bounded partitioning changes when Re_τ is barely large enough to sustain turbulence. Its snapshots span roughly 160 eddy turnover time units. We use BL0729 and BL1024 to further characterize the partitioning for wall-bounded turbulence subject to mild spatial development. Their broad ranges of Re_τ allow us to characterize how the partitioning evolves as the flows become increasingly turbulent. The snapshots for BL0729 and BL1024 span more than 20 and 7 eddy turnover time units, respectively [24].

When computing the VGT, we adopt the differentiation techniques employed in the original simulations where possible. We further require that all elements of the VGT be collocated prior to partitioning. For FIT315 and FIT610, we use a spectral method to compute all velocity gradients. For Ch0186, we use the second-order accurate staggered finite differences employed in the original simulation and subsequently shift staggered quantities to cell centers. This shifting is performed by adjusting the phases of the Fourier modes in

Case	$\Delta_{iso}\|\Delta'_{iso}$	$\langle A^2_\epsilon\rangle_{A^2}$	$\langle A^2_\varphi\rangle_{A^2}$	$\langle A^2_\gamma\rangle_{A^2}$	$\langle A^2_{\varphi\gamma}\rangle_{A^2}$	$\langle A^2_\epsilon\rangle'_{A^2}$	$\langle A^2_\varphi\rangle'_{A^2}$	$\langle A^2_\gamma\rangle'_{A^2}$	$\langle A^2_{\varphi\gamma}\rangle'_{A^2}$
FIT315	0.2%|0.2%	0.239	0.106	0.521	0.134	0.239	0.106	0.521	0.134
FIT610	– | –	0.240	0.106	0.520	0.134	0.240	0.106	0.520	0.134
Ch0186	5.0%|5.0%	0.250	0.090	0.535	0.125	0.250	0.090	0.535	0.125
Ch1000	0.4%|0.4%	0.242	0.105	0.519	0.134	0.242	0.105	0.519	0.134
BL0729	1.2%|1.0%	0.242	0.101	0.524	0.133	0.245	0.104	0.517	0.134
BL1024	0.8%|0.6%	0.239	0.102	0.523	0.136	0.242	0.104	0.518	0.136

Table 3.2: Velocity gradient partitioning for each flow and the corresponding deviation metrics. The partitioning is reported at the channel centerline for Ch0186 and Ch1000 and at $(Re_\tau, y^+) \approx (729, 159)$ and $(1000, 155)$ for BL0729 and BL1024, respectively. The column shadings reflect our partitioning color scheme.

x and z and by averaging adjacent values in y [22]. For Ch1000, we use a spectral method in x and z and collocated finite differences with a stencil size of $N_s = 7$ in y. The original BL0729 and BL1024 simulations employed second-order accurate staggered finite differences; however, the published datasets are collocated and subsampled by a factor of two in y and z [24]. As a result, we employ collocated finite differences with $N_s = 3$ in x and y. Since the z direction has periodic boundary conditions, we compute spanwise derivatives using a spectral method with the modified wavenumbers associated with the original staggered finite difference scheme.

3.4 Partitioning in nearly isotropic turbulence

The isotropic velocity gradient partitioning characterizes the contributions of $\boldsymbol{A}_\epsilon$, $\boldsymbol{A}_\varphi$, and $\boldsymbol{A}_\gamma$ in the idealized setting of forced isotropic turbulence. It has been established previously for $Re_\lambda \approx 1{-}588$ [14] and is roughly invariant for $Re_\lambda \gtrsim 200$. Here, we use FIT610 to confirm this isotropic partitioning, which we denote by $\langle A^2_\zeta\rangle^{iso}_{A^2}$. We characterize deviations from this partitioning using the following metric:

$$\Delta_{iso} = \sum_{\zeta\in\{\epsilon,\varphi,\gamma,\varphi\gamma\}} \left|\langle A^2_\zeta\rangle_{A^2} - \langle A^2_\zeta\rangle^{iso}_{A^2}\right| \Big/ \sum_{\zeta\in\{\epsilon,\varphi,\gamma,\varphi\gamma\}} \left|\langle A^2_\zeta\rangle^{iso}_{A^2}\right|, \tag{3.4}$$

in which the denominator sums to unity. An analogous metric, Δ'_{iso}, is defined for the fluctuation partitioning by replacing $\langle A^2_\zeta\rangle_{A^2}$ with $\langle A^2_\zeta\rangle'_{A^2}$ in (3.4). One advantage of these metrics is that they are not affected by further decomposing $\boldsymbol{A}_\gamma$ into its symmetric and antisymmetric parts. In the present study,

they produce results similar to those produced by relative root-mean-square deviations, which are more commonplace.

Table 3.2 shows the partitioning alongside the deviation metrics for each dataset. Consistent with previous results [14], the FIT315 partitioning is nearly identical to the FIT610 partitioning. For the wall-bounded flows, the partitioning is taken from regions where the mean shearing is relatively weak. Further, for the boundary layers, it is taken sufficiently far from the boundary-layer thickness to mitigate the imprint of the exterior potential flow.

The partitioning in the selected regions of Ch1000, BL0729, and BL1024 is remarkably similar to the isotropic partitioning, with deviations of 1.2% or less. Since the mean flow has a minimal imprint on the velocity gradients in these regions, the total partitioning is quite similar to the fluctuation partitioning. These results highlight that the isotropic partitioning is broadly applicable in appropriate regions of inhomogeneous turbulent flows.

3.5 Partitioning in wall-bounded turbulence

3.5.1 Effect of mean shearing

The velocity gradient partitioning in wall-bounded turbulence is heavily influenced by the mean shearing imposed by the wall. Figure 3.1 shows the partitioning profiles as a function of both wall-normal location (in inner units) and mean shearing strength. Consistent with Table 3.2, the partitioning approaches the isotropic values far from the wall[1], starting near the top of the log-law region. However, the boundary-layer partitioning begins to diverge from these values near the edge of the boundary layer, reflecting the transition to a potential flow. Beyond the boundary-layer thickness (not shown), this transition is associated with monotonic enhancement of normal straining and decay of the other constituents. As observed in Table 3.2, the Ch0186 partitioning does not converge as well onto the isotopic values since it is barely turbulent. The partitioning throughout this minimal channel is generally associated with enhanced contributions from shearing.

For all wall-normal profiles in Figure 3.1, the near-wall partitioning is dominated by shearing. This feature reflects the strong imprint of the mean shearing on the near-wall velocity gradients. The imprint of the mean shearing is also responsible for the enhanced contribution of shearing (at the expense of the other constituents) to the total partitioning relative to the fluctuation parti-

[1]The partitioning far from the wall reflects small-scale isotropy associated with velocity gradients and does not preclude the development of large-scale anisotropy (e.g., in the velocity fluctuation statistics).

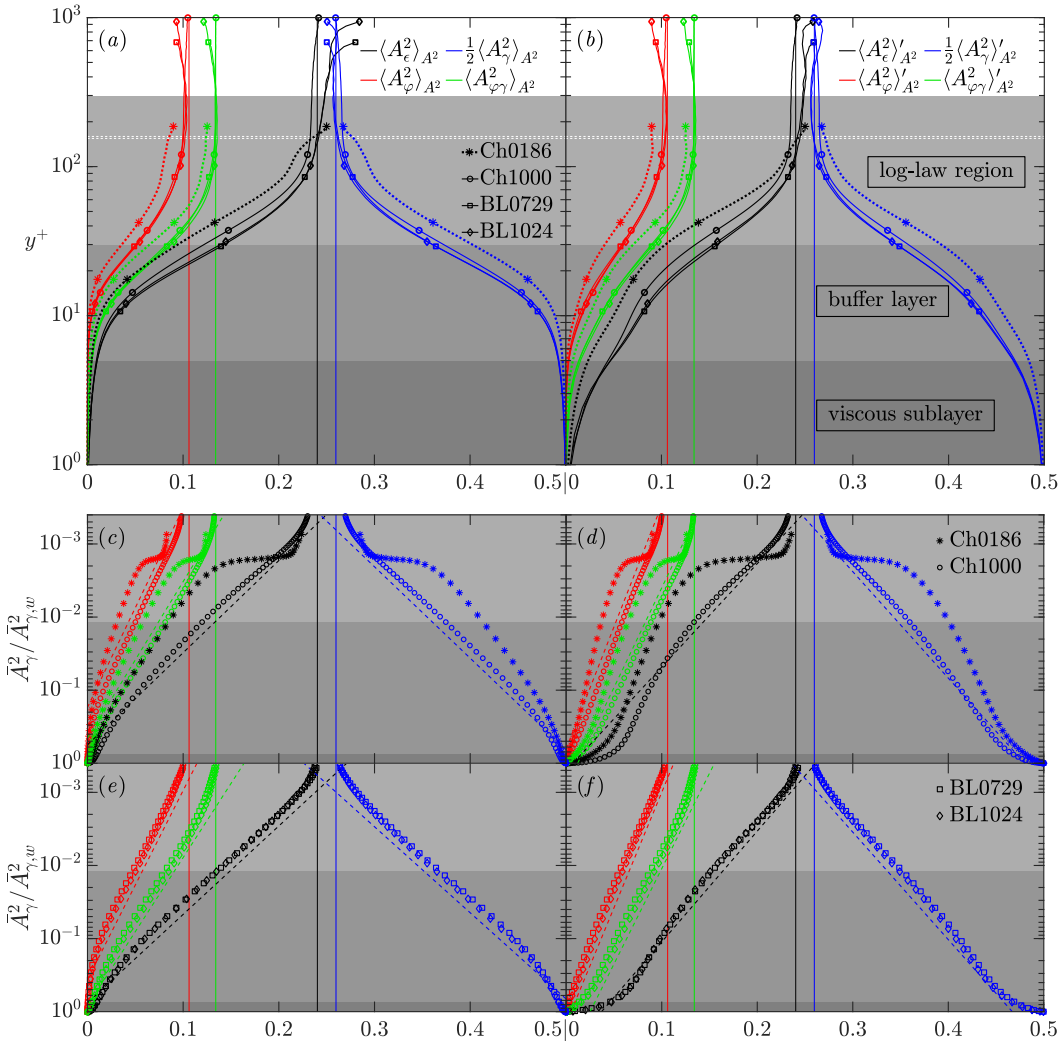

Figure 3.1: Total (a,c,e) and fluctuation (b,d,f) partitioning profiles for the channels and boundary layers in terms of wall-normal location in inner units (a,b) and mean shearing strength $(c–f)$. The vertical lines represent the isotropic values. The BL0729 and BL1024 profiles are shown for $Re_\tau \approx 729$ and 1000, respectively, and the top boundary of the log-law region represents Ch1000. The dashed white lines in (a,b) represent the locations of the partitioning values reported in Table 3.2 for BL0729 and BL1024. In (a,b), the markers are used to distinguish between the profiles and, in $(c–f)$, they represent actual data points. In $(c–f)$, the mean shearing axis is reversed and the dashed lines represent comparable linear–log trends for each dataset, with the partitioning as the dependent variable.

tioning for $y^+ \lesssim 20$. Between the near-wall regime and the nearly isotropic regime far from the wall, the collapse of the partitioning profiles is particularly striking for BL0729, BL1024, and (to a lesser extent) Ch1000. The most significant differences between the channel and boundary-layer profiles occur in the buffer layer. For the channels, the contributions of shearing and normal straining in this region are enhanced and reduced, respectively, relative to their contributions in the boundary layers. While beyond the scope of the present work, characterizing how the flow structures in the buffer layer reflect these differences (e.g. through the imprint of the exterior potential flow) would be interesting future work.

The mean shearing strength profiles in Figure 3.1 provide a complementary view to the wall-normal profiles. The mean shearing strength parameter is normalized as $\bar{A}_\gamma^2/\bar{A}_{\gamma,w}^2$, where $\bar{A}_{\gamma,w}^2$ represents the (maximum) value at the wall. This parameter quantifies the effect of the wall in terms of velocity gradients and can be determined directly from the mean flow. Further, for the channels and boundary layers we consider, it can be well-approximated using the wall-normal gradient of the mean streamwise velocity, $\partial\bar{u}/\partial y$. For these profiles, we focus primarily on the buffer layer and log-law region since they capture the majority of the evolution from the near-wall regime to the nearly isotropic regime. As observed for the wall-normal profiles, the partitioning in these regions collapses very well as a function of the mean shearing strength for BL0729, BL1024, and (to a lesser extent) Ch1000.

The partitioning in wall-bounded flows becomes similar to the isotropic partitioning when $\bar{A}_\gamma^2/\bar{A}_{\gamma,w}^2 \lesssim 10^{-3}$. The dashed lines in Figure 3.1 illustrate the similarity of the partitioning profiles to linear–log variations with the mean shearing strength for $10^{-3} \lesssim \bar{A}_\gamma^2/\bar{A}_{\gamma,w}^2 \lesssim 10^{-1}$. The slopes of these variations for the total partitioning are slightly steeper than those for the fluctuation partitioning due to the enhanced contribution from the mean shearing for $\bar{A}_\gamma^2/\bar{A}_{\gamma,w}^2 \gtrsim 10^{-1}$. The slopes for shearing and normal straining tend to be similar in magnitude and steeper than those of rigid rotation and shear-rotation interactions. This feature mirrors the relative contributions in the isotropic partitioning, for which $\langle A_\epsilon^2\rangle_{A^2}^{iso} \sim \frac{1}{2}\langle A_\gamma^2\rangle_{A^2}^{iso} \sim \langle A_\varphi^2\rangle_{A^2}^{iso} + \langle A_{\varphi\gamma}^2\rangle_{A^2}^{iso}$.

More rigorous modeling approaches may help enable predictions of the partitioning profiles in terms of mean flow variables. While we do not propose an explicit model for these profiles in the present study, our analysis suggests that

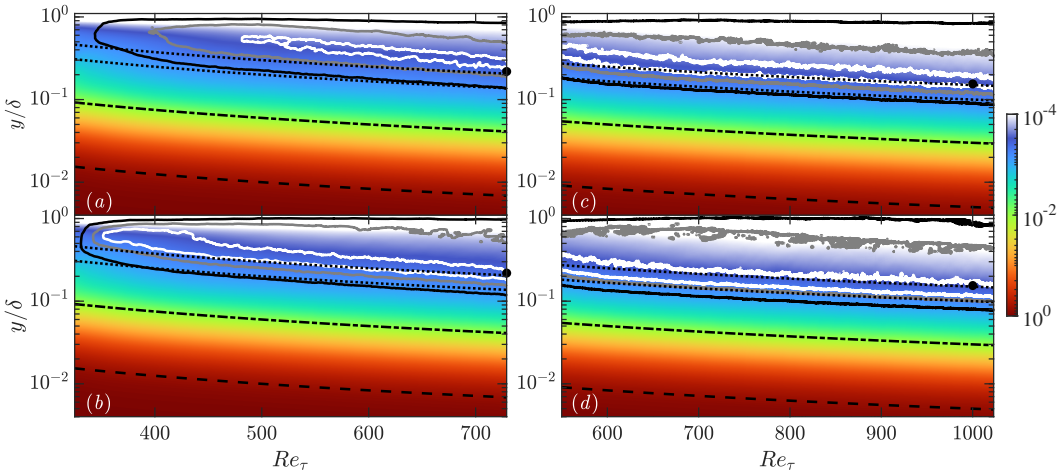

Figure 3.2: Streamwise development of BL0729 (a,b) and BL1024 (c,d) in terms of Re_τ, where the color axis represents $\bar{A}^2_\gamma/\bar{A}^2_{\gamma,w}$. The white, gray, and black contours represent $\Delta_{iso} = 1\%$, $\Delta_{iso} = 2\%$, and $\Delta_{iso} = 5\%$, respectively, for the total partitioning (a,c) and $\Delta'_{iso} = 1\%$, $\Delta'_{iso} = 2\%$, and $\Delta'_{iso} = 5\%$, respectively, for the fluctuation partitioning (b,d). The dashed and dash-dotted black lines represent the top of the viscous sublayer ($y^+ = 5$) and the top of the buffer layer ($y^+ = 30$), respectively, and the dotted black lines represent $y^+ = 100$ and $y^+ = 150$. The black circles represent the locations of the partitioning values reported in Table 3.2 and δ represents the boundary-layer thickness.

both y^+ and the mean shearing are appropriate for modeling the partitioning and sufficiently high Re_τ. Beyond mean flow variables, characterizing how the strength of the velocity gradient fluctuations relative to the mean shearing strength impacts these profiles may provide further insight.

The pronounced, roughly monotonic variations of the normality-based partitioning profiles strikingly capture the development from the near-wall regime to the nearly isotropic regime far from the wall. By contrast, as depicted and discussed in Appendix 3.A1, the variations for the symmetry-based partitioning are non-monotonic and do not exceed ± 0.02 of their isotropic values in the regimes of interest. Supplemented by previous findings [15], these results highlight that the expressivity of the normality-based partitioning provides a key advantage over considering symmetry alone.

3.5.2 Effect of friction Reynolds number

Beyond wall-normal variations, the streamwise spatial development in the boundary layers is associated with increasing Re_τ. Figure 3.2 shows how the

region where the isotropic partitioning is applicable evolves as a function of Re_τ. For BL0729, this region grows appreciably in size as Re_τ increases. The same is true to a lesser extent for BL1024, where the turbulence is more well-developed throughout the domain. The Δ_{iso} and Δ'_{iso} contours identify regions where the isotropic partitioning is most applicable. Throughout BL1024 and at the downstream end of BL0729, it is most applicable around $y^+ \approx 170$ and $y^+ \approx 140$ for the total and fluctuating velocity gradients, respectively. The domain of applicability of the isotropic partitioning is slightly larger for the velocity fluctuations than for the total velocity.

Except at the upstream end of BL0729, Δ_{iso} and Δ'_{iso} are less than roughly 5% for $y^+ \gtrsim 100$. Alongside Figure 3.1, these results complement the findings of Johnson et al. [6], which suggest that velocity gradient statistics associated with vortex stretching approach their isotropic values for $y^+ \gtrsim 100$. Therefore, our results further support their conclusion that this collapse provides support for the local isotropy hypothesis sufficiently far from the wall.

The inner unit scaling of this collapse contrasts with the boundary-layer thickness, which scales in outer units and captures the divergence from the isotropic partitioning near the free stream. Our results therefore suggest that, while inner unit scalings can be used to determine when the partitioning approaches the isotropic values, outer unit scalings may more appropriately capture the divergence to a potential flow in the boundary layers. They further suggest that $Re_\tau \gtrsim 700$ is a reasonable regime in which to expect a collapsed partitioning. This estimate is consistent with the collapse of the partitioning profiles for BL0729, BL1024, and (to a lesser extent) Ch1000 as well as the lack of collapse for Ch0186 in Figure 3.1.

3.6 Concluding remarks

We have analyzed the normality-based partitioning of velocity gradients in several canonical turbulent flows. The partitioning we compute for forced isotropic turbulence agrees well with previous results [14]. Moreover, we show that the isotropic partitioning also applies to velocity gradients near and beyond the top of the log-law region in wall-bounded flows over a broad range of Re_τ. The broad applicability of the isotropic partitioning for $y^+ \gtrsim 100$ complements previous results [6], thereby providing further support for the local isotropy hypothesis for well-developed turbulence far from solid boundaries.

Our results suggest that $Re_\tau \gtrsim 700$ is sufficiently high to expect the partitioning profiles to collapse as they transition from the shearing-dominated near-wall regime to the nearly isotropic regime. Further, the mean shearing provides a reasonable mean flow parameter for modeling their variations in the buffer layer and the log-law region. Altogether, our results highlight expressivity as a key advantage of the normality-based partitioning over symmetry-based approaches.

Moving forward, analyzing the partitioning profiles at higher Re_τ would help further characterize their sensitivity and collapse for wall-bounded flows. Developing more rigorous models for the partitioning in terms of mean flow variables would also be useful, especially models that do not depend strongly on the flow configuration. The partitioning may aid turbulence modeling efforts in RANS, LES, Lagrangian, or input-output settings, e.g. by directly informing closure models or by providing an evaluation metric for models of interest. Finally, connecting the statistical features we report to the turbulence structures that produce them would provide an enhanced view of the roles of the partitioning constituents.

Acknowledgements: The authors gratefully acknowledge the reviewers for helpful feedback, A. Nekkanti and M. Wadas for discussions, and H.J. Bae for providing the Ch0186 dataset.

Funding: R.A. was supported by the Department of Defense (DoD) through the National Defense Science & Engineering Graduate (NDSEG) Fellowship Program.

Data availability statement: Sample code for computing the velocity gradient partitioning is available at https://doi.org/10.22002/17h15-gr910.

3.A1 Symmetry-based partitioning profiles

The standard symmetry-based decomposition of the VGT identifies the strain-rate tensor as $\boldsymbol{S} = \frac{1}{2}(\boldsymbol{A}+\boldsymbol{A}^{\mathrm{T}})$ and the vorticity tensor as $\boldsymbol{W} = \frac{1}{2}(\boldsymbol{A}-\boldsymbol{A}^{\mathrm{T}})$. These tensors can be expressed in terms of the normality-based triple decomposition of the VGT as $\boldsymbol{S} = \boldsymbol{A}_\epsilon + \boldsymbol{S}_\gamma$ and $\boldsymbol{W} = \boldsymbol{A}_\varphi + \boldsymbol{W}_\gamma$, where $\boldsymbol{S}_\gamma = \frac{1}{2}(\boldsymbol{A}_\gamma + \boldsymbol{A}_\gamma^{\mathrm{T}})$ and $\boldsymbol{W}_\gamma = \frac{1}{2}(\boldsymbol{A}_\gamma - \boldsymbol{A}_\gamma^{\mathrm{T}})$.

Using the definition in (3.3), the symmetry-based partitioning characterizes the relative contributions of the strain-rate and vorticity tensors to the velocity gradient strength. In isotropic turbulence, these contributions are equiparti-

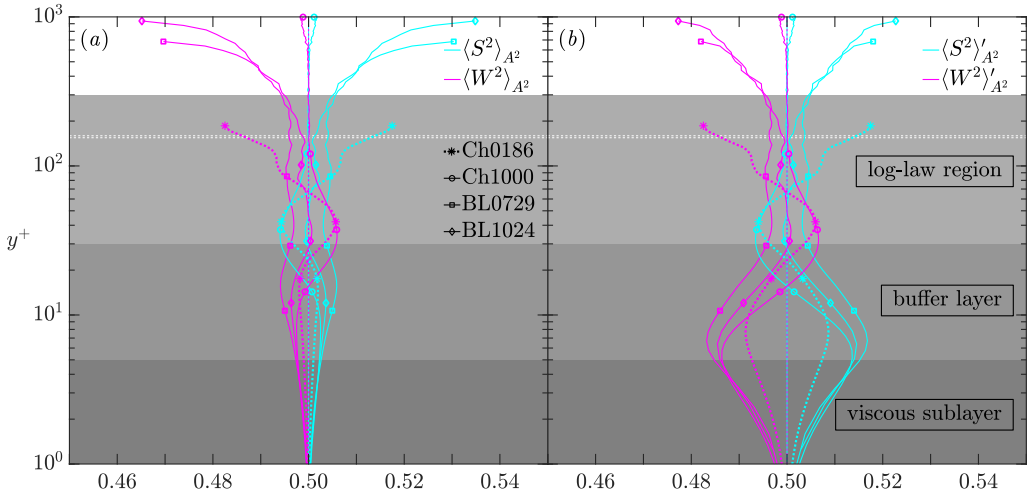

Figure 3.3: Symmetry-based total (a) and fluctuation (b) partitioning profiles for the channels and boundary layers in terms of wall-normal location in inner units. The plots are in the same style as those in Figure 3.1.

tioned as $\langle S^2\rangle_{A^2} = \langle W^2\rangle_{A^2} = 0.500$. Figure 3.3 shows the symmetry-based partitioning profiles for the wall-bounded flows we consider. Except near the potential flow regime of the boundary layers, these profiles do not deviate more than ± 0.02 from the isotropic values for both the total and fluctuating velocities. Further, unlike the normality-based partitioning profiles in Figure 3.1, the symmetry-based profiles do not vary monotonically with y^+. These results show that the normality-based partitioning is significantly more expressive of the spatial variations in turbulence characteristics from the near-wall regime to the nearly isotropic regime. This finding complements the results of Arun and Colonius [15], which show that the normality-based partitioning is more expressive than the symmetry-based partitioning in capturing the temporal evolution of a vortex ring collision, including its transition and turbulent decay. Together, these results highlight the superior expressivity of the normality-based partitioning.

References

[1]Kolmogorov, A.N. The local structure of turbulence in incompressible viscous fluid for very large Reynolds numbers. *Dokl. Akad. Nauk SSSR* **30**, 301–305, reprinted in *Proc. R. Soc. Lond.* A **434**, 9–13. (1941).

[2]Kolmogorov, A.N. A refinement of previous hypotheses concerning the local structure of turbulence in a viscous incompressible fluid at high Reynolds number. *J. Fluid Mech.* **13**, 82–85 (1962).

[3]Oboukhov, A.M. Some specific features of atmospheric tubulence. *J. Fluid Mech.* **13**, 77–81 (1962).

[4]Meneveau, C. Lagrangian dynamics and models of the velocity gradient tensor in turbulent flows. *Annu. Rev. Fluid Mech.* **43**, 219–245 (2011).

[5]Johnson, P.L. and Wilczek, M. Multiscale velocity gradients in turbulence. *Annu. Rev. Fluid Mech.* **56**, 463–490 (2024).

[6]Johnson, P.L., Hamilton, S.S., Burns, R., and Meneveau, C. Analysis of geometrical and statistical features of Lagrangian stretching in turbulent channel flow using a database task-parallel particle tracking algorithm. *Phys. Rev. Fluids* **2**, 014605 (2017).

[7]Kolář, V. Vortex identification: new requirements and limitations. *Intl J. Heat Fluid Flow* **28**, 638–652 (2007).

[8]Liu, C., Gao, Y., Tian, S., and Dong, X. Rortex—a new vortex vector definition and vorticity tensor and vector decompositions. *Phys. Fluids* **30**, 035103 (2018).

[9]Gao, Y. and Liu, C. Rortex and comparison with eigenvalue-based vortex identification criteria. *Phys. Fluids* **30**, 085107 (2018).

[10]Gao, Y. and Liu, C. Rortex based velocity gradient tensor decomposition. *Phys. Fluids* **31**, 011704 (2019).

[11]Keylock, C.J. The Schur decomposition of the velocity gradient tensor for turbulent flows. *J. Fluid Mech.* **848**, 876–905 (2018).

[12]Kronborg, J. and Hoffman, J. The triple decomposition of the velocity gradient tensor as a standardized real Schur form. *Phys. Fluids* **35**, 031703 (2023).

[13]Haller, G. Can vortex criteria be objectivized?, *J. Fluid Mech.* **908**, A25 (2021).

[14]Das, R. and Girimaji, S.S. Revisiting turbulence small-scale behavior using velocity gradient triple decomposition. *New J. Phys.* **22**, 063015 (2020).

[15]Arun, R. and Colonius, T. Velocity gradient analysis of a head-on vortex ring collision. *J. Fluid Mech.* **982**, A16 (2024).

[16]Nagata, R., Watanabe, T., Nagata, K., and da Silva, C.B. Triple decomposition of velocity gradient tensor in homogeneous isotropic turbulence. *Comput. Fluids* **198**, 104389 (2020).

[17]Watanabe, T., Tanaka, K., and Nagata, K. Characteristics of shearing motions in incompressible isotropic turbulence. *Phys. Rev. Fluids* **5**, 072601 (2020).

[18]Enoki, R., Watanabe, T., and Nagata, K. Statistical properties of shear and nonshear velocity components in isotropic turbulence and turbulent jets. *Phys. Rev. Fluids* **8**, 104602 (2023).

[19]Beaumard, P., Buxton, O.R.H., and Keylock, C.J. The importance of non-normal contributions to velocity gradient tensor dynamics for spatially developing, inhomogeneous, turbulent flows. *J. Turbul.* **20**, 577–598 (2019).

[20]Cardesa, J.I., Vela-Martín, A., and Jiménez, J. The turbulent cascade in five dimensions. *Science* **357**, 782–784 (2017).

[21]Yeung, P.K., Donzis, D.A., and Sreenivasan, K.R. Dissipation, enstrophy and pressure statistics in turbulence simulations at high Reynolds numbers. *J. Fluid Mech.* **700**, 5–15 (2012).

[22]Arun, R., Bae, H.J., and McKeon, B.J. Towards real-time reconstruction of velocity fluctuations in turbulent channel flow. *Phys. Rev. Fluids* **8**, 064612 (2023).

[23]Graham, J., Kanov, K., Yang, X.I.A., Lee, M., Malaya, N., Lalescu, C.C., Burns, R., Eyink, G., Szalay, A., R.D., Moser, and Meneveau, C. A Web services accessible database of turbulent channel flow and its use for testing a new integral wall model for LES. *J. Turbul.* **17**, 181–215 (2016).

[24]Towne, A., Dawson, S.T.M., Brès, G.A., Lozano-Durán, A., Saxton-Fox, T., Parthasarathy, A., Jones, A.R., Biler, H., Yeh, C.-A., Patel, H.D., and Taira, K. A database for reduced-complexity modeling of fluid flows. *AIAA J.* **61**, 2867–2892 (2023).

[25]Li, Y., Perlman, E., Wan, M., Yang, Y., Meneveau, C., Burns, R., Chen, S., Szalay, A., and Eyink, G. A public turbulence database cluster and applications to study Lagrangian evolution of velocity increments in turbulence. *J. Turbul.* **9**, N31 (2008).

[26]Jiménez, J. and Moin, P. The minimal flow unit in near-wall turbulence. *J. Fluid Mech.* **225**, 213–240 (1991).

Chapter 4

NORMALITY-BASED ANALYSIS OF MULTISCALE VELOCITY GRADIENTS AND ENERGY TRANSFER IN DIRECT AND LARGE-EDDY SIMULATIONS OF ISOTROPIC TURBULENCE

This chapter consists of the following published journal article.

[1]**Arun, R.**, Kamal, M., Colonius, T., and Johnson, P.L. Normality-based analysis of multiscale velocity gradients and energy transfer in direct and large-eddy simulations of isotropic turbulence. *J. Fluid Mech.* **1021**, A47 (2025).

Abstract

Symmetry-based analyses of multiscale velocity gradients highlight that strain self-amplification and vortex stretching drive forward energy transfer in turbulent flows. By contrast, a strain–vorticity covariance mechanism produces backscatter that contributes to the bottleneck effect in the subinertial range of the energy cascade. We extend these analyses by using a normality-based decomposition of filtered velocity gradients in forced isotropic turbulence to distinguish contributions from normal straining, pure shearing, and rigid rotation at a given scale. Our analysis of direct numerical simulation (DNS) data illuminates the importance of shear layers in the inertial range and (especially) the subinertial range of the cascade. Shear layers contribute significantly to strain self-amplification and vortex stretching and play a dominant role in the backscatter mechanism responsible for the bottleneck effect. Our concurrent analysis of large-eddy simulation (LES) data characterizes how different closure models affect the flow structure and energy transfer throughout the resolved scales. We thoroughly demonstrate that the multiscale flow features produced by a mixed model closely resemble those in a filtered DNS, whereas the features produced by an eddy viscosity model resemble those in an unfiltered DNS at a lower Reynolds number. This analysis helps explain how small-scale shear layers, whose imprint is mitigated upon filtering, amplify the artificial bottleneck effect produced by the eddy viscosity model in the inertial range of the cascade. Altogether, the present results provide a refined interpretation of the flow structures and mechanisms underlying the energy cascade and insight for designing and evaluating LES closure models.

4.1 Introduction

Small-scale flow features form a cornerstone of efforts to understand and model turbulent flows [1–5]. The velocity gradient tensor (VGT), $A_{ij} = \partial u_i/\partial x_j$, is central to our understanding of small-scale turbulence since it encodes a linear approximation of the local flow structure about critical points [6] and underpins descriptions of fundamental dynamical mechanisms [7, 8].

4.1.1 Normality-based analysis of velocity gradients in turbulent flows

Conventionally, the VGT is decomposed as

$$A_{ij} = S_{ij} + \Omega_{ij}, \tag{4.1}$$

where $S_{ij} = \frac{1}{2}(A_{ij} + A_{ji})$ is the (symmetric) strain-rate tensor and $\Omega_{ij} = \frac{1}{2}(A_{ij} - A_{ji})$ is the (antisymmetric) vorticity tensor. This symmetry-based decomposition forms the basis for mechanisms like strain self-amplification and vortex stretching, vortex identification criteria like Q [9] and λ_2 [10], and alignment analyses in the strain-rate eigenframe [11, 12]. However, despite its ubiquity, the symmetry-based decomposition provides relatively limited insight into local flow structure.

A more detailed description can be obtained by analyzing the normality properties of the VGT. These properties can be identified by considering a 'principal' reference frame, denoted by $(\cdot)^*$, in which the VGT obtains a quasi-triangular form. This form can be expressed as $A^*_{ij} = U_{ik}A_{km}U_{jm}$, where U_{ij} is an orthogonal matrix that can be interpreted as a rotation of the local coordinate axes in physical space. In this principal frame, the normality-based decomposition of the VGT can be expressed as

$$A^*_{ij} = \underbrace{\begin{bmatrix} \dot{\epsilon}^*_1 & 0 & 0 \\ 0 & \dot{\epsilon}^*_2 & 0 \\ 0 & 0 & \dot{\epsilon}^*_3 \end{bmatrix}}_{S^{\epsilon*}_{ij}} + \underbrace{\begin{bmatrix} 0 & \dot{\gamma}^*_3 & \dot{\gamma}^*_2 \\ 0 & 0 & \dot{\gamma}^*_1 \\ 0 & 0 & 0 \end{bmatrix}}_{A^{\gamma*}_{ij}} + \underbrace{\begin{bmatrix} 0 & 0 & 0 \\ 0 & 0 & \dot{\varphi}^*_1 \\ 0 & -\dot{\varphi}^*_1 & 0 \end{bmatrix}}_{\Omega^{\varphi*}_{ij}}, \tag{4.2}$$

where $S^{\epsilon*}_{ij}$, $A^{\gamma*}_{ij}$, and $\Omega^{\varphi*}_{ij}$ denote the normal straining, pure shearing, and rigid rotation tensors, respectively. The normal straining tensor is symmetric and normal whereas the rigid rotation tensor is antisymmetric and normal. The pure shearing tensor is non-normal and it can be further decomposed into the (symmetric) shear straining tensor, $S^{\gamma}_{ij} = \frac{1}{2}(A^{\gamma}_{ij} + A^{\gamma}_{ji})$, and the (antisymmetric)

shear vorticity tensor, $\Omega^{\gamma}_{ij} = \frac{1}{2}(A^{\gamma}_{ij} - A^{\gamma}_{ji})$. Therefore, (4.2) can be viewed as a refinement of (4.1) since $S_{ij} = S^{\epsilon}_{ij} + S^{\gamma}_{ij}$ and $\Omega_{ij} = \Omega^{\varphi}_{ij} + \Omega^{\gamma}_{ij}$. The tensors in (4.2) can be determined and transformed to the original coordinate system using the ordered real Schur form of the VGT [13]. Arun and Colonius [14] provided an instructional code for implementing the normality-based decomposition, which is available at https://doi.org/10.22002/17h15-gr910.

Identifying a frame in which normal straining, pure shearing, and rigid rotation can be distinguished is a key advantage of the normality-based decomposition. Kolář [15, 16] originally distinguished these motions by identifying a 'basic' reference frame in which pure shearing is extracted as a purely asymmetric tensor. While that approach typically produces results similar to the present normality-based decomposition, it requires solving a more challenging pointwise optimization problem that may yield non-unique solutions. Some related studies [17–21] analyze the normality properties of the VGT using its complex Schur form, which is triangular (as opposed to quasi-triangular). While that approach resembles our approach for locally non-rotational points, where the VGT has three real eigenvalues, it differs from our approach for locally rotational points, where the VGT has a pair of complex conjugate eigenvalues. In the latter case, the complex Schur form requires a complex transformation matrix that cannot be interpreted in physical space. Regardless of the differences in these approaches, the results produced by the original triple decomposition and the complex Schur form motivate and complement those produced by the present normality-based framework.

The flow statistics associated with the normality-based decomposition of the VGT concisely express key features of small-scale turbulence. For example, the strength of velocity gradients can be partitioned as

$$A^2 = A_{ij}A_{ij} = \underbrace{S^{\epsilon}_{ij}S^{\epsilon}_{ij}}_{S^2_{\epsilon}} + \overbrace{\underbrace{S^{\gamma}_{ij}S^{\gamma}_{ij}}_{S^2_{\gamma}} + \underbrace{\Omega^{\gamma}_{ij}\Omega^{\gamma}_{ij}}_{\Omega^2_{\gamma}}}^{A^2_{\gamma}} + \underbrace{\Omega^{\varphi}_{ij}\Omega^{\varphi}_{ij}}_{\Omega^2_{\varphi}} + \underbrace{2\Omega^{\varphi}_{ij}\Omega^{\gamma}_{ij}}_{\Omega^2_{\varphi\gamma}}, \tag{4.3}$$

where S^2_{ϵ}, A^2_{γ}, and Ω^2_{φ} represent the strengths of the constituents in (4.2), $\Omega^2_{\varphi\gamma}$ represents shear–rotation correlations, and $S^2_{\gamma} = \Omega^2_{\gamma} = \frac{1}{2}A^2_{\gamma}$. The relative contributions of S^2_{ϵ}, A^2_{γ}, and $\Omega^2_{\varphi} + \Omega^2_{\varphi\gamma}$ to A^2 can be expressed as exact algebraic functions of the normalized invariants of the VGT, whereas distinguishing the contributions of Ω^2_{φ} and $\Omega^2_{\varphi\gamma}$ requires an additional parameter [22]. An

averaged form of this partitioning can be expressed as

$$\left\langle A^2 \right\rangle = \left\langle S_\epsilon^2 \right\rangle + \underbrace{\left\langle S_\gamma^2 \right\rangle + \left\langle \Omega_\gamma^2 \right\rangle}_{\left\langle A_\gamma^2 \right\rangle} + \left\langle \Omega_\varphi^2 \right\rangle + \left\langle \Omega_{\varphi\gamma}^2 \right\rangle, \tag{4.4}$$

where $\langle(\cdot)\rangle$ denotes ensemble averaging. This averaged partitioning distinguishes the contributions of normal straining and shear straining to $\langle S^2 \rangle$ and the contributions of shear vorticity, rigid rotation, and their correlations to $\langle \Omega^2 \rangle$ [23]. Recent work has shown that, for a broad class of flows, it is expressive of various flow features and regimes that are obscured by the symmetry-based partitioning into $\langle S^2 \rangle$ and $\langle \Omega^2 \rangle$. For wall-bounded flows, Arun and Colonius [14] showed that it can distinguish between near-wall turbulence, which is dominated by shearing, and turbulence far from walls, which is more reminiscent of isotropic turbulence. Furthermore, Arun and Colonius [22] showed that it can distinguish between the initial, transitional, and turbulent regimes of a vortex ring collision. The normality-based analysis of that flow also identified enhanced shear–rotation correlations as an imprint of the elliptic instability that reflects relevant structural features of local streamlines.

Beyond statistical flow features, the normality-based decomposition can also distinguish tube-like vortical structures, which are associated with rigid rotation, from sheet-like vortical structures, which are associated with shear vorticity. This distinction underpins recently-developed vortex identification criteria that preferentially identify tubular vortical structures [24–26]. However, recent evidence highlights that shear layers are also critical to the structure and dynamics of small-scale turbulence [27–29]. The Burgers vortex layer forms a reasonable model for these (strained) small-scale shear layers, which typically have widths of $9\eta - 11\eta$ [12, 27, 30] and half-widths of 4.5η [28, 29], where η is the Kolmogorov scale. Interestingly, the typical diameters of intense vortex tubes at small scales, which are often modeled as Burgers vortex tubes, lie in a similar range [31, 32]. In Appendix 4.A1, we use the normality-based partitioning of Burgers vortex tubes and layers to illustrate how rigid rotation and shear vorticity are associated with vortex cores and shear layers, respectively.

Although vortex tubes and shear layers capture many essential features of Kolmogorov-scale flow structures, a complete 'recipe' for turbulence must effectively capture its *multiscale* structure. Therefore, motivated by the discussion in this section, the present study aims to characterize the structure of

isotropic turbulence in the subinertial and inertial ranges using the enhanced statistical and structural expressivity of the normality-based velocity gradient analysis.

4.1.2 Multiscale velocity gradients and interscale energy transfer

Spatial filtering frameworks enable tailored consideration of multiscale flow features by specifying a filter width, ℓ, that controls the range of resolved scales. They also facilitate insights into closure models for large-eddy simulation (LES), which are often formulated in terms of the filtered (i.e., resolved) flow field [8]. We denote filtered quantities as $\overline{(\cdot)}^{\ell} = G_\ell \star (\cdot)$, where G_ℓ represents the filter kernel and $\star$ represents the spatial convolution operator.

Applying a uniform filtering operation to the incompressible Navier–Stokes equations yields

$$\frac{\partial \overline{u}_i^\ell}{\partial t} + \overline{u}_j^\ell \frac{\partial \overline{u}_i^\ell}{\partial x_j} = -\frac{1}{\rho}\frac{\partial \overline{p}^\ell}{\partial x_i} + \nu \frac{\partial^2 \overline{u}_i^\ell}{\partial x_j^2} + \overline{f}_i^\ell - \frac{\partial \sigma_{ij}^\ell}{\partial x_j}, \quad \frac{\partial \overline{u}_i^\ell}{\partial x_i} = 0, \tag{4.5}$$

where ρ, ν, and p denote the density, kinematic viscosity, and pressure, respectively. The forcing, f_i, is typically designed to sustain the flow by injecting energy at large scales (e.g., in forced isotropic turbulence). The residual stress tensor, σ_{ij}^ℓ, represents the effective stress imposed on the resolved motions by the unresolved motions. It is the subject of closure models in LES [5] and plays a key role in the interpretation of interscale energy transfer. The kinetic energy equation associated with the filtered velocity field is given by

$$\frac{\partial E^\ell}{\partial t} + \frac{\partial T_i^\ell}{\partial x_i} = \overline{u}_i^\ell \overline{f}_i^\ell - \Pi^\ell - \Phi^\ell, \tag{4.6}$$

where $\partial T_i^\ell / \partial x_i$, $\overline{u}_i^\ell \overline{f}_i^\ell$, and $\Phi^\ell = 2\nu \overline{S}_{ij}^\ell \overline{S}_{ij}^\ell$ represent spatial redistribution, energy injected by the forcing, and the resolved dissipation rate, respectively. The term $\Pi^\ell = -\overline{S}_{ij}^\ell \sigma_{ij}^\ell$ represents the interscale energy transfer (or cascade rate) across scale ℓ. By convention, $\Pi^\ell > 0$ and $\Pi^\ell < 0$ correspond to downscale and upscale energy transfer, respectively. For incompressible flows, the isotropic part of σ_{ij}^ℓ does not contribute to interscale energy transfer since $\overline{S}_{ij}^\ell$ is traceless.

The filtering framework for interscale energy transfer has provided sustained insight into salient features of the energy cascade [33–36]. Recent studies have employed conditional averaging to identify a statistical imprint of small-scale

flow structures that contribute to forward energy transfer. Remarkably, in both isotropic [37] and shear [38] turbulence, this imprint manifests as a localized region of energy transfer located between hairpin-like vortical structures with opposite orientations. The filtering perspective of energy transfer has been extended to the settings of compressible turbulence [39] and magnetohydrodynamic turbulence [40–42], among others, and it has aided the development of global maps of energy transfer in the ocean [43, 44]. Beyond filtering, energy transfer can also be analyzed using a structure function approach, which is formulated in terms of the scale-integrated local Kolmogorov–Hill equation [45]. This approach provides a less ambiguous interpretation of upscale energy transfer (i.e., backscatter) than the filtering formulation. However, since both formulations typically produce similar results [46], we focus on the filtering framework as it provides pragmatic implications for LES modeling.

Recent work has begun to refine our understanding of interscale energy transfer by decomposing the VGT into contributions from normal straining, pure shearing, and rigid rotation. Enoki et al. [47] found that the interaction of shearing with the residual stresses dominates interscale energy transfer over a broad range of scales in isotropic turbulence. Using a different formulation, Fathali and Khoei [48] concluded that the contributions of shearing and normal straining dominate spectral energy transfer in isotropic turbulence. Both of these results were obtained by decomposing the velocity gradient term in the expressions used to represent interscale energy transfer. Enoki et al. [47] also decomposed the residual stress tensor based on contributions from the shearing and non-shearing velocity fields, which were identified using the Biot–Savart law. Beyond these studies, there remains a significant gap in our understanding of how interscale energy transfer at scale ℓ is influenced by flow features at smaller scales. We address this gap, which has significant implications for LES modeling, by analyzing multiscale contributions to the residual stress tensor using the normality-based decomposition of the VGT.

The present study utilizes Gaussian filtering, for which the filter kernel is given by

$$G_\ell(\boldsymbol{r}) = \frac{1}{\left(2\pi\ell^2\right)^{3/2}} \exp\left(-\frac{|\boldsymbol{r}|^2}{2\ell^2}\right), \quad \mathcal{F}\left\{G_\ell\right\}(\boldsymbol{k}) = \exp\left(-\frac{|\boldsymbol{k}|^2\ell^2}{2}\right), \tag{4.7}$$

where $\boldsymbol{r}$ and $\boldsymbol{k}$ represent the spatial offset and wavenumber vectors, respectively, and $\mathcal{F}\{\cdot\}$ represents the spatial Fourier transform. The Gaussian fil-

tering framework allows the residual stress tensor to be expressed in terms of multiscale velocity gradients as

$$\sigma_{ij}^{\ell} = \int_0^{\ell^2} \mathrm{d}\theta^2 \left(\overline{\overline{A}_{ik}^{\theta} \overline{A}_{jk}^{\theta}}^{\phi} \right), \tag{4.8}$$

where $\phi = \sqrt{\ell^2 - \theta^2}$. As discussed in detail by Johnson [49, 50], this expression is derived by treating the Gaussian-filtered velocity field as the solution to a diffusion equation where ℓ^2 represents a time-like variable. This formulation leads to a forced diffusion equation for the residual stress tensor, for which (4.8) is the formal solution. While we limit our attention to Gaussian filtering, the results we cite have been shown to be insensitive to the filter shape for non-negative filter kernels [49].

Using (4.8), a multiscale velocity gradient expansion for interscale energy transfer can be expressed as

$$\Pi^{\ell} = -\overline{S}_{ij}^{\ell} \int_0^{\ell^2} \mathrm{d}\theta^2 \left(\overline{\overline{A}_{ik}^{\theta} \overline{A}_{jk}^{\theta}}^{\phi} \right). \tag{4.9}$$

Following Johnson [49, 50], this expression can be decomposed in terms of familiar energy transfer mechanisms by inserting the symmetry-based decomposition of the VGT to obtain

$$\Pi^{\ell} = \Pi^{\ell,s} + \Pi^{\ell,\omega} + \Pi^{\ell,c}, \tag{4.10}$$

where

$$\Pi^{\ell,s} = -\overline{S}_{ij}^{\ell} \int_0^{\ell^2} \mathrm{d}\theta^2 \left(\overline{\overline{S}_{ik}^{\theta} \overline{S}_{jk}^{\theta}}^{\phi} \right), \tag{4.11}$$

$$\Pi^{\ell,\omega} = -\overline{S}_{ij}^{\ell} \int_0^{\ell^2} \mathrm{d}\theta^2 \left(\overline{\overline{\Omega}_{ik}^{\theta} \overline{\Omega}_{jk}^{\theta}}^{\phi} \right), \tag{4.12}$$

$$\Pi^{\ell,c} = -\overline{S}_{ij}^{\ell} \int_0^{\ell^2} \mathrm{d}\theta^2 \left(\overline{\overline{S}_{ik}^{\theta} \overline{\Omega}_{jk}^{\theta}}^{\phi} + \overline{\overline{\Omega}_{ik}^{\theta} \overline{S}_{jk}^{\theta}}^{\phi} \right). \tag{4.13}$$

Here, $\Pi^{\ell,s}$, $\Pi^{\ell,\omega}$, and $\Pi^{\ell,c}$ represent the contributions of strain self-amplification, vortex stretching, and strain–vorticity covariance at scales $\theta \leq \ell$ to the interscale energy transfer at scale ℓ. These terms can be further decomposed as

$$\Pi^{\ell,s} = \Pi^{\ell,s1} + \Pi^{\ell,s2}, \tag{4.14}$$

$$\Pi^{\ell,\omega} = \Pi^{\ell,\omega 1} + \Pi^{\ell,\omega 2}, \tag{4.15}$$

$$\Pi^{\ell,c} = \Pi^{\ell,c1} + \Pi^{\ell,c2}, \tag{4.16}$$

where terms with superscripts of $(\cdot)^1$ and $(\cdot)^2$ represent scale-local and scale-nonlocal contributions, respectively. These contributions are given by

$$\Pi^{\ell,s1} = -\ell^2 \overline{S}^\ell_{ij} \overline{S}^\ell_{ik} \overline{S}^\ell_{jk}, \qquad \Pi^{\ell,s2} = \Pi^{\ell,s} - \Pi^{\ell,s1}, \tag{4.17}$$

$$\Pi^{\ell,\omega 1} = -\ell^2 \overline{S}^\ell_{ij} \overline{\Omega}^\ell_{ik} \overline{\Omega}^\ell_{jk}, \qquad \Pi^{\ell,\omega 2} = \Pi^{\ell,\omega} - \Pi^{\ell,\omega 1}, \tag{4.18}$$

$$\Pi^{\ell,c1} = -\ell^2 \overline{S}^\ell_{ij} \left(\overline{S}^\ell_{ik} \overline{\Omega}^\ell_{jk} + \overline{\Omega}^\ell_{ik} \overline{S}^\ell_{jk} \right) = 0, \quad \Pi^{\ell,c2} = \Pi^{\ell,c} - \Pi^{\ell,c1} = \Pi^{\ell,c}, \tag{4.19}$$

and the scale-nonlocal contributions can equivalently be expressed using scale-space integrals of generalized second moments of velocity gradient fields [49, 50]. The scale-local strain–vorticity covariance term vanishes since it can be expressed as the contraction of symmetric tensors with antisymmetric tensors. Therefore, only strain self-amplification and vortex stretching contribute to scale-local energy transfer, and their combined contribution resembles that produced by the nonlinear gradient model for the residual stress tensor [5, 34, 51].

The resulting decomposition of interscale energy transfer,

$$\Pi^\ell = \Pi^{\ell,s1} + \Pi^{\ell,\omega 1} + \Pi^{\ell,s2} + \Pi^{\ell,\omega 2} + \Pi^{\ell,c}, \tag{4.20}$$

provides insight into mechanisms underlying the energy cascade. As shown in Figure 4.1(a), the relative contributions of the constituents are approximately $\left\langle \Pi^{\ell,s1} \right\rangle : \left\langle \Pi^{\ell,\omega 1} \right\rangle : \left\langle \Pi^{\ell,s2} \right\rangle : \left\langle \Pi^{\ell,\omega 2} \right\rangle : \left\langle \Pi^{\ell,c} \right\rangle \approx 3 : 1 : 2 : 2 : 0$ in the inertial range for isotropic turbulence [49, 50]. The implication that $\left\langle \Pi^{\ell,s} \right\rangle : \left\langle \Pi^{\ell,\omega} \right\rangle = 5 : 3$ supports the claim that strain self-amplification contributes more to the cascade than vortex stretching, extending prior results that focused on single-scale contributions [46]. While the covariance term, $\Pi^{\ell,c}$, has a negligible net contribution in the inertial range of the cascade, it produces significant upscale energy transfer (i.e., backscatter) in the subinertial range. This feature bears resemblance to two-dimensional turbulence, where the covariance term is responsible for the inverse cascade [50].

This backscatter occurs at scales that coincide with the bottleneck effect in the subinertial range of the cascade. As shown in Figure 4.1(b), the bottleneck effect in direct numerical simulation (DNS) manifests as a bump in the energy spectrum that exceeds the $k^{-5/3}$ scaling from the inertial range, where $k = |\boldsymbol{k}|$. This spectral bump is centered around $k\eta \approx 0.13$ and, while its location and width are relatively insensitive to Re_λ, its height decreases with increasing Re_λ [52]. There have been various interpretations of the bottleneck effect,

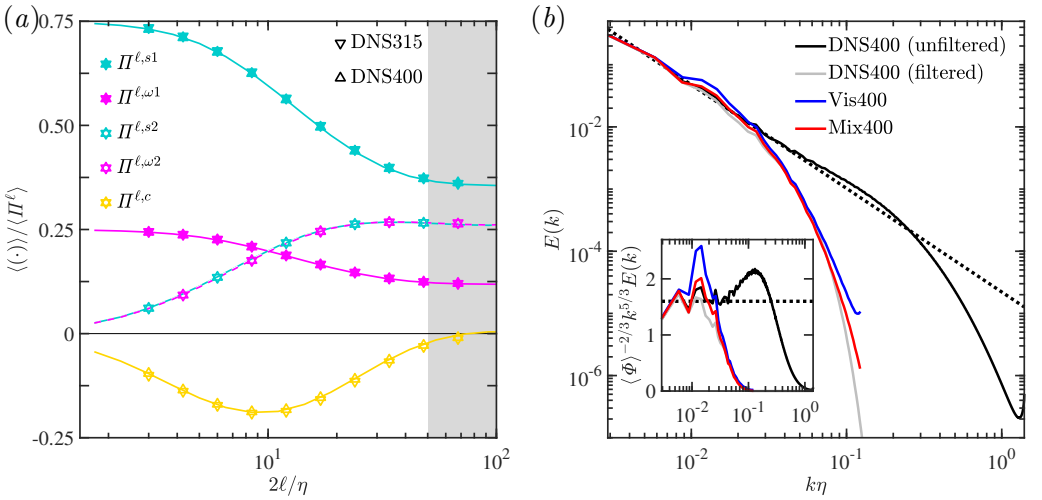

Figure 4.1: (a) Symmetry-based scale-local and scale-nonlocal contributions to interscale energy transfer in forced isotropic turbulence. The symbols represent DNS datasets at Taylor-scale Reynolds numbers of $Re_\lambda \approx 315$ (DNS315) and $Re_\lambda \approx 400$ (DNS400) and the curves represent the $Re_\lambda \approx 400$ results of Johnson [49, 50]. The shaded region captures the bottom of the inertial range for DNS400. (b) Energy spectra for the unfiltered and filtered velocity fields in DNS400 as well as LES cases that employ eddy viscosity (Vis400) and mixed (Mix400) models at $Re_\lambda \approx 400$. The filtered DNS and LES cases employ a filter width of $2\ell/\eta = 48$. The dotted line represents the inertial range scaling, $E(k) = 1.6\,\langle\Phi\rangle^{2/3}\,k^{-5/3}$, and the inset depicts a linear–log plot of the compensated energy spectra. Technical details of the simulations are described in §4.3.

including as a result of quenched local interactions due to viscous effects [53], helicity dynamics [54], incomplete thermalization [55], and insufficient width of the inertial range [56]. More recently, inspired by the backscatter produced by $\Pi^{\ell,c}$ in two-dimensional turbulence, Johnson [50] proposed vortex thinning [57–59] as a plausible mechanism responsible for the subinertial bottleneck effect in three-dimensional turbulence. Despite significant attention, a complete understanding of the origins of the bottleneck effect remains elusive. The present study aims to clarify its structural and statistical imprints using our normality-based analysis of filtered velocity gradients.

While the bottleneck effect is an expected feature of a fully-resolved DNS, it is mitigated when the flow field is filtered at scales typically employed for LES (e.g., $2\ell/\eta = 48$). However, as shown in Figure 4.1(b), the dynamic eddy viscosity model introduced by Kamal and Johnson [60] produces a significant 'artificial' bottleneck effect at scales that are larger than the LES filter scale

and, thus, larger than the scales associated with the true bottleneck effect. By contrast, the dynamic mixed model introduced by Kamal and Johnson [60], which synthesizes the nonlinear gradient model with an eddy viscosity model, mitigates this artificial bottleneck to more accurately represent the spectrum of the corresponding filtered DNS. These results reflect that, while the scale-nonlocal terms in (4.20) are reasonably modeled by eddy viscosity physics, explicitly capturing the scale-local terms, which are associated with the nonlinear gradient model, produces more realistic energy transfer. Statistical analyses more broadly suggest that eddy viscosity and mixed models tend to replicate flow features associated with unfiltered and filtered DNS data, respectively [60, 61]. Further, preliminary two-dimensional visualizations suggest that the unfiltered DNS and eddy viscosity model LES cases produce sheet-like vorticity structures that are not observed in the filtered DNS and mixed model LES cases [60]. In the present study, our normality-based velocity gradient analysis definitively links these observations and captures their relationship to the artificial bottleneck effect.

4.1.3 Contributions

Motivated by the preceding discussion, the present study aims to refine our understanding of multiscale flow structures and energy transfer mechanisms in turbulent flows. In §4.2, we formulate the normality-based analysis of filtered velocity gradients and use it to develop a novel decomposition of interscale energy transfer. We apply this normality-based analysis to filtered velocity gradients obtained from DNS and LES data that represent forced isotropic turbulence. The technical details of these simulations are described in §4.3. The results of our analysis are presented in §4.4, including identifying the effect of filtering and LES modeling on the velocity gradient partitioning (§4.4.1), vortical flow structures (§4.4.2), and interscale energy transfer (§4.4.3). Finally, we summarize the implications of these results for energy cascade physics, LES modeling, and future prospects in §4.5.

4.2 Theoretical framework

The analysis described in §4.1.1 can be reformulated in a multiscale setting by applying it to filtered velocity gradients. The corresponding normality-based decomposition of the filtered VGT can be expressed as

$$\overline{A}_{ij}^{\ell} = \overline{S}_{ij}^{\ell,\epsilon} + \overline{A}_{ij}^{\ell,\gamma} + \overline{\Omega}_{ij}^{\ell,\varphi}, \tag{4.21}$$

where the order of the superscripts indicates that filtering is performed *prior* to the decomposition. The order of these operations is important since, unlike the symmetry-based decomposition, the normality-based decomposition does not commute with the filtering operation. We choose to decompose the filtered velocity gradients since this approach retains the normality properties of each tensor in the decomposition. It also enables consistent analysis of LES data, for which only the resolved (i.e., filtered) flow field is available. Using this filtering-first approach, the normality-based partitioning of the filtered velocity gradients can be expressed as

$$A_\ell^2 = \overline{A}_{ij}^\ell \overline{A}_{ij}^\ell = \underbrace{\overline{S}_{ij}^{\ell,\epsilon}\overline{S}_{ij}^{\ell,\epsilon}}_{S_{\ell,\epsilon}^2} + \overbrace{\underbrace{\overline{S}_{ij}^{\ell,\gamma}\overline{S}_{ij}^{\ell,\gamma}}_{S_{\ell,\gamma}^2} + \underbrace{\overline{\Omega}_{ij}^{\ell,\gamma}\overline{\Omega}_{ij}^{\ell,\gamma}}_{\Omega_{\ell,\gamma}^2}}^{A_{\ell,\gamma}^2} + \underbrace{\overline{\Omega}_{ij}^{\ell,\varphi}\overline{\Omega}_{ij}^{\ell,\varphi}}_{\Omega_{\ell,\varphi}^2} + \underbrace{2\overline{\Omega}_{ij}^{\ell,\varphi}\overline{\Omega}_{ij}^{\ell,\gamma}}_{\Omega_{\ell,\varphi\gamma}^2}, \tag{4.22}$$

where $S_{\ell,\gamma}^2 = \Omega_{\ell,\gamma}^2 = \frac{1}{2}A_{\ell,\gamma}^2$.

The normality-based decomposition of the filtered VGT can also be applied to the multiscale velocity gradient expansions of the residual stress tensor and interscale energy transfer discussed in §4.1.2. Previous studies employing related approaches have primarily decomposed terms analogous to $\overline{S}_{ij}^\ell$ in the expression, $\mathit{\Pi}^\ell = -\overline{S}_{ij}^\ell \sigma_{ij}^\ell$, for interscale energy transfer [47, 48]. The analysis of Enoki et al. [47] briefly considered the residual stress tensor using the Biot–Savart law, but it did not address its multiscale composition and did not employ a filtering-first framework. Therefore, the following normality-based formulation of interscale energy transfer provides novel insight by explicitly capturing multiscale contributions to the residual stress tensor in a manner amenable to the assessment and development of LES models.

When applied to the expression in (4.9), the normality-based decomposition of interscale energy transfer yields

$$\mathit{\Pi}^\ell = \mathit{\Pi}_{\epsilon\epsilon}^\ell + \mathit{\Pi}_{\varphi\varphi}^\ell + \mathit{\Pi}_{\gamma\gamma}^\ell + \mathit{\Pi}_{\epsilon\gamma}^\ell + \mathit{\Pi}_{\varphi\gamma}^\ell, \tag{4.23}$$

where

$$\mathit{\Pi}_{\epsilon\epsilon}^\ell = -\overline{S}_{ij}^\ell \int_0^{\ell^2} \mathrm{d}\theta^2 \left(\overline{\overline{S}_{ik}^{\theta,\epsilon}\overline{S}_{jk}^{\theta,\epsilon}}^{\phi} \right), \tag{4.24}$$

$$\mathit{\Pi}_{\varphi\varphi}^\ell = -\overline{S}_{ij}^\ell \int_0^{\ell^2} \mathrm{d}\theta^2 \left(\overline{\overline{\Omega}_{ik}^{\theta,\varphi}\overline{\Omega}_{jk}^{\theta,\varphi}}^{\phi} \right), \tag{4.25}$$

$$\Pi^{\ell}_{\gamma\gamma} = -\overline{S}^{\ell}_{ij} \int_0^{\ell^2} \mathrm{d}\theta^2 \left(\overline{\overline{A}^{\theta,\gamma}_{ik} \overline{A}^{\theta,\gamma}_{jk}}^{\phi} \right), \tag{4.26}$$

$$\Pi^{\ell}_{\epsilon\gamma} = -\overline{S}^{\ell}_{ij} \int_0^{\ell^2} \mathrm{d}\theta^2 \left(\overline{\overline{S}^{\theta,\epsilon}_{ik} \overline{A}^{\theta,\gamma}_{jk}}^{\phi} + \overline{\overline{A}^{\theta,\gamma}_{ik} \overline{S}^{\theta,\epsilon}_{jk}}^{\phi} \right), \tag{4.27}$$

$$\Pi^{\ell}_{\varphi\gamma} = -\overline{S}^{\ell}_{ij} \int_0^{\ell^2} \mathrm{d}\theta^2 \left(\overline{\overline{\Omega}^{\theta,\varphi}_{ik} \overline{A}^{\theta,\gamma}_{jk}}^{\phi} + \overline{\overline{A}^{\theta,\gamma}_{ik} \overline{\Omega}^{\theta,\varphi}_{jk}}^{\phi} \right), \tag{4.28}$$

and $\phi = \sqrt{\ell^2 - \theta^2}$. Here, $\Pi^{\ell}_{\epsilon\epsilon}$, $\Pi^{\ell}_{\varphi\varphi}$, and $\Pi^{\ell}_{\gamma\gamma}$ represent contributions from normal straining, rigid rotation, and pure shearing, respectively, at scales $\theta \leq \ell$. Similarly, $\Pi^{\ell}_{\epsilon\gamma}$ and $\Pi^{\ell}_{\varphi\gamma}$ represent contributions from the covariance of normal straining with pure shearing and the covariance of rigid rotation with pure shearing, respectively, at these scales.

The normality-based approach can also be used to refine the symmetry-based analysis of interscale energy transfer discussed in §4.1.2. The cascade rates associated with strain self-amplification, vortex stretching, and strain–vorticity covariance, as defined in (4.11), (4.12), and (4.13), respectively, can be decomposed as

$$\Pi^{\ell,s} = \Pi^{\ell,s}_{\epsilon\epsilon} + \Pi^{\ell,s}_{\gamma\gamma} + \Pi^{\ell,s}_{\epsilon\gamma}, \tag{4.29}$$

$$\Pi^{\ell,\omega} = \Pi^{\ell,\omega}_{\varphi\varphi} + \Pi^{\ell,\omega}_{\gamma\gamma} + \Pi^{\ell,\omega}_{\varphi\gamma}, \tag{4.30}$$

$$\Pi^{\ell,c} = \Pi^{\ell,c}_{\epsilon\gamma} + \Pi^{\ell,c}_{\gamma\gamma} + \Pi^{\ell,c}_{\varphi\gamma}, \tag{4.31}$$

respectively. The strain self-amplification terms in (4.29), defined as

$$\Pi^{\ell,s}_{\epsilon\epsilon} = -\overline{S}^{\ell}_{ij} \int_0^{\ell^2} \mathrm{d}\theta^2 \left(\overline{\overline{S}^{\theta,\epsilon}_{ik} \overline{S}^{\theta,\epsilon}_{jk}}^{\phi} \right), \tag{4.32}$$

$$\Pi^{\ell,s}_{\gamma\gamma} = -\overline{S}^{\ell}_{ij} \int_0^{\ell^2} \mathrm{d}\theta^2 \left(\overline{\overline{S}^{\theta,\gamma}_{ik} \overline{S}^{\theta,\gamma}_{jk}}^{\phi} \right), \tag{4.33}$$

$$\Pi^{\ell,s}_{\epsilon\gamma} = -\overline{S}^{\ell}_{ij} \int_0^{\ell^2} \mathrm{d}\theta^2 \left(\overline{\overline{S}^{\theta,\epsilon}_{ik} \overline{S}^{\theta,\gamma}_{jk}}^{\phi} + \overline{\overline{S}^{\theta,\gamma}_{ik} \overline{S}^{\theta,\epsilon}_{jk}}^{\phi} \right), \tag{4.34}$$

represent the contributions associated with normal straining, shear straining, and their covariance, respectively, at scales $\theta \leq \ell$. The vortex stretching terms in (4.30), defined as

$$\Pi^{\ell,\omega}_{\varphi\varphi} = -\overline{S}^{\ell}_{ij} \int_0^{\ell^2} \mathrm{d}\theta^2 \left(\overline{\overline{\Omega}^{\theta,\varphi}_{ik} \overline{\Omega}^{\theta,\varphi}_{jk}}^{\phi} \right), \tag{4.35}$$

$$\Pi^{\ell,\omega}_{\gamma\gamma} = -\overline{S}^{\ell}_{ij} \int_0^{\ell^2} \mathrm{d}\theta^2 \left(\overline{\overline{\Omega}^{\theta,\gamma}_{ik} \overline{\Omega}^{\theta,\gamma}_{jk}}^{\phi} \right), \tag{4.36}$$

$$\Pi^{\ell,\omega}_{\varphi\gamma} = -\overline{S}^{\ell}_{ij} \int_0^{\ell^2} \mathrm{d}\theta^2 \left(\overline{\overline{\Omega}^{\theta,\varphi}_{ik} \overline{\Omega}^{\theta,\gamma}_{jk}}^{\phi} + \overline{\overline{\Omega}^{\theta,\gamma}_{ik} \overline{\Omega}^{\theta,\varphi}_{jk}}^{\phi} \right), \tag{4.37}$$

represent the contributions associated with rigid rotation, shear vorticity, and their covariance, respectively, at scales $\theta \leq \ell$. The strain–vorticity covariance terms in (4.31), defined as

$$\Pi^{\ell,c}_{\epsilon\gamma} = -\overline{S}^{\ell}_{ij} \int_0^{\ell^2} \mathrm{d}\theta^2 \left(\overline{\overline{S}^{\theta,\epsilon}_{ik} \overline{\Omega}^{\theta,\gamma}_{jk}}^{\phi} + \overline{\overline{\Omega}^{\theta,\gamma}_{ik} \overline{S}^{\theta,\epsilon}_{jk}}^{\phi} \right), \tag{4.38}$$

$$\Pi^{\ell,c}_{\gamma\gamma} = -\overline{S}^{\ell}_{ij} \int_0^{\ell^2} \mathrm{d}\theta^2 \left(\overline{\overline{S}^{\theta,\gamma}_{ik} \overline{\Omega}^{\theta,\gamma}_{jk}}^{\phi} + \overline{\overline{\Omega}^{\theta,\gamma}_{ik} \overline{S}^{\theta,\gamma}_{jk}}^{\phi} \right), \tag{4.39}$$

$$\Pi^{\ell,c}_{\varphi\gamma} = -\overline{S}^{\ell}_{ij} \int_0^{\ell^2} \mathrm{d}\theta^2 \left(\overline{\overline{S}^{\theta,\gamma}_{ik} \overline{\Omega}^{\theta,\varphi}_{jk}}^{\phi} + \overline{\overline{\Omega}^{\theta,\varphi}_{ik} \overline{S}^{\theta,\gamma}_{jk}}^{\phi} \right), \tag{4.40}$$

represent the contributions associated with the covariance of normal straining with shear vorticity, the covariance of shear straining with shear vorticity, and the covariance of shear straining with rigid rotation, respectively, at scales $\theta \leq \ell$. Using the form of the VGT in (4.2), it can be shown that the analogous covariance term associated with normal straining and rigid rotation is identically zero. The contributions from the terms in (4.29), (4.30), and (4.31) can be used to reconstruct the terms in (4.23) as

$$\Pi^{\ell}_{\epsilon\epsilon} = \Pi^{\ell,s}_{\epsilon\epsilon}, \tag{4.41}$$

$$\Pi^{\ell}_{\varphi\varphi} = \Pi^{\ell,\omega}_{\varphi\varphi}, \tag{4.42}$$

$$\Pi^{\ell}_{\gamma\gamma} = \Pi^{\ell,s}_{\gamma\gamma} + \Pi^{\ell,\omega}_{\gamma\gamma} + \Pi^{\ell,c}_{\gamma\gamma}, \tag{4.43}$$

$$\Pi^{\ell}_{\epsilon\gamma} = \Pi^{\ell,s}_{\epsilon\gamma} + \Pi^{\ell,c}_{\epsilon\gamma}, \tag{4.44}$$

$$\Pi^{\ell}_{\varphi\gamma} = \Pi^{\ell,\omega}_{\varphi\gamma} + \Pi^{\ell,c}_{\varphi\gamma}. \tag{4.45}$$

A further refinement can be obtained by identifying scale-local and scale-nonlocal contributions to the strain self-amplification terms in (4.29) and the vortex stretching terms in (4.30) as

$$\Pi^{\ell,s}_{\epsilon\epsilon} = \Pi^{\ell,s1}_{\epsilon\epsilon} + \Pi^{\ell,s2}_{\epsilon\epsilon}, \quad \Pi^{\ell,s}_{\gamma\gamma} = \Pi^{\ell,s1}_{\gamma\gamma} + \Pi^{\ell,s2}_{\gamma\gamma}, \quad \Pi^{\ell,s}_{\epsilon\gamma} = \Pi^{\ell,s1}_{\epsilon\gamma} + \Pi^{\ell,s2}_{\epsilon\gamma}, \tag{4.46}$$

$$\Pi^{\ell,\omega}_{\varphi\varphi} = \Pi^{\ell,\omega1}_{\varphi\varphi} + \Pi^{\ell,\omega2}_{\varphi\varphi}, \quad \Pi^{\ell,\omega}_{\gamma\gamma} = \Pi^{\ell,\omega1}_{\gamma\gamma} + \Pi^{\ell,\omega2}_{\gamma\gamma}, \quad \Pi^{\ell,\omega}_{\varphi\gamma} = \Pi^{\ell,\omega1}_{\varphi\gamma} + \Pi^{\ell,\omega2}_{\varphi\gamma}, \tag{4.47}$$

respectively. We do not identify scale-local and scale-nonlocal contributions to the strain–vorticity covariance decomposition in (4.31) since, as expressed in (4.19), the scale-local contributions identically sum to zero. The scale-local terms in (4.46) and (4.47) contribute to scale-local strain self-amplification

and vortex stretching as

$$\Pi^{\ell,s1} = \underbrace{-\ell^2\overline{S}^{\ell}_{ij}\overline{S}^{\ell,\epsilon}_{ik}\overline{S}^{\ell,\epsilon}_{jk}}_{\Pi^{\ell,s1}_{\epsilon\epsilon}} \underbrace{-\ell^2\overline{S}^{\ell}_{ij}\overline{S}^{\ell,\gamma}_{ik}\overline{S}^{\ell,\gamma}_{jk}}_{\Pi^{\ell,s1}_{\gamma\gamma}} \underbrace{-2\ell^2\overline{S}^{\ell}_{ij}\overline{S}^{\ell,\epsilon}_{ik}\overline{S}^{\ell,\gamma}_{jk}}_{\Pi^{\ell,s1}_{\epsilon\gamma}}, \tag{4.48}$$

$$\Pi^{\ell,\omega 1} = \underbrace{-\ell^2\overline{S}^{\ell}_{ij}\overline{\Omega}^{\ell,\varphi}_{ik}\overline{\Omega}^{\ell,\varphi}_{jk}}_{\Pi^{\ell,\omega 1}_{\varphi\varphi}} \underbrace{-\ell^2\overline{S}^{\ell}_{ij}\overline{\Omega}^{\ell,\gamma}_{ik}\overline{\Omega}^{\ell,\gamma}_{jk}}_{\Pi^{\ell,\omega 1}_{\gamma\gamma}} \underbrace{-2\ell^2\overline{S}^{\ell}_{ij}\overline{\Omega}^{\ell,\varphi}_{ik}\overline{\Omega}^{\ell,\gamma}_{jk}}_{\Pi^{\ell,\omega 1}_{\varphi\gamma}}, \tag{4.49}$$

respectively. Here, the leading strain-rate tensor, $\overline{S}^{\ell}_{ij}$, is not decomposed since the normality-based analysis is applied to the multiscale velocity gradient expansion of the residual stress tensor. However, the mechanisms underlying scale-local strain self-amplification and vortex stretching can be more clearly expressed by further decomposing $\overline{S}^{\ell}_{ij}$, which leads to

$$\Pi^{\ell,s1} = \underbrace{-\ell^2\overline{S}^{\ell,\epsilon}_{ij}\overline{S}^{\ell,\epsilon}_{ik}\overline{S}^{\ell,\epsilon}_{jk}}_{\Pi^{\ell,s1}_{\epsilon\epsilon\epsilon}} \underbrace{-3\ell^2\overline{S}^{\ell,\epsilon}_{ij}\overline{S}^{\ell,\gamma}_{ik}\overline{S}^{\ell,\gamma}_{jk}}_{\Pi^{\ell,s1}_{\epsilon\gamma\gamma}} \underbrace{-\ell^2\overline{S}^{\ell,\gamma}_{ij}\overline{S}^{\ell,\gamma}_{ik}\overline{S}^{\ell,\gamma}_{jk}}_{\Pi^{\ell,s1}_{\gamma\gamma\gamma}}, \tag{4.50}$$

$$\Pi^{\ell,\omega 1} = \underbrace{-\ell^2\overline{S}^{\ell,\epsilon}_{ij}\overline{\Omega}^{\ell,\varphi}_{ik}\overline{\Omega}^{\ell,\varphi}_{jk}}_{\Pi^{\ell,\omega 1}_{\epsilon\varphi\varphi}} \underbrace{-\ell^2\overline{S}^{\ell,\epsilon}_{ij}\overline{\Omega}^{\ell,\gamma}_{ik}\overline{\Omega}^{\ell,\gamma}_{jk}}_{\Pi^{\ell,\omega 1}_{\epsilon\gamma\gamma}} \underbrace{-\ell^2\overline{S}^{\ell,\gamma}_{ij}\overline{\Omega}^{\ell,\gamma}_{ik}\overline{\Omega}^{\ell,\gamma}_{jk}}_{\Pi^{\ell,\omega 1}_{\gamma\gamma\gamma}} \underbrace{-2\ell^2\overline{S}^{\ell,\epsilon}_{ij}\overline{\Omega}^{\ell,\varphi}_{ik}\overline{\Omega}^{\ell,\gamma}_{jk}}_{\Pi^{\ell,\omega 1}_{\epsilon\varphi\gamma}}. \tag{4.51}$$

These terms are related to those in (4.48) and (4.49) in that

$$\Pi^{\ell,s1}_{\epsilon\epsilon} = \Pi^{\ell,s1}_{\epsilon\epsilon\epsilon}, \quad \Pi^{\ell,s1}_{\gamma\gamma} = \Pi^{\ell,s1}_{\gamma\gamma\gamma} + \frac{1}{3}\Pi^{\ell,s1}_{\epsilon\gamma\gamma}, \quad \Pi^{\ell,s1}_{\epsilon\gamma} = \frac{2}{3}\Pi^{\ell,s1}_{\epsilon\gamma\gamma}, \tag{4.52}$$

$$\Pi^{\ell,\omega 1}_{\varphi\varphi} = \Pi^{\ell,\omega 1}_{\epsilon\varphi\varphi}, \quad \Pi^{\ell,\omega 1}_{\gamma\gamma} = \Pi^{\ell,\omega 1}_{\gamma\gamma\gamma} + \Pi^{\ell,\omega 1}_{\epsilon\gamma\gamma}, \quad \Pi^{\ell,\omega 1}_{\varphi\gamma} = \Pi^{\ell,\omega 1}_{\epsilon\varphi\gamma}. \tag{4.53}$$

In (4.50), $\Pi^{\ell,s1}_{\epsilon\epsilon\epsilon}$, $\Pi^{\ell,s1}_{\gamma\gamma\gamma}$, and $\Pi^{\ell,s1}_{\epsilon\gamma\gamma}$ represent scale-local strain self-amplification due to normal straining, shear straining, and their interaction, respectively. In (4.51), $\Pi^{\ell,\omega 1}_{\epsilon\varphi\varphi}$, $\Pi^{\ell,\omega 1}_{\epsilon\gamma\gamma}$, and $\Pi^{\ell,\omega 1}_{\epsilon\varphi\gamma}$ represent scale-local vortex stretching due to the normal straining of rigid rotation, shear vorticity, and shear–rotation interactions, respectively, and $\Pi^{\ell,\omega 1}_{\gamma\gamma\gamma}$ is due to the shear straining of shear vorticity. Using the VGT in the principal frame, as expressed in (4.2), it can be shown that all terms omitted from these equations, including the $\Pi^{\ell,s1}_{\epsilon\epsilon\gamma}$ term in (4.50) and the $\Pi^{\ell,\omega 1}_{\gamma\varphi\varphi}$ and $\Pi^{\ell,\omega 1}_{\gamma\varphi\gamma}$ terms in (4.51), are identically zero. It can also be shown that $\Pi^{\ell,s1}_{\epsilon\gamma\gamma} = 3\Pi^{\ell,\omega 1}_{\epsilon\gamma\gamma}$ and $\Pi^{\ell,s1}_{\gamma\gamma\gamma} = 3\Pi^{\ell,\omega 1}_{\gamma\gamma\gamma}$ hold as exact pointwise relationships. When combined with the fact that $\left\langle \Pi^{\ell,s1} \right\rangle = 3\left\langle \Pi^{\ell,\omega 1} \right\rangle$ for homogeneous turbulence [62], these relationships imply that the relative contributions of the shear straining terms, $\Pi^{\ell,s1}_{\epsilon\gamma\gamma}$ and $\Pi^{\ell,s1}_{\gamma\gamma\gamma}$, to $\left\langle \Pi^{\ell,s1} \right\rangle$ are

Case	Type	Model	Reynolds number	Resolution	Reference
DNS315	DNS	–	$Re_\lambda \approx 315$	$k_{max}\eta \approx 2.0$	Cardesa et al. [63]
DNS400	DNS	–	$Re_\lambda \approx 400$	$k_{max}\eta \approx 1.4$	Kamal and Johnson [60]
Vis400	LES	Eddy viscosity	$Re_\lambda \approx 400$	$k_{max}\ell_{LES} \approx 3.0$	Kamal and Johnson [60]
Mix400	LES	Mixed	$Re_\lambda \approx 400$	$k_{max}\ell_{LES} \approx 3.0$	Kamal and Johnson [60]

Table 4.1: Primary simulations considered in the present study. The DNS cases employ $N_x^3 = 1024^3$ collocation points and are dealiased using the $2\sqrt{2}/3$ truncation rule with phase-shifting [64] such that $k_{max} = N_x\sqrt{2}/3$. The LES cases employ $N_x^3 = 128^3$ collocation points and filter widths of $2\ell_{LES}/\eta = 48$. They are dealiased using the 2/3 truncation rule such that $k_{max} = N_x/3$. Additional cases, including random velocity gradients, DNS cases at lower Reynolds numbers, and LES cases with different filter widths are described and analyzed in Appendix 4.A2.

equivalent to the relative contributions of the shear vorticity terms, $\Pi^{\ell,\omega 1}_{\epsilon\gamma\gamma}$ and $\Pi^{\ell,\omega 1}_{\gamma\gamma\gamma}$, to $\left\langle \Pi^{\ell,\omega 1} \right\rangle$ in the absence of inhomogeneities. This, in turn, implies that the relative contribution of the normal straining term, $\Pi^{\ell,s1}_{\epsilon\epsilon\epsilon}$, to $\left\langle \Pi^{\ell,s1} \right\rangle$ is equivalent to the relative contribution of the rigid rotation terms, $\Pi^{\ell,\omega 1}_{\epsilon\varphi\varphi} + \Pi^{\ell,\omega 1}_{\epsilon\varphi\gamma}$, to $\left\langle \Pi^{\ell,\omega 1} \right\rangle$. These relationships typify insights that can be garnered from the present normality-based formulation of interscale energy transfer.

4.3 Simulation details

We apply the multiscale normality-based analysis formulated in §4.2 to filtered velocity gradients produced by simulations of forced isotropic turbulence. All simulations solve the incompressible Navier–Stokes equations a triply-periodic box using pseudo-spectral methods. Table 4.1 summarizes the primary cases we consider, which include DNS cases at two different Reynolds numbers and LES cases that employ two different models at the higher Reynolds number. The references for these simulations further expound their numerical implementations, forcing schemes, and other relevant parameters and results. Each DNS dataset includes 21 temporal snapshots that are spaced one large-eddy turnover time apart and each LES dataset includes 68 temporal snapshots that are spaced half of a large-eddy turnover time apart. All snapshots are obtained from a statistically stationary regime (i.e., after initial transients).

For the LES cases, the eddy viscosity model (Vis400) and the mixed model (Mix400) were formulated and discussed by Kamal and Johnson [60] using the Stokes flow regularization (SFR) framework [61]. They are dynamic models

that assume local equilibrium for the residual kinetic energy and employ local clipping of the eddy viscosity to satisfy this assumption. We utilize these SFR-based models since they do not require the specification of a free model parameter and do not require test filter calculations. However, since they perform similarly to other formulations [60], we do not expect our insights to be limited to the SFR-based approach.

For the eddy viscosity model, the residual stress tensor at the LES filter scale, $\ell = \ell_{LES}$, is modeled as

$$\sigma_{ij}^{\ell} = -2\nu_T \overline{S}_{ij}^{\ell}, \tag{4.54}$$

where the eddy viscosity, ν_T, is the solution to

$$\nu_T = \frac{3\ell^2}{4}\left(\nabla^2\nu_T - \frac{\overline{S}_{ij}^{\ell}\overline{A}_{ik}^{\ell}\overline{A}_{jk}^{\ell}}{S_{\ell}^2}\right). \tag{4.55}$$

Therefore, the interscale energy transfer at the LES filter scale is modeled as

$$\Pi^{\ell} = 2\nu_T S_{\ell}^2. \tag{4.56}$$

For the mixed model, the residual stress tensor at the LES filter scale is modeled as

$$\sigma_{ij}^{\ell} = \ell^2 \overline{A}_{ik}^{\ell}\overline{A}_{jk}^{\ell} - 2\nu_T \overline{S}_{ij}^{\ell}. \tag{4.57}$$

The first term in this model resembles the nonlinear gradient model [5, 34, 51]. Only its deviatoric part is relevant since its isotropic part, which can be lumped with pressure in the momentum equations, does not contribute to the dynamics of the resolved velocity field. The second term in (4.57) resembles an eddy viscosity model, for which ν_T is the solution to

$$\nu_T = \frac{3\ell^2}{4}\left(\nabla^2\nu_T - \ell^2\frac{\overline{S}_{ij}^{\ell}\overline{B}_{imn}^{\ell}\overline{B}_{jmn}^{\ell}}{S_{\ell}^2}\right), \tag{4.58}$$

where $B_{ijk} = \partial^2 u_i/\partial x_j \partial x_k$ is the velocity Hessian tensor. The corresponding interscale energy transfer at the LES filter scale is modeled as

$$\Pi^{\ell} = -\ell^2 \overline{S}_{ij}^{\ell}\overline{A}_{ik}^{\ell}\overline{A}_{jk}^{\ell} + 2\nu_T S_{\ell}^2. \tag{4.59}$$

Here, the first term explicitly captures the contributions from scale-local vortex stretching and strain self-amplification (i.e., $\Pi^{\ell,s1} + \Pi^{\ell,\omega 1}$) and the second term models the residual contribution from the scale-nonlocal terms (i.e., $\Pi^{\ell,s2} + \Pi^{\ell,\omega 2} + \Pi^{\ell,c2}$). This contrasts with the eddy viscosity model, for which

the scale-local and scale-nonlocal contributions are modeled together. Explicitly capturing the scale-local energy transfer allows the mixed model to more accurately reproduce the statistics of a DNS filtered at scale ℓ_{LES}, whereas the eddy viscosity model instead mimics an unfiltered DNS [60, 61]. This theme is further explored in §4.4 using the normality-based analysis.

4.4 Results

4.4.1 Multiscale velocity gradient partitioning

The normality-based partitioning of filtered velocity gradients defined in (4.22) identifies the contributions of normal straining, pure shearing, rigid rotation, and shear–rotation correlations to the strength of filtered velocity gradients. We consider the averaged form of this partitioning to characterize how the velocity gradients in forced isotropic turbulence vary as a function of scale. For unfiltered velocity gradients ($\ell = 0$), the partitioning is given by $\left\langle S_\epsilon^2 \right\rangle / \left\langle A^2 \right\rangle = 0.240$, $\left\langle A_\gamma^2 \right\rangle / \left\langle A^2 \right\rangle = 0.520$, $\left\langle \Omega_\varphi^2 \right\rangle / \left\langle A^2 \right\rangle = 0.106$, and $\left\langle \Omega_{\varphi\gamma}^2 \right\rangle / \left\langle A^2 \right\rangle = 0.134$, and it is relatively insensitive to Re_λ for $Re_\lambda \gtrsim 200$ [14, 23]. This unfiltered partitioning serves as a baseline for our analysis of the effects of filtering and LES modeling in this section.

4.4.1.1 The DNS cases: the effect of filtering

Figure 4.2 shows how the partitioning varies as a function of the filter width, $2\ell/\eta$, for the DNS cases. Increasing the filter width mitigates the relative contribution of pure shearing and increases the relative contributions of normal straining, rigid rotation, and, to a lesser extent, shear–rotation correlations. This behavior occurs primarily for $2\ell \lesssim \delta_\gamma$, where $\delta_\gamma = 9\eta$ represents the typical thickness of small-scale shear layers [12, 27–30]. It highlights that filtering mitigates the imprint of small-scale shear layers until the filter width surpasses their thickness, whereafter filtering at larger scales does not significantly affect the partitioning statistics, including in the inertial range. For $2\ell \gtrsim \delta_\gamma$, this scale-invariant partitioning is given by $\left\langle S_{\ell,\epsilon}^2 \right\rangle / \left\langle A^2 \right\rangle \approx 0.27$, $\left\langle A_{\ell,\gamma}^2 \right\rangle / \left\langle A^2 \right\rangle \approx 0.46$, $\left\langle \Omega_{\ell,\varphi}^2 \right\rangle / \left\langle A^2 \right\rangle \approx 0.13$, and $\left\langle \Omega_{\ell,\varphi\gamma}^2 \right\rangle / \left\langle A^2 \right\rangle \approx 0.14$. The distinction between this and the unfiltered partitioning would be obscured by an analogous symmetry-based analysis since $\left\langle S_\ell^2 \right\rangle = \left\langle \Omega_\ell^2 \right\rangle$ at all scales for homogeneous turbulence [62]. This highlights the ability of the normality-based decomposition to capture how flow structures in the viscous range differ from those in the inertial range.

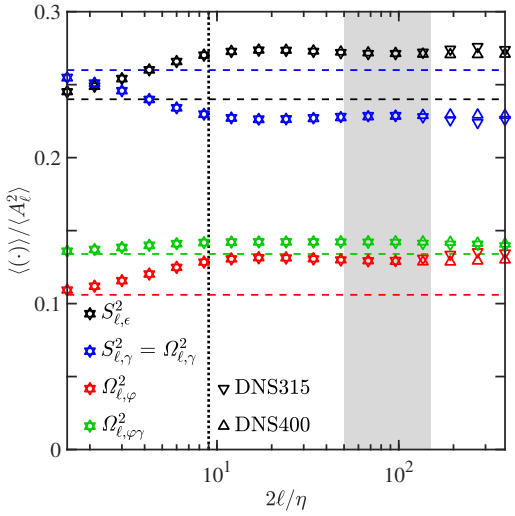

Figure 4.2: Partitioning of filtered velocity gradients for the DNS cases, where shearing is represented using $S^2_{\ell,\gamma} = \Omega^2_{\ell,\gamma} = \frac{1}{2}A^2_{\ell,\gamma}$. The horizontal dashed lines represent the unfiltered partitioning in the high-Re_λ limit, the vertical dotted line represents the typical thickness of small-scale shear layers, $\delta_\gamma = 9\eta$, and the shaded region approximates the inertial range for DNS400 as $50 \leq 2\ell/\eta \leq 150$.

The comparison between the filter width, 2ℓ, and the shear layer thickness, δ_γ, can be interpreted in terms of velocity increments. Johnson [50] highlighted that filtered velocity gradients can be expressed in terms of spatially integrated velocity increments that are weighted by the gradient of the filter kernel [65]. For a Gaussian kernel, the weighting is an odd function of the spatial offset, $\boldsymbol{r}$, and its magnitude is maximized when $|\boldsymbol{r}| = \ell$. These features imply that velocity increments given by $\boldsymbol{u}(\boldsymbol{x} + \ell\hat{\boldsymbol{e}}) - \boldsymbol{u}(\boldsymbol{x} - \ell\hat{\boldsymbol{e}})$, where $\hat{\boldsymbol{e}}$ represents an arbitrary unit vector, have the strongest weighting in the construction of the filtered velocity gradients, $\overline{A}^\ell_{ij}(\boldsymbol{x})$. Hence, the filtered velocity gradients at a given point are most strongly related to velocity increments of size 2ℓ that are centered at the same point. This result provides a direct relationship to δ_γ, which is often formulated in a similar manner using the velocity jump across a shear layer [12, 30]. Even alternative definitions of δ_γ, e.g., in terms of vorticity [27–29], are empirically associated with this velocity jump. Therefore, the comparison of 2ℓ and δ_γ is appropriate since it has strong physical foundations based on velocity increments.

For the Reynolds numbers shown in Figure 4.2, the partitioning collapses as a function of the filter width except at very large scales, where it becomes more sensitive to the details of the forcing and the number of samples. Appendix

4.A2 further investigates the collapse of the partitioning statistics in terms of Re_λ and ℓ. It highlights that the partitioning at small filter widths collapses well for $Re_\lambda \gtrsim 200$, consistent with the collapse of the unfiltered partitioning [23]. As Re_λ increases, the collapse extends to larger filter widths, including within the inertial range. The collapse observed in the present study also complements the collapsed power law scalings for the intensities of shearing and rigid rotation obtained by Watanabe et al. [66], which were normalized using the Kolmogorov time scale instead of $\langle A_\ell^2 \rangle$. Based on the excellent collapse we observe for DNS315 and DNS400, we use $Re_\lambda \approx 400$ to represent the partitioning statistics at moderately high Reynolds numbers and as the primary subject of our LES analyses.

4.4.1.2 The LES cases: the effect of closure modeling

Previous investigations have demonstrated that the eddy viscosity and mixed models we consider produce flow statistics at the LES filter scale, ℓ_{LES}, that resemble the statistics of unfiltered and filtered DNS data, respectively [60, 61]. We consider the multiscale partitioning statistics of the resolved velocity gradients for each model, thereby providing a more holistic assessment than the previous single-scale analyses. Figure 4.3(a) shows how the partitioning produced by each LES model varies as a function of the filter width for $\ell \geq \ell_{LES}$. The filtered velocity gradients at scale ℓ are obtained by applying a complementary filter, of width $\ell_* = \sqrt{\ell^2 - \ell_{LES}^2}$, to the resolved velocity gradients, which are filtered at scale ℓ_{LES}. Consistent with the previous results, the mixed model accurately reproduces the multiscale partitioning statistics of the filtered DNS across all resolved scales. By contrast, the partitioning produced by the eddy viscosity model deviates from the filtered DNS near the LES filter width, where it instead approaches the unfiltered DNS partitioning. This result qualitatively agrees with the notion that the flow field produced by the eddy viscosity model tends to behave like an unfiltered DNS at a lower Reynolds number [60, 61].

In Figure 4.3(b), we quantitatively evaluate this claim by replotting the Vis400 partitioning statistics as a function of $2\ell_*/\eta_*$ instead of $2\ell/\eta$, where $\eta_* \approx 15\eta$ represents an effective Kolmogorov scale that is determined empirically. In effect, replacing ℓ with ℓ_* treats the resolved velocity gradients as if they are unfiltered and replacing η with η_* treats the flow statistics as if they were pro-

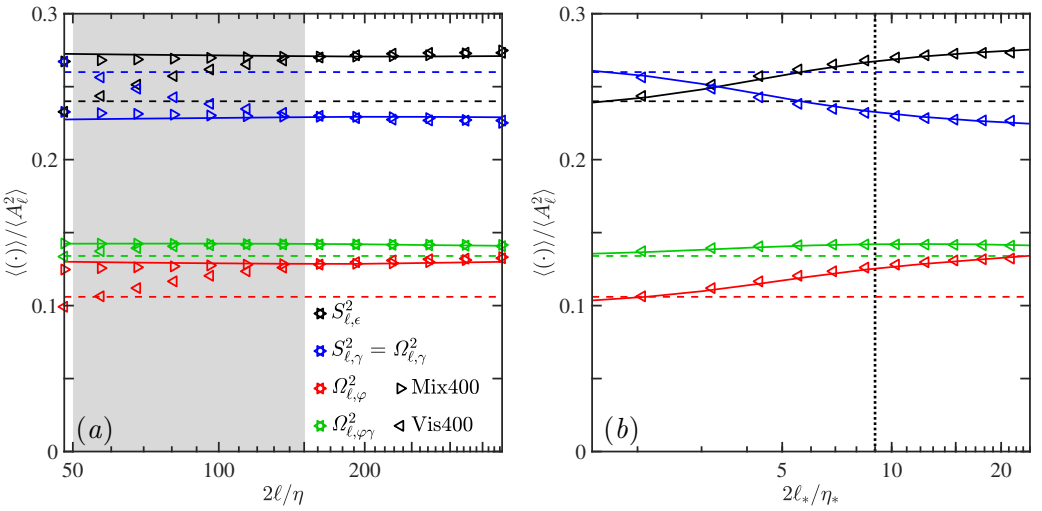

Figure 4.3: (a) Partitioning of filtered velocity gradients for the LES cases. The solid curves represent the filtered DNS400 partitioning and the horizontal dashed lines represent the unfiltered partitioning in the high-Re_λ limit. The lower limit of the filter width axis represents the LES filter width, $2\ell_{LES}/\eta = 48$, and the shaded region approximates the inertial range. (b) Partitioning for Vis400 replotted as a function of $2\ell_*/\eta_*$, where $\ell_* = \sqrt{\ell^2 - \ell_{LES}^2}$ is the complementary filter width and $\eta_* \approx 15\eta$ is an effective Kolmogorov scale. The solid curves represent the partitioning produced by a DNS at $Re_\lambda \approx 61$, which has a Kolmogorov scale of approximately η_*. The vertical dotted line represents the typical thickness of small-scale shear layers, $\delta_\gamma = 9\eta$.

duced by a simulation at a lower Reynolds number. Using these modifications, we compare the multiscale partitioning statistics for Vis400 with those produced by a DNS at $Re_\lambda \approx 61$, which has a Kolmogorov scale of approximately η_* (see Appendix 4.A2 for computational details). This comparison shows that, when plotted as a function of $2\ell_*/\eta_*$, the Vis400 partitioning statistics collapse well onto those of the lower-Re_λ DNS. It thus quantitatively validates the claim that the eddy viscosity model produces multiscale flow statistics that resemble an unfiltered DNS at a lower Reynolds number. In Appendix 4.A2, we show that the partitioning statistics produced by LES cases that employ different filter widths, ℓ_{LES}, yield a similar conclusion.

Whereas η_* is determined empirically in the present study, developing techniques to predict it *a priori* could provide valuable insight into the behavior of eddy viscosity models. A logical approach would be to hypothesize that $\eta_* = \left(\nu_*^3 \middle/ \left\langle \Phi \right\rangle\right)^{1/4}$, where $\nu_* = \nu \left\langle \Phi \right\rangle \middle/ \left\langle \Phi^{\ell_{LES}} \right\rangle$ represents an effective viscosity that captures the statistical imprint of the dynamic eddy viscosity field

in terms of the total dissipation rate, Φ, and the resolved dissipation rate, $\Phi^{\ell_{LES}}$. However, this approach leads to a prediction of $\eta_*/\eta \approx 10.6$ for Vis400, which does not satisfactorily agree with the empirical value of $\eta_*/\eta \approx 15$. Furthermore, a similar analysis for Mix400 would yield $\eta_*/\eta \approx 8.6$, which does not reflect that the mixed model statistics resemble those of the filtered DNS. We leave formulating and validating improved predictions of η_*, which would likely require a more nuanced approach, to future work.

4.4.2 Tube-like and sheet-like vortical structures

The partitioning statistics analyzed in §4.4.1 encode information about the flow structures that produce them. We analyze how these structures manifest in the DNS and LES cases to characterize how filtering and LES modeling affect their spatial organization. Our analysis focuses on tube-like and sheet-like vortical structures, which can be distinguished using the contributions of rigid rotation and shear vorticity and, as shown in Appendix 4.A1, are associated with vortex cores and shear layers, respectively.

Figure 4.4 depicts the vortical structures associated with rigid rotation and shear vorticity. The unfiltered DNS at $Re_\lambda \approx 61$ confirms that rigid rotation and shear vorticity are associated with tube-like and sheet-like vortical structures, respectively. The structures for this case qualitatively resemble typical structures from DNS400 (not shown) in a subdomain of size $(2\pi/15)^3$. This resemblance reflects that the Kolmogorov scale for $Re_\lambda \approx 61$ is roughly 15 times larger than the Kolmogorov scale for $Re_\lambda \approx 400$. When filtered at $2\ell/\eta = 48$, DNS400 still produces rigid rotation structures that resemble vortex tubes. However, the shear vorticity structures appear less sharp (i.e., more blob-like) since the filter scale is larger than the typical thickness of small-scale shear layers (i.e., $2\ell > \delta_\gamma$). This highlights that the decreasing relative contribution from shearing with increasing filter width observed in Figure 4.2 reflects the progressive smoothing of the vorticity profiles across shear layers in the subinertial range. Regardless of the filter scale, shear vorticity tends to be more space-filling than rigid rotation, which is consistent with previous findings [66].

The LES visualizations in Figure 4.4 provide insight into the structural implications of the partitioning statistics in Figure 4.3. Just as the multiscale partitioning for Mix400 resembles that of DNS400 filtered at $2\ell/\eta = 48$, the corresponding vortical flow structures are also qualitatively similar. Likewise,

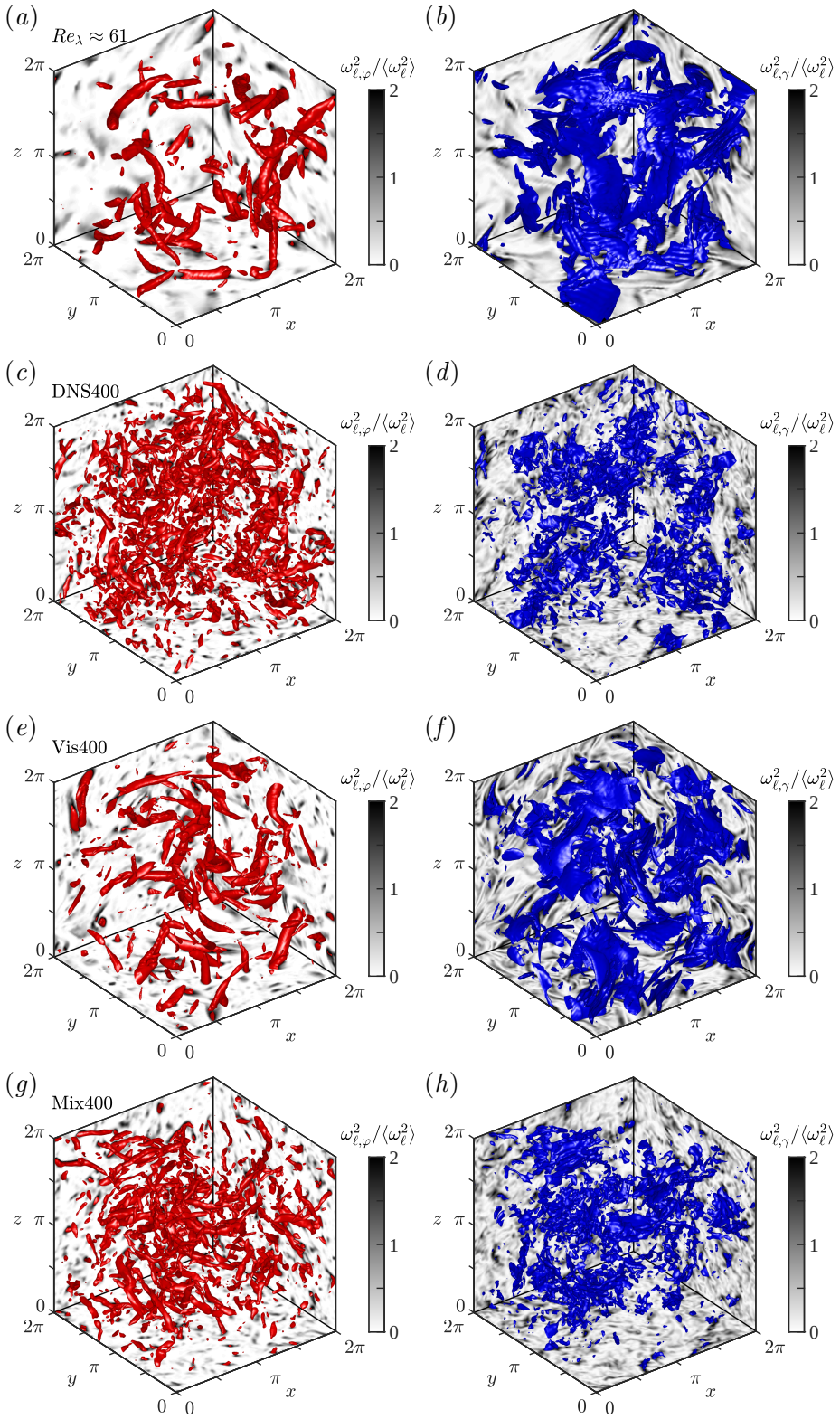

Figure 4.4: Vortical flow structures associated with rigid rotation and shear vorticity for an unfiltered ($\ell = 0$) DNS at $Re_\lambda \approx 61$ (a,b), DNS400 filtered at $2\ell/\eta = 48$ (c,d), and Vis400 (e,f) and Mix400 (g,h) at the LES filter width, $2\ell_{LES}/\eta = 48$. The grayscale visualizations depict the strengths of rigid rotation, $\omega^2_{\ell,\varphi}$, and shear vorticity, $\omega^2_{\ell,\gamma}$, normalized by the spatially averaged vorticity strength, $\left\langle \omega^2_\ell \right\rangle$, and the isosurfaces represent $\omega^2_{\ell,\varphi} \Big/ \left\langle \omega^2_\ell \right\rangle = 2$ (red) and $\omega^2_{\ell,\gamma} \Big/ \left\langle \omega^2_\ell \right\rangle = 2$ (blue).

the vortical flow structures for Vis400 resemble those of the unfiltered DNS at $Re_\lambda \approx 61$, consistent with the collapse of their multiscale partitioning statistics in Figure 4.3(b), where the Vis400 partitioning is replotted as a function of $2\ell_*/\eta_*$. The distinctive sheet-like vortical flow structures observed for these cases are significantly less prominent in the Mix400 and filtered DNS400 visualizations. These observations augment previous observations made using two-dimensional snapshots of out-of-plane vorticity [60] by unambiguously identifying and distinguishing the three-dimensional imprint of vortex tubes and shear layers in a principled manner.

The visualizations analyzed in this section provide structural validation for the observations made in §4.4.1 using the multiscale partitioning statistics. Specifically, they highlight that the enhanced shearing at small scales reflects contributions from sharp velocity gradients across small-scale shear layers, which are softened upon filtering. They also highlight that the flow structures produced by the eddy viscosity model resemble those of an unfiltered DNS at a lower Reynolds number, whereas the structures produced by the mixed model resemble those of a filtered DNS at the same Reynolds number. These results emphasize that the ability of an LES to produce realistic multiscale flow structures can be highly sensitive to the choice of closure model. Together, the DNS and LES results highlight that a key advantage of the normality-based analysis is its ability to distinguish vortex cores from shear layers in a manner that would be obscured by an analogous symmetry-based analysis (e.g., of vorticity alone). In §4.4.3, we use this expressivity to provide insight into flow structures that contribute to various mechanisms of interscale energy transfer.

4.4.3 Interscale energy transfer analysis

As formulated in §4.2, we characterize mechanisms responsible for interscale energy transfer by identifying how the normality-based constituents of the filtered VGT contribute to the multiscale velocity gradient expansion of Π^ℓ. Numerically evaluating this expansion at a given scale, ℓ, involves computing scale-space integrals over scales $0 \leq \theta \leq \ell$. Following previous studies [49, 50], the scale-space integrals for each ℓ are discretized using the trapezoidal rule with filter widths that are logarithmically spaced such that $\Delta\log_{10}\theta = 0.376$ for the DNS cases and $\Delta\log_{10}\theta = 0.188$ for the LES cases. We have confirmed that our results are insensitive to the details of these discretization schemes, including the smallest non-zero filter width ($2\theta/\eta = 0.75$) for the DNS cases.

They are also insensitive to the number of snapshots used to compute the energy transfer statistics. To reduce computational costs, we only use two snapshots to compute these statistics for the DNS cases. This is sufficient since, as demonstrated in Appendix 4.A2, the velocity gradient statistics for these cases are approximately converged even with a single snapshot. As depicted in Figure 4.1(a), the collapse of our symmetry-based cascade rate computations onto those of Johnson [49, 50] further validates the statistical convergence of our results.

4.4.3.1 The DNS cases: multiscale mechanisms in the energy cascade

Figure 4.5 summarizes the normality-based contributions to interscale energy transfer for the DNS cases. Since these contributions are formulated by decomposing the multiscale velocity gradient expansion of the residual stress tensor, they represent the straining of flow features at scales $\theta \leq \ell$ by the flow at scale ℓ. We specifically identify contributions associated with multiscale strain self-amplification, vortex stretching, and strain–vorticity covariance, as expressed in (4.29), (4.30), and (4.31), respectively.

The multiscale strain self-amplification term, $\mathit{\Pi}^{\ell,s}$, is known to provide the strongest contribution to the energy cascade from the perspective of the symmetry-based analysis [49, 50]. As shown in Figure 4.5(a), the contributions of normal straining, shear straining, and their interaction at scales $\theta \leq \ell$ to this term are all significant, with normal straining providing the strongest contribution. The multiscale vortex stretching term, $\mathit{\Pi}^{\ell,\omega}$, also contributes significantly to forward energy transfer across scale ℓ. As shown in Figure 4.5(b), the stretching of shear vorticity at scales $\theta \leq \ell$ by the flow at scale ℓ provides the strongest contribution to this term, exceeding the contributions associated with rigid rotation and shear–rotation interactions. Since shear vorticity and rigid rotation at a given scale are associated with shear layers and vortex cores, respectively, our results highlight the stretching of small-scale shear layers as a significant mechanism underlying multiscale vortex stretching. However, the significant contribution from shear–rotation interactions, which are typically strongest between the cores and boundaries of vortex tubes (see Appendix 4.A1 and Arun and Colonius [22]), suggests that vortex stretching near the boundaries of vortex tubes may also contribute to some fraction of $\mathit{\Pi}^{\ell,\omega}_{\gamma\gamma}$. Nevertheless,

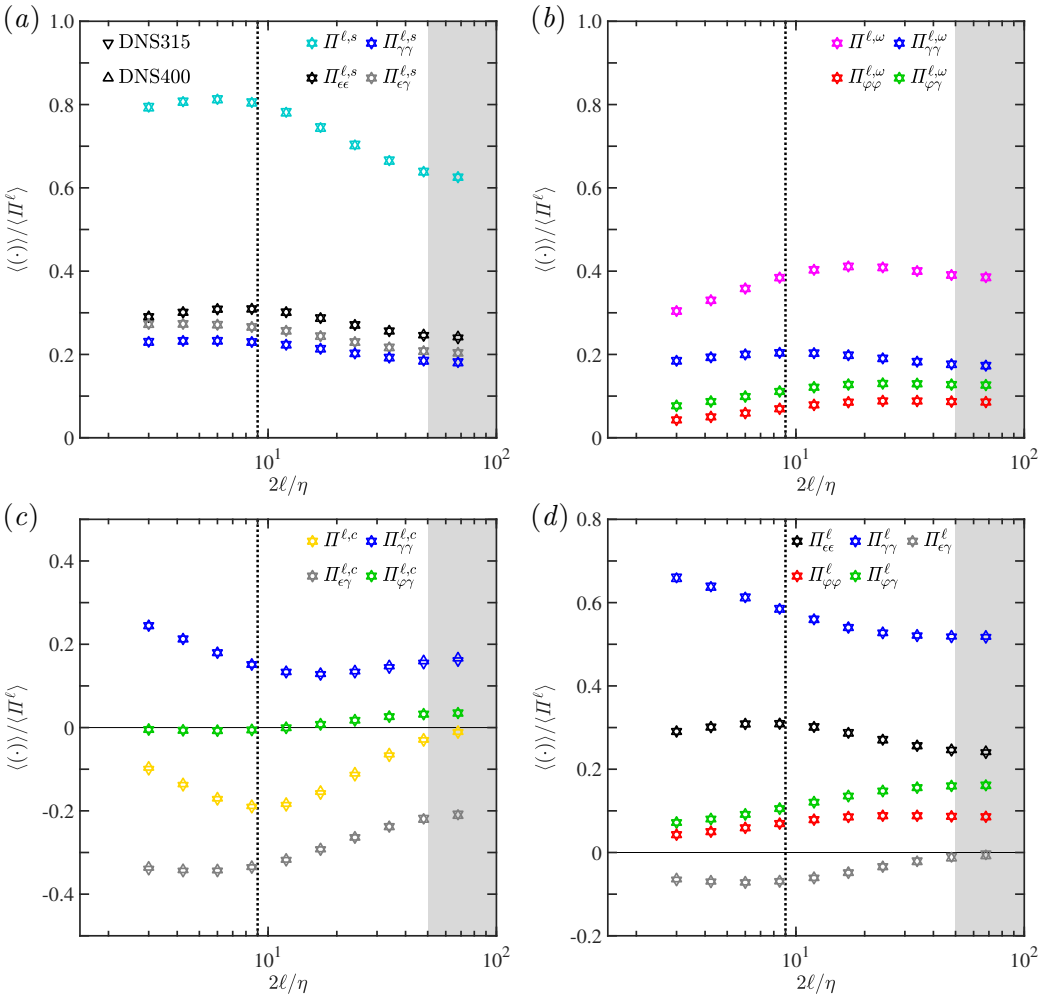

Figure 4.5: Normality-based contributions to interscale energy transfer for the DNS cases. The contributions represent multiscale strain self-amplification (a), vortex stretching (b), strain–vorticity covariance (c), and aggregates across these three mechanisms (d). The vertical dotted lines represent the typical thickness of small-scale shear layers, $\delta_\gamma = 9\eta$, and the shaded regions capture the bottom of the inertial range for DNS400.

the strong association of shear vorticity with sheet-like vortical structures in the visualizations in §4.4.2 highlights that, in addition to vortex tubes, shear layers are essential to the description of multiscale vortex stretching.

In contrast to the forward energy transfer produced by $\Pi^{\ell,s}$ and $\Pi^{\ell,\omega}$, the net contribution of the strain–vorticity covariance term, $\Pi^{\ell,c}$, produces upscale energy transfer that drives the bottleneck effect in the subinertial range (see Figure 4.1). Therefore, the normality-based decomposition of $\Pi^{\ell,c}$, as shown in Figure 4.5(c), provides insight into the flow features that contribute to this backscatter. The $\Pi^{\ell,c}_{\epsilon\gamma}$ and $\Pi^{\ell,c}_{\gamma\gamma}$ terms represent the covariances of

normal straining and shear straining (respectively) with shear vorticity at scales $\theta \leq \ell$ and can thus be associated with small-scale shear layers. The $\Pi^{\ell,c}_{\varphi\gamma}$ term represents the covariance of shear straining with rigid rotation at scales $\theta \leq \ell$ and can thus be associated with small-scale vortex tubes. Since $\left\langle \Pi^{\ell,c}_{\varphi\gamma} \right\rangle$ is negligible throughout the subinertial range, the shear vorticity terms dominate $\left\langle \Pi^{\ell,c} \right\rangle \approx \left\langle \Pi^{\ell,c}_{\epsilon\gamma} \right\rangle + \left\langle \Pi^{\ell,c}_{\gamma\gamma} \right\rangle < 0$ at these scales. This suggests that small-scale shear layers (rather than vortex tubes) are primarily responsible for the backscatter that produces the bottleneck effect in the subinertial range of the energy cascade. It is also consistent with the fact that the filter width associated with the peak relative contribution of this backscatter coincides with the empirical shear layer thickness (at $2\ell \approx \delta_\gamma = 9\eta$). In particular, the covariance of normal straining with shear vorticity is responsible for the backscatter, and its contribution is tempered by a net positive contribution from the covariance of shear straining with shear vorticity. Further work is required to determine whether these findings are consistent with the hypothesis that a mechanism reminiscent of vortex thinning in two-dimensional turbulence drives the backscatter associated with $\Pi^{\ell,c}$ in the subinertial range of three-dimensional turbulence [50]. One such mechanism might involve the flattening of a vortex into a shear layer that results in a misalignment between the strain rates at small and large scales.

Combining the contributions from Figure 4.5(a–c), Figure 4.5(d) summarizes the normality-based contributions to the total interscale energy transfer, as expressed in (4.23). The contribution of $\Pi^{\ell}_{\gamma\gamma}$ accounts for more than half of the energy transfer in the subinertial and inertial ranges, with significant contributions to multiscale strain self-amplification, vortex stretching, and strain–vorticity covariance. This highlights that the energy transfer across scale ℓ is largely attributed to the straining of shear layers at scales $\theta \leq \ell$. The next strongest contribution is due to $\Pi^{\ell}_{\epsilon\epsilon}$, which represents strain self-amplification associated with normal straining at scales $\theta \leq \ell$. The combined contribution of these two terms becomes increasingly dominant at small scales and accounts for more than 90% of the energy transfer when $2\ell/\eta \sim O(1)$. The vortex stretching associated with rigid rotation, $\Pi^{\ell}_{\varphi\varphi}$, and the cascade rate associated with shear–rotation interactions, $\Pi^{\ell}_{\varphi\gamma}$, which is primarily due to vortex stretching, also account for significant (albeit smaller) forward energy transfer. From the normality-based perspective, the $\Pi^{\ell}_{\epsilon\gamma}$ term, which represents the interaction between normal straining and pure shearing at scales $\theta \leq \ell$, is the

only term with a negative net contribution to energy transfer in the subinertial range. This negative contribution is produced by the strain–vorticity covariance term, $\Pi^{\ell,c}_{\epsilon\gamma}$, and tempered by the strain self-amplification term, $\Pi^{\ell,s}_{\epsilon\gamma}$. It becomes negligible in the inertial range, which is consistent with our claim that it is associated with the subinertial bottleneck effect. From strongest to weakest, the relative contributions of the normality-based mechanisms in the inertial range can be summarized as $\left\langle \Pi^{\ell}_{\gamma\gamma} \right\rangle \big/ \left\langle \Pi^{\ell} \right\rangle \approx 0.52$, $\left\langle \Pi^{\ell}_{\epsilon\epsilon} \right\rangle \big/ \left\langle \Pi^{\ell} \right\rangle \approx 0.24$, $\left\langle \Pi^{\ell}_{\varphi\gamma} \right\rangle \big/ \left\langle \Pi^{\ell} \right\rangle \approx 0.16$, $\left\langle \Pi^{\ell}_{\varphi\varphi} \right\rangle \big/ \left\langle \Pi^{\ell} \right\rangle \approx 0.08$, and $\left\langle \Pi^{\ell}_{\epsilon\gamma} \right\rangle \big/ \left\langle \Pi^{\ell} \right\rangle \approx 0$. These relative contributions are qualitatively similar to the corresponding partitioning contributions in the inertial and subinertial ranges, which highlights that the energy transfer across a given scale is related to the strength of the filtered velocity gradients that produce it.

In Figure 4.6, we refine the results presented in Figure 4.5 by identifying scale-local and scale-nonlocal contributions to energy transfer associated with strain self-amplification and vortex stretching, as formulated in §4.2. Our analysis focuses primarily on the scale-local terms with three subscripts, as defined in (4.50) and (4.51), to facilitate detailed interpretations of the underlying energy transfer mechanisms. The scale-local and scale-nonlocal terms with two subscripts, as defined in (4.48) and (4.49), are also shown for completeness and reflect a direct decomposition of the terms in Figure 4.5. They are related to the terms with three subscripts through the expressions in (4.52) and (4.53).

As depicted in Figure 4.6(a) the $\Pi^{\ell,s1}_{\epsilon\gamma\gamma}$ term provides the strongest contribution to scale-local strain self-amplification. It can be interpreted as the normal straining of the strain rate associated with shear layers at scale ℓ. Its contribution is closely followed by that of $\Pi^{\ell,s1}_{\epsilon\epsilon\epsilon}$, which reflects how the self-interaction of normal straining amplifies strain rates. Together, these two terms are responsible for more than 90% of the scale-local strain self-amplification throughout the subinertial range and the bottom of the inertial range. Their contribution dominates that of $\Pi^{\ell,s1}_{\gamma\gamma\gamma}$, which reflects how the self-interaction of shear straining, which is associated with shear layers, amplifies strain rates.

As depicted in Figure 4.6(b), the $\Pi^{\ell,\omega1}_{\epsilon\gamma\gamma}$ term provides the strongest contribution to scale-local vortex stretching. It represents the normal straining of the shear vorticity at scale ℓ and can be interpreted as a 'shear layer stretching' term. Its contribution is considerably stronger than that of $\Pi^{\ell,\omega1}_{\epsilon\varphi\varphi}$, which represents the normal straining of rigid rotation at scale ℓ and can be interpreted as

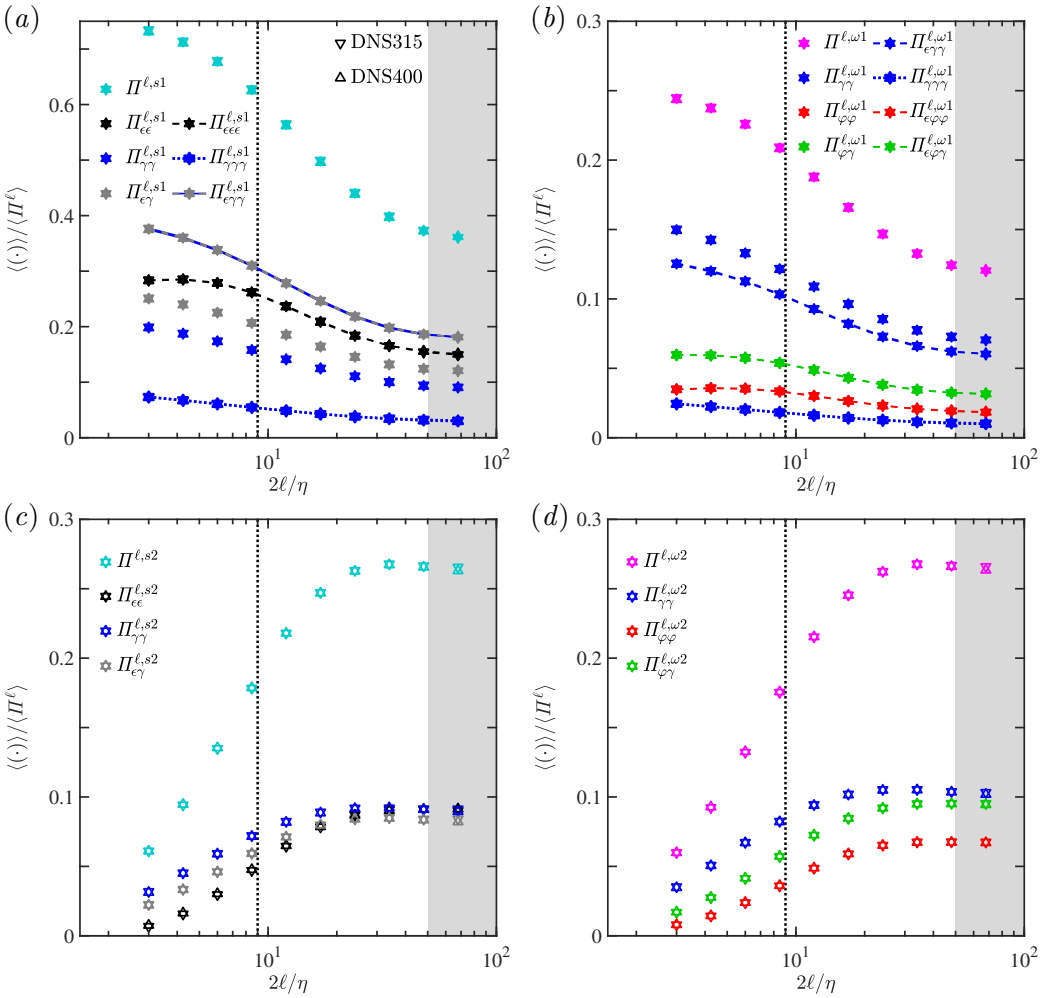

Figure 4.6: Normality-based contributions (as defined in §4.2) to the cascade rates associated with scale-local strain self-amplification (a) and vortex stretching (b) and scale-nonlocal strain self-amplification (c) and vortex stretching (d). The vertical dotted lines represent the typical thickness of small-scale shear layers, $\delta_\gamma = 9\eta$, and the shaded regions capture the bottom of the inertial range for DNS400.

a 'vortex core stretching' term. As discussed for multiscale vortex stretching, this suggests that prototypical models of stretched vortex tubes (e.g., Burgers vortex tubes) may provide an incomplete picture of vortex stretching. Supplementing these models with contributions from stretched shear layers, which are often modeled using Burgers vortex layers, is likely to more accurately capture the flow features that contribute to scale-local vortex stretching. The inclusion of stretched shear layers is particularly important given that they also contribute significantly to scale-local strain self-amplification through the $\Pi^{\ell,s1}_{\epsilon\gamma\gamma}$ term.

Case	SS: $\epsilon\epsilon\epsilon$	SS: $\epsilon\gamma\gamma$	SS: $\gamma\gamma\gamma$	VS: $\epsilon\varphi\varphi$	VS: $\epsilon\gamma\gamma$	VS: $\gamma\gamma\gamma$	VS: $\epsilon\varphi\gamma$
DNS315	0.349	0.536	0.115	0.123	0.536	0.115	0.226
DNS400	0.354	0.531	0.115	0.125	0.531	0.115	0.229

Table 4.2: Comparison of the normality-based contributions to strain self-amplification (SS) and vortex stretching (VS) for the unfiltered DNS cases. The contributions to SS and VS are normalized by $\left\langle -S_{ij}S_{ik}S_{jk}\right\rangle$ and $\left\langle -S_{ij}\Omega_{ik}\Omega_{jk}\right\rangle$. respectively, such that they sum to unity for each mechanism.

While Π^{ℓ} vanishes in the limit of $\ell \to 0$, strain self-amplification and vortex stretching are still relevant since they modulate the strength of unfiltered velocity gradients. Therefore, the normality-based analysis of these mechanisms at $\ell = 0$ provides insight into their contributions to the dynamics of velocity gradients at small scales. Table 4.2 summarizes the average contributions of the normality-based constituents of these mechanisms, which can be interpreted as the relative contributions of the terms in (4.50) and (4.51) in the limit of $\ell \to 0$. Consistent with our scale-local energy transfer analysis, the $\epsilon\gamma\gamma$ terms, associated with the normal straining of shear layers, are the most significant contributors to strain self-amplification and vortex stretching at $\ell = 0$. Importantly, normal straining contributes significantly more to the stretching of shear layers than shear straining, which is represented by the $\gamma\gamma\gamma$ terms. This highlights that the Burgers vortex layer forms a reasonable (albeit crude) model for small-scale shear layers, as its strain self-amplification and vortex stretching are entirely attributed to the $\epsilon\gamma\gamma$ terms. Appendix 4.A1 provides further analysis of the strain self-amplification and vortex stretching associated with Burgers vortex layers and tubes.

Our results are also qualitatively consistent with the statistics reported by Watanabe et al. [28] using the original triple decomposition [15, 16]. However, their approach yields non-zero contributions from terms analogous to the $\epsilon\epsilon\gamma$ strain self-amplification term and the $\gamma\varphi\varphi$ and $\gamma\varphi\gamma$ vortex stretching terms, which are identically zero in our normality-based formulation. This reflects that their approach relies on a (potentially sensitive) optimization problem to identify a frame that maximizes an interaction scalar. By contrast, our normality-based approach has unambiguous foundations derived from the form of the VGT in the principal reference frame, as expressed in (4.2).

4.4.3.2 The LES cases: closure models and the artificial bottleneck effect

Whereas our analysis of energy transfer for the DNS cases involves scales ($0 \leq 2\ell/\eta \leq 67.9$) primarily associated with the subinertial range, our analysis of the LES cases is constrained to the resolved scales ($2\ell \geq 2\ell_{LES} = 48\eta$), which are primarily associated with the inertial range. This constraint poses a challenge for computing the multiscale expansion of σ_{ij}^{ℓ}, as formulated in (4.8), since we do not have access to the unresolved motions at scales $\ell < \ell_{LES}$. For the LES cases, we compute the residual stress tensor at scales $\ell \geq \ell_{LES}$ as

$$\sigma_{ij}^{\ell} = \overline{\sigma_{ij}^{\ell_{LES}}}^{\ell_*} + \underbrace{\overline{u_i^{\ell_{LES}} u_j^{\ell_{LES}}}^{\ell_*} - \overline{u_i^{\ell_{LES}}}^{\ell_*} \overline{u_j^{\ell_{LES}}}^{\ell_*}}_{\tilde{\sigma}_{ij}^{\ell}}, \tag{4.60}$$

where $\ell_* = \sqrt{\ell^2 - \ell_{LES}^2}$. Here, the first term represents the contribution from the unresolved motions, as modeled by (4.54) and (4.57) for Vis400 and Mix400, respectively, and $\tilde{\sigma}_{ij}^{\ell}$ represents the contribution from the resolved flow field. The term $\tilde{\sigma}_{ij}^{\ell}$ contributes to the interscale energy transfer associated with the resolved motions, $\tilde{\Pi}^{\ell} = -\overline{S}_{ij}^{\ell} \tilde{\sigma}_{ij}^{\ell}$, which can be expanded analogously to (4.9) as

$$\tilde{\Pi}^{\ell} = -\overline{S}_{ij}^{\ell} \int_{\ell_{LES}^2}^{\ell^2} \mathrm{d}\theta^2 \left(\overline{\overline{A}_{ik}^{\theta} \overline{A}_{jk}^{\theta}}^{\phi} \right) = -\overline{\overline{S}_{ij}^{\ell_{LES}}}^{\ell^*} \int_0^{\ell_*^2} \mathrm{d}\theta_*^2 \left(\overline{\overline{A}_{ik}^{\ell_{LES}}}^{\theta_*} \overline{\overline{A}_{jk}^{\ell_{LES}}}^{\theta_*} \right)^{\phi}, \tag{4.61}$$

where $\theta_* = \sqrt{\theta^2 - \ell_{LES}^2}$, $\phi = \sqrt{\ell^2 - \theta^2} = \sqrt{\ell_*^2 - \theta_*^2}$, and the remaining energy transfer, $\Pi^{\ell} - \tilde{\Pi}^{\ell}$, is supplied by the closure model. We use analogous expansions, denoted with tildes, to capture the resolved part of other multiscale cascade rates (e.g., $\tilde{\Pi}^{\ell,s}$, $\tilde{\Pi}^{\ell,\omega}$, and $\tilde{\Pi}^{\ell,c}$). The resolved scale-nonlocal contributions to the cascade rates associated with strain self-amplification and vortex stretching are defined as $\tilde{\Pi}^{\ell,s2} = \tilde{\Pi}^{\ell,s} - \Pi^{\ell,s1}$ and $\tilde{\Pi}^{\ell,\omega 2} = \tilde{\Pi}^{\ell,\omega} - \Pi^{\ell,\omega 1}$, respectively. In this section, we use these resolved cascade rates to provide insight into the structural origins of the artificial bottleneck effect in LES, as depicted in Figure 4.1(b).

Figure 4.7 shows the resolved symmetry-based cascade rates alongside the normality-based decomposition of the resolved strain–vorticity covariance term for the LES cases. For Mix400, the scale-local cascade rates associated with strain self-amplification and vortex stretching are reasonably consistent with those of an analogously filtered DNS. This reflects that the scale-local terms

at scales $\ell \geq \ell_{LES}$ are fully resolved and it is consistent with the partitioning results in Figure 4.3(a). By contrast, the corresponding scale-nonlocal cascade rates do not match the filtered DNS and account for nearly all of the unresolved net energy transfer, $\left\langle \Pi^{\ell} \right\rangle - \left\langle \tilde{\Pi}^{\ell} \right\rangle$. There is virtually no backscatter associated with the resolved contribution from the strain–vorticity covariance term. This is consistent with the inertial range DNS results and reflects that the negative contribution from $\tilde{\Pi}^{\ell,c}_{\epsilon\gamma}$ is roughly balanced by the positive contribution from $\tilde{\Pi}^{\ell,c}_{\gamma\gamma}$. Therefore, the lack of a pronounced bottleneck effect for the mixed model is associated with the absence of backscatter from the $\tilde{\Pi}^{\ell,c}$ term that, in particular, reflects the behavior of the shear layer terms.

For Vis400, the scale-local cascade rates are significantly stronger than those of the filtered DNS. Furthermore, the resolved cascade rate associated with the strain–vorticity covariance term produces significantly more backscatter than the negligible contribution observed for the filtered DNS. This backscatter reflects that the negative contribution from the $\tilde{\Pi}^{\ell,c}_{\epsilon\gamma}$ term significantly outweighs the positive contribution from the $\tilde{\Pi}^{\ell,c}_{\gamma\gamma}$ term, consistent with the DNS results in the subinertial range, as shown in Figure 4.5(c). Therefore, the pronounced artificial bottleneck effect produced by the eddy viscosity model is associated with backscatter from the $\tilde{\Pi}^{\ell,c}$ term that, in this case, reflects that the resolved shear layer terms behave similarly to the shear layer terms in the subinertial range for DNS.

As was done for the partitioning in Figure 4.3(b), the resolved cascade rates for Vis400 can be interpreted as if they were produced by an unfiltered DNS at a lower Reynolds number. Figure 4.7(e,f) shows these cascade rates normalized by the total resolved cascade rate, $\left\langle \tilde{\Pi}^{\ell} \right\rangle$, instead of the total cascade rate, $\left\langle \Pi^{\ell} \right\rangle$, and plotted as a function of $2\ell_*/\eta_*$ instead of $2\ell/\eta$. Consistent with Figure 4.3(b), we select $\eta_* \approx 15\eta$ and compare these results with those from a DNS at $Re_\lambda \approx 61$, which has a Kolmogorov scale of approximately η_*. For the symmetry-based results in Figure 4.7(e), there is a remarkable collapse between the replotted Vis400 cascade rates and the $Re_\lambda \approx 61$ cascade rates, except at very large scales, where the effects of the forcing and the number of snapshots may be relevant. The fact that both the partitioning statistics and the energy transfer statistics for Vis400 collapse well for the same η_* provides solid quantitative evidence that the eddy viscosity model behaves like an unfiltered DNS at a lower Reynolds number.

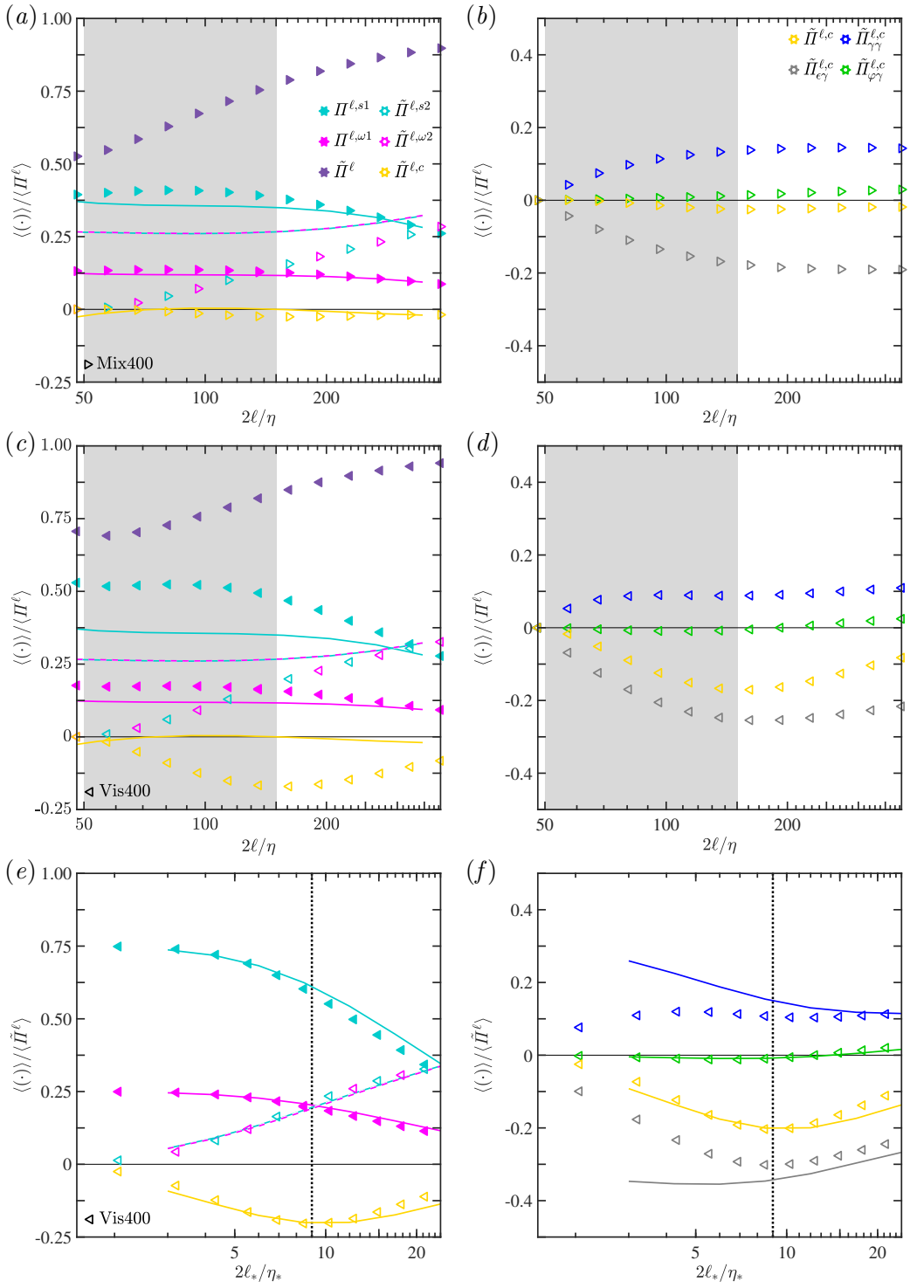

Figure 4.7: (a,c) Resolved symmetry-based scale-local and scale-nonlocal cascade rates for Mix400 (a) and Vis400 (c) overlaid on curves that represent the DNS results of Johnson [49, 50] in the same style as Figure 4.1(a). (b,d) Normality-based contributions to $\tilde{\Pi}^{\ell,c}$ for Mix400 (b) and Vis400 (d). Panels (e) and (f) replot the Vis400 results from panels (c) and (d), respectively, normalized by $\left\langle\tilde{\Pi}^\ell\right\rangle$ and as a function of $2\ell_*/\eta_*$, where $\eta_* \approx 15\eta$. The curves (e,f) represent a DNS at $Re_\lambda \approx 61$, which has a Kolmogorov scale of approximately η_*. The shaded regions approximate the inertial range and the vertical dotted lines represent $\delta_\gamma = 9\eta$.

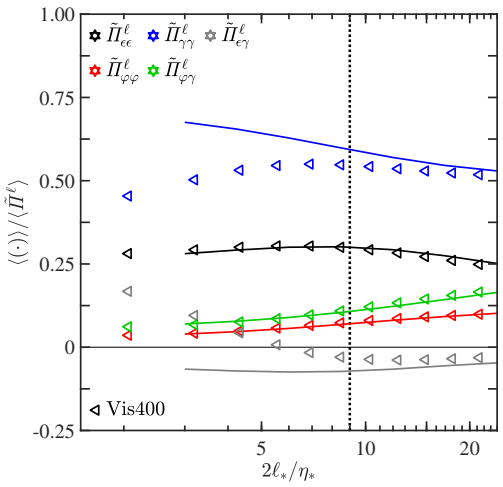

Figure 4.8: Resolved normality-based cascade rates for Vis400, plotted in the same style as Figure 4.7(e,f).

The collapse for the strain–vorticity covariance term highlights that the backscatter responsible for the artificial bottleneck effect in LES can be interpreted similarly to the backscatter responsible for the true bottleneck effect in DNS. Specifically, as shown in Figure 4.7(f), both bottleneck effects are almost entirely the result of contributions from shear vorticity (i.e., shear layers). However, close to the LES filter width (i.e., at small ℓ_*), the contributions of $\tilde{\Pi}^{\ell,c}_{\epsilon\gamma}$ and $\tilde{\Pi}^{\ell,c}_{\gamma\gamma}$ for Vis400 depart from those of $\Pi^{\ell,c}_{\epsilon\gamma}$ and $\Pi^{\ell,c}_{\gamma\gamma}$ for the $Re_\lambda \approx 61$ DNS. More generally, as shown in Figure 4.8, the contributions from the cascade rates associated with shearing and the interaction between normal straining and shearing are the only ones that exhibit this departure. All other normality-based cascade rates collapse extremely well onto the $Re_\lambda \approx 61$ DNS results. We hypothesize that these differences reflect the imprint of the dynamic variations in the eddy viscosity field on the resolved motions since, if the eddy viscosity were truly constant, we would expect the eddy viscosity simulation results to collapse exactly onto those of an unfiltered DNS at a lower Reynolds number. Hence, while we observe remarkable similarities between these cases, the dynamic model does produce subtle differences that are appreciable at scales sufficiently close to the LES filter width. Despite these subtle differences, the striking similarity in the shear-layer origins of the true bottleneck effect in DNS and the artificial bottleneck effect produced by the eddy viscosity LES case provides insight that may aid the design of improved closure models.

4.5 Concluding remarks

We have employed a normality-based analysis of filtered velocity gradients to identify the multiscale imprints of normal straining, pure shearing, and rigid rotation in turbulent flows. Our analysis of Gaussian-filtered velocity gradients obtained from DNS data representing forced isotropic turbulence refines symmetry-based approaches for characterizing the structures and mechanisms underlying the energy cascade. Our concurrent analysis of resolved velocity gradients obtained from LES data characterizes how well closure models, including eddy viscosity and mixed models, capture these flow features.

Our normality-based approach provides a principled framework for distinguishing tube-like vortex cores, which are associated with rigid rotation, from sheet-like shear layers, which are associated with shearing. Partitioning multiscale velocity gradients based on this approach reveals that filtering induces key structural changes in the subinertial range of the cascade. Filtering mitigates the relative contribution of shearing in this range by smoothing transverse velocity gradients across shear layers. This effect persists until the filter width exceeds the empirical thickness of small-scale shear layers, whereafter the partitioning is relatively constant as a function of scale, including in the inertial range. The variations we observe would be obscured by an analogous symmetry-based analysis since the average strengths of the strain-rate and vorticity tensors are equipartitioned at all scales in homogeneous turbulence.

Our interscale energy transfer analysis shows that, in the subinertial and inertial ranges of the cascade, the forward energy transfer across a given scale is driven primarily by the straining of multiscale shear layers. The strain self-amplification associated with multiscale normal straining and the vortex stretching associated with multiscale rigid rotation and shear–rotation interactions also contribute significantly to forward energy transfer. Our scale-local energy transfer analysis highlights that the normal straining of shear layers (i.e., shear layer stretching) is responsible for the majority of scale-local strain self-amplification and vortex stretching at all scales considered. This suggests that supplementing prototypical models involving stretched vortex tubes (e.g., Burgers vortex tubes) with contributions from stretched shear layers (e.g., Burgers vortex layers) would more realistically capture the structure of energy transfer and velocity gradient amplification in turbulent flows.

Previous symmetry-based analyses [49, 50] pinpoint multiscale strain–vorticity

covariance as a source of net backscatter that contributes to the bottleneck effect in the subinertial range of the energy cascade. Our analysis refines this notion by revealing that the net backscatter is almost entirely attributed to contributions from shear vorticity (i.e., shear layers). In particular, it is primarily associated with the interaction between normal straining and shear vorticity, which is tempered by the interaction between shear straining and shear vorticity. By contrast, the interaction between shear straining and rigid rotation, which can be associated with vortex tubes, provides a negligible net contribution. When combined with the fact that the backscatter is most significant at the scale associated with the thickness of small-scale shear layers, these results imply that shear layers are critical to the bottleneck effect.

Broadly speaking, our partitioning and energy transfer analyses for the LES cases highlight that the mixed model effectively reproduces the statistical and structural flow features of an appropriately filtered DNS. By contrast, the eddy viscosity model instead reproduces flow features associated with an unfiltered DNS at a lower Reynolds number. Using the present (dynamic) eddy viscosity model, an LES at $Re_\lambda \approx 400$ reproduces the statistics associated with a DNS at $Re_\lambda \approx 61$, which has a Kolmogorov scale roughly 15 times larger. In conjunction with the enhanced shearing at small scales identified by our partitioning analysis, this behavior helps explain why the eddy viscosity model produces prominent shear layer structures in the inertial range. It also reveals that the pronounced artificial bottleneck effect produced by this model in the inertial range has the same (shear layer) origins as the true bottleneck effect in the subinertial range for the DNS cases. Altogether, our LES analyses highlight the superior ability of the mixed model to mimic a filtered DNS. More generally, they provide a promising framework to assess (and potentially formulate) LES closure models.

The partitioning and energy transfer statistics that we compute for forced isotropic turbulence exhibit excellent collapse at relatively high Re_λ. Given related analyses of unfiltered velocity gradients [14, 22], it is reasonable to expect a similar collapse for the statistics at small filter scales in appropriate regions of inhomogeneous flows. Characterizing how (and at what scale) inhomogeneities induce differences from the flow features we observe would provide insight into how turbulence is sustained in a broader class of flows. Beyond computing velocity gradient statistics, identifying precisely how flow

structures contribute to those statistics would refine our understanding of the 'recipe' for turbulence. In the spirit of Shen et al. [67], Burgers vortex layers and tubes of various sizes and strengths might be versatile building blocks for this task. Our normality-based approach may also help identify unique imprints of flow structures that contribute to other vector gradients. For example, the ability to identify sheet-like structures may provide insight into the structures responsible for the current sheet thinning mechanism that dominates energy transfer in the inertial range of magnetohydrodynamic turbulence [42]. Beyond identifying flow structures, characterizing the dynamical evolution of these structures (even empirically) would clarify their roles in fundamental processes that sustain turbulent flows. For example, a time-resolved analysis could clarify how shear layers contribute to the bottleneck effect and whether that is consistent with the vortex thinning hypothesis [50]. Finally, our approach may help guide the development of more effective turbulence models. For example, it would be interesting to develop a model in the spirit of the stretched vortex subgrid-scale model [68] that also incorporates contributions from subgrid-scale shear layers.

Funding: R.A. was supported by the Department of Defense (DoD) through the National Defense Science & Engineering Graduate (NDSEG) Fellowship Program. This material is based upon work supported by the National Science Foundation under Grant No. CBET-2152373.

4.A1 Normality-based analysis of Burgers vortex layers and tubes

We apply the normality-based analysis of the VGT to the Burgers vortex layer and the Burgers vortex tube to provide insight into the structural organization of normal straining, pure shearing, and rigid rotation in canonical vortical flows.

The Burgers vortex layer represents a canonical stretched shear layer. Its velocity field, (u_x, u_y, u_z), in Cartesian coordinates, (x, y, z), is given by

$$u_x = -\alpha x, \quad u_y = U\mathrm{erf}\left(\frac{\sqrt{\alpha}x}{\sqrt{2\nu}}\right), \quad u_z = \alpha z, \tag{4.62}$$

where $\alpha > 0$ is a strain rate parameter and $2U = u_y(x \to +\infty) - u_y(x \to -\infty)$ is the vortex layer strength and represents the circulation per unit length. The

non-dimensional VGT for this flow is given by

$$\frac{1}{\alpha}\boldsymbol{A} = \begin{bmatrix} -1 & 0 & 0 \\ \frac{Re_U}{\sqrt{\pi}}\exp\left(-x_*^2\right) & 0 & 0 \\ 0 & 0 & 1 \end{bmatrix}, \tag{4.63}$$

where $x_* = x\sqrt{\alpha/2\nu}$ is the non-dimensional transverse coordinate and $Re_U = U\sqrt{2/\alpha\nu}$ is the shear layer Reynolds number.

The Burgers vortex tube represents a canonical stretched vortex tube. Its velocity field, (u_r, u_ϑ, u_z), in cylindrical coordinates, (r, ϑ, z), is given by

$$u_r = -\alpha r, \quad u_\vartheta = \frac{\Gamma}{2\pi r}\left[1 - \exp\left(-\frac{\alpha r^2}{2\nu}\right)\right], \quad u_z = 2\alpha z, \tag{4.64}$$

where $\alpha > 0$ is again a strain rate parameter and $\Gamma > 0$ represents the circulation. The non-dimensional VGT for this flow is given by

$$\frac{1}{\alpha}\boldsymbol{A} = \begin{bmatrix} -1 & -\frac{Re_\Gamma}{4\pi r_*^2}\left[1 - \exp\left(-r_*^2\right)\right] & 0 \\ -\frac{Re_\Gamma}{4\pi r_*^2}\left[1 - \exp\left(-r_*^2\right)\right] + \frac{Re_\Gamma}{2\pi}\exp\left(-r_*^2\right) & -1 & 0 \\ 0 & 0 & 2 \end{bmatrix}, \tag{4.65}$$

in cylindrical coordinates, where $r_* = r\sqrt{\alpha/2\nu}$ is the non-dimensional radial coordinate and $Re_\Gamma = \Gamma/\nu$ is the circulation Reynolds number.

Figure 4.9(a) shows the velocity gradient partitioning for Burgers vortex layers at various values of Re_U. Rigid rotation and shear–rotation correlations do not contribute to this flow since the eigenvalues of the VGT are real at all spatial locations. As expected, the partitioning is dominated by shearing inside the shear layer and normal straining far from the shear layer. The far-field behavior reflects that normal straining, which is purely symmetric, must dominate velocity gradients in regions where the vorticity is relatively weak (i.e., in nearly potential flow regimes). The value of x_* where the partitioning transitions from the shearing regime to the normal straining regime increases with increasing Re_U, and it has been shown that $Re_U \lesssim 100$ for typical small-scale shear layers [28]. Regardless of Re_U, strain self-amplification and vortex stretching (not shown) are entirely associated with the $\epsilon\gamma\gamma$ terms (i.e., $-3S_{ij}^{\epsilon}S_{ik}^{\gamma}S_{jk}^{\gamma}$ and $-S_{ij}^{\epsilon}\Omega_{ik}^{\gamma}\Omega_{jk}^{\gamma}$) at all spatial locations. As shown in §4.4.3.1, these mechanisms provide the strongest relative contributions to scale-local vortex stretching and strain self-amplification throughout the cascade.

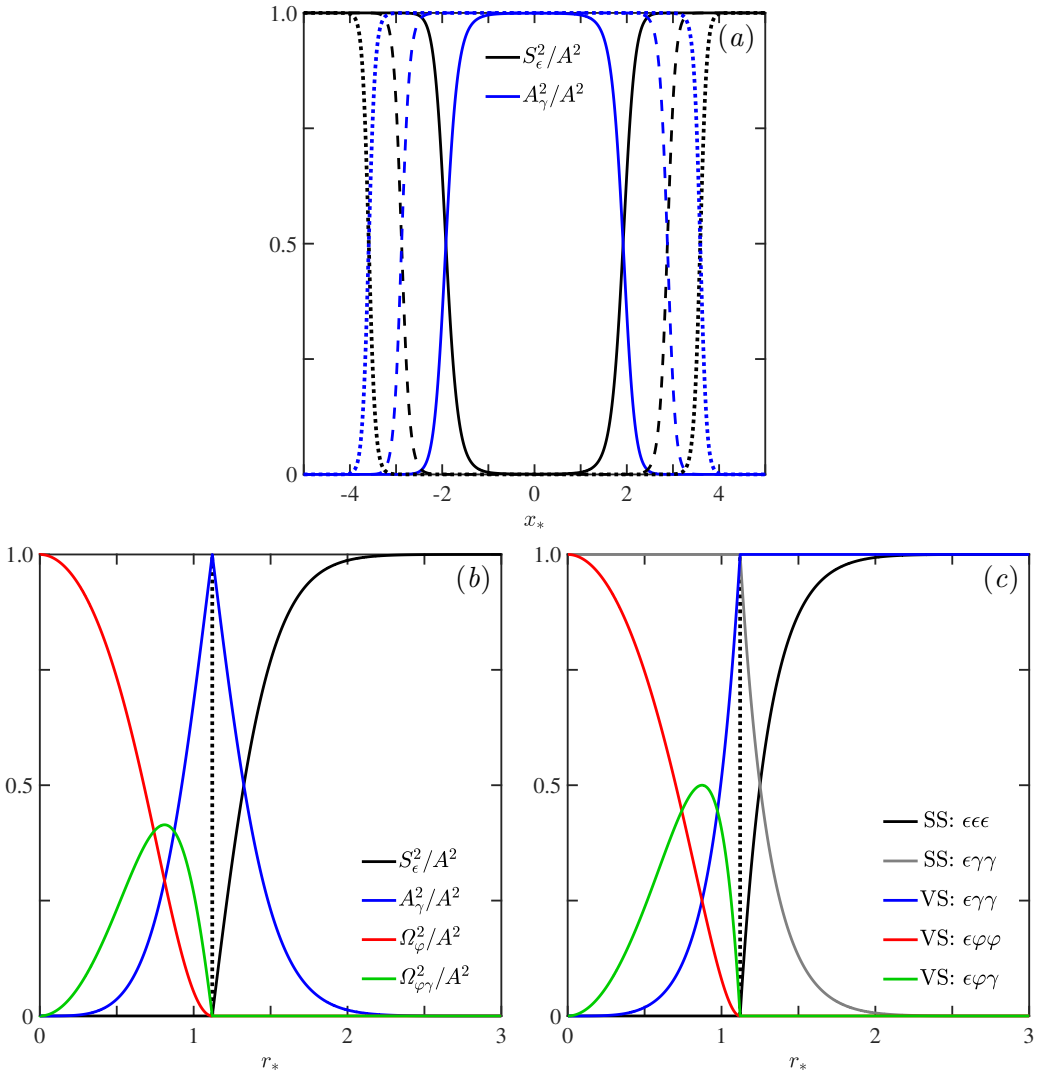

Figure 4.9: (a) Velocity gradient partitioning for Burgers vortex layers at $Re_U = 10^2$ (solid), $Re_U = 10^4$ (dashed), and $Re_U = 10^6$ (dotted). (b) Velocity gradient partitioning for the Burgers vortex tube in the limit of $Re_\Gamma \to \infty$. (c) Normality-based contributions to strain self-amplification (SS) and vortex stretching (VS) for the Burgers vortex tube from (b). The vertical dotted lines (b,c) represent the vortex boundary as identified by $Q = 0$ and $\Delta = 0$, where Q is the second invariant of the VGT and Δ is the discriminant of the VGT.

Figure 4.9(b) shows the velocity gradient partitioning for a Burgers vortex tube in the limit of $Re_\Gamma \to \infty$. The inner core of this Burgers vortex tube is dominated by rigid rotation, whereas the region near the vortex boundary is dominated by pure shearing. This highlights that the vortex can be crudely described as a rigidly rotating inner core with a shear annulus wrapped around it. The shear–rotation correlations are most significant between the core and

boundary regions, which is consistent with previous observations of vortex structures [22]. As observed for the Burgers vortex layer, the velocity gradients are dominated by normal straining in the nearly potential flow regime far from the vortex core. At the vortex boundary, the partitioning profiles are continuous but not differentiable. This reflects that the eigenvalues of the VGT are not differentiable at this location, where they transition from a regime with one real eigenvalue and a pair of complex conjugate eigenvalues to a regime with three real eigenvalues.

Figure 4.9(c) shows the relative contributions of normality-based strain self-amplification and vortex stretching mechanisms for the Burgers vortex tube. The contributions of the $\epsilon\varphi\varphi$ and $\epsilon\varphi\gamma$ vortex stretching terms are constrained to within the vortex boundary. They highlight that the 'vortex core stretching' term is primarily associated with the inner vortex core and the shear–rotation interaction term is associated with the region between the core and the boundary. By contrast, the $\epsilon\gamma\gamma$ vortex stretching term, which represents 'shear layer stretching,' is primarily associated with the shear annulus near the vortex boundary and the region outside the vortex boundary. In the nearly potential flow regime far from the vortex core, strain self-amplification is negative and dominated by the $\epsilon\epsilon\epsilon$ (normal straining) term. However, within the vortex boundary, it is positive and dominated by the $\epsilon\gamma\gamma$ term in the limit of $Re_\Gamma \to \infty$.

4.A2 Collapse of the multiscale velocity gradient partitioning

We analyze the multiscale velocity gradient partitioning for various simulations of forced isotropic turbulence to identify how key features of the partitioning collapse in terms of Re_λ and ℓ. In addition to the simulations discussed in Table 4.1, we consider DNS cases at $Re_\lambda \approx 61$, 100, and 160. These simulations are conducted on grids of size $N_x^3 = 64^3$, 128^3, and 256^3 and have spatial resolutions of $k_{max}\eta \approx 1.3$, 1.4, and 1.3, respectively. Each of these supplementary DNS cases consists of 68 temporal snapshots that are spaced one large-eddy turnover time apart.

Figure 4.10 shows how the partitioning varies as a function of filter width for $100 \lesssim Re_\lambda \lesssim 400$. It shows that the multiscale partitioning statistics collapse at sufficiently high values of Re_λ. The collapse at small scales is consistent with previous findings that the unfiltered partitioning collapses well for $Re_\lambda \gtrsim 200$ [23]. Table 4.3 further shows that the unfiltered partitioning statistics collapse

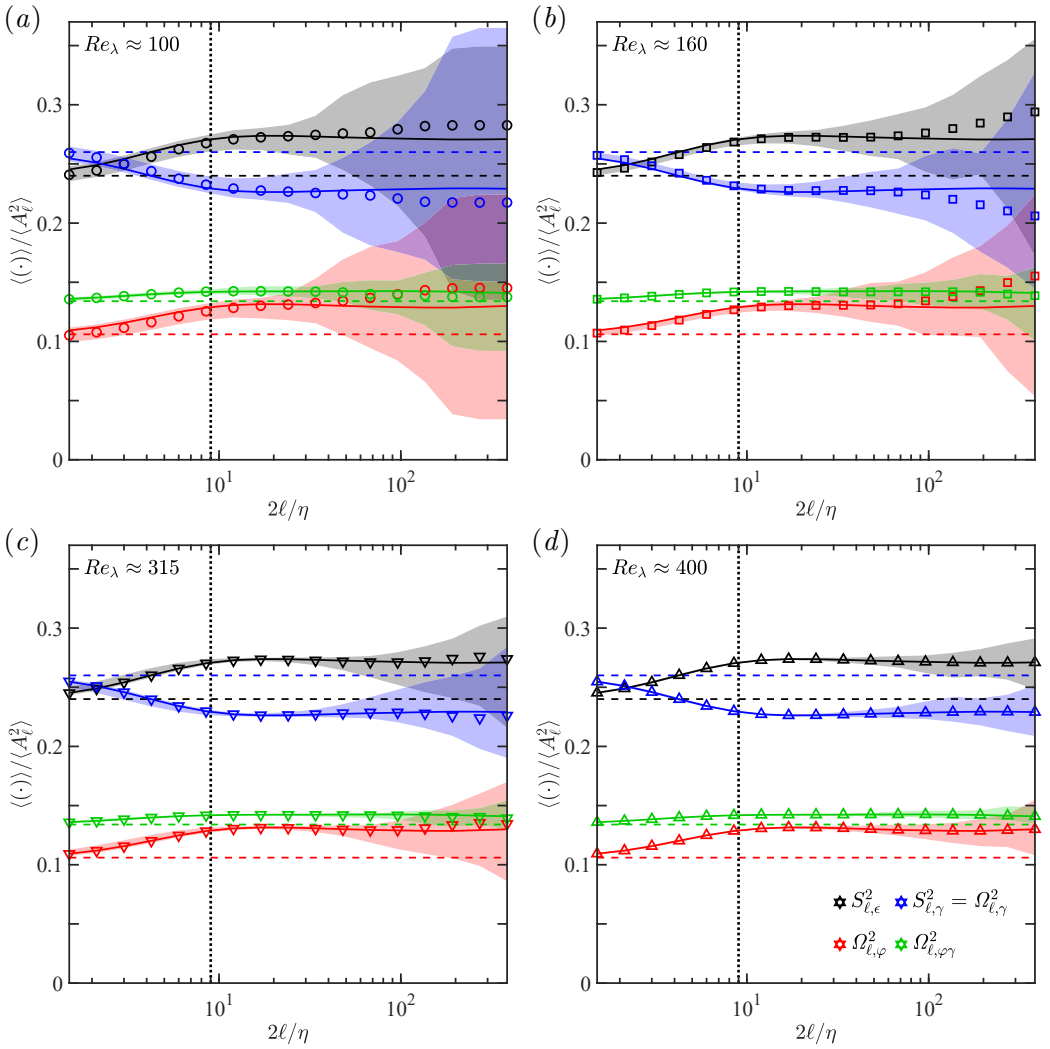

Figure 4.10: (a) Partitioning of filtered velocity gradients for DNS cases at various Reynolds numbers. The symbols represent averages over all snapshots and the shading represents ranges for single-snapshot averages. In all panels, the solid curves represent the averaged partitioning at $Re_\lambda \approx 400$, the horizontal dashed lines represent the unfiltered partitioning in the high-Re_λ limit, and the vertical dotted lines represent the typical thickness of small-scale shear layers, $\delta_\gamma = 9\eta$.

to within ± 0.001 for $Re_\lambda \gtrsim 315$. The collapse extends to larger scales as Re_λ increases and, for $Re_\lambda \gtrsim 315$, it extends well into the inertial range (to within ± 0.002), where the partitioning is also relatively insensitive to scale. The shaded regions in Figure 4.10 capture the extent to which the spatially averaged partitioning statistics vary in time for each simulation. For all cases, the magnitude of these variations decreases as ℓ decreases since the degree of scale separation from the forcing increases. This scale separation, combined

Type	Model	Re_λ	$2\ell/\eta$	$\frac{\langle S^2_{\ell,\epsilon}\rangle}{\langle A^2_\ell\rangle}$	$\frac{\langle A^2_{\ell,\gamma}\rangle}{\langle A^2_\ell\rangle}$	$\frac{\langle \Omega^2_{\ell,\varphi}\rangle}{\langle A^2_\ell\rangle}$	$\frac{\langle \Omega^2_{\ell,\varphi\gamma}\rangle}{\langle A^2_\ell\rangle}$
Random	Pope [69]	400	–	0.279	0.442	0.139	0.140
DNS	–	61	0	0.235	0.531	0.100	0.134
DNS	–	100	0	0.236	0.528	0.102	0.134
DNS	–	160	0	0.238	0.524	0.104	0.134
DNS	–	315	0	0.239	0.521	0.106	0.134
DNS	–	400	0	0.240	0.520	0.106	0.134
DNS	–	315	24	0.274	0.453	0.131	0.142
DNS	–	315	48	0.272	0.456	0.130	0.142
DNS	–	315	96	0.271	0.458	0.129	0.142
DNS	–	400	24	0.274	0.453	0.131	0.142
DNS	–	400	48	0.273	0.455	0.130	0.142
DNS	–	400	96	0.272	0.457	0.129	0.142
LES	Eddy viscosity	400	24	0.234	0.532	0.100	0.134
LES	Eddy viscosity	400	48	0.233	0.534	0.099	0.134
LES	Eddy viscosity	400	96	0.234	0.533	0.099	0.134
LES	Mixed	400	24	0.267	0.466	0.125	0.142
LES	Mixed	400	48	0.267	0.465	0.125	0.143
LES	Mixed	400	96	0.268	0.464	0.125	0.143

Table 4.3: Partitioning statistics produced by random velocity gradients and various DNS and LES cases. Each LES case represents a separate simulation where $\ell = \ell_{LES}$ represents the LES filter width.

with an increasing number of grid points, also explains why the variations at a given scale become smaller as Re_λ increases. For the $Re_\lambda \approx 315$ and 400 simulations, which correspond to DNS315 and DNS400 in Table 4.1, our results suggest that a single snapshot is sufficient to obtain converged velocity gradient statistics in the range $0 \leq 2\ell/\eta \leq 67.9$. This helps justify our use of two snapshots to compute the interscale energy transfer statistics in that range of scales for DNS315 and DNS400 (see §4.4.3).

Table 4.3 also provides a complementary view to the multiscale partitioning analysis for the LES cases in §4.4.1.2. Here, instead of plotting the multiscale partitioning statistics for a single LES, we consider the partitioning at the LES filter scale, ℓ_{LES}, and vary ℓ_{LES} across three different simulations. These simulations employ LES filter widths of $2\ell_{LES}/\eta = 24$, 48, and 96 and have grid sizes of $N_x^3 = 256^3$, 128^3, and 64^3, respectively. They each have a spatial resolution of $k_{max}\ell_{LES} \approx 3.0$, which is comparable to a DNS reso-

lution of $k_{max}\eta \approx 1.5$ [60]. Each of these supplementary LES cases consists of 68 temporal snapshots that are spaced half of a large-eddy turnover time apart. For all values of ℓ_{LES}, the partitioning statistics for the eddy viscosity simulations resemble those of the unfiltered DNS at $Re_\lambda \approx 61$, which has a Kolmogorov scale roughly 15 times larger. Further, the partitioning statistics for the mixed model simulations resemble those of the $Re_\lambda \approx 400$ DNS filtered at scale ℓ_{LES} and, as such, are relatively insensitive to ℓ_{LES}. These results support our main conclusions regarding the behavior of the eddy viscosity and mixed models over a broad range of LES filter widths. Although not shown, our conclusions are robust to different model formulations, including those considered by Kamal and Johnson [60].

Finally, we compare the partitioning statistics with those produced by random velocity gradients. The random case consists of 20 snapshots of size $N_x^3 = 1024^3$, where each snapshot represents a synthetic, divergence-free velocity field constructed from Fourier modes with Gaussian-random complex weights. These weights are rescaled to obey the model energy spectrum described in section 6.5.3 of Pope [69] with a Kolmogorov constant of $C = 1.5$ and a viscous roll-off parameter of $\beta = 5.2$. Interestingly, the inertial range partitioning statistics are more similar to those associated with the random case than they are to the unfiltered partitioning statistics. Moreover, the partitioning statistics for the random case, which are constant to within ± 0.002 for $0 \leq 2\ell/\eta \leq 384$, do not capture the enhanced relative contribution of shearing in the subinertial range. This suggests that the imprint of viscous-scale shear layers can be viewed as a defining feature of turbulence associated with the incompressible Navier–Stokes equations. The imprint may be encoded in the phases of the Fourier modes of the velocity field, which are uncorrelated for the random case.

References

[1]Kolmogorov, A.N. The local structure of turbulence in incompressible viscous fluid for very large Reynolds numbers. *Dokl. Akad. Nauk SSSR* **30**, 301–305, reprinted in *Proc. R. Soc. Lond.* A **434**, 9–13. (1941).

[2]Kolmogorov, A.N. A refinement of previous hypotheses concerning the local structure of turbulence in a viscous incompressible fluid at high Reynolds number. *J. Fluid Mech.* **13**, 82–85 (1962).

[3]Oboukhov, A.M. Some specific features of atmospheric tubulence. *J. Fluid Mech.* **13**, 77–81 (1962).

[4]Sreenivasan, K.R. and Antonia, R.A. The phenomenology of small-scale turbulence. *Annu. Rev. Fluid Mech.* **29**, 435–472 (1997).

[5]Meneveau, C. and Katz, J. Scale-invariance and turbulence models for large-eddy simulation. *Annu. Rev. Fluid Mech.* **32**, 1–32 (2000).

[6]Chong, M.S., Perry, A.E., and Cantwell, B.J. A general classification of three-dimensional flow fields. *Phys. Fluids A* **2**, 765–777 (1990).

[7]Meneveau, C. Lagrangian dynamics and models of the velocity gradient tensor in turbulent flows. *Annu. Rev. Fluid Mech.* **43**, 219–245 (2011).

[8]Johnson, P.L. and Wilczek, M. Multiscale velocity gradients in turbulence. *Annu. Rev. Fluid Mech.* **56**, 463–490 (2024).

[9]Hunt, J.C.R., Wray, A.A., and Moin, P. Eddies, streams, and convergence zones in turbulent flows. In Proceedings of the 1988 Summer Program (Center for Turbulence Research, 1988), pp. 193–208.

[10]Jeong, J. and Hussain, F. On the identification of a vortex. *J. Fluid Mech.* **285**, 69–94 (1995).

[11]Elsinga, G.E. and Marusic, I. Universal aspects of small-scale motions in turbulence. *J. Fluid Mech.* **662**, 514–539 (2010).

[12]Elsinga, G.E., Ishihara, T., Goudar, M.V., Silva, C.B. da, and Hunt, J.C.R. The scaling of straining motions in homogeneous isotropic turbulence. *J. Fluid Mech.* **829**, 31–64 (2017).

[13]Kronborg, J. and Hoffman, J. The triple decomposition of the velocity gradient tensor as a standardized real Schur form. *Phys. Fluids* **35**, 031703 (2023).

[14]Arun, R. and Colonius, T. Velocity gradient partitioning in turbulent flows. *J. Fluid Mech.* **1000**, R5 (2024).

[15]Kolář, V. 2D velocity-field analysis using triple decomposition of motion. In Proceedings of the 15th Australasian Fluid Mechanics Conference (The University of Sydney, 2004), AFMC00017.

[16]Kolář, V. Vortex identification: new requirements and limitations. *Intl J. Heat Fluid Flow* **28**, 638–652 (2007).

[17]Keylock, C.J. The Schur decomposition of the velocity gradient tensor for turbulent flows. *J. Fluid Mech.* **848**, 876–905 (2018).

[18]Keylock, C.J. Turbulence at the Lee bound: maximally non-normal vortex filaments and the decay of a local dissipation rate. *J. Fluid Mech.* **881**, 283–312 (2019).

[19]Keylock, C.J. The role of normal and non-normal contributions to enstrophy production in the near-wall region of a turbulent channel flow. *J. Fluid Mech.* **1006**, A3 (2025).

[20]Beaumard, P., Buxton, O.R.H., and Keylock, C.J. The importance of non-normal contributions to velocity gradient tensor dynamics for spatially developing, inhomogeneous, turbulent flows. *J. Turbul.* **20**, 577–598 (2019).

[21]Bilbao-Ludena, J.C. and Papadakis, G. Non-normality and small-scale statistics in a three-dimensional, separated shear flow. *J. Fluid Mech.* **1010**, A41 (2025).

[22]Arun, R. and Colonius, T. Velocity gradient analysis of a head-on vortex ring collision. *J. Fluid Mech.* **982**, A16 (2024).

[23]Das, R. and Girimaji, S.S. Revisiting turbulence small-scale behavior using velocity gradient triple decomposition. *New J. Phys.* **22**, 063015 (2020).

[24]Gao, Y. and Liu, C. Rortex and comparison with eigenvalue-based vortex identification criteria. *Phys. Fluids* **30**, 085107 (2018).

[25]Liu, C., Gao, Y., Tian, S., and Dong, X. Rortex—a new vortex vector definition and vorticity tensor and vector decompositions. *Phys. Fluids* **30**, 035103 (2018).

[26]Liu, C., Gao, Y., Dong, X., Wang, Y., Liu, J., Zhang, Y., Cai, X., and Gui, N. Third generation of vortex identification methods: Omega and Liutex/Rortex based systems. *J. Hydrodyn.* **31**, 205–223 (2019).

[27]Nagata, R., Watanabe, T., Nagata, K., and da Silva, C.B. Triple decomposition of velocity gradient tensor in homogeneous isotropic turbulence. *Comput. Fluids* **198**, 104389 (2020).

[28]Watanabe, T., Tanaka, K., and Nagata, K. Characteristics of shearing motions in incompressible isotropic turbulence. *Phys. Rev. Fluids* **5**, 072601 (2020).

[29]Watanabe, T. and Nagata, K. The response of small-scale shear layers to perturbations in turbulence. *J. Fluid Mech.* **963**, A31 (2023).

[30]Fiscaletti, D., Buxton, O.R.H., and Attili, A. Internal layers in turbulent free-shear flows. *Phys. Rev. Fluids* **6**, 034612 (2021).

[31]Jiménez, J., Wray, A.A., Saffman, P.G., and Rogallo, R.S. The structure of intense vorticity in isotropic turbulence. *J. Fluid Mech.* **255**, 65–90 (1993).

[32]Ghira, A.A., Elsinga, G.E., and Silva, C.B. da Characteristics of the intense vorticity structures in isotropic turbulence at high Reynolds numbers. *Phys. Rev. Fluids* **7**, 104605 (2022).

[33]Leonard, A. Energy cascade in large-eddy simulations of turbulent fluid flows. In *Turbulent Diffusion in Environmental Pollution*, Vol. 18, edited by Frenkiel, F.N. and Munn, R.E., Advances in Geophysics (Elsevier, 1975), pp. 237–248.

[34]Borue, V. and Orszag, S.A. Local energy flux and subgrid-scale statistics in three-dimensional turbulence. *J. Fluid Mech.* **366**, 1–31 (1998).

[35]Eyink, G.L. and Aluie, H. Localness of energy cascade in hydrodynamic turbulence. I. Smooth coarse graining. *Phys. Fluids* **21**, 115107 (2009).

[36]Ballouz, J.G. and Ouellette, N.T. Tensor geometry in the turbulent cascade. *J. Fluid Mech.* **835**, 1048–1064 (2018).

[37]Park, D. and Lozano-Durán, A. The coherent structure of the energy cascade in isotropic turbulence. *Sci. Rep.* **15**, 14 (2025).

[38]Dong, S., Huang, Y., Yuan, X., and Lozano-Durán, A. The coherent structure of the kinetic energy transfer in shear turbulence. *J. Fluid Mech.* **892**, A22 (2020).

[39]Wang, J., Wan, M., Chen, S., and Chen, S. Kinetic energy transfer in compressible isotropic turbulence. *J. Fluid Mech.* **841**, 581–613 (2018).

[40]Aluie, H. Coarse-grained incompressible magnetohydrodynamics: analyzing the turbulent cascades. *New J. Phys.* **19**, 025008 (2017).

[41]Alexakis, A. and Chibbaro, S. Local fluxes in magnetohydrodynamic turbulence. *J. Plasma Phys.* **88**, 905880515 (2022).

[42]Capocci, D., Johnson, P.L., Oughton, S., Biferale, L., and Linkmann, M. Energy flux decomposition in magnetohydrodynamic turbulence. *J. Plasma Phys.* **91**, E11 (2025).

[43]Aluie, H., Hecht, M., and Vallis, G.K. Mapping the energy cascade in the North Atlantic Ocean: the coarse-graining approach. *J. Phys. Oceanogr.* **48**, 225–244 (2018).

[44]Storer, B.A., Buzzicotti, M., Khatri, H., Griffies, S.M., and Aluie, H. Global cascade of kinetic energy in the ocean and the atmospheric imprint. *Sci. Adv.* **9**, eadi7420 (2023).

[45]Yao, H., Schnaubelt, M., Szalay, A.S., Zaki, T.A., and Meneveau, C. Comparing local energy cascade rates in isotropic turbulence using structure-function and filtering formulations. *J. Fluid Mech.* **980**, A42 (2024).

[46]Carbone, M. and Bragg, A.D. Is vortex stretching the main cause of the turbulent energy cascade?, *J. Fluid Mech.* **883**, R2 (2020).

[47]Enoki, R., Watanabe, T., and Nagata, K. Statistical properties of shear and nonshear velocity components in isotropic turbulence and turbulent jets. *Phys. Rev. Fluids* **8**, 104602 (2023).

[48]Fathali, M. and Khoei, S. Spectral energy transfer analysis of a forced homogeneous isotropic turbulence using triple decomposition of velocity gradient tensor. *J. Turbul.* **25**, 125–143 (2024).

[49]Johnson, P.L. Energy transfer from large to small scales in turbulence by multiscale nonlinear strain and vorticity interactions. *Phys. Rev. Lett.* **124**, 104501 (2020).

[50]Johnson, P.L. On the role of vorticity stretching and strain self-amplification in the turbulence energy cascade. *J. Fluid Mech.* **922**, A3 (2021).

[51]Clark, R.A., Ferziger, J.H., and Reynolds, W.C. Evaluation of subgrid-scale models using an accurately simulated turbulent flow. *J. Fluid Mech.* **91**, 1–16 (1979).

[52]Donzis, D.A. and Sreenivasan, K.R. The bottleneck effect and the kolmogorov constant in isotropic turbulence. *J. Fluid Mech.* **657**, 171–188 (2010).

[53]Falkovich, G. Bottleneck phenomenon in developed turbulence. *Phys. Fluids* **6**, 1411–1414 (1994).

[54]Kurien, S., Taylor, M.A., and Matsumoto, T. Cascade time scales for energy and helicity in homogeneous isotropic turbulence. *Phys. Rev. E* **69**, 066313 (2004).

[55]Frisch, U., Kurien, S., Pandit, R., Pauls, W., Ray, S.S., Wirth, A., and Zhu, J.-Z. Hyperviscosity, Galerkin truncation, and bottlenecks in turbulence. *Phys. Rev. Lett.* **101**, 144501 (2008).

[56]Verma, M.K. and Donzis, D. Energy transfer and bottleneck effect in turbulence. *J. Phys.* A **40**, 4401–4412 (2007).

[57]Kraichnan, R.H. Eddy viscosity in two and three dimensions. *J. Atmos. Sci.* **33**, 1521–1536 (1976).

[58]Chen, S., Ecke, R.E., Eyink, G.L., Rivera, M., Wan, M., and Xiao, Z. Physical mechanism of the two-dimensional inverse energy cascade. *Phys. Rev. Lett.* **96**, 084502 (2006).

[59]Xiao, Z., Wan, M., Chen, S., and Eyink, G.L. Physical mechanism of the inverse energy cascade of two-dimensional turbulence: a numerical investigation. *J. Fluid Mech.* **619**, 1–44 (2009).

[60]Kamal, M. and Johnson, P.L. Artificial bottleneck effect in large eddy simulations. *Phys. Rev. Fluids* **9**, 084605 (2024).

[61]Johnson, P.L. A physics-inspired alternative to spatial filtering for large-eddy simulations of turbulent flows. *J. Fluid Mech.* **934**, A30 (2022).

[62]Betchov, R. An inequality concerning the production of vorticity in isotropic turbulence. *J. Fluid Mech.* **1**, 497–504 (1956).

[63]Cardesa, J.I., Vela-Martín, A., and Jiménez, J. The turbulent cascade in five dimensions. *Science* **357**, 782–784 (2017).

[64]Patterson, G.S. and Orszag, S.A. Spectral calculations of isotropic turbulence: efficient removal of aliasing interactions. *Phys. Fluids* **14**, 2538–2541 (1971).

[65]Eyink, G.L. Local energy flux and the refined similarity hypothesis. *J. Stat. Phys.* **78**, 335–351 (1995).

[66]Watanabe, T., Mori, T., Ishizawa, K., and Nagata, K. Scale dependence of local shearing motion in decaying turbulence generated by multiple-jet interaction. *J. Fluid Mech.* **997**, A14 (2024).

[67]Shen, W., Yao, J., and Yang, Y. Designing turbulence with entangled vortices. *Proc. Natl Acad. Sci.* **121**, e2405351121 (2024).

[68]Misra, A. and Pullin, D.I. A vortex-based subgrid stress model for large-eddy simulation. *Phys. Fluids* **9**, 2443–2454 (1997).

[69]Pope, S.B. Turbulent flows. (Cambridge University Press, 2000).

Chapter 5

CONCLUDING REMARKS

"In a time of turbulence and change, it is more true than ever that knowledge is power; for only by true understanding and steadfast judgment are we able to master the challenge of history."

—John F. Kennedy [1]

5.1 Summary of contributions

We have contributed to the development, application, and interpretation of a normality-based framework for analyzing velocity gradients in turbulent flows. This framework identifies contributions from normal straining, pure shearing, and rigid rotation using the ordered real Schur form of the velocity gradient tensor (VGT). It provides a principled approach to identify flow features, such as vortex cores and shear layers, that are obscured by conventional symmetry-based analyses. In doing so, it yields valuable insights for distinguishing flow regimes, capturing mechanisms that sustain turbulence, and assessing the performance of turbulence models.

In Chapter 2 [2], we used the normality-based framework to partition the strength of velocity gradients in a collision of two vortex rings. The initial vortex rings have a strong imprint from rigid rotation that is associated with their core vorticity profiles. At the relatively high circulation Reynolds number considered, their collision transitions to a turbulent state due to the action of the elliptic instability. We showed that the statistical imprint of the elliptic instability is captured by enhanced shear–rotation correlations. Further, by deriving novel algebraic expressions for the partitioning constituents, we showed how this imprint reflects geometric features of local streamlines that are relevant to the phenomenology of the elliptic instability. Remarkably, the partitioning of the decaying turbulent cloud produced by the collision is similar to the partitioning observed in forced isotropic turbulence, despite the fact that the cloud is neither sustained nor entirely isotropic. These distinctive features of the initial, transitional, and turbulent regimes of the collision are not captured by an analogous symmetry-based partitioning since the averaged strength of the strain-rate and vorticity tensors are equipartitioned throughout the simulation.

In Chapter 3 [3], motivated by the partitioning of the decaying turbulent cloud, we assessed the applicability of the isotropic partitioning in a broad range of wall-bounded turbulent flows, including channels and boundary layers. We showed that, at sufficiently high friction Reynolds numbers, the partitioning far from the wall (where the mean shearing is relatively weak) collapses onto the isotropic partitioning. By contrast, the near-wall partitioning is dominated by shearing. The evolution of the partitioning from the near-wall regime to the nearly-isotropic regime collapses reasonably well in inner units for the flows considered. However, due to the imprint of an exterior potential flow, the partitioning for the boundary layers diverges from the isotropic partitioning in the freestream and, within the boundary layers, has a stronger contribution from normal straining than that for the channels. The distinctive features of these spatial regimes in wall-bounded flows are again not captured by the symmetry-based partitioning since its variations with respect to the isotropic partitioning are small and non-monotonic.

Finally, in Chapter 4 [4], we extended the normality-based framework to a multiscale setting by applying it to filtered velocity gradients in direct and large-eddy simulations of isotropic turbulence. Our multiscale partitioning analysis reveals that filtering mitigates the relative contribution of pure shearing to the velocity gradients in the subinertial range of the energy cascade. As before, this effect is not captured by the multiscale symmetry-based partitioning due to the equipartitioning of the filtered strain-rate and vorticity tensors. Moreover, we developed a novel approach to capture the contributions of normality-based flow features, like vortex cores and shear layers, to interscale energy transfer via a multiscale velocity gradient expansion of the residual stress tensor. Our approach illuminates the significant contribution of shear layers to a broad range of mechanisms responsible for interscale energy transfer. Interestingly, their contribution to vortex stretching is significantly stronger than that of vortex cores. This suggests that supplementing the conventional picture of stretched vortices, which are often modeled as Burgers vortex tubes, with contributions from stretched shear layers, which can be modeled as Burgers vortex layers, would provide a more accurate description of the flow structures responsible for energy transfer. Burgers vortex layers appear particularly suitable given that the normal straining of shear layers is responsible for the majority of scale-local strain self-amplification and vortex stretching in the cascade. We also showed that shear layers dominate the

net backscatter produced by a strain–vorticity covariance mechanism, which contributes to the bottleneck effect in the subinertial range of the cascade. Furthermore, by developing an analysis of resolved energy transfer in large-eddy simulation (LES), we showed that they are responsible for the artificial bottleneck effect produced by an eddy viscosity model in the inertial range. This reflects that the eddy viscosity model replicates flow features, including pronounced sheet-like shear layers, that are associated with an unfiltered direct numerical simulation (DNS) at a lower Taylor-scale Reynolds number. By contrast, a mixed model more accurately captures the features associated with a filtered DNS by explicitly resolving scale-local energy transfer at the LES filter scale.

Altogether, this thesis makes a case for using a normality-based approach to better understand and model turbulent flows. Although this approach is slightly more involved than the conventional symmetry-based approach, its computational cost is reasonable even for relatively large turbulence datasets. We have made an instructional code that implements the normality-based analysis openly available in the Caltech Data Repository.

5.2 Outlook for future work

This thesis contributes to longstanding efforts to compellingly synthesize the statistical, structural, and dynamical properties of small-scale turbulence. Our normality-based analyses open several lines of further inquiry in this area, ranging from direct extensions of our work to long-term research prospects.

A key finding of this thesis is the applicability of the velocity gradient partitioning associated with isotropic turbulence to appropriate regimes of a broad range of turbulent flows. However, our analyses were limited to canonical unbounded and wall-bounded flows governed by the incompressible Navier–Stokes equations. Direct extensions of our work could assess how compressibility, stratification, multiphase effects, and other complications affect the partitioning and the structural features it encodes. In Chapter 3, we showed that the mean shearing strength is a reasonable parameter for modeling the wall-normal variations of the partitioning in channels and boundary layers. Developing more rigorous and effective techniques to predict the partitioning in terms of mean flow variables would be particularly useful for applications to more complex and realistic flow configurations. This could aid the develop-

ment of predictive models for effects relevant to engineering applications, such as drag and separation in wall-bounded flows and sound generation in free-shear flows. Furthermore, conditional partitioning analyses could elucidate how structures like vortex cores and shear layers contribute to these effects.

Another key finding of this thesis is the ability of the normality-based approach to identify distinctive fingerprints of mechanisms that sustain turbulent flows. In Chapter 2, we showed that it can tease out the statistical imprint of the elliptic instability from an intricate web of vortical flow structures. Assessing how well our approach can distinguish between contributions from the elliptic and Crow instabilities in the turbulent regime would provide insight into the uniqueness of this imprint. This would help address ongoing debates [5–8] regarding the relevance of two proposals for prototypical cascade mechanisms: iterative elliptic instabilities [5] and successive vortex reconnections [6]. Furthermore, given that the partitioning can distinguish the imprints of vortex cores and shear layers, it may also encode an imprint of the Kelvin–Helmholtz instability (which is associated with shear layers) in turbulent settings. Beyond analyzing statistical imprints, analyzing the temporal evolution of the flow structures that produce them could inspire improved models of the mechanisms underlying the energy cascade. For example, time-resolved analyses could clarify whether the hypothesis that a vortex thinning mechanism drives the backscatter associated with the bottleneck effect [9] is consistent with our observation in Chapter 4 that the backscatter is dominated by contributions from shear vorticity. Similar analyses can be used to interrogate the current sheet thinning mechanism proposed to dominate energy transfer in the inertial range of magnetohydrodynamic turbulence [10].

Despite its advantages, the normality-based decomposition we consider has room for improvement. As discussed in Chapters 3 and 4, its application and interpretation in turbulence modeling settings is complicated by the fact that, unlike the symmetry-based decomposition, it does not commute with averaging or filtering operations. In this thesis, we have advocated for averaging-first and filtering-first approaches to facilitate insights relevant to turbulence modeling. Beyond this, it would be interesting to develop a framework that synthesizes the commutativity properties of the symmetry-based decomposition with the expressivity of the normality-based decomposition. As demonstrated in §2.5.1 and §4.A1, another limitation of the normality-based decomposition is that its

constituents are not differentiable when the discriminant of the VGT changes sign due to the behavior of the eigenvalues of the VGT. Although this did not affect our approach, it may hinder the formulation of interpretable models for the dynamics of the normality-based constituents. Developing an approach that alleviates this issue could help characterize the dynamics of vortex cores, shear layers, and other flow features in a manner inaccessible by our approach.

Finally, we identify open-ended research prospects motivated by our results. A striking theme of this thesis is the importance of small-scale shear layers to the sustenance of turbulent flows. However, to our knowledge, there is no compelling explanation for (i) why shear layers are so important to turbulent flows and (ii) why they are so pronounced near the viscous range. An approach that predicts these phenomena from first principles would provide insight into the Navier–Stokes equations and potentially enable predictions of how the structure of small-scale turbulence responds to modifications of the governing equations. Moreover, the interpretation of our results is rooted in the spatially linear approximation of the local velocity field encoded by the VGT. Including higher-order terms in the Taylor expansion of the velocity field could help identify and classify a broader spectrum of local flow structures with larger domains of applicability. It would also be interesting to formulate an analysis of velocity increments in the spirit of our normality-based approach since they are directly related to filtered velocity gradients [9, 11] and interscale energy transfer [12]. Lastly, the results of this thesis are broadly applicable in the realm of turbulence modeling. One particularly intriguing application would be the development of a structural closure model that incorporates subgrid-scale shear layers in the spirit of the stretched vortex subgrid-scale model [13].

5.3 An afterword on the anatomy of turbulence

In closing, we briefly reexamine the proverb that vortices are the 'sinews and muscles of fluid motions' [14, 15]. Arguably, the general acceptance of this description has permeated many facets of turbulence research, including vortex identification, structural modeling, and dynamical analysis. While any such metaphor is doomed to imperfection, it is worth mentioning that the results of this thesis suggest a slightly different picture. We propose that *shear layers* more aptly capture the sinews and muscles of turbulence, whereas vortices form more of a 'skeleton' on which the shear layers are scaffolded. As depicted

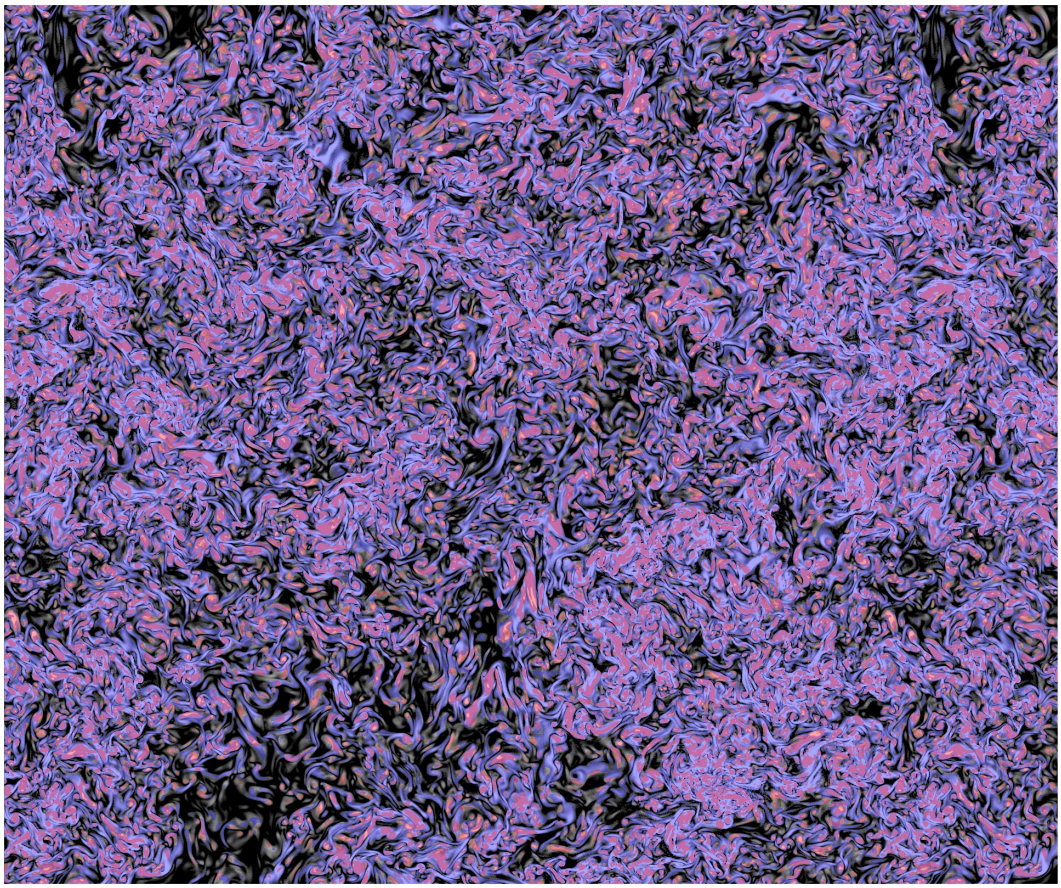

Figure 5.1: Visualization of the vorticity strength, ω^2, in a slice of isotropic turbulence at a Taylor-scale Reynolds number of $Re_\lambda \approx 400$ overlaid with contours of the contributions from rigid rotation (red) and shear vorticity (blue) at a threshold of $0.15\,\langle\omega^2\rangle$, where $\langle\cdot\rangle$ denotes averaging over the slice.

in Figure 5.1, this analogy is consistent with the tendency of space-filling shear layers to connect, wrap around, and otherwise interact with spatially localized vortices. Although it is not worth pursuing this analogy too far, it illustrates a core message of this thesis: *the important (yet perhaps overlooked) role of small-scale shear layers in turbulent flows.*

References

[1]Kennedy, J.F. Address at the University of California at Berkeley. Charter Day, March 23, 1962.

[2]Arun, R. and Colonius, T. Velocity gradient analysis of a head-on vortex ring collision. *J. Fluid Mech.* **982**, A16 (2024).

[3]Arun, R. and Colonius, T. Velocity gradient partitioning in turbulent flows. *J. Fluid Mech.* **1000**, R5 (2024).

[4]Arun, R., Kamal, M., Colonius, T., and Johnson, P.L. Normality-based analysis of multiscale velocity gradients and energy transfer in direct and large-eddy simulations of isotropic turbulence. *J. Fluid Mech.* **1021**, A47 (2025).

[5]McKeown, R., Ostilla-Mónico, R., Pumir, A., Brenner, M.P., and Rubinstein, S.M. Turbulence generation through an iterative cascade of the elliptical instability. *Sci. Adv.* **6**, eaaz2717 (2020).

[6]Yao, J. and Hussain, F. A physical model of turbulence cascade via vortex reconnection sequence and avalanche. *J. Fluid Mech.* **883**, A51 (2020).

[7]Mishra, A., Pumir, A., and Ostilla-Mónico, R. Instability and disintegration of vortex rings during head-on collisions and wall interactions. *Phys. Rev. Fluids* **6**, 104702 (2021).

[8]Ostilla-Mónico, R., McKeown, R., Brenner, M.P., Rubinstein, S.M., and Pumir, A. Cascades and reconnection in interacting vortex filaments. *Phys. Rev. Fluids* **6**, 074701 (2021).

[9]Johnson, P.L. On the role of vorticity stretching and strain self-amplification in the turbulence energy cascade. *J. Fluid Mech.* **922**, A3 (2021).

[10]Capocci, D., Johnson, P.L., Oughton, S., Biferale, L., and Linkmann, M. Energy flux decomposition in magnetohydrodynamic turbulence. *J. Plasma Phys.* **91**, E11 (2025).

[11]Eyink, G.L. Local energy flux and the refined similarity hypothesis. *J. Stat. Phys.* **78**, 335–351 (1995).

[12]Yao, J. and Hussain, F. On singularity formation via viscous vortex reconnection. *J. Fluid Mech.* **888**, R2 (2020).

[13]Misra, A. and Pullin, D.I. A vortex-based subgrid stress model for large-eddy simulation. *Phys. Fluids* **9**, 2443–2454 (1997).

[14]Küchemann, D. Report on the I.U.T.A.M. symposium on concentrated vortex motions in fluids. *J. Fluid Mech.* **21**, 1–20 (1965).

[15]Saffman, P.G. Vortex dynamics. (Cambridge University Press, 1993).